Order Number 9230403

# The Australian monsoon and its mesoscale convective systems

Mapes, Brian E., Ph.D.

University of Washington, 1992

U·M·I
300 N. Zeeb Rd.
Ann Arbor, MI 48106

# The Australian Monsoon and its Mesoscale Convective Systems

by

Brian Mapes

A dissertation submitted in partial fulfillment

of the requirements for the degree of

Doctor of Philosophy

University of Washington

1992

Approved by Robert A. Houze, Jr.

(Chairperson of supervisory committee)

Program Authorized
to offer degree Atmospheric Sciences
Date June 2, 1992

In presenting this dissertation in partial fulfillment of the requirements for the Doctoral degree at the University of Washington, I agree that the Library shall make its copies freely available for inspection. I further agree that extensive copying of this dissertation is allowable only for scholarly purposes, consistent with "fair use" as prescribed in the U.S. Copyright Law. Requests for copying or reproduction of this dissertation may be referred to University Microfilms, 1490 Eisenhower Place, P.O. Box 975, Ann Arbor, MI 48106, to whom the author has granted "the right to reproduce (a) copies of the manuscript in microform and/or (b) printed copies of the manuscript made from microform."

Signature Brian M Mayer

Date JUNE 1, 1992

University of Washington

Abstract

The Australian Monsoon and its Mesoscale Convective Systems

by Brian Mapes

Chairperson of the Supervisory Committee: Professor Robert A. Houze, Jr.
Department of Atmospheric Sciences

The 1987 Australian monsoon was a geographically localized, temporally evolving cloud and wind system observed with satellites, rawinsondes, radar and aircraft. These data are presented, with theory filling the gaps, in illustration of its dynamics.

The engine of the monsoon is its embedded convection, which occurs in the form of mesoscale convective systems (MCSs) of a variety of sizes. Ten such MCSs were explored with aircraft and airborne Doppler radar. They were all consistent with the basic conceptual model of MCSs: multicellular convection, in lines or arcs along the edges of dense surface outflows from convective downdrafts, aging and evolving into areas of stratiform precipitation. This temporal evolution process has been divided into three stages: "convective," "intermediary," and "stratiform." Dozens of Doppler radar divergence profiles have been obtained in precipitation areas within each stage. A remarkable consistency prevails from one MCS to the next, nearly independent of mesoscale morphology or synoptic setting.

Convective areas had low-level convergence, with its peak elevated off the surface, and divergence above ~8 km altitude. Intermediary areas were characterized by very little divergence signal through most of the lower troposphere, but a strong convergence near 10 km altitude, apparently associated with upper-tropospheric ascent. Stratiform areas had midlevel convergence sandwiched between divergent layers, indicating a mesoscale updraft aloft and mesoscale downdraft below the melting level. These divergence profiles are indicative of the thermal forcing of the monsoon by the convection, and in fact may be more useful than the heating profile estimates which could be derived from them.

The response of the atmosphere to embedded thermal forcing is considered. A mechanistic description of the immediate, local response of a fluid to buoyancy forcing is

presented in chapter 2. Because pressure perturbations are related to the vertical gradient of buoyancy through an inverse Laplacian relationship, the pressure field around a buoyant parcel becomes smoother and simpler with distance.

In a stratified fluid, as a buoyant parcel's induced pressure perturbation field pushes down on neighboring fluid, that fluid in turn becomes buoyant, and hence pushes down on its neighboring fluid, *etc.* These dynamics are encapsulated in the gravity wave dispersion relation, which states that thermal disturbances travel through a stratified fluid at a speed proportional to their vertical depth. A heat source with complex vertical structure excites disturbances ("buoyancy bores"), of many depths, that separate themselves out with distance from the heat source. Hence the deeper components of a heat source can be found at greater distances from the heat source, at any given moment in time and also in the limit of long time in a rotating or dissipative fluid.

On synoptic time scales, long compared to gravity wave transit times, the net result of a unit of localized heating is an incremental displacement of air in a vertical (divergent) circulation cell which extends out to a deformation radius from the heating. On the rotating earth, tangential (rotational) flows are induced by this horizontal displacement, and an accompanying thermal structure develops, in accord with thermal wind considerations.

In the monsoon, low-level cyclonic circulation and a warm core aloft are observed, consistent with these expected effects of embedded MCS heating. Low-level dynamical processes initiate a lot of deep convection within the active cyclonic areas of the monsoon trough, despite the warm core aloft and the consequent (small) decrease in CAPE. In 1987, four tropical cyclones were generated in the monsoon by this runaway positive feedback loop (which evidently results from several mechanisms, discussed in chapter 4).

Time-mean horizontal and vertical distributions of monsoon vorticity are examined in chapter 5. Two forcing terms appear in the vorticity equation, representing the two dynamical effects of MCSs. Vertical momentum transport causes small-scale vortex pairs in the upper troposphere, while net MCS divergence "stretches" vorticity at all scales up to a deformation radius. The dispersion of vertical structure is evident in the monsoon. Divergence and vorticity profiles averaged over all north Australia show only a deep, simple "gravest mode" vertical structure, while profiles observed by the much smaller Gulf of Carpentaria rawinsonde array, in the vicinity of the convective heat source, indicate some of its finer vertical structure.

## LIST OF FIGURES

## ACKNOWLEDGEMENTS

Sincere thanks are offered to Professor Robert A. Houze, Jr. for his persistent vision of the "big picture" and his sustaining faith and support. Professor Christopher Bretherton supplied ideas which drew me forward as a carrot draws a donkey. This research would not have been possible without the computational mentorship and software legacy of Dr. Dean Churchill. Dr. Frank Marks and Nancy Figueroa of HRD, and Tony Ross at the UW, worked hard at the thankless task of data preprocessing. The work of Steven Bograd, Chungli Wang, and Stefan Lüthi also contributed to this dissertation.

## FOREWORD

This dissertation joins a vast body of literature concerning tropical convection, mesoscale convective systems (MCSs), the interaction of convection with flows on larger scales, and monsoon meteorology.

This work was impelled by the availability (and limitations) of observations, rather than by hypothesis or theory *per se* (though hypotheses underlay the data collection process). The ultimate goal, as laid out in the grant proposals which funded the research, was to measure the vertical structure of MCS thermal forcing of the tropical troposphere. The Doppler radar measurements of divergence in MCSs (section 3.1.2) are thus the central "results" of this project. But observations alone are somewhat unsatisfying in the absence of simple models of the meaning and implications of features in the observations. Many estimates of heating by tropical convection are already on the shelf, broadly consistent but differing in the details, which are known to matter but in unclear ways.

In this work I have attempted to find a unifying framework, *i.e.* a self-consistent terminology, within which to view all of the available observations of the 1987 Australian monsoon, on all size scales. This framework was designed to express physical principles in terms of observable variables, and in particular to focus attention on horizontal divergence rather that the unobservable heating. This dissertation is thus meant to be *comprehensive* rather than *exhaustive*. The cost of this comprehensiveness is that no quantitative diagnostic calculations beyond a "back of the envelope" level have been performed.

The "buoyancy bore' description of the divergent atmospheric response to heating (chapter 2), and the simple modern formulation of the vorticity equation expressing the rotational response (chapter 5), are important parts of the work. In both cases the mathematics was lifted more or less directly from other authors. But these twin frameworks allowed me to translate the straightforward (and not entirely new) observation that the low-level convergence into MCSs peaks above the surface into statements about important scientific problems: the elevated circulation observed in the early stages of tropical cyclogenesis, and the "superclustering" of tropical convection.

The 1987 Australian monsoon was a well-defined, localized tropical meteorological system subjected to the full scrutiny of much of the best observing

technology available at that time, on a variety of scales from microphysical to planetary. The presumption underlying this dissertation is that it should be possible to say *something* about all outstanding questions in tropical meteorology, on many spatial scales, with the resulting data set. As a result, this is not a tightly focused document or an unwavering line of argument leading inescapably to a final, summarizable thrust. There is much detail, especially in chapter 3, that might not seem very important to the overall theme but that would be a shame to lose. I have tried to include introductiory material at the beginning of each chapter and section to place the material in context.

Several factors made possible the diversity of data analyses utilized in this dissertation. Not least was the wealth of computer resources available to me (especially a MASSCOMP color graphics work station, already obsolete by today's standards). The *lack of* off-the-shelf software forced me to decide what were the best things I could possibly do with the available data, and then write programs to do them. The difficulty of airborne Doppler radar analysis scared off all other users of the Doppler data set, and drove me to devise a new, simple, robust way to extract the most important information from the vast collection of data. The ease (by comparison) of analyzing soundings, gridded synoptic fields, and satellite data encouraged me to perform my own analyses and not just refer to the specialized papers which presented those data in isolation. All this, of course, took place within the breathing room that only a student has: the first publications from this work are just now getting accepted for publication, more than five years after the data collection effort.

Chapter 1 contains a brief historical introduction to tropical convection and its scales of organization, followed by a descriptive overview of the 1987 Australian monsoon and the data available to study it. Chapter 2 contains some theoretical background material on buoyant convection in a stratified fluid, including a new and, to me, illuminating view of the gravity wave-like "buoyancy bores" which mediate the atmospheric response to embedded convection. Aircraft and airborne Doppler radar observations of ten MCSs in the Australian monsoon are presented in Chapter 3, in both a composite or generalized form (section 3.1) and in full detail (section 3.2). Chapter 4 considers the ways in which environmental thermodynamic conditions, representing the effects of larger scales of motion, modulate the occurrence of convection. This is the "down-scale" half of convection-large scale interaction. The "up-scale" half, namely the impact of convection on larger scales of motion, is considered in Chapter 5. Much of this

material is being published in the reviewed literature (Mapes and Houze 1992ab, Mapes 1992).

# CHAPTER 1

# INTRODUCTION

## *1.1 Tropical convection: from hot towers to superclusters*

Deep convection in the "equatorial trough zone" constitutes the major heat source for the atmosphere, as pointed out by Riehl and Malkus (1958). The solar energy absorbed by the vast, dark subtropical oceans evaporates water, which flows as vapor into the trough and condenses out in rain-producing clouds. In this way the solar energy is finally realized as heating, and is exported as potential energy in the upper tropospheric outflow, primarily to the winter hemisphere. Riehl and Malkus noted that the bulk effect of these equatorial precipitating clouds is notably unlike diffusion, in that they carry low-level air with high "total static energy" (a.k.a. moist static energy) through a midtropospheric minimum in that conserved quantity, and deposit the air in the upper troposphere. Their term for these unresolved, penetrative, energy-transporting clouds was "hot towers," although they recognized the existence of downdrafts as well as deep updrafts.

Within the equatorial belt, convective cloudiness is highly clustered and localized. Observations collected during the GARP Atlantic Tropical Experiment (GATE) made clear the fact that tropical convection is frequently organized on the mesoscale (*e.g.* Houze and Betts 1981). This stands in contrast to 1970's models of tropical convection as "cumulus ensembles" (although cumulus ensemble models do appear to have enough internal degrees of freedom to adequately represent the effects of convection on its environment). In addition to, and in association with, precipitating deep convective cells, mesoscale precipitating anvil clouds are observed. These ubiquitous "stratiform precipitation areas" are characterized by upward air motion in the upper troposphere, downward motion in the lower troposphere, and a radar bright band at the melting level. The stratiform precipitation arises form antecedent deep convection, as old convective elements or cells which get cut off from the source of subcloud layer convective updraft air merge together and decay (*e.g.* Houze 1977, Leary and Houze 1979).

The agents of mesoscale organization are convective and mesoscale downdrafts, as outlined by Zipser (1969, 1977) and Houze (1977). Convective downdraft air, which spreads out at the surface, has low equivalent potential temperature $\theta_e$, and as a result is

unsuitable for deep ascent until surface fluxes act on it for a substantial fraction of a day. Mesoscale downdraft air just above the subcloud layer is anomalously dry and warm, with the effect that subcloud layer air not only cannot penetrate through it in buoyant updrafts, but also entrains it, becoming drier in the process (Zipser 1977). These effects supress the formation of new deep convection in the wake of previous convective systems. At the same time, the dense convective downdraft air, often called a "cold pool," lifts subcloud layer air at its edges as is spreads out along the surface, thus triggering the formation of new convection. Downdrafts therefore act, both negatively and positively, to organize deep convective activity on the mesoscale.

The resulting mesoscale units, consisting of an ensemble of deep convective cells, frequently oriented in a line or arc, and the resulting stratiform precipitation areas, were called "mesoscale precipitation features" (MPFs) by Leary and Houze (1979). The term "mesoscale convective systems" (MCSs) will be used synonymously with MPF's in this dissertation. A related term also used by Leary and Houze (1979) is "cloud cluster." This term arose in the satellite literature to denote patches of cold cloudiness with unknown internal structure, and will be used herein only in the context of satellite observations.

Another word frequently used herein is "convection," which can be taken to mean the process occurring in MCSs *in their entirety*. Infrared satellite observations of cold cloud tops will be taken as evidence of "convection," while the effects of "convection" on the larger-scale flow will be taken to mean the effects of the entire process, not just the part occurring in the imprecisely defined "convective cells" or "convective sub-areas" of an MCS. In this sense, Riehl and Malkus's (1958) "hot tower" conceptual model of convection, formulated on the basis of its large-scale effects, should perhaps be thought of as whole MCSs, not simply as the convective cells which happen to superficially (visually) fit the description.

Tropical deep convection also exhibits structure on larger scales. Tropical cyclones, with their circular eyewall and multiple spiral bands of convection, are one well-known example. Another is the "easterly waves" of convective cloudiness seen in time-longitude strips of satellite imagery (*e.g.* Chang 1970). More recently, satellite observations over the oceanic warm pool have revealed the existence of "superclusters" (Nakazawa 1988, Mapes and Houze 1992c). The Australian monsoon consists of convection, including both ordinary MCS's and hurricanes, organized on a continent-

wide scale. As shown below, it can be viewed as a series of objectively-defined superclusters representing a progression of convection stretching over a time period of days. The agents of this larger-than-mesoscale organization (superclustering) are several, as discussed in section 4.2.

## *1.2 Monsoons*

The word monsoon conjures many vivid images, but is notoriously difficult to define. Ramage (1971) settled finally on an entirely wind-based definition: a monsoonal climate is one in which the direction of strong persistent surface winds differs by 120° or more between January and July. This wind difference was envisioned to arise from the thermal contrast between the land and ocean surfaces of low-latitude continents: in winter, a cold anticyclone prevails over land, while in summer a "continental heat low" creates inflowing cyclonic winds.

This wind-based definition is unambiguous from surface observations alone, but is unsatisfying. The economic and cultural importance of the monsoons is due almost entirely to the rain they bring to otherwise dry land areas. Even physically, the latent heating in rain vastly exceeds sensible heating of the land surface. It is also worth noting that most monsoon rainfall occurs offshore [see Janowiak and Arkin (1991) for both winter and summer satellite-based rainfall estimates]. Hence the welcome onset of the rains (which sometimes overstay their welcome) is largely just an anthropocentric view of the shift in the location of convection zones to a position adjacent to land, onto which a little spillover occurs.

The importance of moisture and latent heating to monsoons may be qualitatively appreciated from any visible satellite picture of the earth. As noted above, the vast subtropical oceans are nearly black, and the solar energy they collect is released as heat in the longitudinally confined monsoon regions of the latitudinally narrow equatorial belt of convective cloudiness. The latent heating in those regions thus exceeds local continental heating by a factor something like the ratio of the areas of tropical ocean and land, times their ratio of (1 - albedo). Webster (1987) has explored in thought-experiment style the differences between a dry monsoon and a moist monsoon: the moist monsoon is a much deeper and stronger circulation.

### *1.2.1 The Australian monsoon: background*

The Australian summer monsoon is characterized by an intensification and southward shift off the equator of deep convective activity in the longitudes near 110-150°E, and meridional flow across the equator, from north to south at low levels and south to north in the upper troposphere. Consistent with this meridional circulation, westerly zonal winds at ~10 °S in the lower troposphere and an upper-tropospheric easterly jet over the equator are observed. Cyclonic shear vorticity prevails in the region of the off-equatorial convection. In addition, the southern hemisphere midlatitude upper-tropospheric westerlies shift poleward. For a general review of the Australian monsoon, see McBride (87). Synoptic aspects of the 1987 Australian monsoon season have been described in Gunn *et al*. (1989), while diurnal variations have been considered in Keenan *et al.* (1989). Some speculations concerning planetary aspects of the 1987 monsoon onset have been offered by Hendon *et al.* (1989). The present analysis is focused specifically on the period encompassing the MCSs observed in the Equatorial Mesoscale Experiment (EMEX). Much of this material has been published in Mapes and Houze (1992a).

### *1.2.2 The 1987 monsoon data set*

The data used in this work come from the jointly-conducted Equatorial Mesoscale Experiment (EMEX) and Australian Monsoon Experiment (AMEX). EMEX was an aircraft-based observational program for exploring the internal structure and mesoscale dynamics of nocturnal MCSs over the tropical ocean. It consisted of airborne Doppler radar and multiple aircraft sampling in ten MCSs within the period 14 January - 3 February 1987. The field measurement phase of EMEX was conducted from Darwin, Australia (See base map, Fig. 1.1) during January and February of 1987. This coincided with Phase II of AMEX (Gunn *et al.*1989), which involved an enhanced network of 6-hourly soundings (heavy dots on Fig. 1.1), as well as radars located at Darwin, Gove, and Weipa. The Stratospheric-Tropospheric Exchange Program (STEP) was also conducted during this time period, with flights of a U.S. NASA ER-2 aircraft in the stratosphere above the tops of tropical cyclones and MCSs. A more general description of the EMEX program is given in Webster and Houze (1991).

The gridded fields used in this study are based on the European Centre for Medium-range Weather Forecasting (ECMWF) 12 GMT uninitialized analyses, which took as input the AMEX soundings along with the rest of the global network. We have also examined the individual AMEX soundings, provided by the Australian Bureau of

Meteorology; the characteristics of these data are described in Gunn *et al.* (1989). Three-hourly satellite data is from the Japanese Geosynchronous Meteorological Satellite (GMS).

For the mesoscale studies, data came primarily from the three EMEX research aircraft: U.S. National Oceanic and Atmospheric Administration (NOAA) WP-3D aircraft number N42RF (hereafter referred to as "the P3"), the Electra aircraft of the U.S. National Center for Atmospheric Research (NCAR), and the Australian Commonwealth Scientific and Industrial Research Organization (CSIRO) F27 aircraft. AMEX data from the Australian Bureau of Meteorology's 10-cm wavelength operational radar at Darwin were also used.

Foremost among mesoscale data sources is the P3, which was instrumented with two quantitative radars. The lower fuselage radar has 5 cm wavelength and scans in an approximately horizontal plane, with a maximum useful range of slightly more than 100 km. It has a horizontal beamwidth of 1.1°, which provides good horizontal resolution; however, it has a 4.1° vertical beamwidth, and thus provides values of radar reflectivity that are averages over a vertical depth, which varies with range and is large at far ranges (*e.g.*, Houze *et al.* 1981). The tail radar of the P3 has 3 cm wavelength. During EMEX, this radar scanned in the vertical plane perpendicular to the ground track of the aircraft, with a maximum range of 90 km. Doppler data from the tail radar were obtained only from 0.9 to 40 km range. A more complete description of the EMEX aircraft and their instrumentation can be found in Gamache *et al.* (1987).

### *1.2.3 Rainfall and cloudiness in Jan-Feb 1987*

Figure 1.2 shows the percentage high cloudiness (PHC) from all 3-hourly infrared satellite images during the period 14 January - 15 February 1987. "High" cloudiness is here defined by equivalent blackbody temperatures less than 218 °K (-55 °C), corresponding to the 200 mb level (infrared pictures of the EMEX MCS's, enhanced at the -55 °C level, are in chapter 3). The PHC presentation of satellite data was chosen for its approximate relation to rainfall (*e.g.* Janowiak and Arkin 1991).

Figure 1.2 indicates that most of the precipitating convection in the Australian longitudes occurred south of the equator, over the ocean, but near the coast. A similar offshore enhancement of Indian monsoon cloudiness has been extensively studied (Ogura

and Yoshizaki 1988 and refs.), though it is poorly documented. There was a small maximum in PHC near 120°E, 18°S, corresponding to the cold tops of cyclones Connie and Damien, while a much larger area of frequent cold cloudiness occurred along the north Australian coast. The largest PHC values in the entire field of view of the GMS satellite monsoon cloudiness were associated with the monsoon. The western Pacific also had substantial amounts of convection, in association with the 1987 El Nino conditions. Figure 1.3 shows the mean sea surface temperature map for January 1987. The area of significant cold cloudiness corresponded roughly to the area with SST exceeding 28°C.

Mean maps of cloudiness obscure the wealth of fine structure information available in satellite data. An objective technique developed by Williams and Houze (1987) reveals the connected areas of cold cloudiness, given an arbitrary temperature threshold for "cold." This technique thus gives some indication of the sizes of the "cloud clusters" which make up the mean cloudiness maps. We will show the results obtained with three thresholds: 208K (-65°C), 198K (-75°C), and 193K (-80°C). These are the lowest temperature thresholds in use in the infrared tropical cloudiness literature. While precise comparisons are impossible, my subjective impression from examining the atlases of Houze et al. (1987) and Stephens and Greenwald (1988) is that -65°C and -75°C are slight over- and under-estimates, respectively, of radar echo (precipitation) area in the EMEX MCS's. Williams and Houze (1987) used -60°C, while climatic rainfall estimates use warmer thresholds (Janowiak and Arkin 1991).

Figure 1.4 shows size spectra, as a function of threshold temperature, of spatially connected areas of cold clouds, called "cloudiness elements" (CEs). Fig. 1.4 is a plot of dA/dx, where A is the area covered by cold clouds and x is a measure of the size of the CEs, defined as the square root of the area of each CE. The square root operation widens the width of the "bins" at large size, to improve the presentation of the relatively infrequent but important larger CEs. Area under the curve corresponds to area coverage by CEs in any given size interval. The spectra are nearly flat from the smallest scales out to 200 km or so, then they drop off, the spectra from the colder thresholds dropping off first. There is no evidence for a peak indicating a preferred mesoscale, but compared to the long-term worldwide spectrum, the Australian cloudiness appears to have unusually large contributions from mesoscale CE's in the 300 km range. This may reflect in part

the tropical cyclones which constituted much of the cold cloudiness (and rainfall) of the 1987 monsoon.

Further insight into the temporal interconnectedness of the monsoon cloudiness can be gained by matching the CEs observed in individual frames of satellite imagery to reveal the space-time "cloud clusters" of which they are parts (Williams and Houze 1987). This procedure has been carried out using the same parameters as Williams and Houze: two CE's, both of which must exceed 5000 $km^2$ in size, are said to be a part of the same cloud cluster if their spatial overlap from one frame to the next exceeds half the area of either CE, or a minimum value of 10,000 $km^2$, whichever is less.

The resulting collection of cloud clusters is represented in Fig. 1.5, in which the duration of each cloud cluster, in hours, is plotted in characters whose size is proportional to the total amount of cloudiness (area*time) accounted for by the cluster. As is apparent, the lion's share of cloudiness was associated with a few very long-lived "superclusters." The same procedure was repeated for the threshold temperatures of 198K and 193K, shown in Fig. 1.6. Again, multi-day superclusters, not all of which represent tropical cyclones, dominate the picture.

### *1.2.4 The mean monsoon circulation in 1987*

Figures 1.7 and 1.8 show ECMWF-analyzed mean 12Z fields from the period 14 January to 15 February. At 850 mb, there was mean cross-equatorial flow into the southern hemisphere all along the Australian longitudes (Fig. 1.7a). This flow curved into a mean westerly jet centered at approximately 9°S. The speed of this jet was roughly consistent with the conservation of absolute angular momentum (around the earth's axis) from a zero zonal wind speed at the equator. However, it is clear from the height field of Fig. 1.7b that the gradient of geopotential height also had a small zonal component just upstream of the jet. South of the jet lay an elongated mean trough and cyclonic circulation, with the lowest heights in the mean circulation center located just off the northwestern Australian coast. This semi-permanent circulation center, designated the "Australian Low" by Webster and Houze (1991), contained, during parts of the averaging period, tropical cyclones Connie and Damien, while the eastward protrusion of the mean trough reflects both an actual trough in the area from 15-18 January (Fig. 3.11; Davidson *et al.* 1990 Fig. 11a), and the time-averaged view of cyclones Irma and Jason moving southwestward across north central Australia from the Gulf of Carpentaria.

At 200 mb, the mean flow spiraled outward from a climatological anticyclone over Australia, northwestward across the equator, forming a tropical easterly jet just north of the equator (Fig. 1.8a). The reason for the displacement of the mean tropical easterly jet north of the equator can be seen in Fig. 1.8b: a mean zonal gradient of geopotential on the equator associated with a very large-scale height pattern, with higher heights over the Pacific than over the Indian ocean. This pattern is climatological, and can also be seen, for example, in Ramage (1971, Fig. 7.4). With the twin maxima, somewhat symmetric across the equator, it bears some resemblance to an equatorially trapped planetary wave, and hence to Gill's (1980) simple solutions for heat-induced tropical flow.

### *1.2.5 Progression of the 1987 monsoon*

Figure 1.9 shows time series data of PHC, and of the vertical profile of zonal wind component from daily average soundings at Darwin, Gove, and the EMEX ship (at 11 °S, 139 °E), from 10 January (day 10) to 15 February (day 46), 1987. The timing of the EMEX flights is indicated, as well as the five three-day periods — *onset, cyclones, inactive, second onset,* and *long zonal fetch* — to be described below. After the sudden onset of westerly wind at all levels on 13 January, a layer of westerly zonal wind, typically extending from the surface to ~10 km altitude in active periods, tended to lag the convection in time. This time lag can be understood qualitatively by considering the westerlies as part of a monsoon-scale cyclonic circulation (trough), centered south of the soundings, that gradually intensified as the persistent divergent circulations associated with deep convection concentrated vorticity in that area.

At the surface, winds were westerly even during the *inactive* period, spiraling cyclonically into a shallow heat low over the Australian continent. This "dry monsoon" flow ventilates the daily solar heating of the continent, but was far weaker and shallower than the "moist monsoon," which draws its energy from more intermittent latent heating and ultimately from the oceanic heat source (Webster 1987). In later chapters, evidence will be presented that the depth of the westerly wind layer reflects the depth of the layer of convergence observed in MCSs.

The five three-day time periods discussed in this section were chosen to represent the various synoptic regimes within which the EMEX convective systems were observed. They are denoted *onset* (14-16 January; EMEX flights 1, 2, 3), *cyclones* (18-20

January; EMEX flights 4, 5), *inactive* (23-25 January; no flights), *second onset* (27-29 January; EMEX flights 6, 7), and *long zonal fetch* (1-3 February; EMEX flights 8, 9, 10). High cloudiness and 700 mb wind maps for these periods are shown in Figs. 1.10 - 1.14.

The *onset* convection occurred primarily in the Bonaparte Gulf (12 °S, 129 °E in Fig. 1.10b), over the earth's warmest January-mean sea surface temperature (30 °C, Fig. 1.3). The Australian Low, with cyclone Connie in its center, quickly spun up (Fig. 1.10a). Cyclone Irma developed in the Gulf of Carpentaria, and in the *cyclones* period most high cloudiness was associated with the two cyclones (Fig. 1.11). After the westward and poleward motion of the cyclones, to their demises, the *inactive* period ensued (Fig. 1.12). The Bonaparte Gulf was again the site of the resurgence of convection during *second onset*, as the Australian Low depression, soon to contain cyclone Damien, developed in that region (12 °S, 130 °E in Figs. 1.13). During *long zonal fetch*, strong monsoon westerlies spanned the entire Australian continent, and in addition to Damien's cloudiness, a second convective maximum appeared in the Arafura Sea (10 °S, 135 °E in Figs. 1.14). After the final EMEX aircraft missions were flown in that area, cyclone Jason occurred in the Gulf of Carpentaria, and a two-cyclone pattern not unlike Fig. 1.11 prevailed again, until the cyclones again moved into unfavourable environments and died.

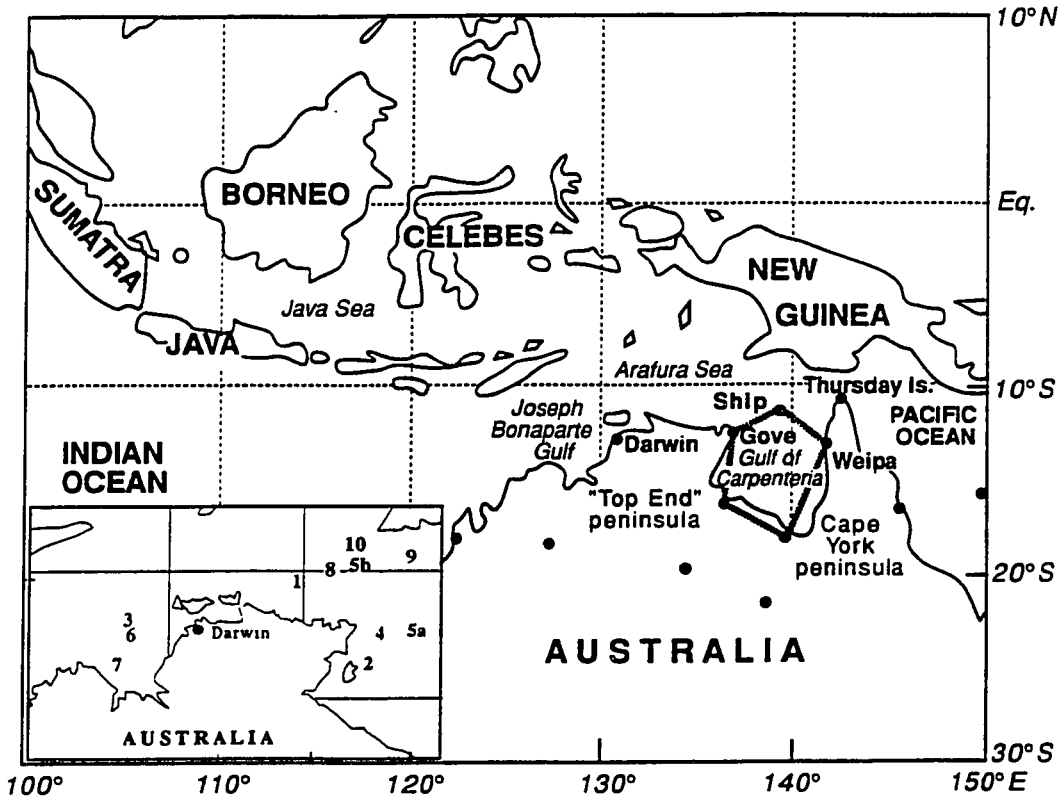


Fig. 1.1 : Base map of northern Australia and surrounding area. Heavy dots indicate AMEX sounding sites. The inset map indicates the locations of the ten EMEX aircraft missions.

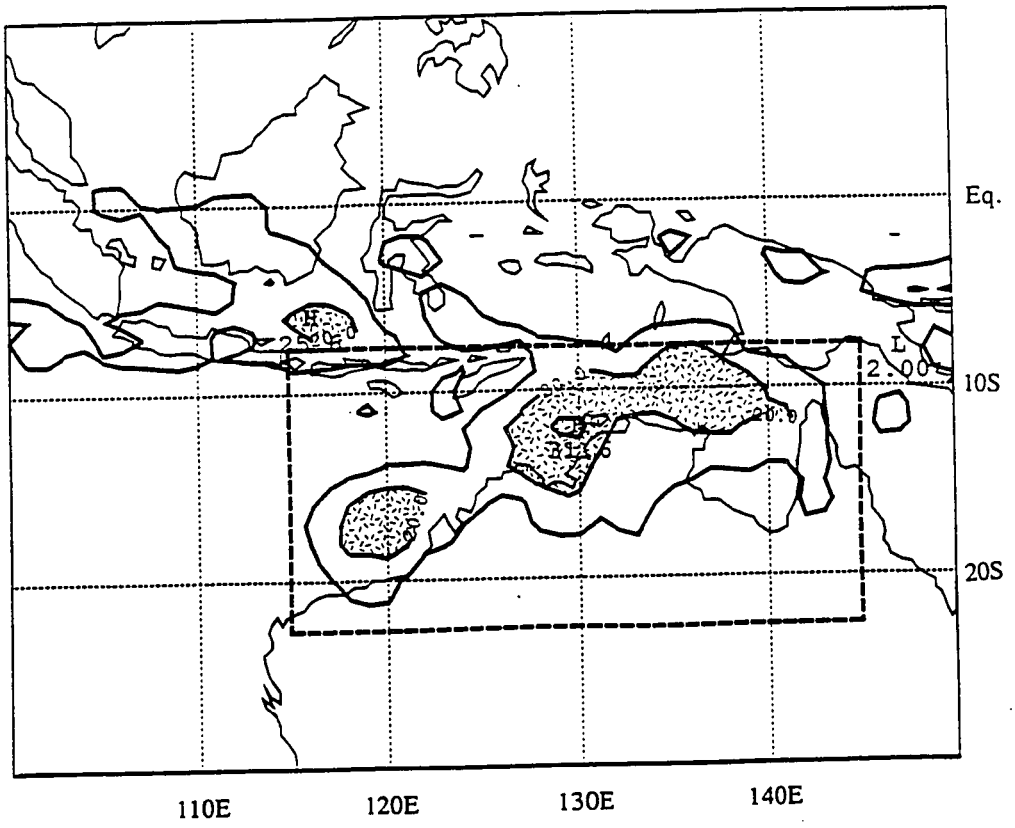


Fig. 1.2 : Percent High Cloudiness (PHC), defined as the percentage of 3-hourly IR satellite images in which the equivalent blackbody temperature was colder than -55 °C, during the time interval 14 January to 3 February 1987. Contour interval 10%, stippling above 20%.

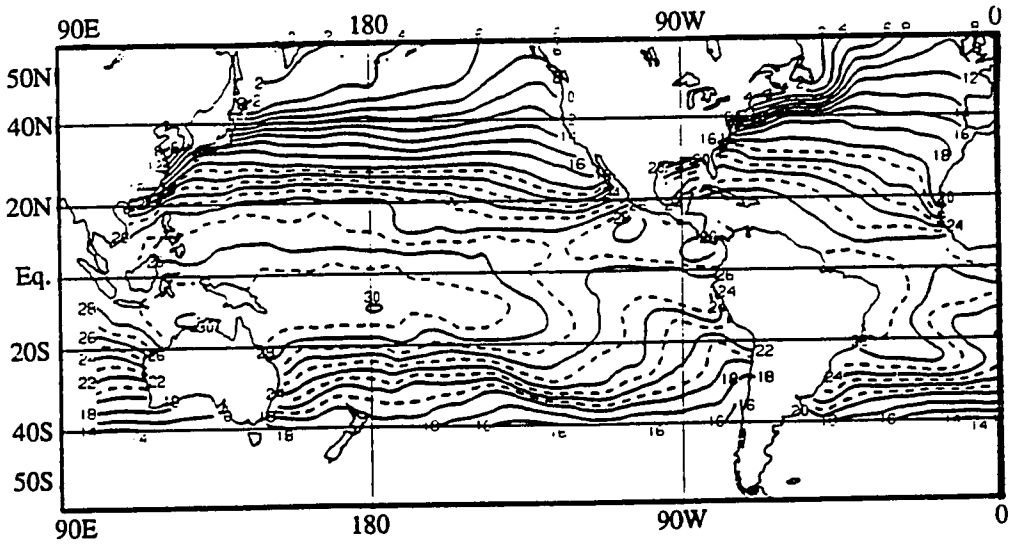


Fig. 1.3 : January 1987 mean SST map, from the NOAA Climate Analysis Center's Climate Diagnostics Bulletin.

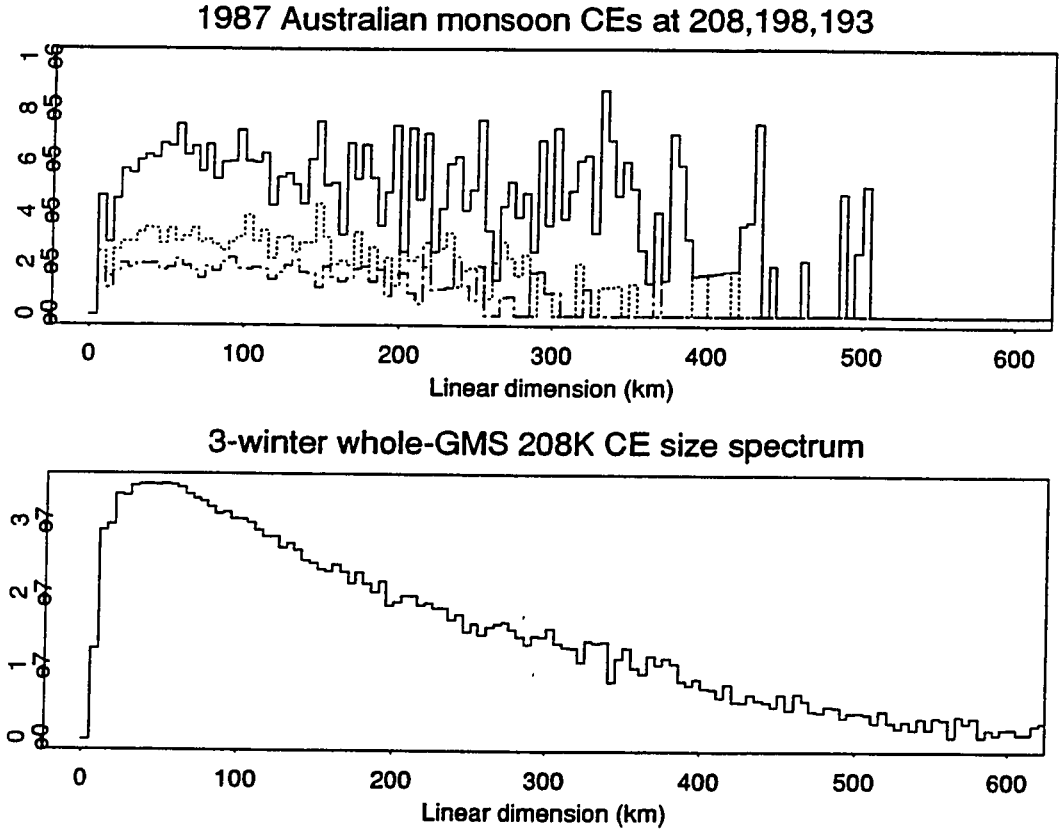


Fig. 1.4 : Cloud coverage by CE size for the 1987 Australian monsoon (top panel, threshold temperatures 208K, 198K, 193K) and the entire GMS field of view (bottom panel, threshold temperature 208K).

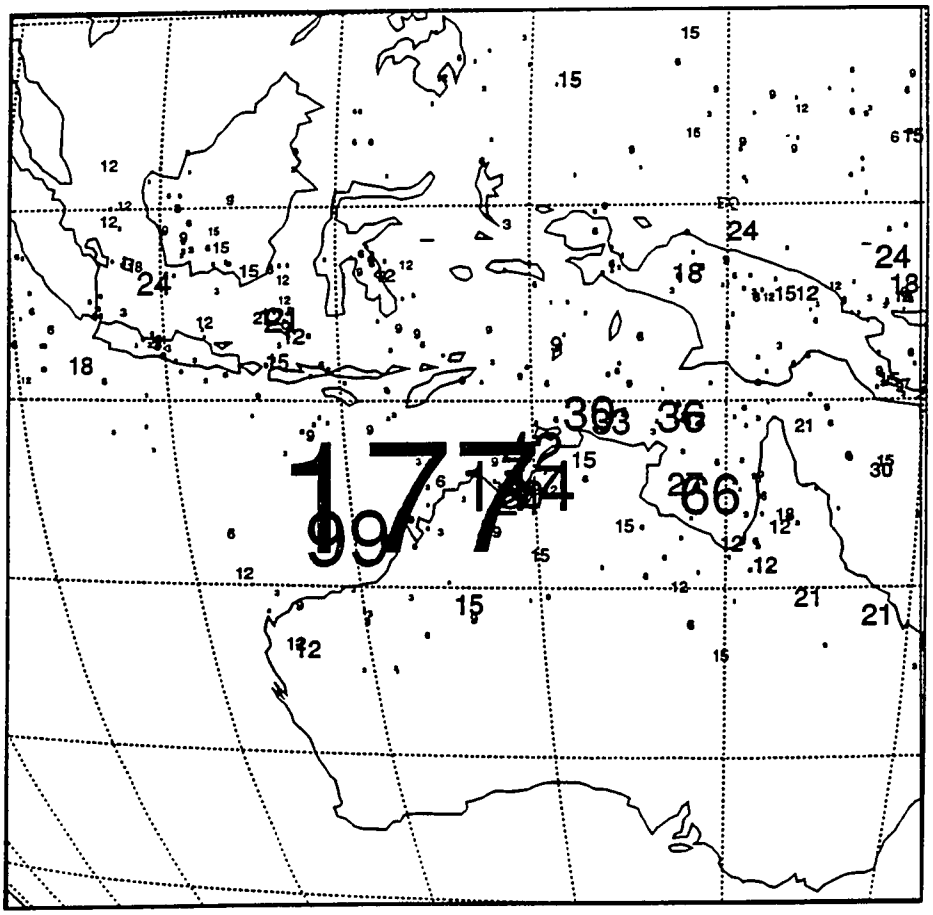

Fig. 1.5 : Cloud clusters at 208K. The plotted value is the duration in hours, while the area of each plotting character is proportional to the area*time coverage of each cluster.

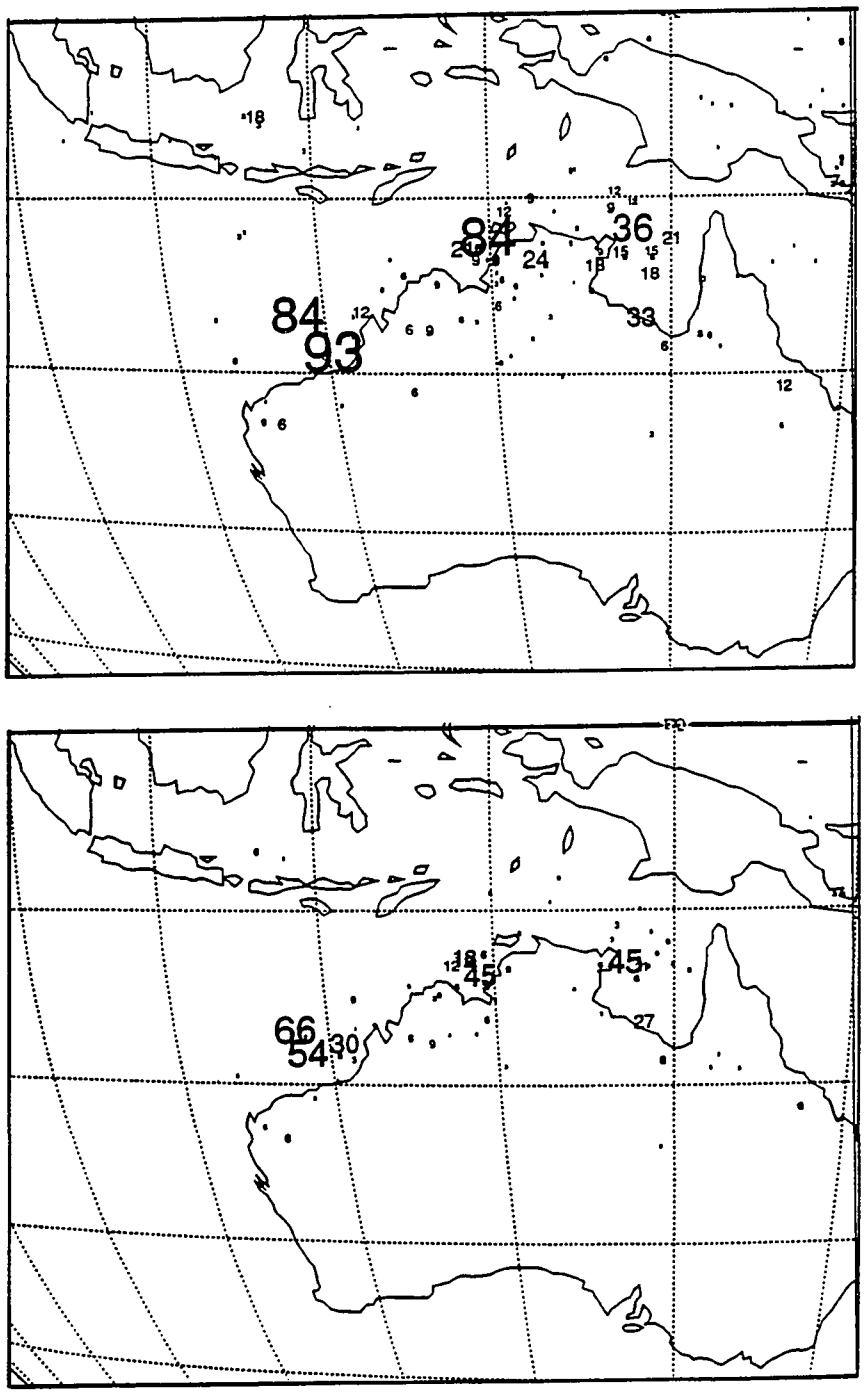


Fig. 1.6 : Cloud clusters at 198K and 193K. The plotted value is the duration in hours, while the area of each plotting character is proportional to the area*time coverage of each cluster.

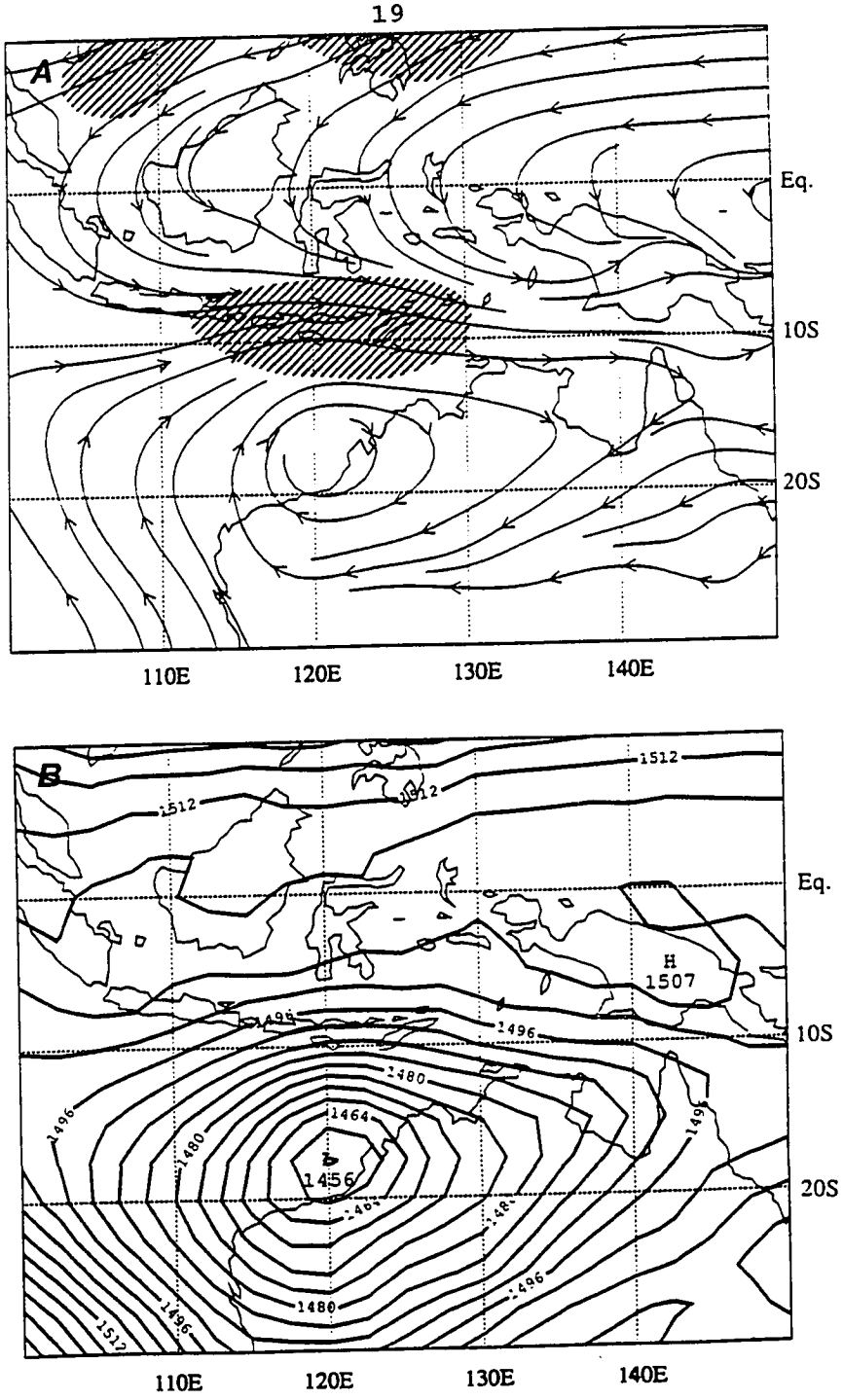


Fig. 1.7 : Mean 850 mb winds and heights from ECMWF 12 GMT analyses for the three-week period 14 January to 3 February 1987, which contained the ten EMEX flight missions. a) Streamlines and isotachs. Hatched areas: wind speed >10 m/s. b) Geopotential height, contour interval 4 m.

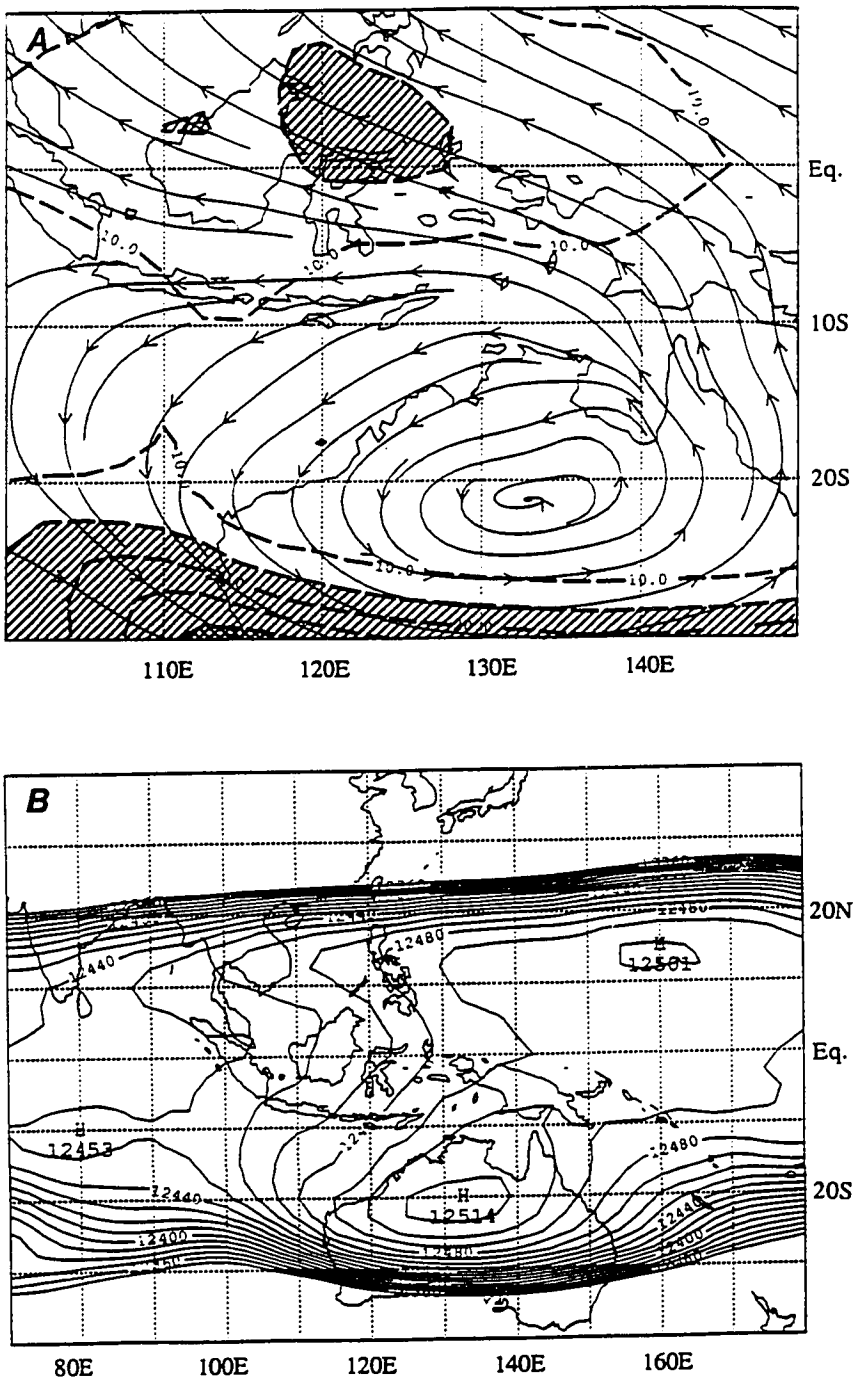


Fig. 1.8 : Mean 200 mb winds and heights. As in Fig. 1.7, except at 200 mb. a) Streamlines and isotachs. Hatched areas: wind speed >15 m/s. b) Geopotential height, contour intervals 10 m.

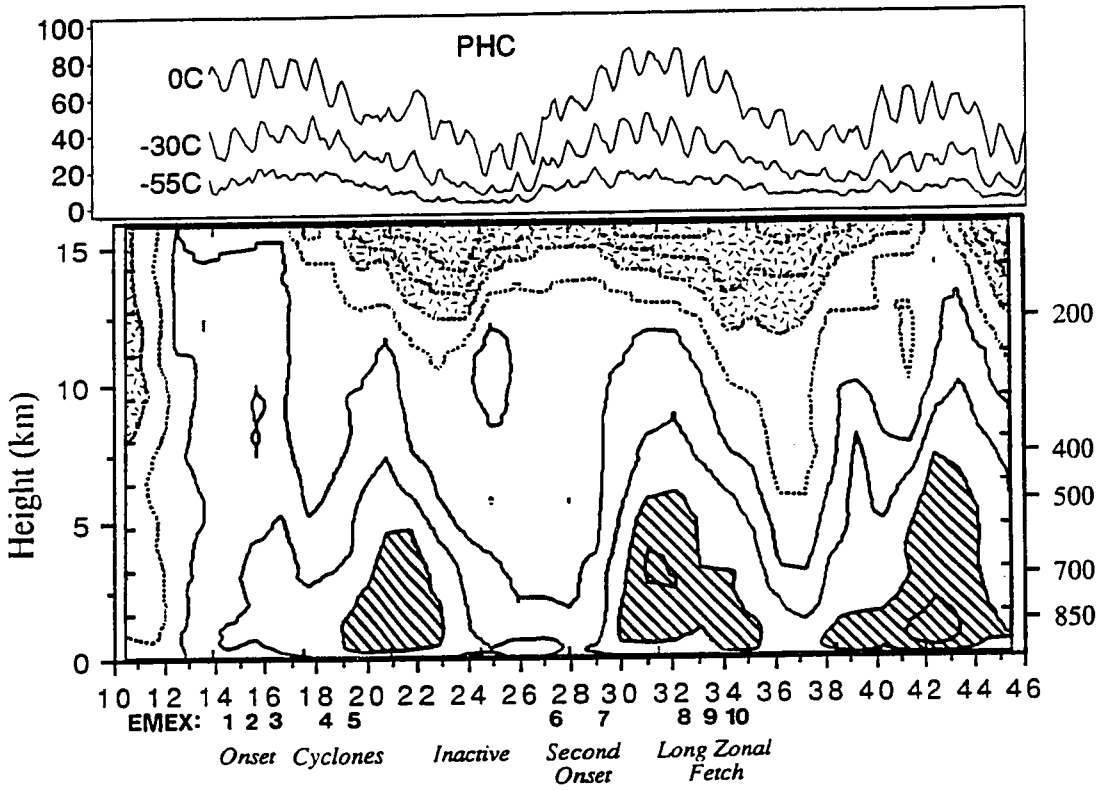


Fig. 1.9 : Time section of monsoon cloudiness and zonal wind component. Upper panel: regional percentage high cloudiness (PHC), defined as the fractional coverage of infrared brightness temperatures colder than the three indicated threshold temperatures, within the dashed box on Fig. 1.2. Lower panel: time-height section of daily-average zonal wind component in soundings from Darwin, Gove, and the ship, from 10 January (Day 10) to 15 February (Day 46) 1987. Solid contours: 0, 5, 10 (hatched), 15 m/s; dotted contours: -5, -10 (stippled), -15, -20 m/s. The timing of the ten EMEX aircraft missions is indicated by EMEX 1,2,...10. Five three-day named periods are also indicated.

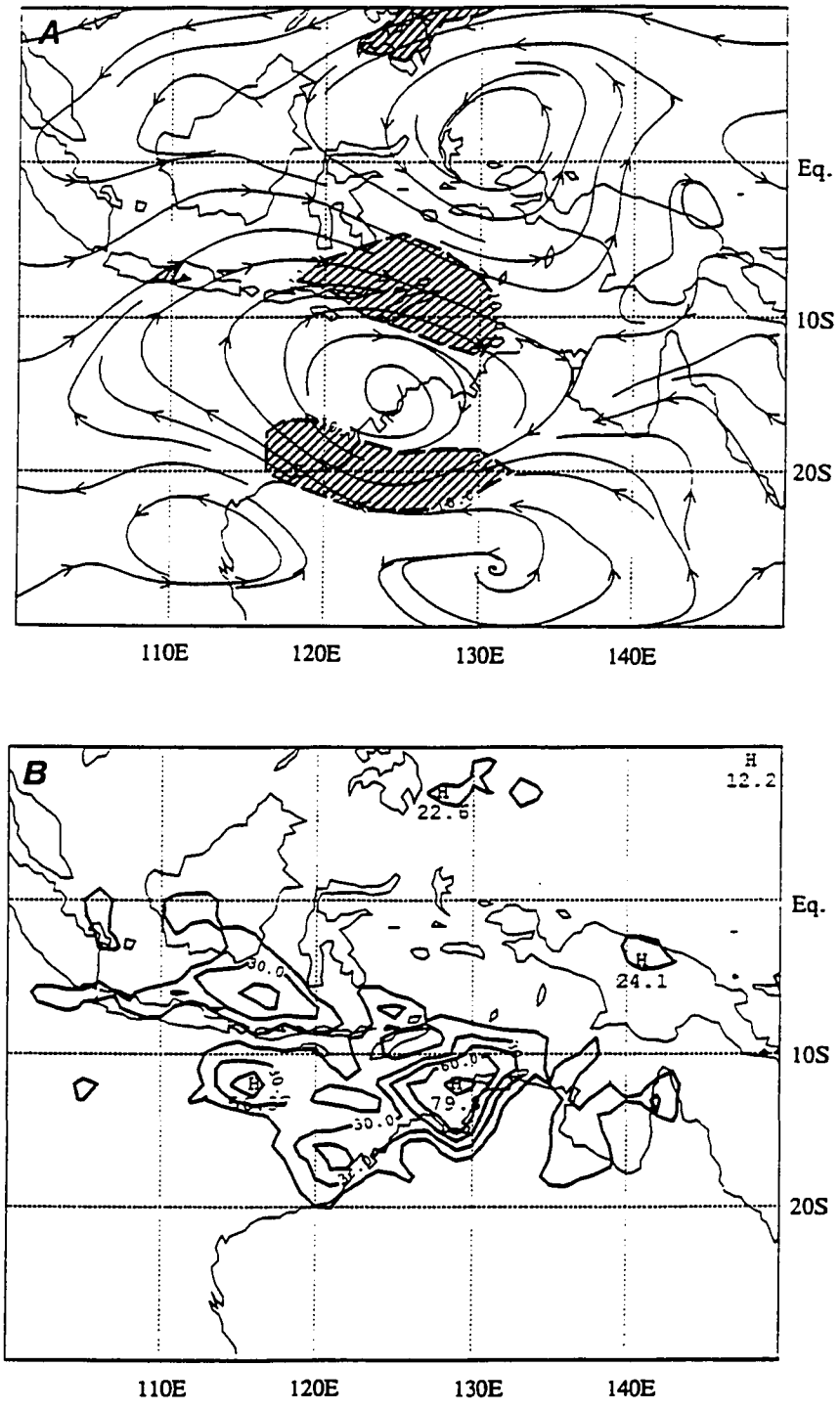


Fig. 1.10 : *Onset* wind and PHC fields, 00 GMT 14 January to 00 GMT 17 January 1987. a) Mean 700 mb winds. Wind speed >10 m/s hatched, >15 m/s cross-hatched. b) PHC, contour interval 15%.

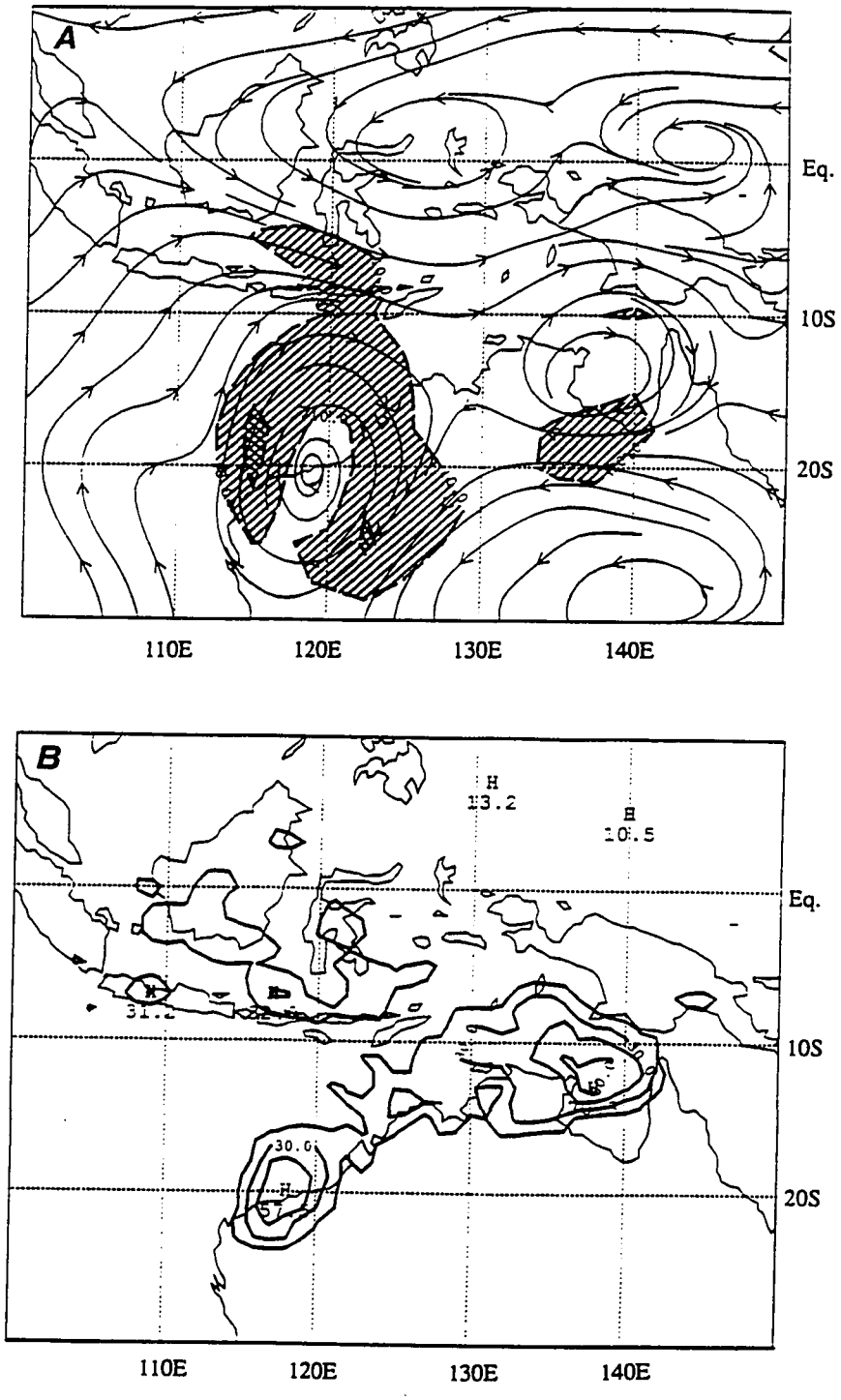


Fig. 1.11 : *Cyclones* wind and PHC fields. As in Fig. 1.10, except for the period 00 GMT 18 January to 00 GMT 21 January.

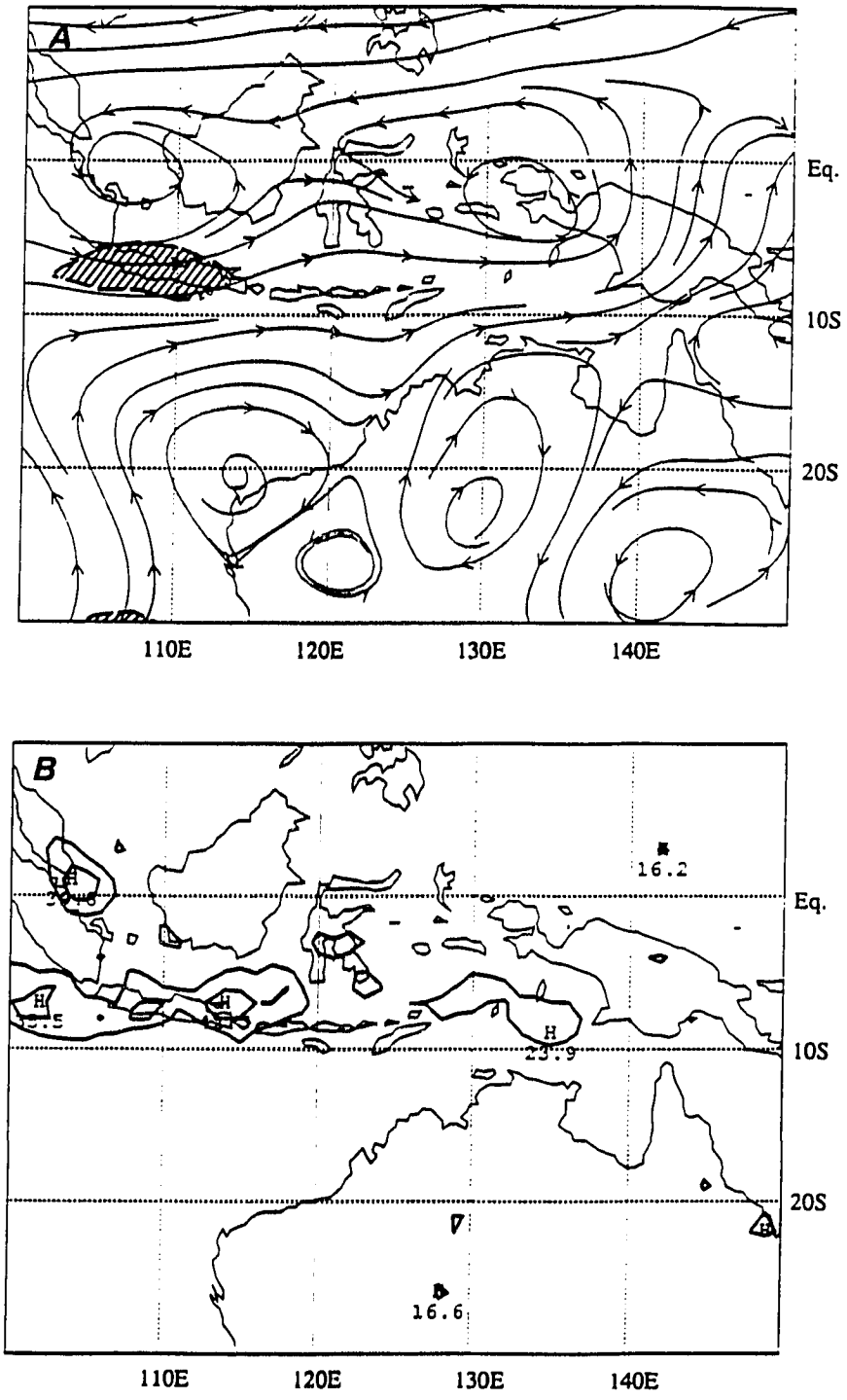


Fig. 1.12 : *Inactive* wind and PHC fields. As in Fig. 1.10, except for the period 00 GMT 23 January to 00 GMT 26 January.

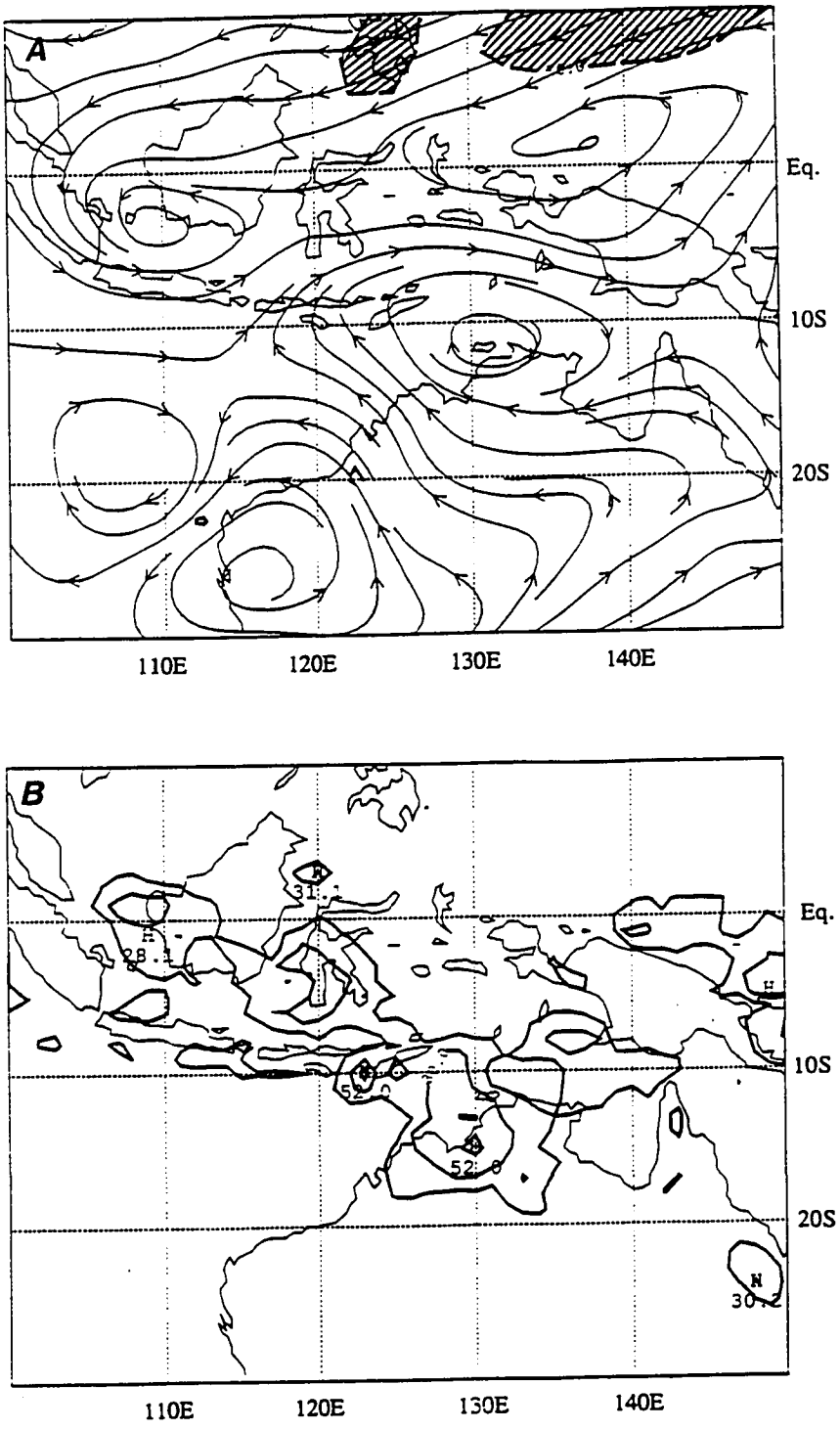


Fig. 1.13 : *Second Onset* wind and PHC fields. As in Fig. 1.10, except for the period 00 GMT 27 January to 00 GMT 30 January.

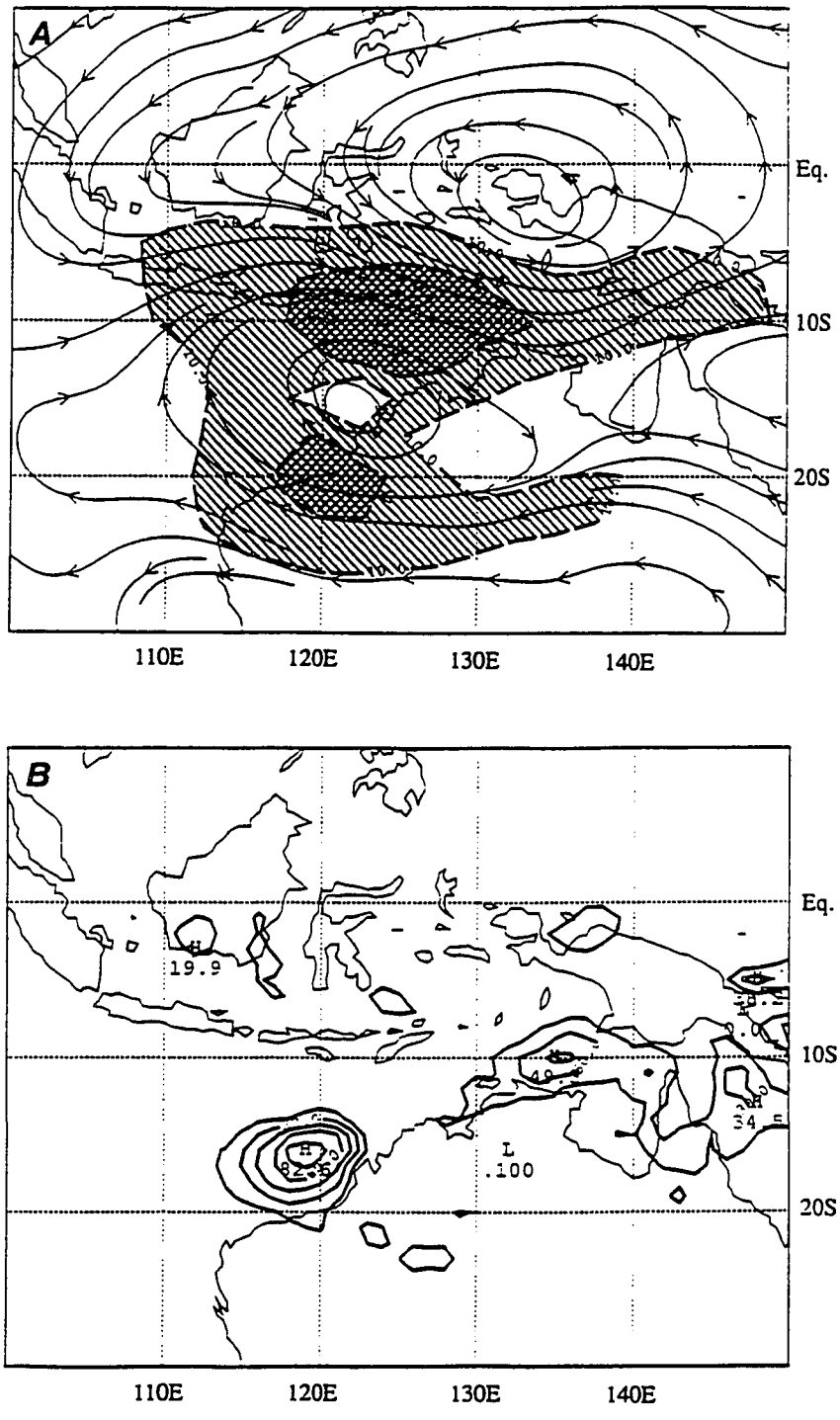


Fig. 1.14 : *Long Zonal Fetch* wind and PHC fields. As in Fig. 1.10, except for the period 00 GMT 1 February to 00 GMT 4 February.

# CHAPTER 2

## SOME THEORY ON BUOYANT CONVECTION IN A STRATIFIED FLUID

In this chapter, some theoretical background on buoyancy-driven accelerations and flows is presented. While the ideas herein are applied to buoyant parcels and small mesoscale heat sources, it is worth remembering that thermally direct circulations come in many sizes; the ideas developed herein are also applicable on larger scales.

Section 2.1 focuses on the pressure distribution around a buoyant parcel in an incompressible (or anelastic) fluid. This pressure field accelerates mass in the ways necessary for the ascent of the buoyant fluid, consistent with the mass continuity condition. The role of boundary conditions is considered, and the approach of anelastic pressure perturbations to the hydrostatic limit is explored. Section 2.2 considers the motions which occur in a stratified fluid in response to a heat source. These motions begin with simple pressure-induced accelerations in and near the buoyant (heated) fluid, but in a stratified fluid vertical motion leads to an evolving buoyancy field, which in turn leads to an evolving pressure field, and so on. The resulting process can be understood in terms of gravity wave theory.

### *2.1 Accelerations in and near a buoyant parcel of air*

#### *2.1.1 The vertical equation of motion: buoyancy*

Vertical accelerations, as governed by the vertical equation of motion, are at the heart of buoyant convection. Neglecting Coriolis, electrical, and molecular diffusion accelerations, we may write the equation of vertical acceleration (in Lagrangian form):

$$dw/dt = -(1/\rho)\,\partial p/\partial z - g \qquad (2.1)$$

where w is vertical velocity, $\rho$ is density, p is pressure, and g is the gravitational acceleration. The two terms on the right substantially cancel, so it is useful to linearize the pressure gradient acceleration about a hydrostatically balanced reference state (function of z only) denoted by the naught subscript:

$$\partial p_o/\partial z = -\rho_o g \qquad (2.2)$$

The pressure and density may be written as $p = p_o + p'$, $\rho = \rho_o + \rho'$ and substituted into (2.1). Upon the assumption $(1+\varepsilon)^{-1} \sim 1-\varepsilon$, using (2.2), and neglecting terms with two primed quantities in them, we obtain:

$$dw/dt = g\rho'/\rho_o - (1/\rho_o)\, \partial p'/\partial z. \qquad (2.3)$$

The two terms on the right hand side of (2.3) are the buoyancy (b) and vertical perturbation pressure gradient acceleration (VPPGA), respectively. Two limiting cases are the *buoyancy limit*, when the VPPGA is neglected, and the *hydrostatic limit*, when (2.3) = 0. As we shall see, these limits correspond to infinitely small and infinitely large values of the aspect ratio L/H of a buoyant fluid element. All real buoyant ascent lies somewhere in between.

### *2.1.2 Buoyancy-induced pressure perturbations*

In this section, the buoyancy b will be taken as given, and the PPGA and net acceleration will be calculated. Qualitatively, the PPGA is necessary to move non-buoyant fluid out of the way of the buoyant fluid, so that it can ascend in a way consistent with mass continuity requirements. The vector equation of motion [utilizing the linearization (2.3)] and the anelastic mass continuity equation codify these conditions:

$$\partial(\rho_o \mathbf{V}_3)/\partial t = -\rho_o \mathbf{V}_3 . \nabla \mathbf{V}_3 + \rho_o b\mathbf{k} - \nabla p' \qquad (2.4)$$

$$\nabla . (\rho_o \mathbf{V}_3) = 0 \qquad (2.5)$$

Here $\mathbf{V}_3$ is the 3-dimensional vector wind. If the divergence operator $\nabla .$ is applied to (2.4) and (2.5) is invoked, a diagnostic equation for p' results:

$$\nabla^2 p' = -\nabla . (\rho_o \mathbf{V}_3 . \nabla \mathbf{V}_3) + \partial(\rho_o b)/\partial z \qquad (2.6)$$

Because the left hand side is linear, the pressure perturbation may be decomposed into a buoyancy-induced part $p'_b$ and a dynamic part $p'_d$, satisfying the Poisson equations:

$$\nabla^2 p'_b = \partial(\rho_o b)/\partial z \qquad (2.7)$$

$$\nabla^2 p'_d = -\nabla . (\rho_o \mathbf{V}_3 . \nabla \mathbf{V}_3) \qquad (2.8)$$

To invert (2.7) and (2.8) for p', boundary conditions must be specified (*e.g.* Schlesinger 1980, comment by Gordon 1981). In general, the "operator" $\nabla^{-2}$ has a

smoothing effect, so that sharp features in the forcing terms on the RHS create smooth pressure perturbation fields of larger scale, extending beyond the forcing. One physical analogy is a rubber sheet, whose displacement (analogous to p') satisfies an equation like (2.7). A sharp object poking the sheet creates a displacement in the whole region around the point of contact. It is a frequent meteorological practice to assume $\nabla^2 x \sim -x$, as is true for wavelike fields. This approach was used for example by Holton (1972). However, cumulus convection is anything but wavelike, and exact solutions for idealizations more realistic than the wave paradigm are not difficult to construct.

It is illuminating to consider the pressure perturbation associated with a parcel of uniformly buoyant air. The p' solutions obtained are exactly analogous to the electrical potential $\Phi$ associated with a space charge analogous to $\partial(\rho b)/\partial z$ (see *e.g.* Feynmann 1964 v II ch 6). For simplicity, $\rho_o = 1$ kg m$^{-3}$ will be assumed in this section (the Boussinesq approximation). In the absence of any boundaries, but with p' required to go to zero at infinite distance, the solution to (2.7) is:

$$p(\mathbf{x}) = \frac{\rho_o}{4\pi} \iiint_{\text{allspace}} \frac{\partial b/\partial z}{|\mathbf{x}-\mathbf{x}'|} dV' \qquad (2.9)$$

where $\mathbf{x}$ is the point (position vector in 3-space) at which p' is evaluated and $\mathbf{x}'$ is the dummy position vector representing the location of the volume element dV'. While integration over all space sounds hard, it is only necessary to integrate over those places where $\partial b/\partial z$ is nonzero. Hence this problem can be solved analytically for simple geometries.

Consider the pressure perturbation along the vertical axis of a spherical parcel of uniform buoyancy b. It is an amusing exercise (trust me) to evaluate (2.9), the result being:

$$p(z) = \frac{\rho_o ab}{2}\left\{\left[\frac{-2(2M-N)}{3N^2}\sqrt{M+N}\right]-\left[\frac{-2(2M+N)}{3N^2}\sqrt{M-N}\right]\right\} \qquad (2.10)$$

where $M = 1+(z/a)^2$, $N = -2z/a$, and a is the radius of the parcel. This quantity is plotted in Fig. 2.1. Note that p' is almost precisely linear in z through the depth of the parcel. This and the subsequent plot are scaled such that the full horizontal range corresponds to the hydrostatic limit $p'_{hyd} = \rho bh$, where h is the depth of the parcel. Hence it may be

seen that the buoyancy-induced VPPGA balances ~40% of the upward buoyancy acceleration along the axis of a spherical parcel of buoyant air (*e.g.* a balloon).

An even simpler problem is to find p' along the axis of a cylindrical parcel, in which $\partial b/\partial z$ is nonzero only on the two circular disks which form the top and bottom of the parcel. The result is:

$$p'(z) = \frac{\rho_o b}{2}\left\{\left[\sqrt{d_1^2+a^2} - d_1\right] - \left[\sqrt{d_2^2+a^2} - d_2\right]\right\} \qquad (2.11)$$

where $d_1 = z + h/2$, $d_2 = z - h/2$, a and h are the radius and height of the cylinder, and z is measured from mid-parcel. This solution has been plotted for various values of aspect ratio $A = 2a/h$ in Fig. 2.2. The A = 0.2 "buoyant pencil" is near the buoyancy limit, in which the VPPGA is neglegible. Parcels with large aspect ratios approach the hydrostatic limit, though deviation is apparent even for A = 100.

It is enlightening to consider a scale analysis for vertical acceleration in an A=100 parcel. Evaluation of (2.11) at the base of the parcel (z = -h/2) yields $p' = -0.99p'_{hyd}$. The net vertical acceleration from (2.3) is thus 0.01b. In the hydrostatic limit, (2.3) = 0 and the vertical acceleration must be calculated using the mass continuity equation and the linearized nonrotating prognostic equation for horizontal divergence:

$$\partial/\partial t\,(\nabla.\rho_o V_2) = -\nabla_h^2 p' \qquad (2.12)$$

Physically, the convergent PPGA associated with the low pressure below the parcel accelerates mass convergence. By mass continuity, the parcel must accelerate upward. For a 250 km radius buoyant ($b = 0.1\ ms^{-2}$) parcel 5 km deep, the pressure perturbation below the parcel is $p' \sim p'_{hyd} = -250$ Pa. We may then roughly estimate $\nabla_h^2 p' \sim 250$ Pa $(250\ km)^{-2}$. If this convergent PPGA acts equally throughout a 10 km deep layer beneath the parcel, the predicted vertical acceleration of the parcel is then $\sim 250$ Pa $(250\ km)^{-2}(10\ km) \sim 10^{-4}\ m\ s^{-2}$, an order of magnitude smaller than .01b, the acceleration calculated from nonhydrostatic considerations. At first glance, this would appear to suggest that the hydrostatic approximation is a failure even at aspect ratios near a hundred!

*2.1.1.2 Importance of boundaries*

The problem with the above analysis is that (2.9)-(2.11) assumed an unbounded homogeneous fluid. The scale analysis above is misleading because in such an unbounded fluid, the perturbation pressure field would extend much farther than 10 km below the 250 km radius parcel discussed above. The presence of boundaries — specifically, horizontal levels at which w=0 for all time — significantly affects the diagnosed pressure field. An easy trick for evaluating (2.7) in a bounded fluid is to use the *method of images*. The effect of a rigid flat boundary is the same as that of a fictitious *image parcel* situated symmetrically across the boundary from the real parcel (see *e.g.* Raymond 1983).

The pressure field for a cylindrical parcel of aspect ratio A=1 near a rigid upper boundary is shown in Fig. 2.3. The figure could be inverted to show a lower boundary. In Fig. 2.3, $p'_{hyd}$ is +/- 150 Pa. The presence of the upper boundary increases the values of both the maximum pressure above the parcel and the minimum pressure below it. Hence the vertical pressure difference across the parcel increases as it nears the boundary, so the parcel's net vertical acceleration is inhibited, a conclusion which holds equally well for a lower boundary. The horizontal pressure gradients in the region of the boundary intensify, as mass is squirted out of the narrowing gap between the parcel and the boundary. The physical situations represented by this simple picture include negatively buoyant downdraft approaching the sea surface, and (to an arguable degree) updrafts approaching the tropopause.

*2.1.1.3 Approach to the hydrostatic limit*

The presence of both an upper and a lower boundary complicates the problem, as one must include images of the image parcels *ad infinitum*. However, for parcels of a scale comparable to the depth of the fluid in question (the tropopause depth in this case), boundaries cannot be ignored. In the "hall of mirrors" between two rigid lids, a simple way to proceed is to consider a cylinder of infinite vertical extent whose buoyancy is sinusoidal in height (Young 1972). The degree to which the tropopause acts like a rigid lid will not be debated here; suffice it to say that cold slabs not unlike the "image parcel" are observed in the stratosphere above mesoscale convective systems (Johnson and Kriete 1982) and predicted analytically above mesoscale layers of heated fluid (Nicholls *et al.* 1991).

Young's (1972) sinusoidal buoyancy assumption leads to a predicted pressure field along the parcel axis given by $p'_{hyd}(1-e^{-ma})$, where m is the vertical wavenumber and a is the radius of the cylinder. Note that $e^{-ma}$ approaches zero much more quickly than (2.11) approaches $p'_{hyd}$ with increasing a. As a result, the hydrostatic approximation becomes valid when $be^{-ma}$ is small compared to the vertical acceleration obtained from integrating (2.12) vertically. This condition is met at aspect ratios ma greater than about 7, in contrast to the frightening scale mis-analysis conducted below (2.12) for A=100. But even this result may come as a surprise to those accustomed to using the hydrostatic equation for everything but cumulus clouds.

Another perspective on the hydrostatic assumption is provided by the equation for a horizontal component of vorticity. In a two dimensional (x-z) hydrostatic Boussinesq framework, the vertical derivative of the u momentum equation, in Lagrangian form, is:

$$d/dt\ (\partial u/\partial z) = -\partial^2 p/\partial x \partial z = \partial b/\partial x \qquad (2.13)$$

where the second equality comes from substitution of the hydrostatic relation. In the full Boussinesq equations, $\partial b/\partial x$ is the source term for horizontal vorticity; here it is the source term for vertical wind shear alone. The hydrostatic assumption does not require w = 0, so it is clear that the scaling approximation $W/L << U/H$ has been made in the horizontal vorticity equation. Since LW~UH, from mass continuity in two dimensions, the approximation amounts to $[H/L]^2 << 1$: again, a small aspect ratio approximation.

Another way in which hydrostatic balance can be achieved is when the horizontal pressure gradient is in a state of balance with the wind field. For example, in the case of a steady state cyclostrophically balanced vortex, of *any* aspect ratio, the advection term and the horizontal components of the PPGA in (4.2) cancel, while the time derivative drops out, leaving (2.4) as the hydrostatic equation. In that special case, the dynamic PPGA given by (2.8) exactly cancels the horizontal component of the buoyancy-induced PPGA given by (2.7), and adds precisely that vertical component which is necessary to make the total pressure field hydrostatic. Hence the hydrostatic assumption has special validity in a balanced flow, independent of the aspect ratio arguments above.

### *2.2 Motions in the stratified environment of a heat source*

In section 2.1, the pressure gradient acceleration induced by the presence of a buoyant parcel was considered. Some of the diagnosed acceleration is vertical; in

particular, downward acceleration is induced outside the buoyant parcel to compensate for its upward acceleration. In a stratified fluid, adiabatic vertical displacements affect buoyancy: downward displacements increase buoyancy, while upward displacements decrease it. As a result, our buoyant parcel with its compensating subsidence creates buoyancy in its environment, which in turn causes vertical PPGAs in the adjacent fluid, *etc.* As noted above, the PPGA is obtained by a smoothing "inverse Laplacian" operation on the vertical derivative of the buoyancy. As a result, the PPGA at increasing distances from the buoyant parcel exhibits an increasingly smooth, simple vertical structure, regardless of the details of the buoyancy profile in the parcel. In a dynamic time-dependent framework, then, we may anticipate that the response of a stratified fluid to localized buoyancy forcing will consist of deeper vertical structures which travel rapidly away from a heat source, followed more slowly by shallower structures as time progresses.

In this section we consider the response of a stratified fluid not merely to a buoyant parcel but to a *heat source.* Initially the heating creates a buoyant parcel. As time progresses, the buoyancy field evolves in response not only to the heating, but also to the buoyancy-induced adiabatic vertical motions, as outlined above.

### *2.2.1 Gravity waves, buoyancy bores, buoyancy rolls*

The dispersion of compensating subsidence according to vertical scale, alluded to above, is predicted by linear gravity wave theory. A convenient framework for illustrating this effect is provided by the linearized Boussinesq equations in two dimensions, with no basic flow:

$$u_t = -\pi_x \tag{2.14}$$

$$w_t = -\pi_z + b \tag{2.15}$$

$$b_t = N^2 w + Q \tag{2.16}$$

$$u_x + w_z = 0 \tag{2.17}$$

where $\pi = p/\rho_o$, $b = g\rho'/\rho_o$, and $N^2$ is the buoyancy frequency $\partial b/\partial z$. Subscripts indicate differentiation. The extension to anelastic flow with $\rho_o(z)$ is not difficult (*e.g.*

Lipps 1990). Under the assumption that all variables vary sinusoidally as exp[i(ωt + kx + mz)], and that Q=0, the gravity wave dispersion relation is obtained:

$$\omega^2 = N^2k^2/(k^2+m^2) \qquad (2.18)$$

This equation describes the free motions of an unbounded stratified Boussinesq fluid. These motions are characterized by a quadrature phase relationship between the motion fields u and w and the temperature perturbation, as represented by b. Hence these waves do not transport any heat either horizontally or vertically, although they do transport momentum. Their group velocity or energy propagation direction is along the phase lines. The slope of the phase lines is given by $\cos\alpha = \omega/N$, where $\alpha$ is the angle of the phase lines with the vertical. Hence, waves of any finite frequency propagate vertically away from the level at which they are excited.

The important motions for present purposes are quasi-horizontal flows in the environment of deep convective heating which carry the heat away. These motions correspond to the low frequency limit of (2.18): $\omega \rightarrow 0$, or $m >> k$, the small aspect ratio assumption again. In that limit, the horizontal phase speed $c = \omega/k$ and the horizontal group velocity $c_g = \partial\omega/\partial k$ are equal:

$$c = c_g = N/m \qquad (2.19)$$

The same relation is obtained if one simply makes the hydrostatic assumption at the outset (Raymond 1983, Bretherton and Smolarkiewicz 1989 (BS89), Nicholls *et al.* 1991 (NPC)).

The motions of a 2-D stratified fluid in response to a heat source have been considered at various levels of approximation in NPC. Their results are reproduced here, but I define new terminology to describe them. Fig. 2.4a shows the response between rigid boundaries to *the initiation of* a heat source of a single vertical wavelength. Upward motion prevails in the heated region, while a pulse of downward motion travels away from the heat source at speed c. This pulse of downward motion, which travels at the gravity wave speed, effects a net downward displacement in the fluid through which it passes, unlike a sinusoidal gravity wave. For this reason, it may be more accurately termed a *buoyancy bore*, in analogy to a tidal bore in shallow water. If the rigid lid is removed, leaving a semi-infinite domain, upward-propagating gravity waves, in addition to the the buoyancy bore, are excited by the heating, as shown in Fig. 2.4b.

For heating whose vertical structure consists of two vertical modes rather than just one, the response of the fluid consists of two buoyancy bores of two vertical wavelengths (Fig. 2.5). Each bore propagates at its speed c given by (2.19). In the example shown, the second bore is half as deep as the first, so it propagates half as fast.

The buoyancy bores shown in Figs. 2.4 and 2.5 were emitted by the heating as it commenced. When heating terminates, buoyancy bores of opposite polarity are emitted. The result of a sinusoidal heat source, *maintained for some time interval*, is thus a traveling layer of buoyancy with a buoyancy bore at each end, propagating at the gravity wave speed (2.19). This structure is shown in Fig. 2.6. A roll circulation in the vertical plane blows around the buoyant layer. For this reason, and for its resemblance to a sandwich, this structure may be called a *buoyancy roll.* The net result of a finite amount of heating with complex vertical structure is a buoyancy roll of warmed fluid per vertical wavenumber present in the heating profile. The widths of the buoyancy rolls are given by $c\tau$, where $\tau$ is the length of time for which the heating acted.

It was noted above that a buoyancy bore leaves in its wake net vertical displacements. Because of the compensating effect of the "anti-bore," a buoyancy roll effects no net vertical displacement in the fluid through which it propagates. All the warming accomplished by the heating is within the propagating buoyancy roll, which travels away from the place where the heating took place, leaving no trace of local warming, in the absence of rotation.

### *2.2.2 Effects of rotation*

Buoyancy rolls do, however, effect net *horizontal* displacements of the fluid through which they pass (dye line in Fig. 2.6). In a rotating fluid, such horizontal displacements induce tangential flows into and out of the page. The resulting vertical wind shear requires, in order for thermal wind balance to hold, that some local warming take place. Hence, a bouyancy roll leaves behind some of its buoyancy as it propagates through a rotating fluid. The resulting state in the long-time limit, after adjustment is complete, is a warm core near the heat source. In a sense, then, buoyancy rolls get gradually absorbed as they travel, according to their vertical scale and the local value of f. A deeper heating leads to a smaller value of the vertical wind shear, a smaller horizontal temperature gradient required for thermal wind balance, and hence a larger e-folding distance over which the subsidence warming is distributed.

The distance scale for this exponential absorbtion of buoyancy rolls is analogous to an optical depth for light. For an f-plane, it is called the Rossby deformation radius, given by $\lambda_R = c/f$ [Eq. (7.5.4) of Gill 1982]. The deformation radius is proportional to vertical wavelength, and hence for a complex heat source with multiple vertical wavelengths there is a whole set of deformation radii. The farther away from the heat source one looks, the more dominant should be the signal, in both the divergent flow and the tangential (rotational) wind, of the deepest, simplest vertical structure. This phenomenon is illustrated with Australian monsoon data in Fig. 5.8.

Numerically, $\lambda_R$ for the gravest mode of the troposphere (with c ~ 50 m/s) is ~500 km at 40° latitude, and ~1000 km on the equatorial β-plane [Eq. (11.5.4) of Gill 1982]. However, this applies only for heating in a rotating atmosphere at rest. In the monsoon trough and cyclones, nonlinear effects — flow curvature as well as the Coriolis acceleration — are important. There is a significant difference in horizontal scale between the small, intense cyclones in the convergent lower tropospheric flow, and the enormous upper-tropospheric anticyclonic gyre over the monsoon region (Figs. 1.7 and 1.8). This observation makes sense from the point of view of elementary gradient wind considerations. These two scales may be called the *cyclonic* and *anticyclonic deformation scales*. The warm-core thermal structure of the monsoon, hypsometrically related to the low surface pressure (Figs. 5.1-5.5), is on a cyclonic deformation scale. But the relative flatness of the 200 mb surface, its height gradients being on the anticyclonic deformation scale, testifies that much of the convective heating which happens in the monsoon and other convective "hot spots" is spread widely, indeed over the entire tropical belt, keeping the 1000-200 mb thicknesses up. Where f is small, the "deformation radius" within which the heating is trapped is set by dissipation, rather than rotation, and is given by $c\tau_d$, where $\tau_d$ is the dissipation time scale (Bretherton 1987). This dissipation radius tends to be very large.

### *2.2.3 Implications and examples of dispersion*

Consider the implications of vertical dispersion for diagnostic rawinsonde budgets of a hypothetical unchanging heating event switched on at a time t = 0, with a heating profile peaked in the upper troposphere, like MCS heating profiles (Houze 1982, 1989). If the heating were at the center of a ~300 km radius sounding array, like the GATE A/B scale (Frank 1978) or AMEX Gulf of Carpentaria arrays, the first divergent winds at the sounding stations, indicating that heating had begun, would arrive at about t

= 100 min. The gravest vertical mode would appear first, and the analyst would report a smooth, troposphere-deep mean upward motion over the array. At t = 6 h, the picture of the heating profile would be sharper, up to tropospheric wavenumber 2, and it would appear that the level of maximum vertical velocity (and hence heating) had risen with time. Of course, MCS's *do* have a life cycle, which involves progressively larger fractions of the rainfall being contributed by nimbostratus, and therefore a rising with time of the system's net upward mass flux and heating. But the point here is that even if that were not the case, the vertical velocity *diagnosed over an area containing the MCS* would rise with time, as is observed (*e.g.* Figs. 13-17 of Houze 1982), the time scale being determined by the size of the sounding array.

Another implication of the dispersion of vertical structure is that if the convergence into MCS's peaks above the surface, as observed, while the far-field wind response consists of the "gravest mode" with maximum inflow at the surface, surface convergence in the intervening fluid is implied. This leads to an increase in integrated convective available potential energy [ICAPE, defined in Eq. (4.1.3)] in that intervening area, rendering it more favorable for additional convection. This mechanism may be partially responsible for the "superclustering" of tropical convection, of which the Australian monsoon is an example (Mapes 1992).

The dispersion of vertical structure with distance from a buoyancy source may be seen in the laboratory. Figure 2.7 shows the results of an experiment I carried out for this purpose. It shows the response of a continuously stratified fluid (salt water) to a localized buoyancy forcing (salty convective plume). The photographs have been inverted, as is traditional in plume literature, so the plume appears to go upward like atmospheric convection. The plume in Fig. 2.7 is not meant realistically to represent atmospheric convection. It is simply one example of a strong, rapid buoyancy forcing with complex vertical structure. The initially vertical dye lines, illuminated by a strobe light at time intervals of half a buoyancy period (nondimensional times are plotted on the figure), register the gradual arrival in the far-field fluid of signals of ever smaller vertical scale. The first displacements are the gravest mode of the layer, half a wave spanning the depth. As time goes on, the shallower vertical structures gradually propagate out from the forced region. In the long-time limit, all the lines are parallel (although the presence of the lateral boundaries makes the amplitude decrease with distance).

An example of the rotational trapping of shallow structure can be seen in the calculations of Schubert et. al. (1991) concerning the Hadley circulation. In their zonal wind fields, which are indicators of meridional displacements, the "gravest vertical mode" structure dominates the solution at latitudes remote from the heating, while shallower features of the heat source are trapped nearer the heating (their Figs. 3c,5c). The dissipative trapping of shallow structure is evident in the forced-damped steady Walker circulation model of Geisler and Stevens (1982). Their Fig. 3 (reproduced in Mapes 1992) shows zonal wind as a function of distance east of the heating. Again, the gravest vertical structure dominates the steady wind response at large distance. In this case, the "gravest mode" is a half-wave through the troposphere depth *as defined by the depth of the heating.*

### *2.3 Heating, vertical velocity, and divergence in the heated zone*

While it is convenient in theoretical and modeling work to formulate the equations governing atmospheric flow in terms of heating, this convention is not ideal for the interpretation of observations. Heating is an impossible quantity to measure directly, and is instead typically diagnosed using the thermodynamic equation, here in isobaric coordinates:

$$\frac{\partial T}{\partial t} + \mathbf{U}\cdot\nabla T = \omega\sigma + Q_1 \qquad (2.20)$$

where $\omega$ is the rate of change of pressure following fluid motion, $\sigma$ is the static stability parameter $(T/\theta)\,(\partial\theta/\partial p)$, and $Q_1$ is heating rate in degrees per unit time.

If temperature varies little from time to time and place to place, as is observed in the tropics, even within MCSs, on scales larger than convective, then the left-hand side is small and the static stability $\sigma$ is a nearly constant proportionality factor between $\omega$ and $Q_1$. $Q_1$ is called the "apparent heat source," defined by (2.20) when $\omega$ is taken to be the mean vertical velocity *as resolved by the measurements in question.* In the case where $\omega$ means mesoscale or synoptic-scale mean vertical motion, $Q_1$ includes eddy heat transports by unresolved convective transports (canceling up and down motions with unequal temperatures), as well as actual heating by water phase changes and radiative energy flux divergence. The close correspondence of measurements of $Q_1$ and $\omega$ can be seen in Fig. 2.8, adapted from Frank and McBride's (1989) composite rawinsonde heat

budget of mature Gulf of Carpentaria MCS's during AMEX/EMEX. Of course, the apparent heating and vertical velocity shown in the figure are not independent measurements. What Fig. 2.8 really shows is that large-scale temperature advection is small (Frank and McBride did not even attempt to estimate the small storage term $\delta T/\delta t$) and that $\sigma$ does not vary much with height through most of the troposphere (though it decreases rapidly above ~350 mb).

But even vertical velocity is not a direct measurement; it is in turn diagnosed from measurements of horizontal divergence [evaluation of Stokes's theorem (3.1) as a function of height] and the mass continuity equation, assuming boundary conditions of zero vertical velocity at the surface and/or at some level near the tropopause. Hence divergence is the primary measurement underlying nearly all diagnoses of vertical velocity and heating. An exception is the wind profiler data of Balsley *et al.* (1988); as shown by Houze (1989), the Balsley *et al.* result is quite different from all other previously reported diagnosed vertical velocities in tropical precipitation.

MCS's contain a broad spectrum of individual vertical velocities, both upward and downward, especially but not solely in the very active convective portions of the system. To illustrate this, Fig. 2.9 shows histograms of hydrometeor vertical velocity at various altitudes, from P3 Doppler radar data at vertical incidence. Each ~9 min flight leg in the sample has been subjectively classified as convective (C), intermediary (I), or stratiform (S), as discussed in Sec. 3.1.1 below, to illustrate the narrowing of the vertical velocity spectrum with time as precipitation areas age. The means of the C, I, and S histograms are not significantly different, and reflectivity-based particle fallspeed corrections do not help. Average vertical air motion simply cannot be reliably estimated by averaging a large number of Doppler radar estimates of vertical velocity. Even *in situ* aircraft measurements of vertical air velocity do not have a reliable mean.

Yet these chaotic masses of up- and down-drafts do average out to repeatable, consistent mean vertical mass flux profiles, as indicated by measurements of horizontal divergence (Section 3.1.2). While the numerous small-scale strong up- and down-drafts are important contibutors to the vertical eddy fluxes of hydrometeors (the 500 $km^2$-mean convective-area ascent rate of ~1 m/s could not loft a raindrop) and horizontal momentum (*e.g.* LeMone 1983), and to a much lesser degree sensible heat (*e.g.* Houze 1982, 1989, Jorgenson and LeMone 1989), their mass fluxes nearly cancel. The residual sum is the much smaller in magnitude, but stable and physically determined, mean mass flux, with

its important relationship (2.20) to *total* heating (which includes the convective heat fluxes).

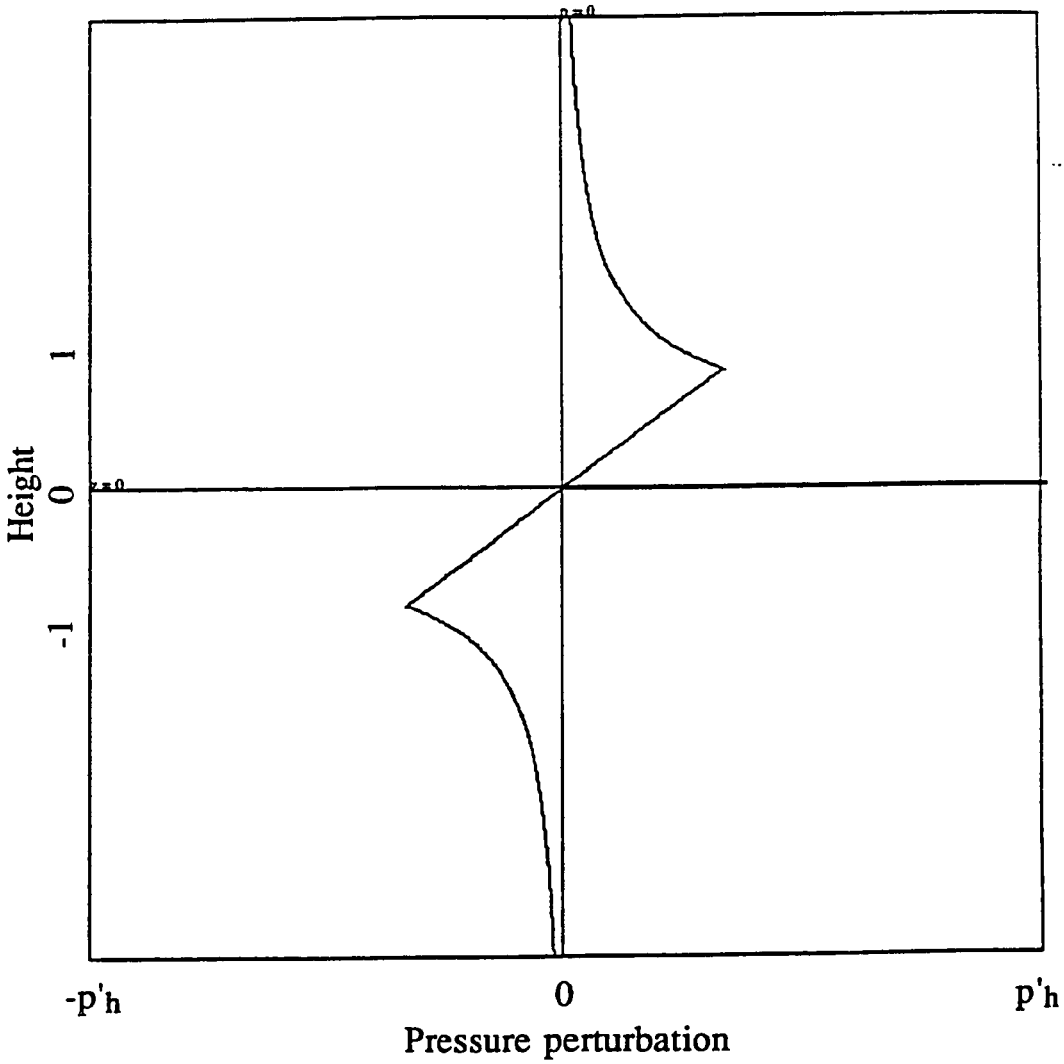


Fig. 2.1 : Pressure perturbation on the vertical axis of a spherical buoyant bubble (Eq. 2.10). The bubble is of unit radius, and pressure is scaled such that the full horizontal axis corresponds to the hydrostatic limit.

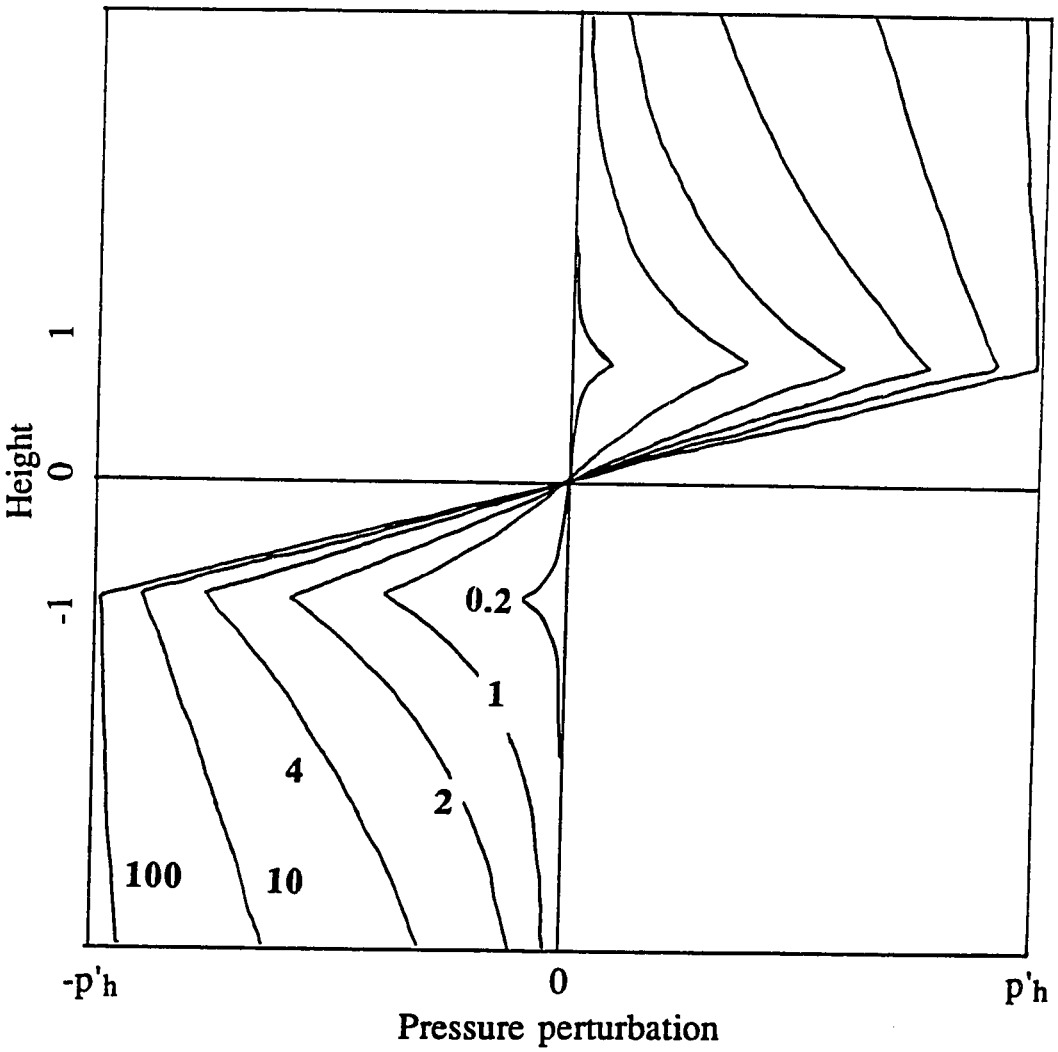


Fig. 2.2 : Pressure perturbation on the vertical axis of cylindrical buoyant bubbles (Eq. 2.11). Buoyant cylinders extend from -1 to 1 in z. Aspect ratios A are indicated on the plot.

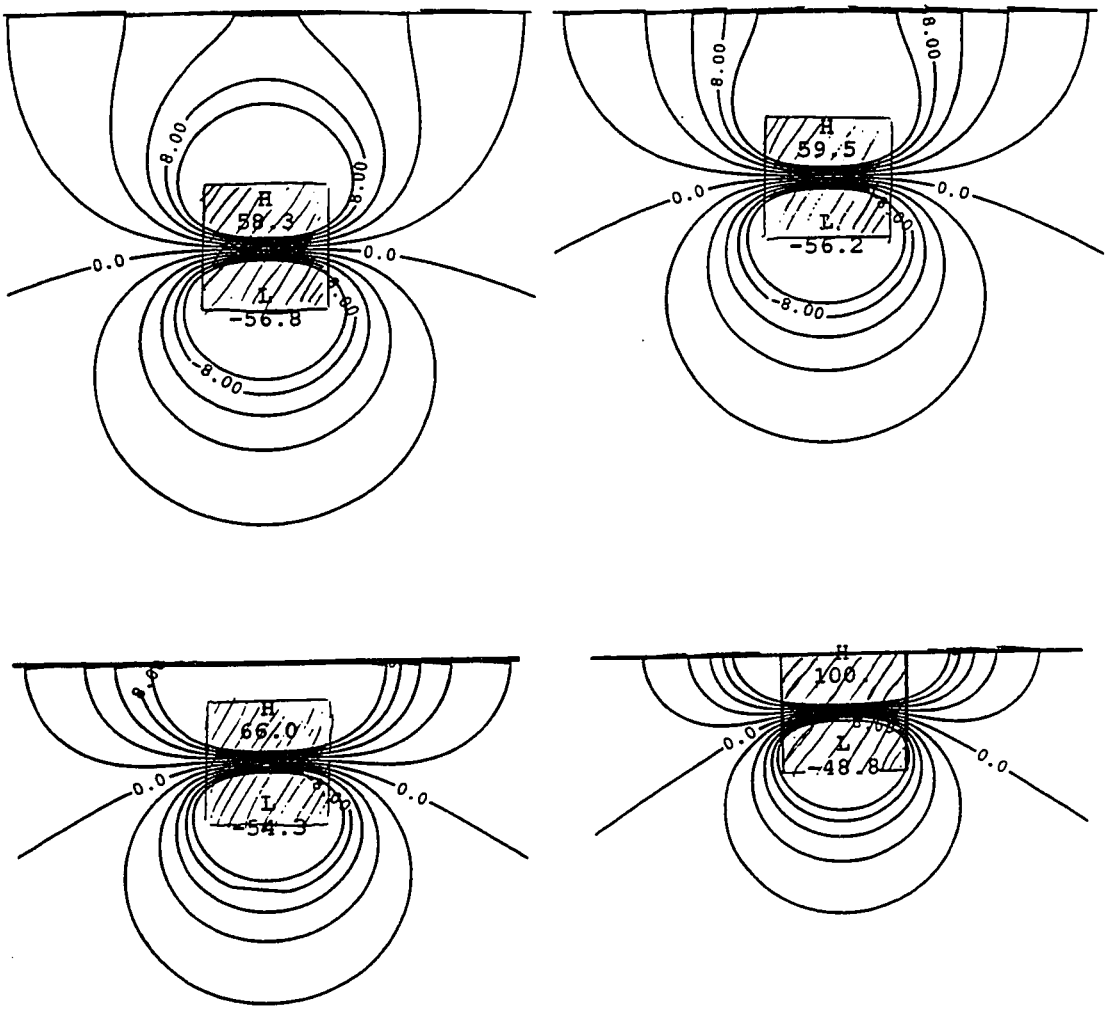


Fig. 2.3 : Pressure perturbations around a buoyant cylinder (hatched) near a boundary.

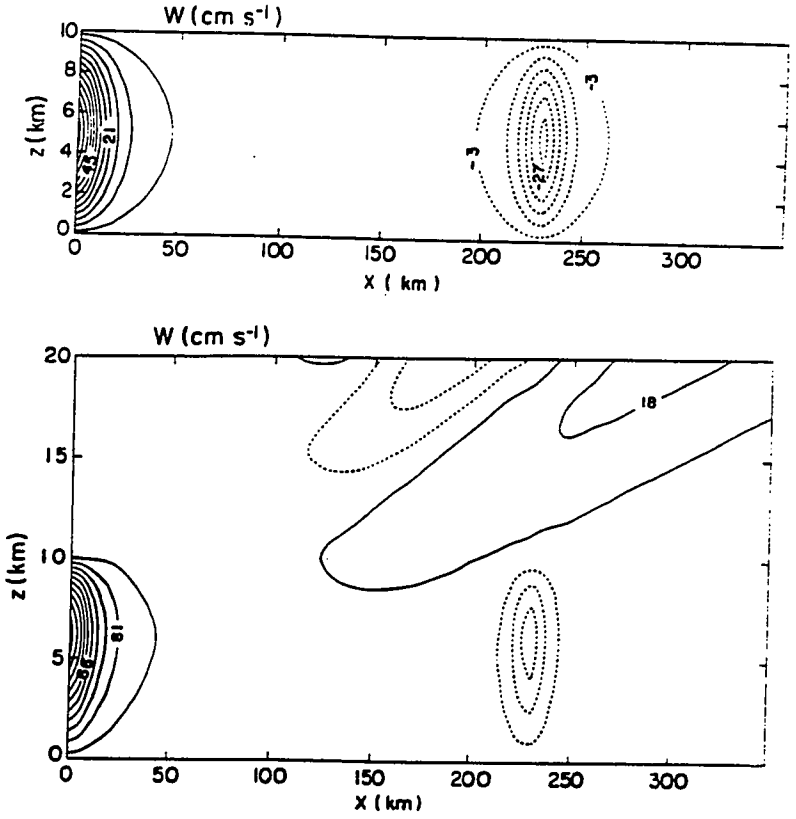


Fig. 2.4 : A "buoyancy bore." Contours of vertical velocity some time after the initiation of a sinusoidal (in the vertical) heat source near the origin a) between rigid boundaries; and b) in a semi-infinite domain. From Figs. 3 and 6 of NPC.

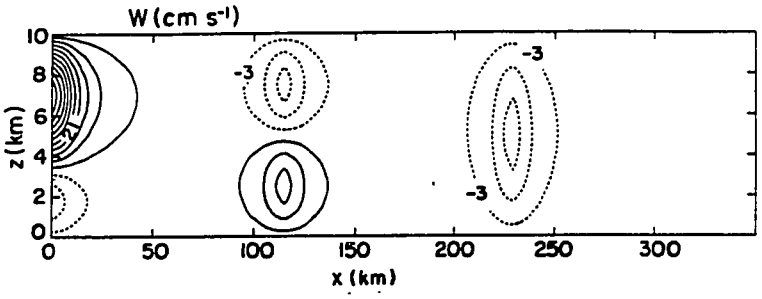


Fig. 2.5 : Two buoyancy bores of different vertical wavelengths. As in Fig. 2.4a, but for a heat source consisting of two sinusoids in the vertical. From Fig. 5 of NPC.

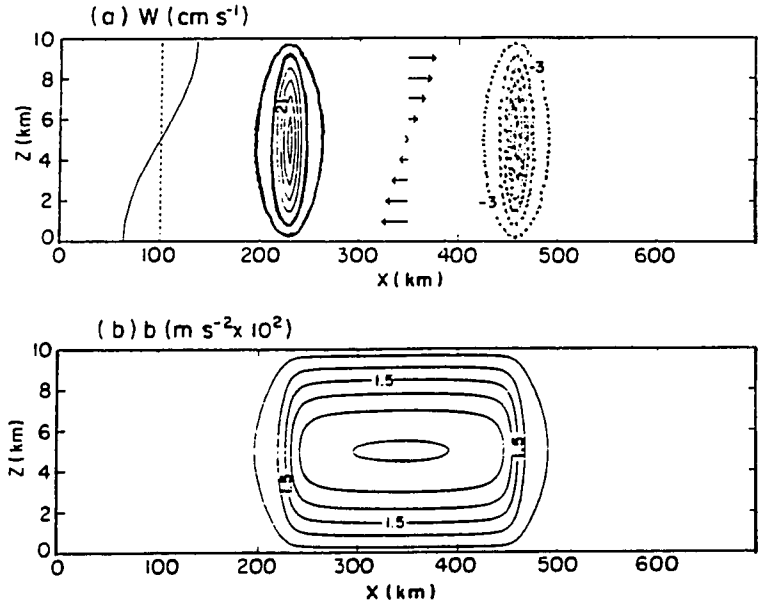


Fig. 2.6 : A "buoyancy roll." As in Fig. 2.4a, but after the termination of a heat source which initiated at an earlier time. From Fig. 10 of NPC.

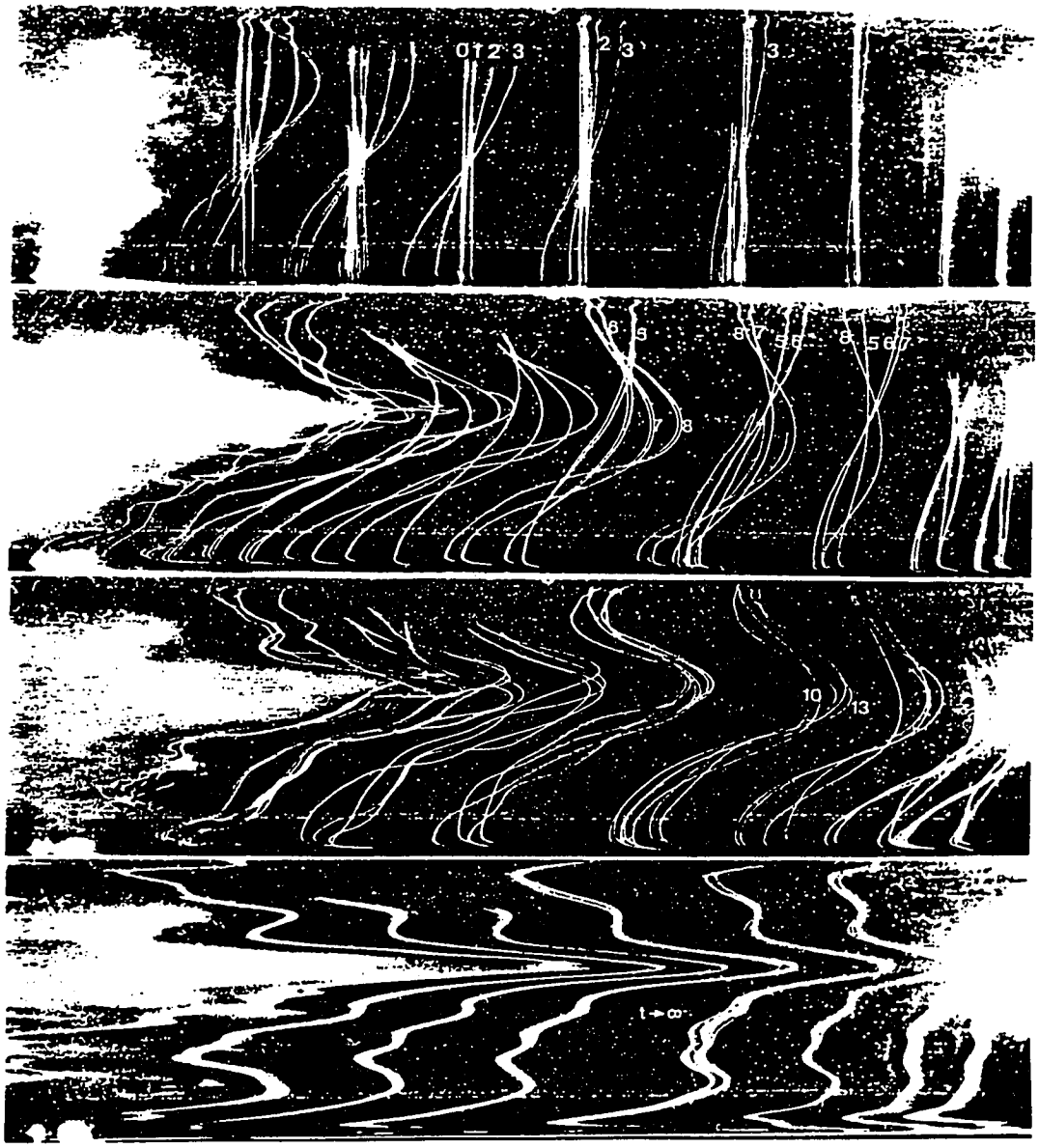


Fig. 2.7 : Dispersion in a laboratory fluid. Strobe photographs of the successive positions of initially vertical dye lines in continuously stratified salt water. Numbers indicate the times, in units of $\pi/N$ (half buoyancy periods), at which the line positions were recorded, after the pulse of "heating" (salt buoyancy forcing). Photographs are inverted.

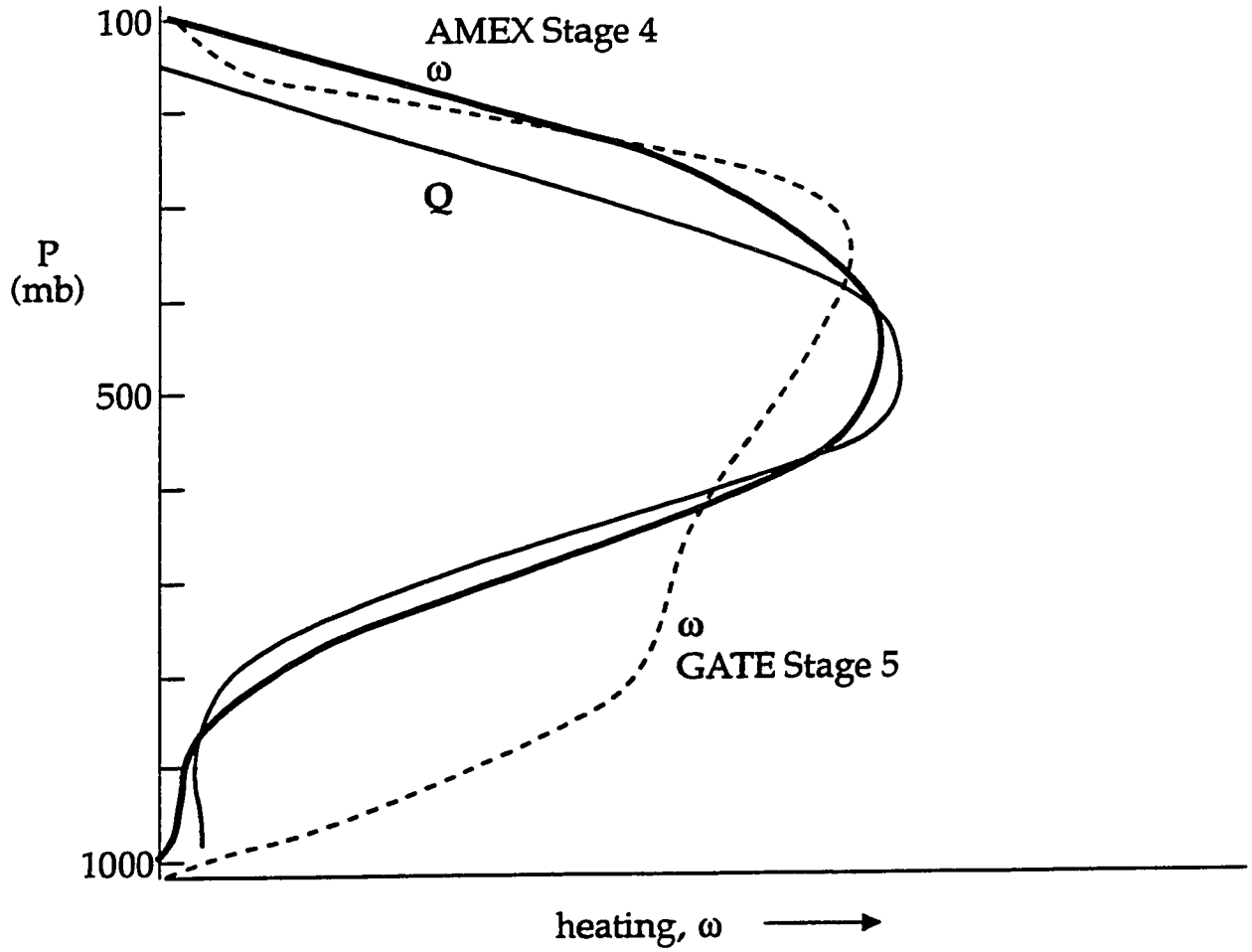


Fig. 2.8 : Comparison of heating (Q, in temperature/time units) and vertical velocity (ω, in pressure/time units) profiles, for composite mature MCS's in the Gulf of Carpentaria. GATE mature MCS ω profile shown for comparison. Adapted from Frank and McBride (1989).

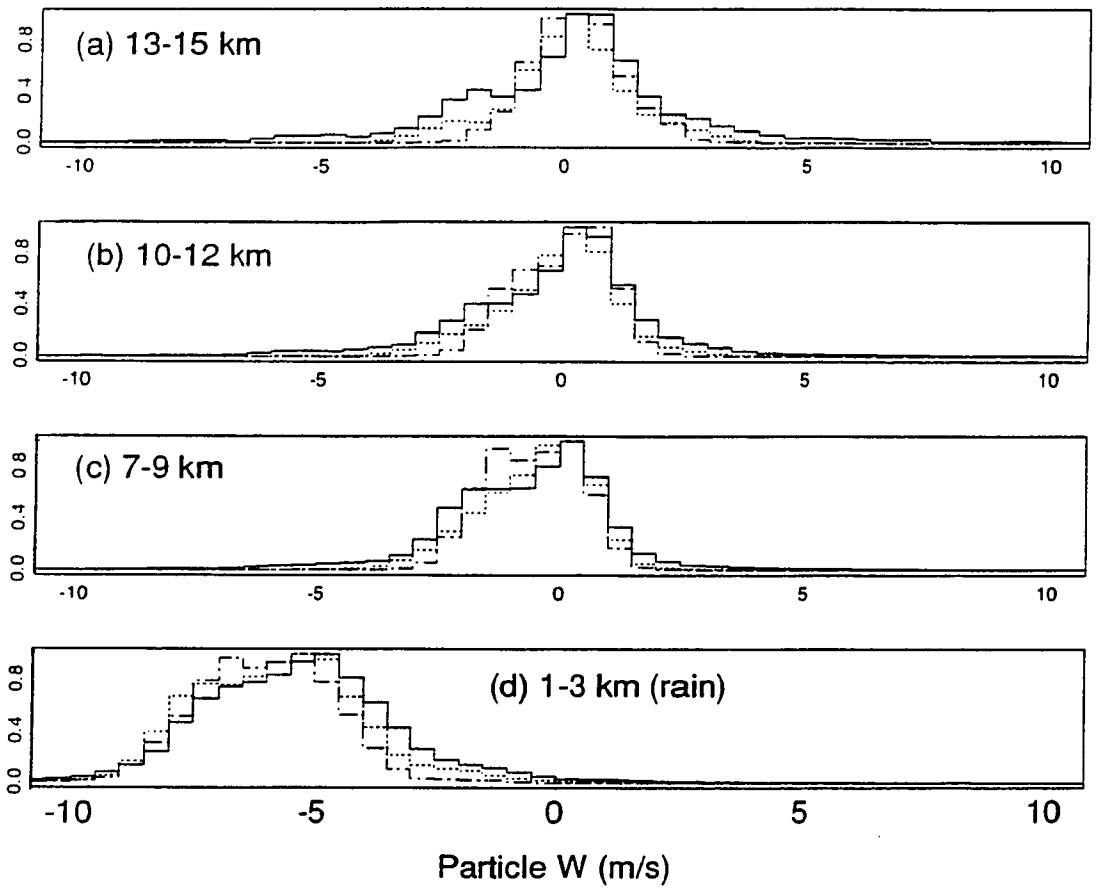


Fig. 2.9 : Vertical incidence Doppler radar data. Normalized number histograms of W, the vertical velocity of hydrometeors (radar scatterers), in the four indicated altitude ranges, from vertical incidence airborne Doppler radar data in 4 vigorous MCS's (EMEX flights 3,6,7, and 10). The three superposed histograms at each altitude are subsets of the data, leg by leg, subjectively classified (see text) as convective (solid lines, 22 legs), intermediary (dashed lines, 19 legs), and stratiform (dash-dot, 21 legs). The total number of independent Doppler measurements in each category is approximately 10,000 in the 2-3 km altitude interval and 20,000 in the 2 km intervals.

# CHAPTER 3

## THE EMEX MCSs

In the Equatorial Mesoscale Experiment (EMEX), aircraft and airborne Doppler radar were used to sample the "convective/transitional" and "stratiform" precipitation areas of ten oceanic tropical MCSs. The "principal scientific objective of EMEX," from the Joint Proposal to the National Science Foundation (1986) was to test the hypothesis that:

> "The vertical profile of diabatic heating in tropical convective systems is a strong function of the heating associated with the mid-tropospheric stratiform part of the disturbance as well as from (sic) the deep convective part."

A second and related objective was to test the hypothesis that "a definable mesoscale circulation exists within the stratiform part of the disturbance..." and a third was to "investigate the physical mechanisms responsible for the formation of the stratiform cloud and its mesoscale circulation."

Ten successful flight missions were conducted, into ten distinct MCSs in various synoptic environments, and Doppler radar and other data sufficient to address these major objectives were obtained. It must be borne in mind that this sample is only for the mature stages of the *MCS* life cycle. For example, the heating in young precipitating convective cells, growing into clear air in the formative stages of the mesoscale system, was entirely missed (a problem endemic to aircraft measurements). For example, although the convective divergence profile sample shown below includes both young and older convective cells, all the observed convection, by the nature of Doppler radar measurements, was growing in environments full of pre-existing precipitation particles. Also missing are the very late stages of MCS decay, including evaporation of the cloud debris, and prolonged radiative heating in the "extended upper-tropospheric anvils," as postulated by Webster and Stephens (1980).

In this chapter I will consider first the generalized results of EMEX, those general qualities which were observed in most or all of the EMEX MCSs. These include the presence of deep convective cells along cold pool boundaries, and stratiform precipitation

as an outgrowth or later stage of earlier convective cells (sec. 3.1.1). Interestingly, the divergence profiles (indicative of heating profiles) within the building blocks of MCSs were very similar from case to case (sec. 3.1.2). In section 3.2, radar, satellite, and aircraft data analyses in each of the ten individual MCSs will be presented, followed at the very end by a summary of the unusual or unique features which may demand some slight modifications or provisos to the "quasi-universal" picture of MCSs presented in sec 3.1.

## *3.1 Aspects common to all the MCSs*

Before plunging into detailed analyses of the specific MCSs sampled in EMEX, it is worthwhile to consider the similarities among them, and the quasi-universal qualities of MCSs in general. The EMEX data are an incremental addition to a substantial standing body of MCS literature. However, the airborne Doppler radar results on internal divergence profiles (related to heating profiles, as reviewed in sec. 2.3) are unique, and constitute some of the major results of this research.

### *3.1.1 Convective, intermediary, and stratiform areas*

Mesoscale convective systems are characterized by the presence of areas of stratiform precipitation, in addition to precipitating deep convective cells. Convective areas are apparent in plan view radar echo maps as small-scale (aspect ratio ~1, so 10-30 km in a horizontal dimension) high-reflectivity "cells" or lines. In vertical sections, quasi-vertically oriented reflectivity cores, often extending above the 0°C level, are apparent. Stratiform precipitation areas, by contrast, appear as smoother, more homogeneous areas of radar echo, with a horizontal radar bright band evident in vertical cross-sections at the 0 °C level. Intermediary structures consist of variable or granular radar echoes, but without the strong solid cores characteristic of convective areas or the well-defined bright band of stratiform areas. The truly defining characteristic of intermediary precipitation areas is that they occur between convective and stratiform precipitation *in the time domain.* As this characteristic is difficult to objectify, particularly with the variable radar coverage provided by a wandering radar platform, all the classifications used below remain somewhat subjective. As shown in section 3.1, these three types of precipitation structures — convective, intermediary, and stratiform — can also be distinguished *a posteriori* by their distinctive divergence profiles.

The convective sub-areas of MCSs are typically oriented in lines or arcs. These lines or arcs lie along the boundaries of surface "cold pools" of dense air, created by the downdrafts in previous convection. The stratiform sub-areas of MCSs evolve from antecedent convective cells. All of these elements of MCS structure and dynamics, familiar from observations made during the GATE (reviewed in Houze and Betts 1981) and Winter MONEX (reviewed in Johnson and Houze 1987) field programs, were also observed in the EMEX MCSs.

### *3.1.2 Horizontal divergence measurements*

#### *3.1.2.1 Measuring divergence with Doppler radar*

Area-mean horizontal divergence was calculated from the Doppler radar data (and from the rawinsonde arrays) using Stokes's theorem:

$$\int\int_A \nabla\cdot\mathbf{V}\, dA = \oint_\ell \mathbf{V}\cdot\hat{\mathbf{n}}\, d\ell \qquad (3.1)$$

where V is the horizontal wind, n the horizontal unit vector normal to the line integral boundary, $d\ell$ a length element along the boundary, and A the area enclosed within the boundary. In this case, the boundary in question is the parallelogram shown in the solid line in Fig. 3.1. The sides of this parallelogram were chosen perpendicular to the radar beams, and hence parallel to the flight tracks, so that the component of the wind normal to the boundary of the parallelogram is simply the horizontal component $U_n$ of the Doppler radial velocity. Since the radar scanned in the vertical, the edges of the parallelogram are really vertical "walls", and the integral (1) was performed in discrete layers in the vertical, 1 km in depth, yielding profiles of divergence. The 1 km depth was chosen because the radar beamwidth (1.9°) is about 1 km at 30 km range.

The horizontal component of the Doppler radial velocity was estimated from the actual radial velocity, as illustrated in Fig. 3.1. For radar beams at elevation angle $\alpha$, the horizontal component $U_n$ is given by:

$$U_n = [V_r - (w-V_t)\sin(\alpha)] / \cos(\alpha) \qquad (3.2)$$

where w is the vertical air velocity and $V_t$ is the reflectivity-weighted terminal fallspeed of radar scatterers. In our calculations, we have neglected the term $w\tan(\alpha)$, and estimated

$V_t$ from radar reflectivity, according to the formulae used by Marks and Houze (1987). An upper limit on the divergence error implied by a constant 1 m/s error in the assumed $(w-V_t)$ can be estimated from 1-dimensional considerations in this same geometry:

$$\delta DIV \sim \delta U_n / \delta x \sim 1 m/s \, [\delta z/r_1 - \delta z/r_2] / (r_2-r_1) = 1.8 \times 10^{-5} \, s^{-1} \quad (3.3)$$

where $\delta z$ (taken as 7 km) is the maximum height of the divergence calculation above or below flight level, and $r_1$ and $r_2$ (taken as 10 and 40 km) are the horizontal distances from the aircraft to the far and near walls, respectively (Fig. 3.1). In calculating each divergence profile, the expected apparent divergence (EAD) due to the assumed particle fallspeed — convergence below the flight level, divergence above — was used to adjust the calculated values. In general EAD was much smaller than the measured divergences (see Fig. 3.3 below), unless the closer wall was put too close to the flight track. Data with elevation angles exceeding +/- 45° were therefore never used.

The edges ("walls") of the parallelograms were chosen interactively, within the constraints of the 45° elevation cutoff, the Doppler range limit, and the area of available Doppler data (precipitation area). Generally these areas were about 500 $km^2$, so the profiles should be interpreted as representing areas of linear dimension ~22 km. Experience shows that the results are not overly sensitive to the exact location of the parallelogram. For each parallelogram the divergence calculation was done with threefold redundancy: the locations of the parallelogram walls were shifted by one Doppler radar range interval (150 m) each way to obtain three profiles, from completely independent data but with neglegibly different geometry. This redundancy has been carried through all calculations and can be seen in the profiles below (Figs. 3.3-3.5); the spread of the three estimates reflects the small fraction of the variability which is due to sampling error.

The time necessary to fly the zigzag pattern shown in Fig. 3.1 was about 15-20 min. A correction for spatial translation during the data collection period was made, based on subjective evaluation of the motion of features in the reflectivity field. The effect of this correction on the results was small. It is impossible to evaluate the effect on our results of other forms of evolution, more complicated than linear spatial translation, during the data collection period. However, the consistency of the results from case to case leads us to believe that for the ~500 $km^2$ horizontal scale inherent in the method, the mean structure lasts long enough to be well sampled.

The integral (1) was evaluated at each level by using all available data on each of the four "walls" to evaluate the mean cross-wall velocity, then summing, with appropriate signs, these four mean velocities, weighted by the lengths of the walls. In this process, it was not necessary to synthesize multiple Doppler radial velocity estimates, collected at different times and from different vantage points, to obtain vector wind estimates. As a result, interpolation error was eliminated, and much computer time was saved. Because a relatively small amount of data was used, and used in its raw form, it was easy to visually inspect and edit all data which entered the calculation. In addition, the process employed none of the "black box" filtering and iterative calculations traditionally used in Doppler radar processing, so that surprising and interesting results could be quickly and unambiguously traced back to the raw observations.

In the upper troposphere, sampling was poor; this accounts for increasing differences among the three estimates above 10 km altitude in Figs. 3.3-3.5. The tops of the observed MCS's were considerably higher than 10 km, typically 14-16 km or more, according to vertical-incidence radar data and satellite-observed cloud top temperature.

In the lowest layer, 0-1 km, special problems arose. Since the radar beam width (full width at half power) was 1.9°, some power was returned by the sea surface, especially at far ranges. The effect of sea-surface echo on radial velocity depends on the relative reflectivities of the precipitation particles and the sea surface. Sea surface reflectivity is a function of sea state, and is higher for upwind-looking beams than downwind-looking beams. In general, the presence of sea clutter tends to bring radial velocities of either sign closer to zero. The effect of sea clutter on the divergence profiles depends on wind speed, and on the orientation of the parallelogram with respect to wind direction. In some cases, particularly when winds were strong, sea clutter was apparent as low radial velocity in the Doppler measurements near the surface, but low wind speeds in the boundary layer could also be real. In short, we could find no simple objective way to remove or correct for sea clutter, so divergence in the lowest layer must simply be viewed as subject to special uncertainty.

### *3.1.2.2 Doppler divergence profile results*

Using the technique outlined above, we have obtained 93 divergence profiles within nine of these ten MCS's (the weak line of convection sampled on flight 2 had so little stratiform precipitation during most of the flight that Doppler radar sampling was

inadequate). These profiles have been subjectively grouped into three categories, representing three archetypal precipitation structures observed to make up MCS's: convective areas, stratiform areas, and intermediary areas undergoing evolution from the former to the latter.

A good example of the evolution of convective to stratiform precipitation areas may be found in the MCS sampled in the sixth EMEX flight, on 27 January 1987. It existed in a weak synoptic-scale depression with light winds. The same geographical area was sampled repeatedly as the precipitation evolved from predominantly convective to predominantly stratiform. Radar reflectivity evolution is shown in Fig. 3.2, with corresponding divergence profiles shown in Fig. 3.3. An initial broad east-west line of echoes along 12.5 - 13°S (Fig. 3.2a) evolved in place into stratiform precipitation (Fig. 3.2d). At the same time, a north-south line of convection developed along the western edge of this area, and can be seen protruding north from the sampled precipitation area in Fig. 3.2d. Note that the sampled stratiform precipitation was formed in place by the evolution of prior convection, and not advected or sheared off of the convective line which happened to be adjacent to it at the sampling time.

In the earliest profile at 2126 GMT (Fig. 3.3a), a strong signature of deep convection — low-level convergence, upper-level divergence — is seen. By 2148 GMT, the reflectivity field is still quite granulated but no longer exhibits strong convective cells (Fig. 3.2b). We would classify this precipitation area as "intermediary;" its divergence profile consists of a thin layer of strong divergence at the surface, with deep convergence, to 12 km altitude at least, above that (Fig. 3.3b). The constraint of mass balance suggests that strong divergence must exist above 12 km, as is evident in rawinsonde divergence profiles (*e.g.* Fig. 3.6). An hour later, at 2254 GMT, the convergence remains only near 10 km (Fig. 3.3c).

By 2317 GMT, the signature of a lower-tropospheric mesoscale downdraft — convergence near the melting level, divergence below — has developed, but the convergence at 10 km is still evident (Fig. 3.3d). A similar divergence profile observed in the trailing stratiform area of a midlatitude squall line may be seen in Fig. 6 of Srivastava *et al.* (1985). Just to the west, at 2328 GMT, the measured profile was more typical of stratiform precipitation areas (reviewed in Houze 1989), with divergence up to 3-4 km altitude, convergence to 8-9 km, and divergence above that (Fig. 3.3e).

Profiles of mean divergence, from the entire EMEX data set, for convective, intermediary, and stratiform areas are shown in Fig. 3.4. We have elected to display these mean profiles against pressure as the vertical coordinate in order to make clear the mass balance constraint: the area under each divergence profile (including the unmeasured upper-tropospheric divergence) must be zero if vertical mass flux is zero at the top and bottom of the troposphere. Note that in all three types of precipitation, net convergence dominated within the measured levels, implying that there must be unmeasured divergence above 12 km, as is found in rawinsonde profiles (*e.g.* Fig. 3.6). In Fig. 3.5, the means have been subdivided according to the different types of MCS's observed in different synoptic environments within the monsoon (see Fig. 3.7). The mean profiles share a basic similarity in all three types of MCS's.

In general, the standard deviations (dashed lines) are comparable to the value of the mean. However, the reader should by no means infer that the sign of mean divergence is everywhere uncertain. Differences among the three solid lines roughly delineate the envelope of sampling error associated with the Doppler radar measurements themselves. Other sources of error include evolution of the flow during the sampling interval (hard to estimate), and errors in horizontal wind estimates owing to incorrecly estimated particle fallspeed (the contribution of assumed fallspeed to divergence [see Eq. (3.3)] is shown on Fig. 3.3a-e). The remainder of the variance is meteorological, and is therefore not a measure of the validity of the means, but rather an additional quantity of interest.

The convective-area mean profiles show convergence from the surface up to about 500 mb or 6 km, then divergence above that (Figs. 3.4a, 3.5a). The level of maximum convergence is elevated off the surface. It must be remembered that the sample represented here is of convective areas, identified by radar reflectivity cells, in the mature stages of the MCS life cycle. Some young convection was sampled, but in general the early growth stages of convective cells, when surface convergence might be higher, are probably undersampled. Simple thermodynamic arguments suggest that much of the elevated convergence must feed into downdrafts, since this much mass of low-$\theta_e$ air entrained into updrafts would spoil their buoyancy. Aircraft measurements of downdraft mass flux in deep convection (Fig. 3 of Jorgenson and LeMone 1989), while noisy, support the idea that convergence at 2-4 km altitude feeds into downdrafts.

A distinct maximum in the standard deviation of the convective divergence profiles, just below the crossover point at ~500 mb or 5 km (in Figs. 3.4a, 3.5a respectively), indicates that divergence at this level fluctuated more than at other levels. This may be related to the variations in the presence and strength of the isothermal layer often found near the 0°C level. The theory of Bretherton and Smolarkiewicz (1989) predicts that convection penetrating an environmental cold layer should entrain mass below, and detrain mass above, the cold layer.

In the mean stratiform profiles, divergence is observed below the 650 mb level, with convergence peaking at midlevels (6-7 km or ~450 mb), above the melting level (Figs. 3.4c, 3.5c). The predominance of mass convergence in the measured profiles suggests that unmeasured divergence lay above this convergent layer. This divergence-convergence-divergence profile is common to the results of essentially all previous studies of MCS stratiform areas in the tropics and midlatitudes (reviewed by Houze, 1989). The fact that the convergent layer extends as high as it does may reflect "contamination" of the stratiform sample by intermediary profiles, with their upper-tropospheric convergence. Most of the stratiform profiles simply did not extend above 9 km, so the sample at 11 km is biased toward the deeper structures, which were younger and hence closer to the intermediary stage. An exception is the convergence extending up to 11 km in pure stratiform precipitation areas in the "strong straight flow cases" (Fig. 3.5c), contributed mostly by the EMEX 3 stratiform areas, which were consistently unusual in that way. In EMEX 3, the strongest environmental winds were at midlevels, and the reflectivity fields in the stratiform areas of that MCS, both ahead of and behind the convective line, were eroded away at midlevels. The connection between that observation and the unusual divergence profiles remains unclear.

The mean "intermediary" precipitation area divergence profiles (Figs. 3.4b, 3.5b), as foreshadowed by Fig. 3.3c above, were characterized by a convergence peak high in the troposphere, near the top of the data. The proponderance of mass convergence in the profile suggests that this convergence feeds into mean ascent in the upper troposphere, and that, as in the convective and stratiform areas, substantial unsampled divergence existed above ~250 mb. This upper-level convergence is a new and interesting feature and begs for speculation about its physical significance.

The dispersion of vertical structure in the stratified environment (section 2.2) provides a framework for one explanation. The atmosphere cannot instantly accomodate

a large amount of mass, ascending in the convection, whose level of neutral buoyancy is near the top of the troposphere. Initially, convective cells are thus forced (by a perturbation pressure gradient force opposing the buoyancy force) to detrain their mass flux over a deep layer (as observed in Figs. 3.4a and 3.5a), much of it below its level of neutral buoyancy. The resulting deep slab or lens of cloudy outflow air then gradually collapses in the vertical, and spreads out in the horizontal at its level of neutral buoyancy, as described by Lilly (1988). In the weakly stratified upper troposphere, below the highly stratified stratosphere, this collapse process would be asymmetrical, involving mostly upper tropospheric ascent. However, downward motions just above the stratiform portions of MCSs, consistent with this hypothesized slumping or collapse, are observed in both the tropics (Balsley *et al.* 1988) and midlatitudes (Johnson *et al.* 1990).

This process may be seen in a laboratory fluid in Fig. 2.7, which shows a convective plume initially detraining in a single fat bulge, and then gradually separating into the thin detrainment layers which characterize the state of the fluid in the long-time limit, after several tens of buoyancy periods (corresponding to several hours in the tropical troposphere). Only in that limit can one assume that fluid parcels have found their level of neutral buoyancy.

In this view, the upper-tropospheric ascent in the intermediary and stratiform precipitation areas may be viewed as a continuation of the deep convective process, in which high-$\theta_e$ air from low levels ascends to the level in the upper troposphere where the ambient value of saturated $\theta_e$ equals the ascending air's $\theta_e$. The air converging into the midtropospheric base of the mesoscale ascent is apparently high-$\theta_e$ air which has previously diverged out of convective cells, since environmental midlevel air is absolutely stable. This mesoscale part of the convective ascent simply occurs at a larger aspect ratio, and hence under slower, quasi-hydrostatic dynamics. The "hot tower" conceptual model of convection (Riehl and Malkus 1958) was devised as an explanation for the vertical transport of low-level (high-$\theta_e$) air through the mean mid-tropospheric $\theta_e$ minimum. In a sense, then, it applies not to cumulonimbus or to the convective cell parts of MCSs, which happen to visually fit the description of "towers", but to MCS's in their entirety. MCSs do ultimately deliver a lot of mass to the upper troposphere, but only after a stopover of a few hours in the midtroposphere.

It seems likely that the divergence profiles of an ensemble of convective cells, plus the intermediary and stratiform precipitation structures to which it gives rise, have a

stable, physically determined sum. This whole-MCS divergence profile might turn out to be similar from case to case, as the constituent divergence profiles in Fig. 3.5 are. It is unfortunately impossible to determine such mean properties with only a collection of small-scale profiles, as there is no way to accurately measure the proportions of convective, intermediary, and stratiform precipitation. The accurate determination of *mesoscale-mean* divergence profiles, as well as of sub-area profiles as presented here, should be a high priority in future field studies.

In our sample as a whole, no matter what proportions of mean convective, intermediary, and stratiform precipitation are added together, the low-level convergence maximum is elevated off the surface. This has implications for convection favoring neighboring convection (Fig. 4.10; Mapes 1992), and for the elevated initial spinup of tropical cyclones (Fig. 5.7; Davidson *et al.* 1990).

*3.1.2.3 Comparison with rawinsonde profiles*

The above divergence profiles in various parts of MCS's can be better appreciated in light of larger-scale measurements which illustrate whole-system divergence profiles for similar tropical MCS's. Unfortunately, the convection within the Gulf of Carpentaria sounding array was substantially less vigorous and organized than the EMEX aircraft-sampled MCS's. Nevertheless, we have computed divergence profiles for the Gulf array by evaluating the line integral (1) with rawinsonde winds, interpolating the vector wind linearly between sounding sites. A mass-balance correction, constant with height, has been applied, since in our judgement the errors in wind interpolation exceed the error of the boundary conditions ($\omega$=0 at surface and ~20 km). The resulting profiles are noisy, so some averaging is necessary.

Mean profiles of mass divergence over the Gulf of Carpentaria are shown in Fig. 3.6. The first panel shows mass divergence for the five stages — formative, growing, mature, late, and decaying — of the life cycle of a composite of four MCS's selected by Frank and McBride (1989). Note that the low-level convergence in mature MCS's is elevated off the surface, as was found in the Doppler radar measurements. The second panel shows mass divergence, for the four sounding times of day, averaged over the pre-cyclone active periods 16-18 Jan. and 30 Jan.- 4 Feb. Again the low-level convergence peak is elevated, and an interesting kink in the profiles at 10 km is evident. This divergence minimum near 10 km is near the level of the convergence peak in the mean

intermediary precipitation area profiles and the slight secondary peak in the mean stratiform profiles in Figs. 7 and 8. It is also at this level that the static stability drops rapidly from its lower-tropospheric value to its lower upper-tropospheric value. The meaning of these observations is not clear. The third panel shows divergence profiles for composite categories based on percent high cloudiness (PHC). The cloudiest categories (hurricanes) show strong surface convergence, while the moderately cloudy categories have their convergence more evenly through a deep layer.

### *3.2 Analyses of the individual EMEX MCSs by synoptic period*

In this section we describe the mesoscale structure of each of the ten EMEX storms and its evolution during the period of data collection, noting and interpreting some of the especially interesting features of each case. The order is chronological, but to some extent it is also a natural order, since MCS's within the synoptic periods described in section 3 had some similarities and will be discussed together. Figure 3.7 is a schematic guide to the ten EMEX-sampled MCS's, relative to the midlevel flow pattern in weak-flow (Fig. 3.7a) and strong-flow (Fig. 3.7b) states. This section serves the dual purposes of showing the evidence upon which the generalizations in Fig. 3.7 are based, and of presenting a balanced view of the entire population of EMEX MCS's, so that the several case studies of individual storms, in preparation by various researchers, can be viewed in a larger context.

All of these MCS's, except possibly EMEX 2, can be considered to have been in the mature to late stages of the *mesoscale system* life cycle (Leary and Houze, 1979) during the aircraft sampling, with widespread areas of convective and stratiform precipitation already well developed at the beginnings of the flights, and with the areal coverage and intensity of new convection decreasing during the later parts of the flights. However, within this mature phase of the mesoscale systems, precipitation areas in all phases of *precipitation element* life cycle were sampled: new convective cells, mature convective cells, transitional forms, and various types and ages of stratiform areas, occasionally including precipitation falling from sheared-over anvil clouds as well as from decaying convection.

The comments in this section are the results of a comprehensive examination of lower fuselage and tail radar reflectivity data, Doppler data and pseudo-dual Doppler

analyses of wind and divergence, *in situ* measurements from multiple aircraft and dropwinsondes, as well as satellite, sounding, and synoptic data.

The sampling strategy within which these measurements were obtained was identical on each flight. Although the exact routes of the aircraft were decided flexibly in light of real-time radar measurements of the evolving mesoscale systems, all flights were undertaken with the same goal: to conduct repeated, intensive sampling of the internal structure of these systems, using pre-planned flight pattern templates. The P3 flight pattern consisted of zigzagging patterns of straight legs approximately 75 km in length, at 60° angles to each other, at ~5 km altitude (see Fig. 3.1); the Electra and F27 flew straight legs back and forth across convective regions and L-shaped patterns in stratiform areas, at various altitudes below 5 km, with the F27 sampling, when available, focused on the boundary layer. The sampling strategy is discussed in detail in Webster and Houze (1991), and will be well illustrated in the examples presented below.

Takeoff time on all flights was predawn local time (1700-1900 GMT), to take advantage of the climatological early morning maximum in tropical oceanic convection (*e.g.* Mapes and Houze 1992c, Keenan *et al.* 1989). Landing times were ~8 h later, near local midday (0100-0300 GMT the following day). All times and dates below are GMT; Darwin local time may be obtained by adding 9 h 30 min.

### *3.2.1 Onset period*

The *onset* period from 14 to 16 January featured almost continuous large cloud clusters in the Bonaparte gulf, with cold cloud cover for up to 80% of this period (Fig. 1.10b). This period included the development, intensification, and southward drift of cyclone Connie in the Australian Low, which resulted in increasingly straight and strong northwesterly flow at low levels in the Bonaparte gulf and the Darwin area (Fig. 1.10a). The shear line protruding into the Gulf of Carpentaria from the Australian Low developed into a closed circulation that eventually became cyclone Irma; conveniently, analyses of 850 mb winds for EMEX 1-5 flight times have been, published by Davidson et al. (1990, their Fig. 11a) for this reason.

#### *3.2.1.1 EMEX 1: evaporating stratiform precipitation, with an embedded elevated convective arc*

On January 14, low-level westerlies had recently set in along the Top End and were intensifying (Fig. 1.9). The 21Z infrared satellite picture (Fig. 3.8) shows that considerable convective activity was underway in the Bonaparte Gulf and Arafura Sea. The P3 flight track, though sometimes hard to see, is also indicated in this and all other satellite pictures. Because the flight plans for EMEX had anticipated the Gulf of Carpentaria as the focus of the most interesting convection, and the F27 was therefore based in Gove, the P3 flew northeast from Darwin to the eastern edge of the active area on its survey. At the 550 mb flight level, northwesterlies were observed to weaken from west to east, with winds turning to southeasterly at the extreme eastern extent of the flight.

Convective sampling was performed in the easternmost cloud cluster (Fig. 3.8). Radar shows a stratiform precipitation area with an arc of shallow, weakly convective cells, oriented NW-SE, embedded within it (hard to appreciate in Fig. 3.8, 9.2-9.7 °S along 134.4 °E); this arc propagated through toward the east as the P3 and Electra sampled the area. This convective line appeared to be a form of secondary convection within the stratiform area, associated with the convergence ahead of a Doppler- and Electra-measured low-level westerly jet, localized *above the boundary layer* (1-3km, as suggested in the mean hodograph in Fig 3.8). This situation is illustrated in Figure 3.9, which is a vertical cross section of radar reflectivity and Doppler radial velocity, approximately normal to the arc of weak convection marking the leading edge of the jet. The convection was not tall, and had its maximum reflectivity near the melting level; in some sections, it appears merely as an enhancement of the bright band with a shower of heavier precipitation below. Although this cross section is not exactly normal to the leading edge, it accurately illustrates the full 3 dimensional wind and reflectivity geometry. Similar elevated "secondary squalls" were observed in the EMEX 6 stratiform area, and I have also observed them with a land-based Doppler radar at Darwin in January of 1988.

The Electra encountered one narrow convective updraft, and P3 Doppler radar data at vertical incidence indicate others (quite narrow and weak by general EMEX standards), so some free buoyant ascent was occurring. The P3 attack angle probe was out of order on this flight, however, so its *in situ* measurements of midlevel vertical velocity were not reliable.

The stratiform portion of the mission was conducted in the decaying stage of the rain band near 10.3°S (Fig. 3.8). The F27 observed a nearly constant $10^{-4}$ $s^{-1}$ divergence of the almost exactly zonal wind at 990, 950, and 870 mb during east-west passes through this area, and airborne Doppler measurements of full 2-dimensional divergence yield a similar result. Radar reflectivity declined strongly below the melting level in this area, implying that evaporation was taking place. Electra data and dropwinsonde soundings outside the rain area confirm that relatively intense unsaturated mesoscale subsidence had taken place.

*3.2.1.2 EMEX 2: development of a line with strong pressure perturbation from a group of cells*

The following day, on 15 January, the second aircraft deployments were made. Again, the preconceived plan of flying all 3 aircraft in the Gulf of Carpentaria was followed, although the monsoonal westerlies did not extend into the Gulf, and the Bonaparte gulf was again very convectively active. The 00 GMT 16 January satellite picture (Fig. 3.10) shows the Gulf cloudiness, unconnected to the gigantic Bonaparte gulf cluster, the most dramatic non-hurricane event in the EMEX satellite data. Flight level winds at 550 mb, meaured during the P3 ferry and survey parts of the flight (Fig. 3.11), show a very sharp wind shift, possibly associated with the midlevel vorticity precursor to Irma (Davidson et al. 1990), in an area free of cloud and precipitation.

Dropwinsonde measurements show that the northeasterly flow extended to the surface in mid-Gulf, while nearer the western shore weak low-level westerly flow fed into a nearly stationary convective line with little stratiform precipitation (radar, Figure 3.10). The F27 and Electra extensively documented the low-level structure of this isolated line. Very little stratiform precipitation formed in association with the sporadic convective cells in this line, until just before the P3 ferried back to Darwin. A vertical incidence radar cross-section and *in situ* data from the final, westbound P3 flight leg is shown in Fig. 3.12. The updraft had westerly (front to rear) momentum, within an environment at that level of easterlies. A 15 m minimum in D-value (a measurement of the relative height of the pressure surface), very substantial by EMEX standards, lay immediately behind the updraft. Thus, this line was acting as an organized system to enhance, by means of its induced pressure field, the front-to-rear cross-line (westerly) momentum of its updraft, similar to the line studied by LeMone (1983).

*3.1.1.3 EMEX 3: a deep convective line with leading and trailing stratiform precipitation*

On the next day, 16 January, it was decided to direct the aircraft to the Joseph Bonaparte gulf, where the very large cold cloud shields had been forming. Consequently, the F27, based in Gove, could not participate. Convection in the gulf was weaker than on the previous day (cf satellite Figs 3.10, 3.13); cyclone Connie (18 °S, 120 °E) had developed central convection, and began to intensify rapidly.

The MCS studied on this day was an offshore convective line protruding approximately 300 km northwestward from Darwin (satellite, Fig 3.13). Low-level inflow into the convective line came from near-northerly winds on the northeast side (dropwinsonde, Fig. 3.13), spiraling into the intensifying pressure field of Connie. After a spacious circumnavigation of the MCS, during which 7 dropwinsondes were dropped, the P3 joined the Electra in intensive sampling of the weakening convective line and the associated stratiform rain areas. The entire region had strong northwesterly winds through the lower troposphere, with maximum winds at about 5 km, near the P3 flight altitude (hodograph, Fig. 3.14). Winds were strongest and most westerly in the western part of the survey area, far behind the convective line, with maximum winds measured by the P3 exceeding 25 m/s.

During the flight, a cross-wind oriented squall feature at the southeastern end of the line (at 130 °E, 12-13 °S, on the extreme eastern edge of Fig. 3.14) developed, intensified and moved over Darwin, accompanied by high surface winds and heavy rain. The northwestern, aircraft-sampled end weakened, as the line to its northwest intensified, possibly obstructing the low level inflow (cf. satellite pictures, Figs. 3.13 and 3.14) and as virga shafts and then widespread rain began to fall out of the forward anvil and evaporate into the inflow air (cf. radar images, Figs. 3.13 and 3.14: echo near and north of 11.5 °S in Fig. 3.14 is forward anvil).

The stratiform precipitation sample included both the trailing area, undergoing erosion from behind by the strong unsaturated flow along the line and from the rear, and the forward anvil precipitation area, reminiscent of the leading anvil in the GATE squall line system described by Houze and Rappaport (1984). In the forward anvil area, reflectivity was maximum above the melting level, and fingers of rain were just beginning to reach the surface. Electra sampling of the boundary layer under this anvil showed that

it was warm and moist, with $\theta_e \sim 360$ °K, and the P3 unexpectedly encountered a tiny but intense convective updraft, apparently sprouting along an old outflow boundary, while sampling this forward stratiform area. A reintensification of convective activity in the area was underway as the P3 conducted a late-flight survey before returning to Darwin.

### *3.2.2 Irma period*

After one day without any flight activity (17 January), the Bonaparte Gulf convection diminished rather suddenly, coincident with the weakening of the onshore flow as Connie drifted southwestward, and with the beginning of enhanced convection in the Gulf of Carpentaria depression (as indicated by comparison of Figs. 1.10 and 1.11). The latter depression intensified rapidly, and became cyclone Irma on 19 January. Analyses of 850 mb winds for EMEX 4 and 5 flight times can be found in Davidson et al. (1990, their Fig. 11a)

#### *3.2.2.1 EMEX 4: broad cyclone rainband at 250 km radius*

The fourth mission was flown on 18 January, in and near the intensifying depression in the Gulf of Carpentaria. The 21 GMT satellite photo (Figure 3.15) shows the large cold cloud area outlining the westward-moving depression and the small rainband in its WSW sector. Winds and heights on the 595 mb surface (not shown), as measured by the P3, clearly show the depression, while radar data indicates that spiral bands were present near the center, especially on the northeast side, within the widespread area of radar echo. A reflectivity-free area existed at the circulation center, in the lower troposphere, but the P3 did not fly through it. Conditions were particularly gusty and turbulent, with widespread rain and low cloud; poor visibility was reported by all aircraft.

After its depression flyby, the P3 joined the Electra and F27 in sampling a broad, chaotic band of convective rain features 200-300 km west-southwest of the center, spanning about a 45° sector of the cyclone (Fig 3.15). The overall band structure was oriented roughly SSW-NNE, across the lower-troposphere mean shear vector, which had a large magnitude (mean hodograph, Fig. 3.15). The inner side of the band had a crisper reflectivity outline. These observations are very similar to observations of two hurricane rainbands, at similar radii, described by Powell (1990a).

All over the P3 flight domain, wind measurements exhibited remarkably high variability, often correlated with vertical velocity, and therefore representing large vertical fluxes of horizontal momentum (and also horizontal fluxes of vertical momentum). Updrafts at P3 flight level had strong westerly momentum, qualitatively consistent with down-gradient transport. The broad zone of vigorous convection in this high-shear environment made for confusing, turbulent flow; this may account for the complexity of the reflectivity patterns. Height perturbations at P3 flight pressures near 550 mb were relatively large (10-20 m), and complex in their spatial pattern, but in general low heights prevailed on the inside (east) of the band.

The low-level humidity (and therefore $\theta_e$) measured by the F27 was extraordinarily high within the rainband, near saturation even at 935 and 870 mb. Barnes et al. (1983) presented a saturated sounding in a hurricane rainband, and Powell (1990a) also shows very high relative humidities in similar rainbands. These observations, and the breadth of the area undergoing vigorous convection, suggest that hurricane rainbands occur within areas of cyclone-forced *mesoscale* ascent, rather than merely having, like most of the other EMEX cases, cells or lines of buoyant convective ascent, in unsaturated air, with a positive mesoscale mean value.

The convective sample in this case was of young, powerful deep convective cells, often growing in echo-free surroundings, without a solid, well-developed stratiform area. The "stratiform" sample on this flight contained convective areas, and even the smoothest radar reflectivity fields show extensive streaks and channels, in association with wind variations.

A case study of this system is currently in preparation (Zipser, Barnes, and Ryan 1992).

#### *3.2.2.3 EMEX 5: outer cyclone rainband, a squall arc, and the back edge of a PBL cold pool*

On 19 January, the P3 was directed back to the Gulf depression, which was named Tropical Cyclone Irma during the flight. The 21 GMT satellite image, inner core radar structure, and midlevel P3 winds are shown in Fig 3.16. Flight level data at 695 mb from the P3 penetration show 25 m/s maximum winds, in cyclostrophic balance with the height depression, which had a total depth near 100 m. Temperature in the eye

reached 20 °C, fully 10 °C over environmental values. Radar showed a layer of precipitation above 7 km covering the eye, apparently sheared over from the southern part of the eyewall, which exhibited a visible outward slope.

After this P3 pass through Irma, the three EMEX aircraft gathered ~450 km north-northwest of the center to investigate the precipitation system in the zone of confluence between the curving southwesterly flow around the westward-moving cyclone and the straighter westerly flow through the Arafura Sea (P3 winds, Fig. 3.16). At this radius, the height field at P3 and Electra levels, while beyond the strongest influence of the depression, still had a geopotential height difference of 10-20 m across the band, comparable to EMEX 4. The layer of strongest west-southwesterly winds along the surface was 2-3 km thick (hodograph, Fig. 3.17), deeper than the EMEX 4 surface jet. This flow was stronger to the west of the precipitation area, such that the broad NW-SE precipitation zone lay in an area of mesoscale low-level convergence.

At first, the multi-banded, WNW-ESE oriented precipitation zone in the north of Fig. 3.17 (7.5-9 °S) was probed. Multiple updrafts were observed within it, each with relatively small maximum vertical velocities (< 5 m/s in P3 *in situ* data). As in EMEX 4, a large variance of horizontal winds was observed, in association with the vertical drafts in the cross-band shear. When the northern bands weakened, the small arc along 9.5 °S in Fig. 3.17 was selected for 3-aircraft sampling. This arc was ~100 km in length, oriented W-E, with a southward hook at its ragged eastern end (not very clear on Fig. 3.17). It propagated to the north and east, toward the great mass of stratiform precipitation. The three aircraft documented its well-developed cold pool and classic squall structure (Fig. 3.18) extensively, with multiple crossings at several levels up to 6 km. Updrafts carried the westerly along-line wind from low levels upward.

Stratiform sampling was conducted in the area of heavy stratiform precipitation to the north, which despite its relatively low echo top had very high reflectivity in and below the bright band and quite turbulent conditions above, at the unusually high P3 flight altitude of 7.1 km (425 mb).

The back edge of the boundary layer cold pool, to the west of the whole system, was sampled by the Electra at 987 mb (~200 m altitude) on its way back to Darwin. Data from this southbound flight segment along 135.8 °E, more than two hours after the time of Fig. 3.17, are shown in Fig. 3.19. From 0 to 70 km distance, temperature gradually

increases, while D value decreases as the "wake low" (Johnson and Nicholls, 1983) is approached; decreasing v indicates divergence as this cold pool spread out along the sea surface. At about 70 km, a stable layer is crossed to warmer, dryer air, with stronger westerly winds insulated by the stable layer from the frictional boundary layer, just 200m thick at that point. The conceptual model of warm unsaturated mesoscale downdrafts overlying cold convective-downdraft air, as described by Zipser (1977), was very much confirmed in EMEX. The background radiometric sky temperature undergoes a gradual decrease, a result of the instrument seeing gradually higher cloud base, punctuated by warm protrusions of virga, rain or scud.

### *3.2.3 Second Onset period*

Following the landfall and demise of Connie and Irma, deep convective activity, which had been concentrated in those two centers (Fig. 1.11), became rare during the *Inactive* period (Fig. 1.12). *Second Onset* began as a resurgence of diurnally modulated convective activity in a band across the entire continent (NW-SE diagonal of satellite picture, Fig. 3.20). This band distantly trailed a southern hemisphere midlatitude cold front. Just east of the band lay a several hundred km wide clear slot. In the concave Bonaparte gulf, large nocturnal cloud clusters were apparently initiated by daytime convection over adjacent land areas, and a gentle rotation in the middle and lower troposphere, which was to become cyclone Damien, began to take shape (centered at 11 °S, 131 °E in Fig. 1.13).

#### *3.2.3.1 EMEX 6: intense MCS along a midlevel cyclonic shearline*

On the night of 27 January, a major convective system, associated with the strengthening cyclonic circulation which was to develop into the cyclone Damien in the next incarnation of the Australian Low, developed in the Bonaparte Gulf (21 GMT satellite photo, Fig. 3.20). This event was within range of the 10 cm AMEX radar at Darwin, which showed its life cycle clearly. The F27 had been moved to Darwin, so all three aircraft participated in EMEX 6.

An east-west oriented collection of extraordinarily wide, strong echoes blossomed during the early part of the P3's survey pattern (not shown). By the time the P3 arrived on the scene 90 minutes later, precipitation filled the troposphere to a depth of 16 km over a large area, constituting the highest widespread radar echo tops in EMEX. Within the

precipitation area, winds were very turbulent, and lightning forced the decision to fly below the melting level to avoid damage to the radar equipment. Turbulent vertical motions were observed all over the broad, east-west precipitation area marking the extent of the initial east-west band (flight area, Fig. 3.20), with several peak updrafts at 600 mb (P3 flight level) exceeding 10 m/s. Numerous deep vertical drafts were seen in vertical incidence Doppler radar data, especially strong upper-tropospheric drafts both upward and downward. Over the course of the next three hours, the P3 flew in overlapping zigzag patterns east, west, east, west, and back to the east again, as the vertical air motions quieted and the precipitation became more stratiform in character. A westward-moving north-south line of convective echoes developed along and north of the western edge of this disturbed area (Fig. 3.21, along 129 °E).

The Electra made repeated north-south passes at 129.2°E at various levels in the lower troposphere, and recorded especially prominent downdraft activity. Strong convective-scale downdrafts were observed, some with recorded dewpoint temperatures below saturation, a rarity in the EMEX data (saturated conditions seem to be the norm, while instrument wetting sometimes makes the recorded dewpoint temperature values exceed the temperature in heavy precipitation conditions). In addition, a widespread, progressively increasing warming and drying trend, indicative of mesoscale subsidence, was recorded as the precipitation area aged. The F27 flew segments in the boundary layer, and found low-$\theta_e$ air under the main precipitation area. However, ahead of (west of) the developing north-south line in Fig. 3.21, some of the highest $\theta_e$ values of the EMEX flights were recorded, with significant areas of 360 °K and a maximum value of 362 °K at 990 mb.

Midlevel cyclonic circulation was apparent, in the form of a sharp NNW-SSE oritnted shearline along the northern edge of the east-west precipitation area (Fig. 3.21). Figure 3.22 illustrates this shear zone with Doppler radar radial velocity data at 5 km (P3 flight altitude), along with P3 flight-level winds, in the box indicated on Fig. 3.21. A height perturbation (low to the north) was associated with the shear line. Vertical structure along the line XY (of Figs. 3.21 and 3.22) is indicated in cross-section in Fig. 3.23; the shear was apparently confined to midlevels. The layer of easterly winds (stippled in Fig. 3.23) was deeper to the south, resulting in horizontal shear at midlevels. Notice in the P3 winds in Fig. 3.20 that cyclonic net circulation at this level prevailed over the region as a whole.

*3.2.3.2 EMEX 7: low-drag depression convection and a midlevel cyclonic vortex*

On 29 January, another large convective event occurred in association with the cyclonic circulation centered in the Bonaparte gulf. On this flight the P3 survey pattern included a pass through early stages of this near-depression convection. The lower fuselage radar picture from this westbound flight segment (Figure 3.24) shows a wide area of high reflectivity oriented roughly SW-NE. Time series of vertical velocity, temperature and zonal wind from this P3 flight leg are shown in Fig. 3.25a. The vertical velocity trace shows a zone of uninterrupted updraft (1-8 m/s) over a distance of nearly 40 km, with other updrafts alongside. This broad updraft feature is reminiscent of the wide updraft documented by Zipser and Gautier (1978) from aircraft data in an Atlantic depression during GATE. It may be that near the center of depressions, where winds and wind shear are relatively light (hodograph, Fig. 3.26), larger updraft structures — mesoscale sheets or columns of ascent rather than cellular turrets — can form, relatively free from entrainment of environmental air. The temperature, derived from radiometric measurements reliable in wet conditions, shows that this meso-updraft had a roughly 1 °C temperature excess over its environment; if saturation is assumed, the maximum temperature of 1.5 °C at 548 mb implies $\theta_e$ = 352 °K, suggesting nearly undilute ascent (Electra measurements in the boundary layer on this flight never exceeded that, but without the F27, the boundary layer sample was skimpy). The u plot shows that significant upward transport of zonal momentum was occurring.

Figure 3.25b shows vertical incidence radar and Doppler radial velocity data from this leg. This deep reflectivity feature was associated with strong updrafts in the upper troposphere, as indicated by the *radar scatterers* ascending at speeds exceeding 6 m/s

(shaded). Depending on particle fallspeed, the 6m/s downward motion at 12 km altitude, 55 km into the leg, may or may not indicate downward air motion. The maximum upward *particle* velocity in the upper-tropospheric updraft (15 m/s) substantially exceeds all the midlevel *air* vertical velocities in the flight-level data for the entire flight; furthermore, vertical incidence Doppler measurement on two other flight legs also indicated particle ascent exceeding 15 m/s in the upper troposphere (one of these was 2054-2104; the truncated stub of this leg is the southernmost portion of the flight track in Fig. 3.26). These observations taken together strongly suggest that updrafts in this environment continued to accelerate well beyond the 5 km level.

After the P3 survey pattern, the broad precipitation belt had spread northwestward, and another separate line was evident to the north, intersected by the P3 flight track at about 12.5 °S (Fig. 3.26). This line was sampled extensively by the P3 and Electra. It had relatively low reflectivity cell tops, ~13km, and a layer of anvil precipitation which trailed back toward the north above the melting layer; below this anvil, Electra measurements indicate subsidence-induced warming and drying. The line moved toward the south slowly, and rather than having a midlevel pressure minimum behind it, it traveled up the regional pressure gradient toward the incipient depression in the southern gulf.

The stratiform area sampled by the P3 featured a midlevel cyclonic vortex. Fig. 3.27 shows the D-value analysis and flight-level winds from flight legs beginning with the southbound second leg in Fig. 3.28. Doppler winds from the three pairs of flight legs in Figs. 3.27 and 3.28, spanning a 1-hour period, are also shown. The persistent cyclonic winds and the low center were associated with a ring of enhanced reflectivity surrounding a reflectivity-free "eye" (Fig. 3.28), even at the surface. The cross-section in Fig. 3.28 indicates that this vortex was strongest near the melting layer, and extended farther above that than below.

### *3.2.4 Long Zonal Fetch period*

Although the Australian Low (with Damien formed within it) was the center of 700 mb circulation during the *long zonal fetch* period (Fig. 1.14), the monsoon shear zone extended far to the east, with a second circulation center — soon to be cyclone Jason — in the Pacific Ocean, just off the edge of the figure. Monsoonal westerlies at 10°S, exceeding 10 m/s at 700 mb, spanned almost the entire width of the Australian

continent. Squall arcs, pushed along by this strong midlevel westerly flow, propagated rapidly eastward, leaving long trailing E-W lines of convection over the Arafura Sea along the edges of their cold pools (EMEX 8, 9). Also during *long zonal fetch*, a col developed in the trough (Fig. 1.14a, at 17 °S, 137 °E), as Damien drifted westward in the eastern Indian ocean, while the Jason circulation intensified over the Pacific. Hence, the southerly wind component at midlevels increased in the Gulf of Carpentaria, converging, as rear inflow, into the E-W oriented Arafura Sea convective bands, which propagated northward across the sea each night. Satellite images suggest that these lines formed from various combinations of squall arcs surging in from the west over the sea, convection forming each evening along the east-west oriented Top End coast, and convective bands in the Gulf of Carpentaria, related to the developing Jason circulation. The prodigious EMEX 10 line, for example (satellite, Fig. 3.38) formed as a merger of all these elements.

#### *3.2.4.1 EMEX 8: along-wind line with cross-wind squall propagator*

On 1 February, EMEX mission 8 was conducted in the Arafura Sea by all three EMEX aircraft. The 21Z satellite picture and P3 survey pattern radar composite (Fig. 3.29) indicate two east-west elongated cloud clusters, separated by a gap. The northern feature had been in existence and slowly moving north since the previous afternoon; the strong diurnal rhythm of evening line formation, observed on subsequent days, had not quite set up yet. The southern cloud cluster, which was selected for 3-aircraft sampling, had moved in from the west in the northern cluster's wake.

During its survey pattern, the P3 encountered very strong midlevel westerly flow (>20 m/s). In the gap between the cloud clusters, a pocket of unusually warm, dry air with elevated D-values indicated that significant deep subsidence had occurred. A second wind maximum at low levels (850-900 mb) was indicated in some dropwinsonde and aircraft data, although this does not appear in the mean Doppler hodograph (Fig. 3.32). All three aircraft found substantial cyclonic shear across the precipitation zone (strongest westerlies confined to the pre-line area), especially the F27, both at 952 mb (Fig. 3.31a) and at 870 mb; both P3 and Electra data show mesoscale depressed heights south of the line.

The main convective line (southern one-third of Fig. 3.29) was oriented WNW-ESE, with stratiform precipitation to the south. In the dry channel between the cloud

clusters, convective features moved by at speeds exceeding 15 m/s from west to east, so rapidly that they appear to be elongated east-west in the smeared time composite view of Fig. 3.29. The cold pool left behind by these convective entities was apparently responsible for a discrete northward propagation of the larger E-W line, with the remains of the convective line along 10 °S in Fig. 3.29 constituting the stratiform area reflectivity maximum seen in Figure 3.32.

Data from the F27 and Electra illustrate this discrete propagation mechanism. Flight tracks of all three aircraft are indicated on the P3 tail radar reflectivity (at 3 km altitude) image of Fig. 3.30; in the figure, all data, including the radar data, have been translated to their approximate location at 2130 GMT. Time series of data from the F27 and Electra are shown in Fig. 3.31. The F27, flying at 952 mb, encountered large liquid water mixing ratios and the coldest air under the high reflectivity line at y=60. Also at that point, zonal winds increased dramatically, to the values prevailing ahead of the system. The leading edge of the cold pool, however, is at y~75, where the temperature jump and convergent wind shift are marked by a small peak in liquid water. The Electra, flying at 695 mb, also encountered two distinct convective zones with a clearing between them (Fig. 3.31b). Reflectivity in the area of the northern convective zone was very weak, as a consequence both of the microphysical immaturity of the new convection, and of attenuation of the P3's X-band tail radar. In a lower fuselage radar view (not shown) from the P3's position at 2118 GMT (the earliest part of the P3 flight track indicated on Fig. 3.30), a faint but distinct NNW-ESE band of radar echo is evident in that area, oriented along the gust front symbol in Fig. 3.30.

A later view of this system (Fig. 3.32) shows a classic leading line with trailing stratiform region, and a precipitation-free strip between them. As indicated above, however, the propagation of this structure was discrete; there is no frame of reference in which the line was approximately steady. In fact, some of the *trailing* stratiform precipitation in Fig. 3.32 was actually *overhanging leading anvil* precipitation from the old convective line; like the overhanging anvil precipitation in EMEX 3, it had tiny convective cells sprouting within it.

A case study of this storm is in preparation (Zipser, personal communication).

*3.2.4.2 EMEX 9: 4-aircraft sampling of along-wind and squall arc lines*

The next night, 2 February, another east-west precipitation band formed near the north Australian coast and propagated across the Arafura Sea. Once again, the band was studied by all 3 EMEX aircraft; also, the STEP project's NASA ER-2 flew a coordinated mission overhead in the lower stratosphere. This band was longer and farther east than the EMEX 8 line, as some Gulf of Carpentaria convection had merged with a coastal line (satellite, Fig. 3.33). The wind environment had an increased southerly component at all levels (cf. hodographs, Figs. 3.32 and 3.35); near-southerly winds at midlevels were blowing out of the Gulf (P3 winds, Fig. 3.33).

The zonal wind had a maximum at low levels (2-3 km altitude), especially to the north of the line (hodograph, Fig. 3.35). This was manifest in the midlevel vertical flux of zonal (along-line) momentum, as P3-measured updrafts had larger values of u than their midlevel environment. As in EMEX 8, the precipitation zone had significant cyclonic shear across it, with the strongest westerlies at all levels ahead of the line.

The broad, E-W oriented line of precipitation seen in Fig. 3.33 was drifting to the north and was composed of nearly upright convective cells with stratiform rain on both sides. The stratiform area to the south, behind the convection, exhibited much higher reflectivity *at and below* the bright band, while the reflectivity top height and reflectivity *above* the bright band were greater to the north of the convection, where northerly shear above 5 km (hodograph, Fig. 3.35) was advecting detrained snow, as in Houze and Rappaport (1984).

In a scenario not unlike that of EMEX 8, a squall arc, which can be seen in the western part of Fig. 3.33, passed eastward down the band. Both ahead of and behind this surge, parallel reflectivity bands (for example, along 9.1 and 9.5 °S at 137.5 °E in Fig. 3.33) were observed. At the leading edge of the arc (near 138 °E, 9.5 °S in Fig. 3.33), the reflectivity field has a smooth, diffuse arcus-like appearance, suggestive of smooth, wavelike lifting.

An interesting dynamic interaction can be seen in Electra data, taken during a northward pass along 138.1 °E through this rapidly changing area of intersection between the E-W band and the squall arc (Fig. 3.34). An downdraft-updraft couplet, each associated with a peak in liquid water, can be seen near 9.7 °S; a large (cf. Fig. 3.12) D-value signal was observed there, with the low centered precisely between the updraft and downdraft. Hence, the pressure field was acting to accelerate the updraft rearward

(southward) and the downdraft forward (northward). This suggests that air entering the cold pool with enhanced northward momentum (as in Fig. 3.39 below) may be a product of dynamic interactions as well as of the ambient rear inflow (Smull and Houze 1987). This observation was taken in a highly 3-dimensional, transient situation, however; we have not seen this process occurring in data from passes through the more 2-dimensional parts of these convective lines. A second, much smaller updraft was observed at 9.5 °S.

Behind the squall arc, P3- and Electra-measured winds levels in this geographical area veered to southwesterly, then gradually weakened as it receded to the east. The old precipitation band along 9.5 - 10 °S evolved into the trailing stratiform precipitation behind the new E-W convective line at 8.8 °S; at a later time (not shown) the system took on an appearance like Fig. 3.32, with few clues left of its extremely non-steady propagation history.

An excellent example of the mesoscale structure of low-level conditions in the wake of this line can be seen in Fig. 3.36. The F27 flew north out of Gove at 950 mb, through the wake of the squall arc, finally crossing the leading convective line near the time of Fig. 3.35. Zonal wind speed (not shown) was nearly constant at 10-15 m/s, while the meridional wind speed shows a nearly constant divergence of about 20 m/s over ~400 km, then a sudden convergence at the leading edge of a saturated cold pool, just ahead of the zone of high liquid water values, at 8.9 °S. The time series of $\theta_e$ closely parallels dewpoint, with a minimum of 340 °K near 10.7 °S in the divergent unsatureted mesoscale downdraft zone, and inflow values of 355 °K ahead of the line. A weaker liquid water signal at the old line position (9.8 °S) was associated with cool saturated conditions, as the aircraft probably skimmed the top of the cold layer there. Data from the F27's subsequent pass southward through the squall at 990 mb have been presented in Webster and Houze (1991).

The ER-2 arrived after 00Z and flew at 70-90 mb, gathering valuable radiation measurements. A detailed case study of this the EMEX 9 MCS, including dual-Doppler radar analysis, is in preparation (F. Marks, personal communication). A modeling study , focusing especially on the radiative properties of the stratiform area, is also being conducted (T.-M. Wong, personal communication)

*3.2.4.3 EMEX 10: glimpse of the Jason circulation and a very long, tiered convective band*

The target feature of EMEX 10 was yet another nocturnal E-W line of convection in the Arafura Sea, this time an arched line fully 1000 km in length (satellite, Fig. 3.38) which formed, like the EMEX 9 MCS, from the merging of Gulf of Carpentaria and evening coastal convective bands. Initially, however, the P3's survey pattern took it out over the ship in the northern Gulf of Carpentaria. Cyclonic shear and flow curvature were observed (Fig. 3.37), a fertile environment for the rapid development of tropical cyclone Jason after it crossed into the Gulf (Davidson et al. 1990).

After the excursion over the ship, the P3, together with the F27, began sampling the convective line. Radar (Fig. 3.38) shows that the main, broad line was composed of tiers of east-west sub-lines forming the curved arc shape seen in the satellite view (Fig. 3.38), with other precipitation features to the north. As in EMEX 9, southerly shear above the melting level led to higher reflectivity *aloft* to the north of the convection, while heavier stratiform precipitation *at the surface* lay to the south. Convective vertical motions at P3 flight level were quite strong, as was the upward flux of zonal (along-line) momentum; updrafts had values of westerly momentum lower than the midlevel environmental values, but always positive; as discussed in chapter 5, this led to the vorticity structure seen in Fig. 5.6c.

Once again, the precipitation band lay in a cyclonic shear zone; westerly winds exceeding 20 m/s were detected north of the line by the P3, while within and south of the line, winds were weaker. The cellular convective features north of 9 °S in Fig. 3.38 moved by rapidly from west to east north of the main line. A hole in the reflectivity field (at 8.9 °S, 136.4 °E). This hole was apparently created by intense subsidence and evaporation ahead of the advancing convection (see point 4 in section 3.2.5 below).

A possible mechanism for the continuous northward propagation of these bands (in addition to the discrete squall propagation illustrated in EMEX 8 and 9), is that midlevel rear inflow from the south is carried downward in saturated convective downdrafts, and arrives at the surface with southerly momentum (dynamic enhancement of this southerly momentum also occurs, as discussed above (Fig. 3.34)). On north-south passes through the EMEX 10 convective zone boundary layer, the F27 observed a broad cold pool, typically with a sharper northern edge, where new convective development was occurring. Data from one such pass (Fig. 3.39) shows that positive (southerly) meridional wind values in the cold pool are almost perfectly correlated with low temperature.

### *3.2.5 Summary of peculiartites in the EMEX MCSs*

The unusual observations of MCS behaviour from EMEX may be summarized as follows:

1. Elevated convection, apparently based above the boundary layer and apparently triggered by the convergence ahead of an elevated mesoscale airmass with inertia, was observed in EMEX 1. This convection occurred within a stratiform rain area, and precipitated (radar echo, Fig. 3.9), but was not very deep.

2. Tiny but intense convective cells [just one sweep on the tail radar (~1 km)!] within overhanging leading anvil rain areas were observed in EMEX 3 and 8. These may be due to the evaporation of light rain from aloft bringing the lower troposphere toward saturation, at constant $\theta_e$. Both the temperature and dewpoint curves would move toward the wet-bulb temperature profile in such a process. Reference to a thermodynamic chart shows that this process reduces convective inhibition ("negative area"), and thereby permits the growth of deep convective cells without the usual need for large or organized initiation mechanisms like a gust front.

3. Erosion of stratiform radar echo by the strong midlevel flow was apparent in the EMEX 3 MCS. The EMEX 3 stratiform areas also had unusual divergence profiles, with the midlevel convecrgence higher than usual. Is this because of the unusually strong evaporative cooling above the melting level in that case? This is not unlike the descending rear inflow jet problem in squall lines.

4. An unusual divergence profile in EMEX 10, with very strong divergence all the way from the surface to 6.5 km, may indicate that we lassooed a buoyancy bore, perhaps focused by the encircling convection. This profile is shown in Fig. 3.40. Strong troposphere-deep subsidence is implied. The stratiform rain area within which this profile was obtained was just east of an onrushing (west-to-east moving) group of developing convective cells, and did develop an unusual reflectivity "hole" shortly thereafter (8.9S, 136.5E in Fig. 3.38). F27 measurements in that area also indicated the presence of subsidence warming and drying at low levels, but that is not an uncommon observation at F27 flight levels. The evidence remains tantalizing but inconclusive.

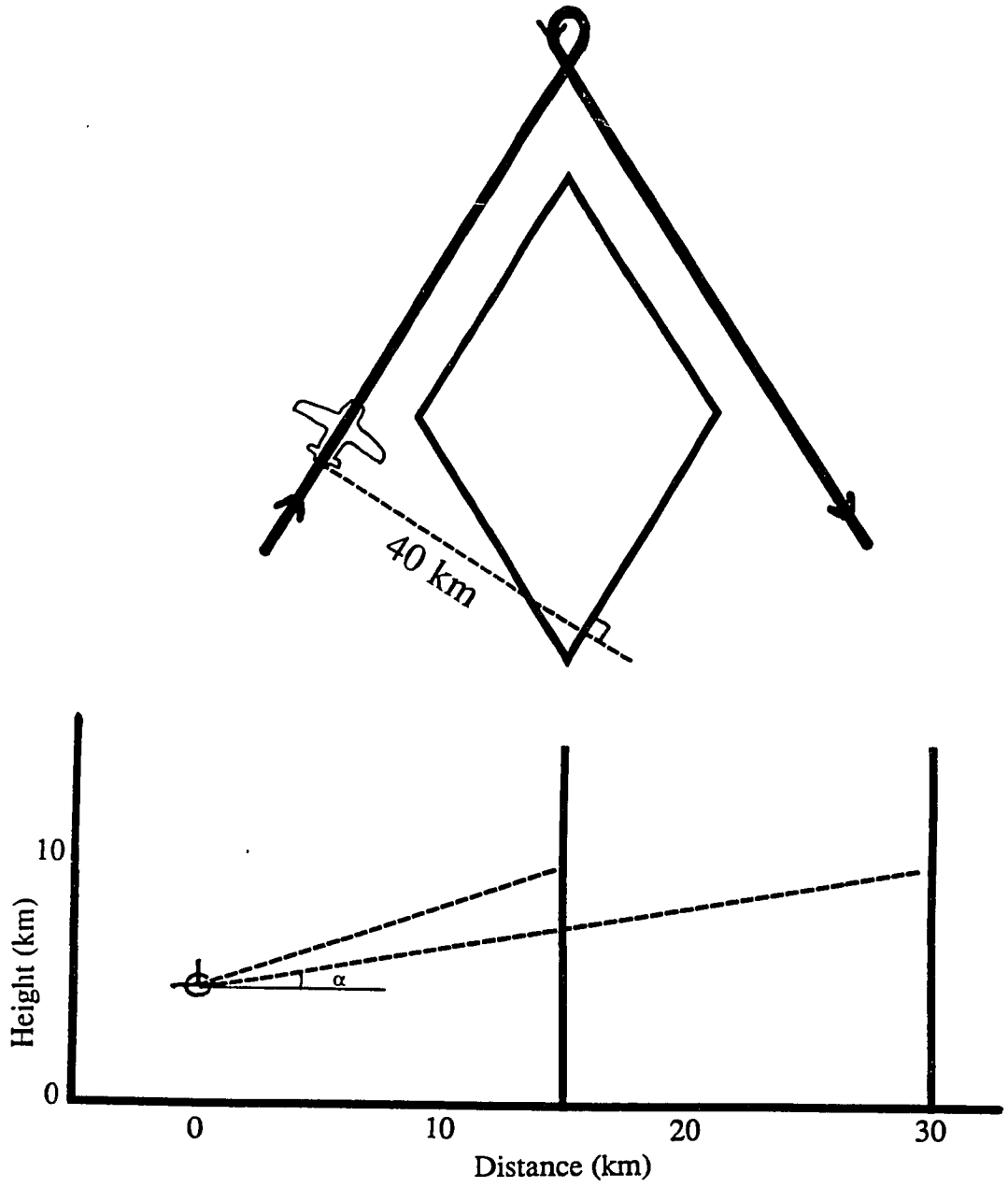


Fig. 3.1 : Geometry of the airborne Doppler divergence measurement, in plan view (above) and vertical cross-section (below).

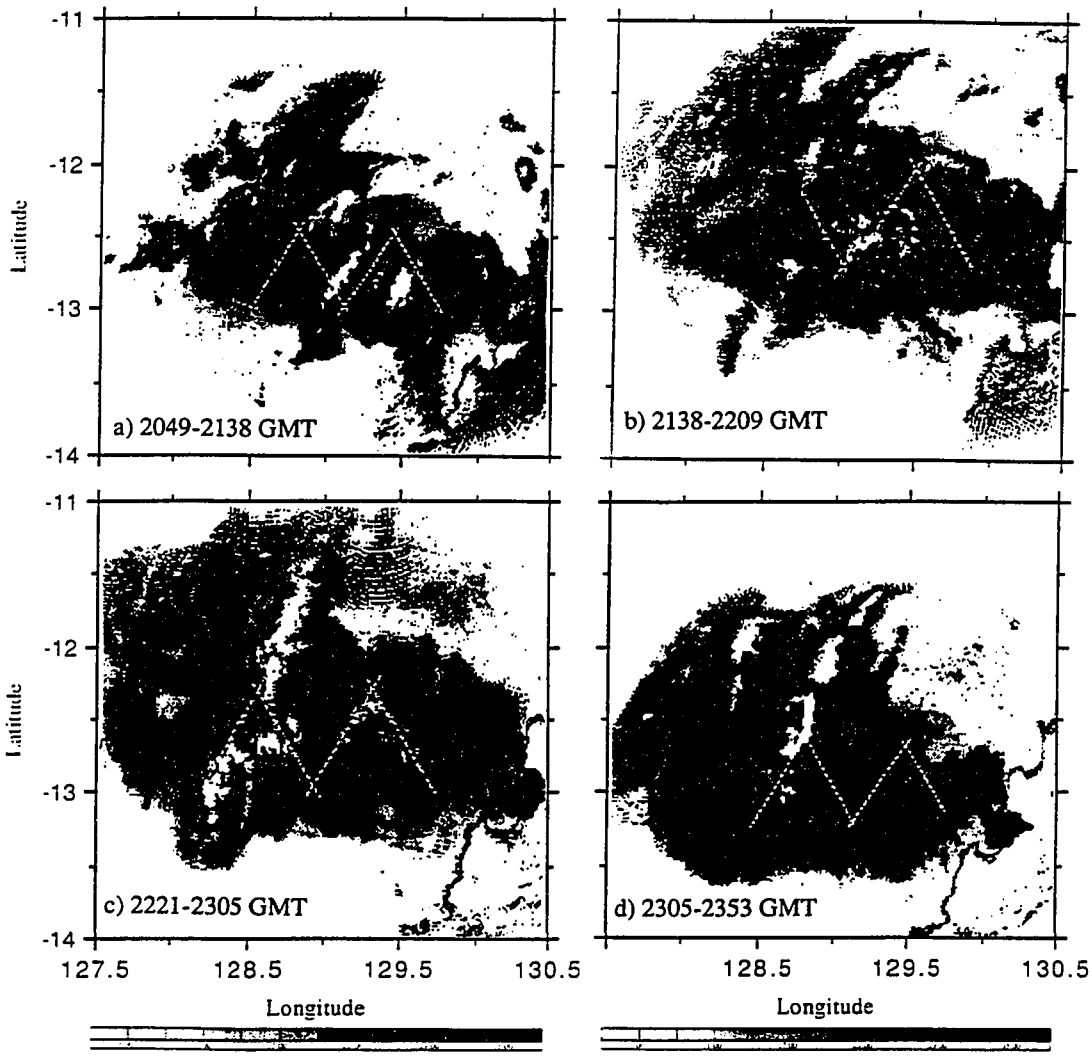


Fig. 3.2 : EMEX 6 radar reflectivity time composite images from the indicated time intervals during EMEX flight 6 on 27 January 1987. The reflectivity shown at each point is the maximum observed during the interval. Flight tracks during the intervals are shown in white, and proceed left to right in (a), right to left in (b), *etc.* Ground clutter at lower right.

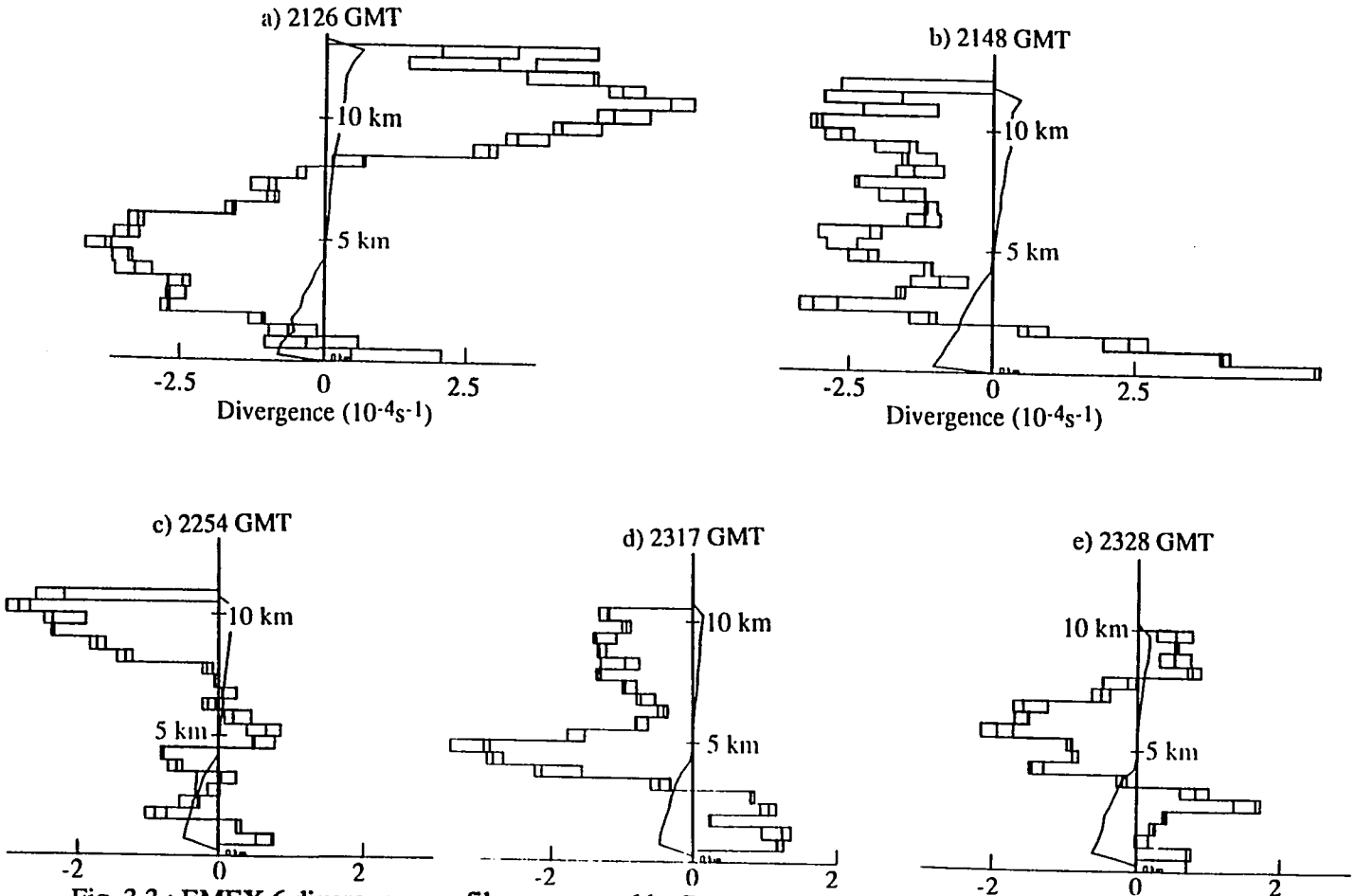


Fig. 3.3 : EMEX 6 divergence profiles, measured by Doppler radar. The 3 blocked lines are 3 independent Doppler estimates. The single solid line is the expected apparent divergence, calculated from reflectivity-estimated particle fallspeeds [see Eq. (3.3)], which has been subtracted from the measurements to yield actual divergence. a) - d) are for parallelograms as in Fig. 3.1 within the rightmost inverted-"V"-shaped flight tracks on a) - d) of Fig. 3.2, while e) comes from the upright-"V"-shaped flight track in Fig. 3.2d.

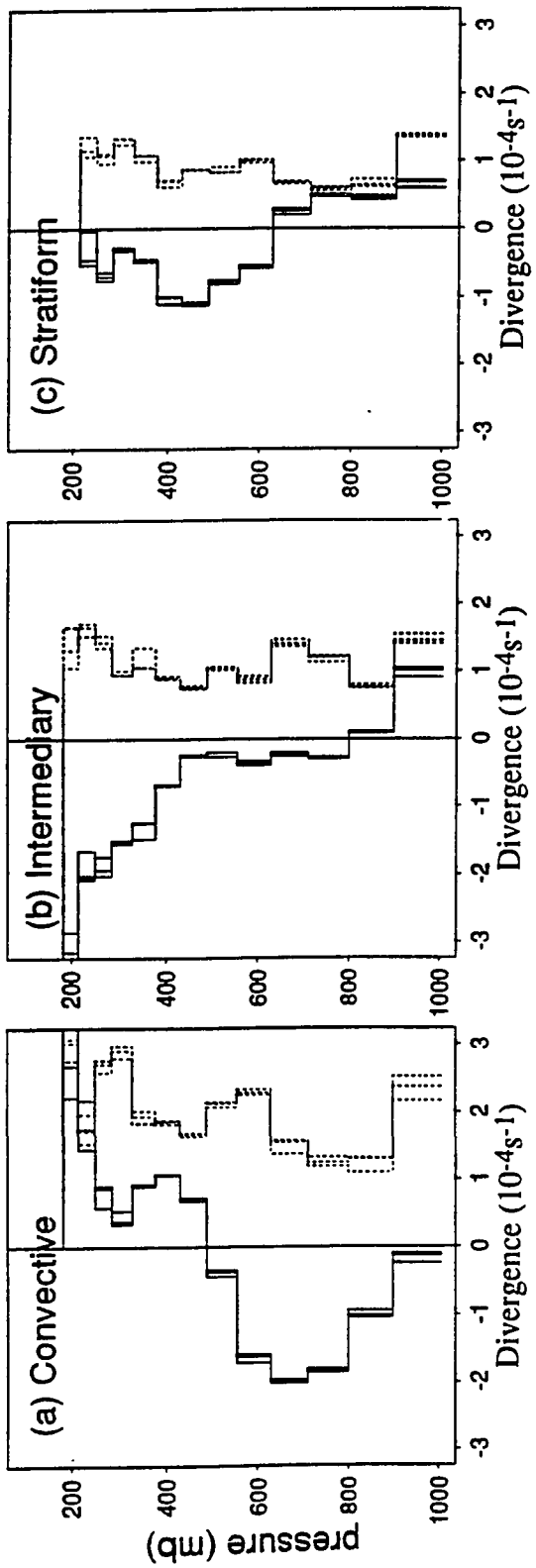


Fig. 3.4 : EMEX mean divergence profiles. Mean (solid) and standard deviation (dotted) of divergence for all of the EMEX Doppler-measured profiles, subdivided (see text) into 26 convective, 31 intermediary, and 37 stratiform precipitation areas. Profiles have been plotted against pressure so area is proportional to mass divergence.

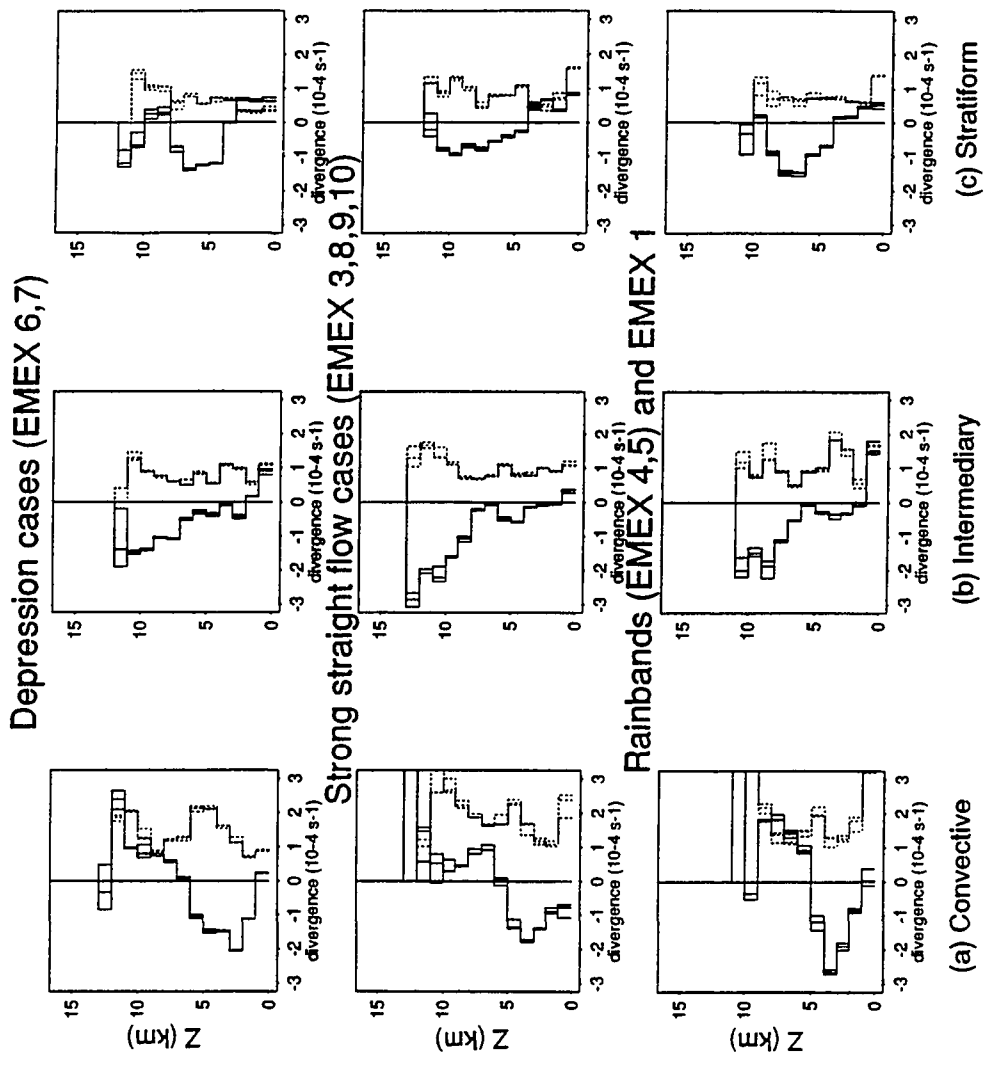


Fig. 3.5 : Mean divergence profiles by MCS type. As in Fig. 3.4, except further subdivided according to the synoptic environment within which the MCS's were observed, and plotted against height.

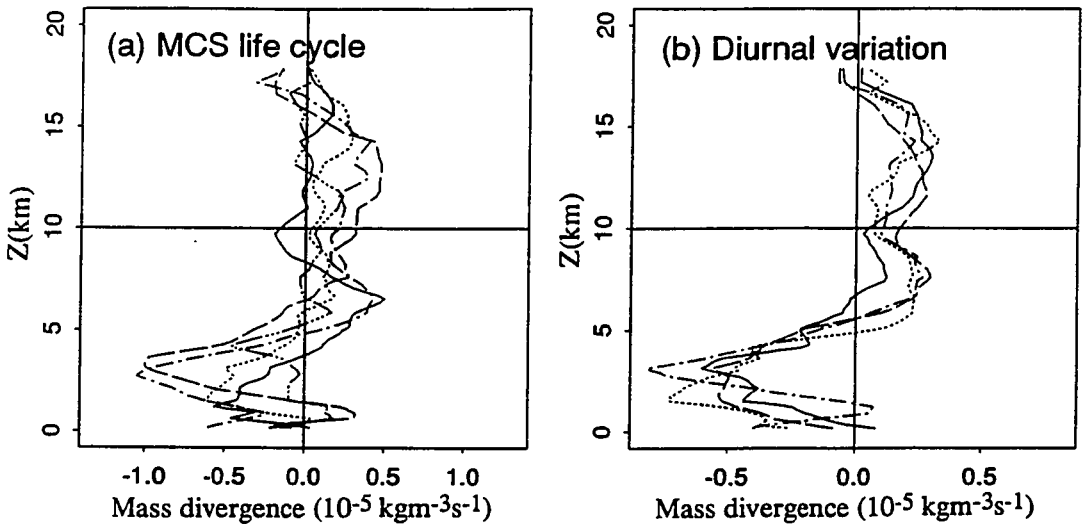


Fig. 3.6 : Rawinsonde-derived mass divergences in the Gulf of Carpentaria. a) The 5 stages of the MCS life cycle, for the composite of 4 MCS's, after Frank and McBride (1989). "Initial" stage solid, "growth" stage dotted, "maximum intensity" stage dash-dotted, "early decay" dashed, "late decay" stage dash-triple-dotted. b) The four sounding times per day averaged over the non-cyclone active days 15-17 Jan. and 30 Jan. to 4 Feb. 1987. 5 GMT (afternoon) solid, 11 GMT (nightfall) dotted, 17 GMT (after midnight) dashed, 23 GMT (dawn) dash-dotted.

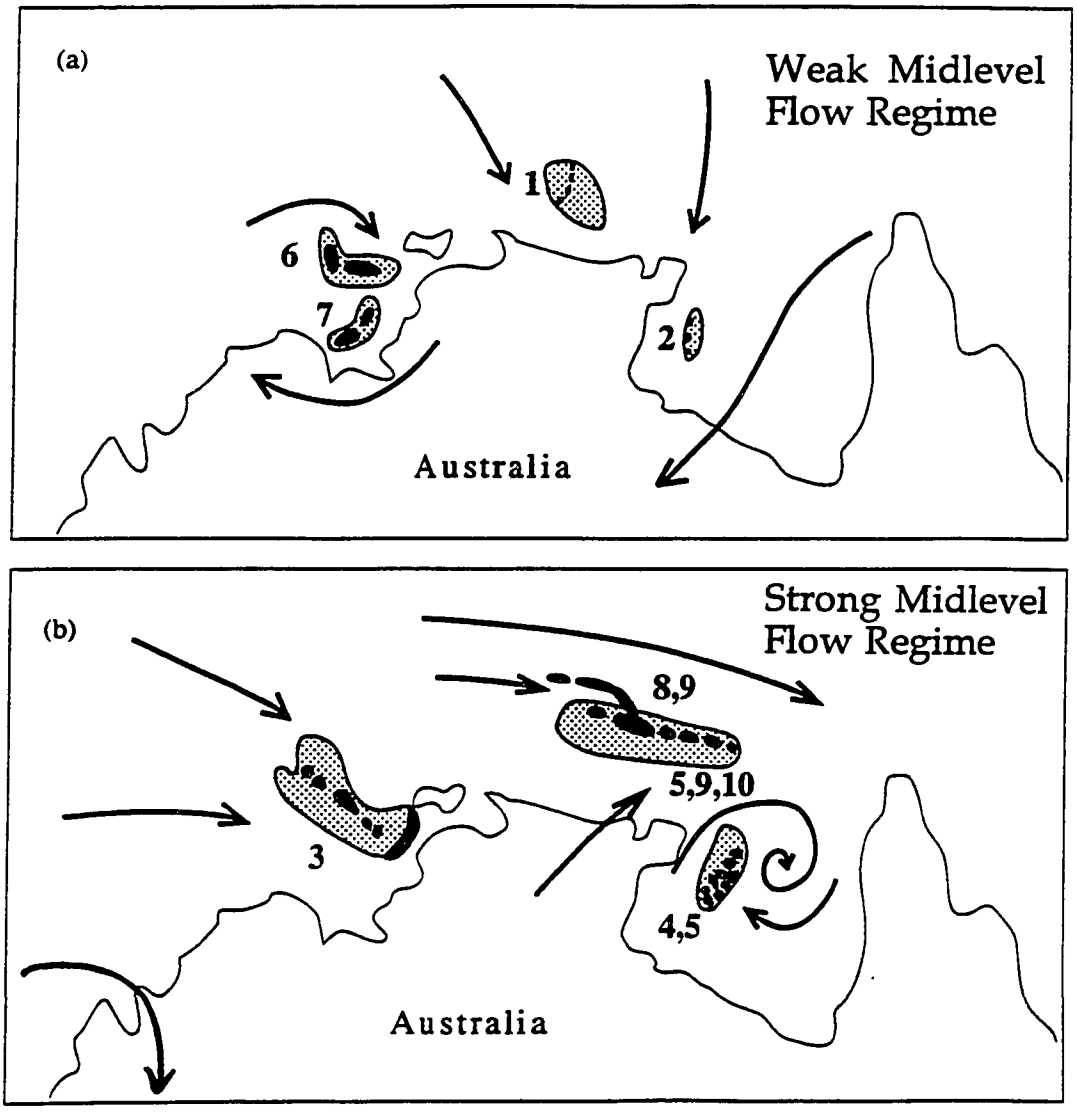


Fig. 3.7 : Schematic guide to the EMEX MCS's relative to midlevel flow streamlines. Light outlines roughly represent radar echo boundaries; convective areas are black, while stratiform precipitation areas are stippled. In panel (a), a weak wind regime is depicted, while panel (b) corresponds to a strong wind regime.

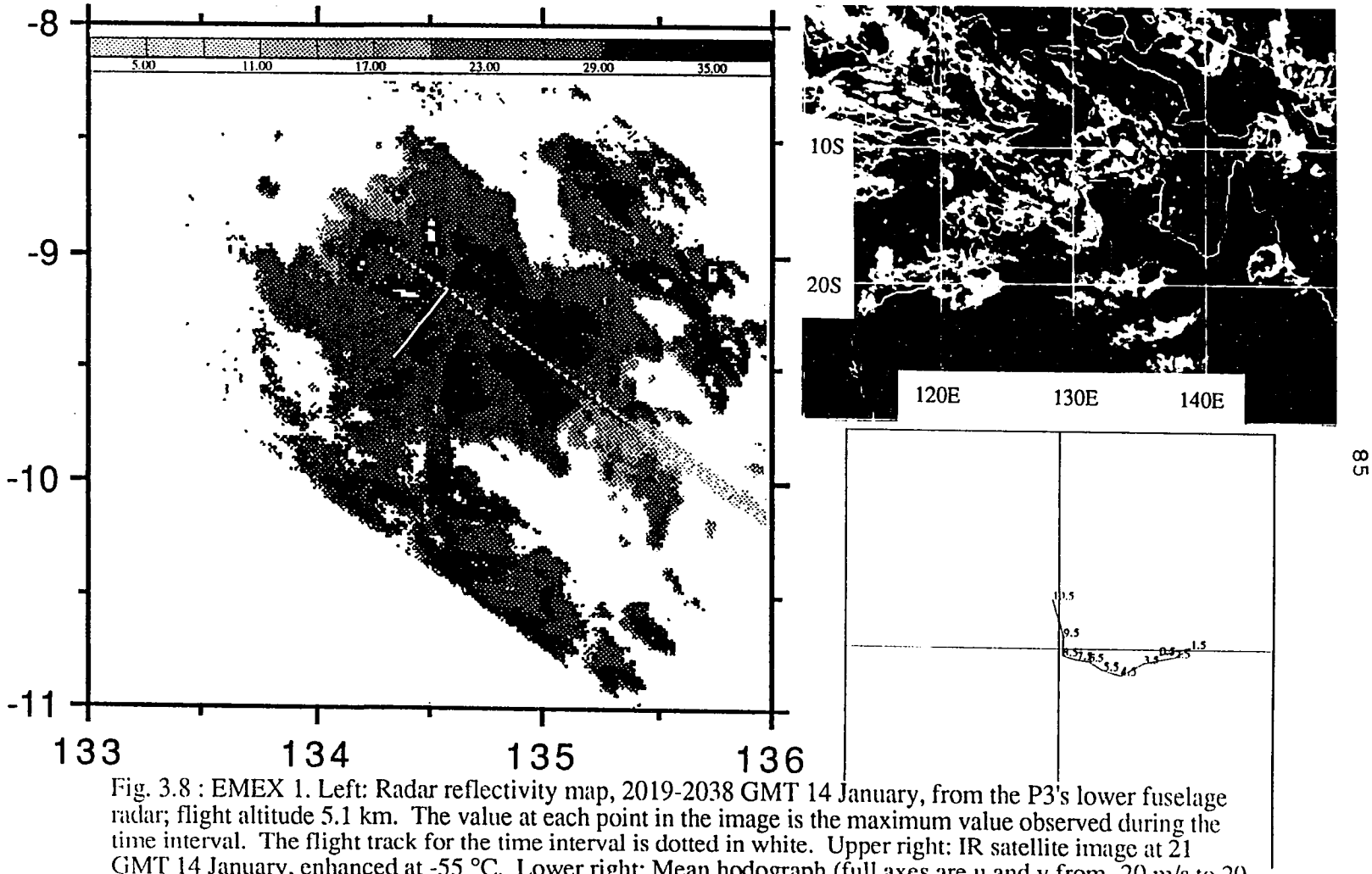


Fig. 3.8 : EMEX 1. Left: Radar reflectivity map, 2019-2038 GMT 14 January, from the P3's lower fuselage radar; flight altitude 5.1 km. The value at each point in the image is the maximum value observed during the time interval. The flight track for the time interval is dotted in white. Upper right: IR satellite image at 21 GMT 14 January, enhanced at -55 °C. Lower right: Mean hodograph (full axes are u and v from -20 m/s to 20 m/s, heights in km plotted) for the MCS as a whole, from numerous averaged Doppler wind profiles.

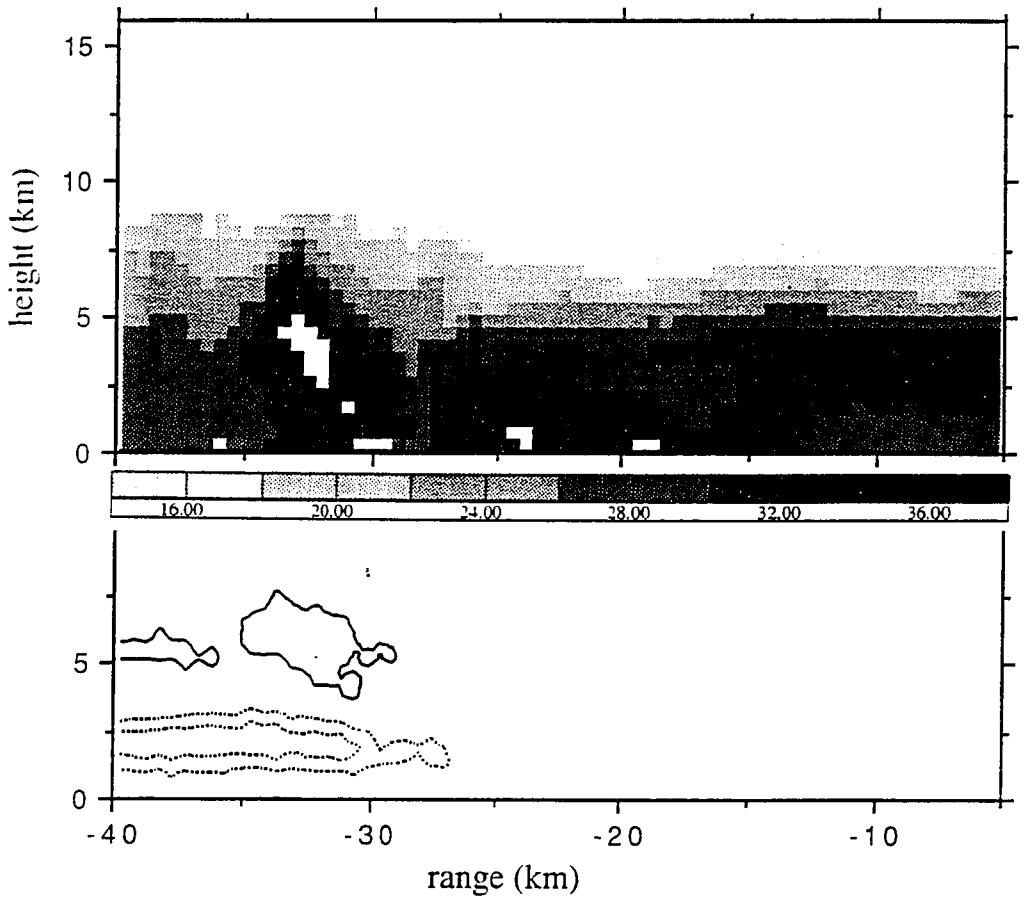


Fig. 3.9 : EMEX 1 elevated convection. Cross-section of reflectivity (top, dbZ) and Doppler radial velocity (bottom, contours at 3 and 6 m/s), along the line indicated in white on radar image of Fig. 3.8.

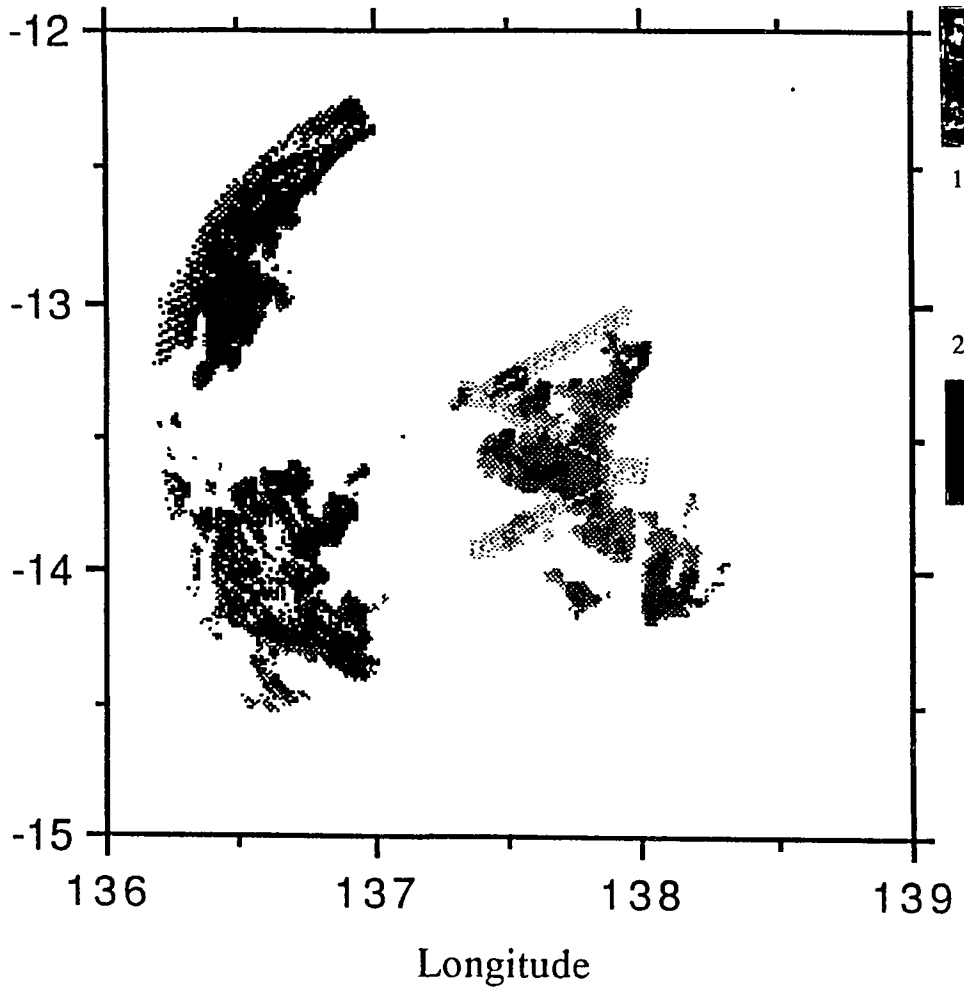


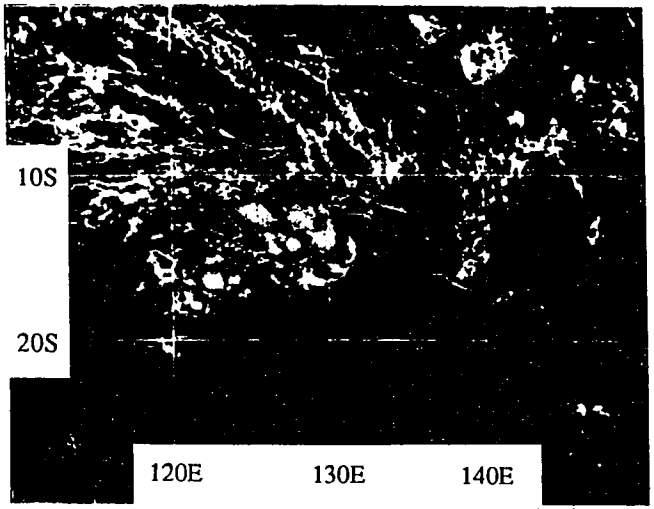


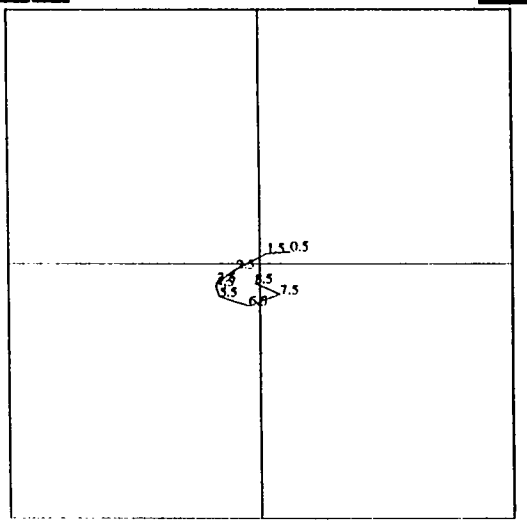


Fig. 3.10 : EMEX 2. As in Fig. 3.8, except 2050-2122 15 January, altitude 5.2 km (western echoes are ground clutter); satellite picture 23 GMT 15 January.

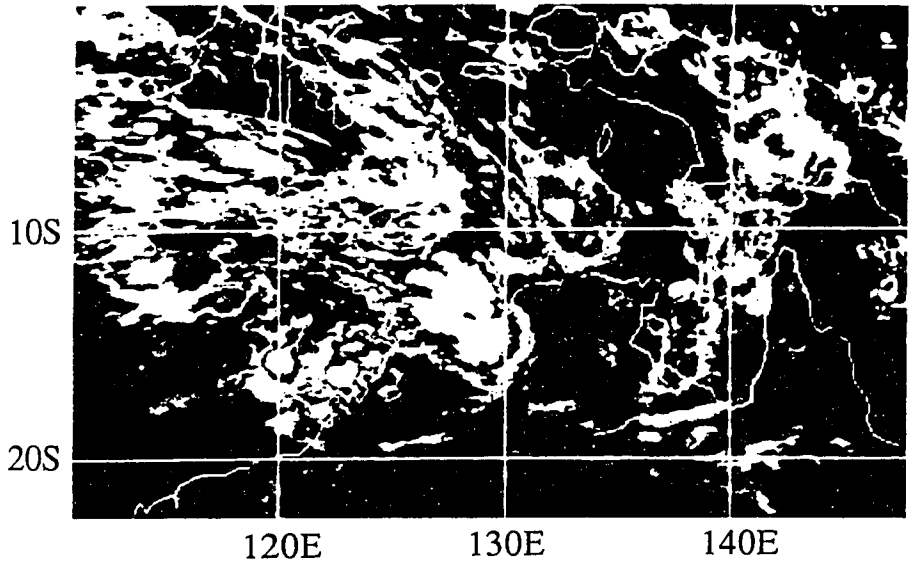


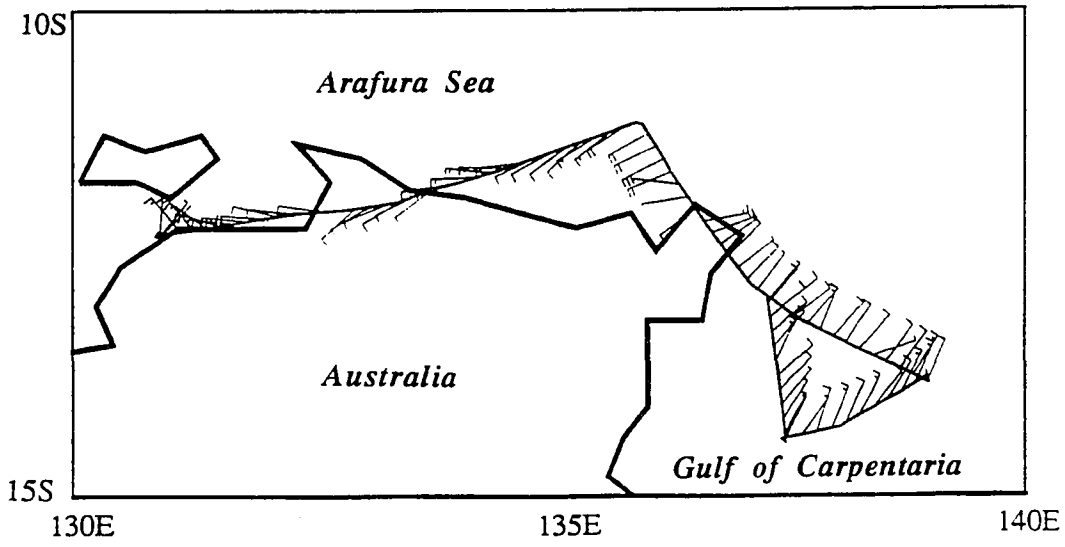


Fig. 3.11 : Winds at 550 mb as measured by the P3, 18-20 GMT 15 January 1987, and 20 GMT satellite picture showing flight track.

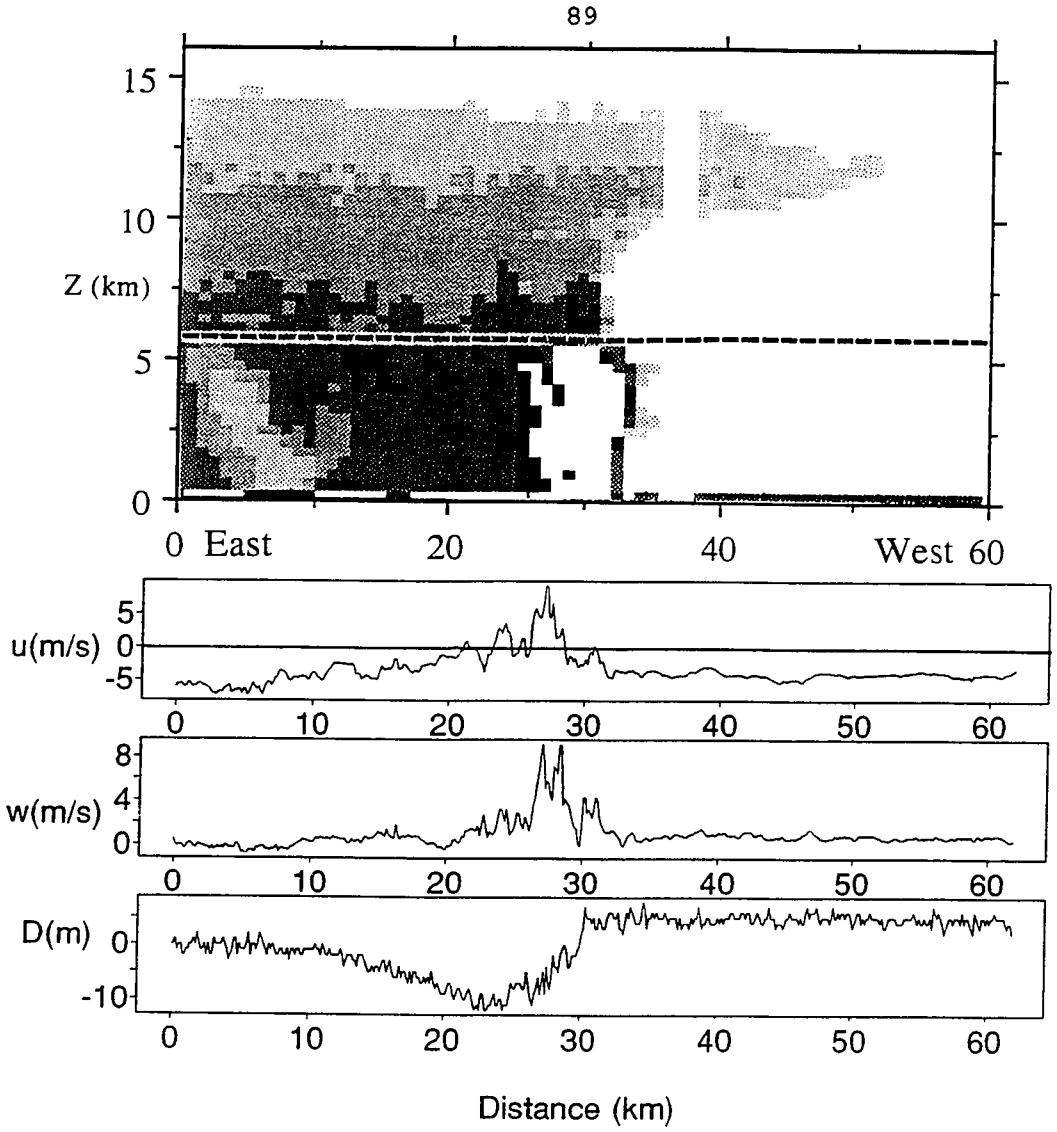


Fig. 3.12 : EMEX 2 cross section. Radar reflectivity (gray scales are 9 dbZ intervals starting at 5 dbZ; contained white area exceeds 41 dbZ; horizontal white line is flight track), and P3 1-second measurements of cross-line wind, vertical velocity, and relative D-value (a measure of geopotential height) from the westbound P3 flight leg 0047-0054 GMT 16 January.

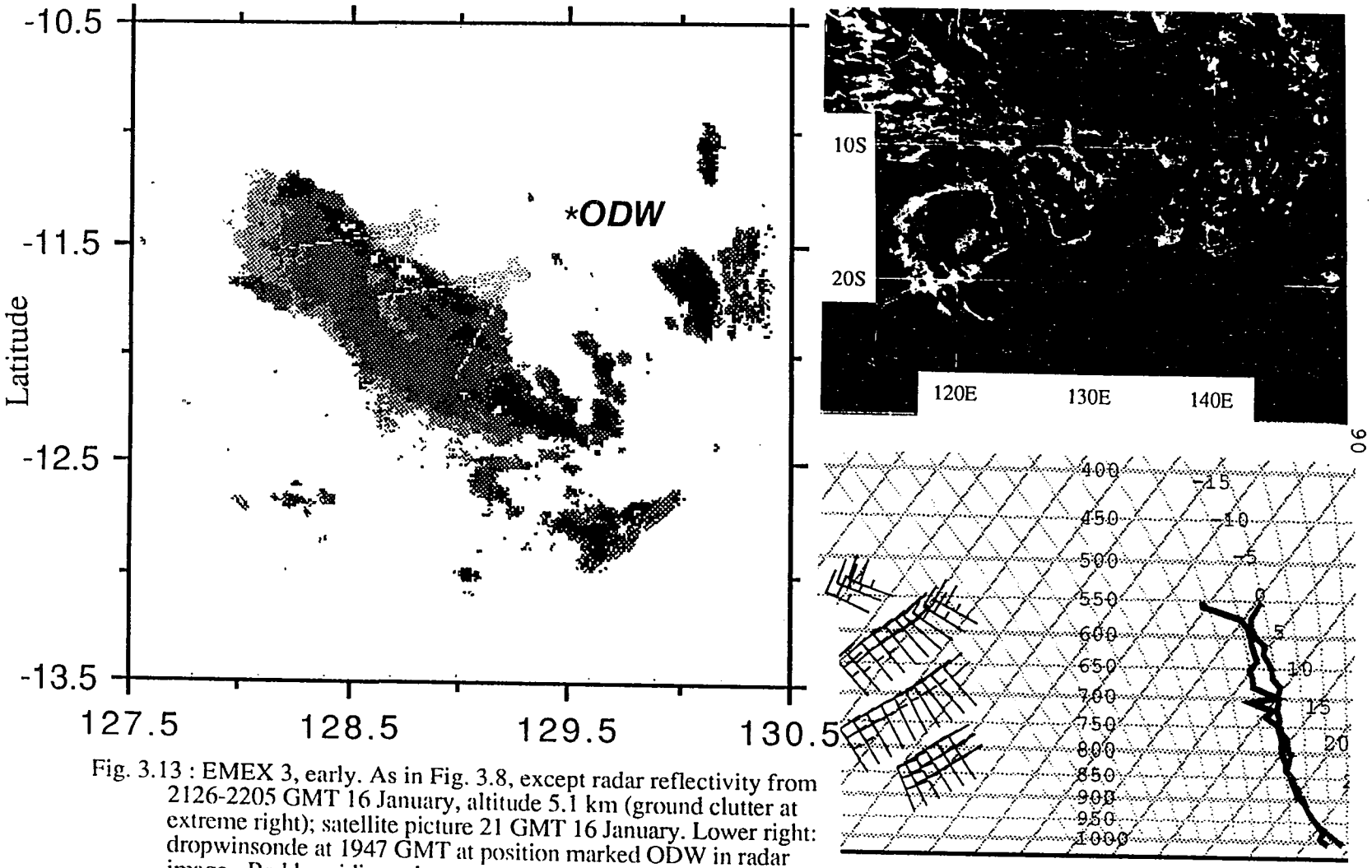


Fig. 3.13 : EMEX 3, early. As in Fig. 3.8, except radar reflectivity from 2126-2205 GMT 16 January, altitude 5.1 km (ground clutter at extreme right); satellite picture 21 GMT 16 January. Lower right: dropwinsonde at 1947 GMT at position marked ODW in radar image. Bad humidity values.

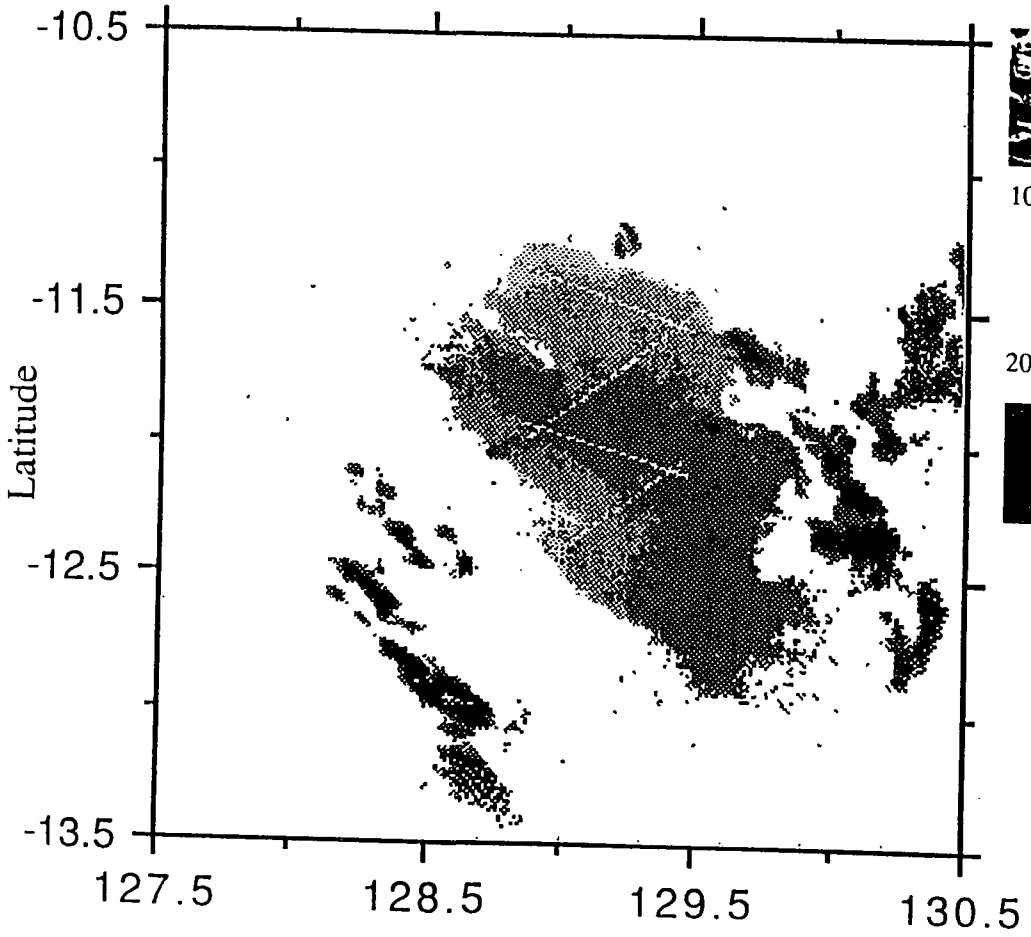


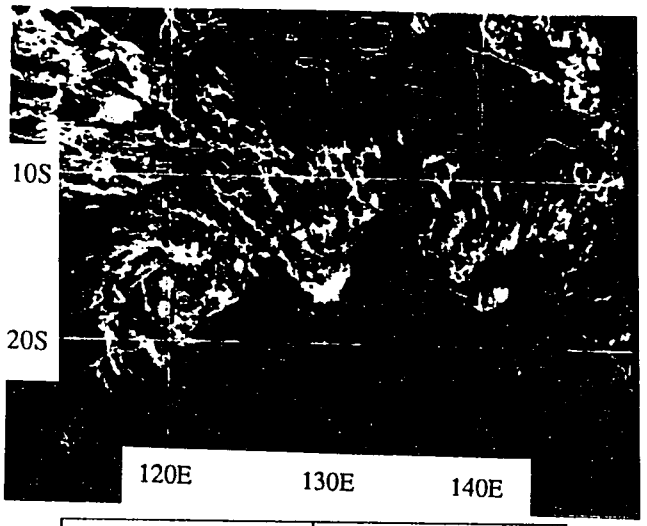


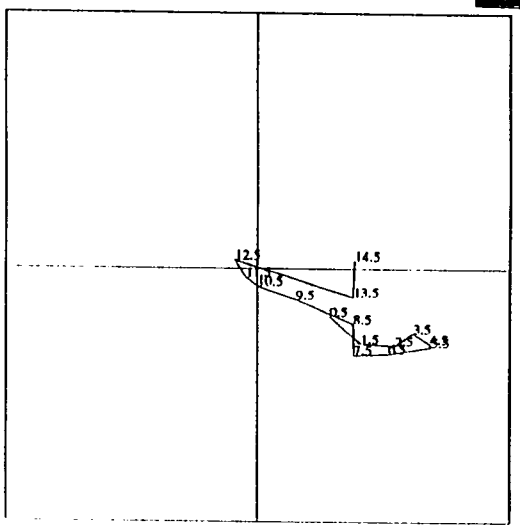

Fig. 3.14 : EMEX 3, late. As in Fig. 3.8, but reflectivity from 2253-2346 GMT 16 January, altitude 5.1 km; satellite picture 00 GMT 17 January.

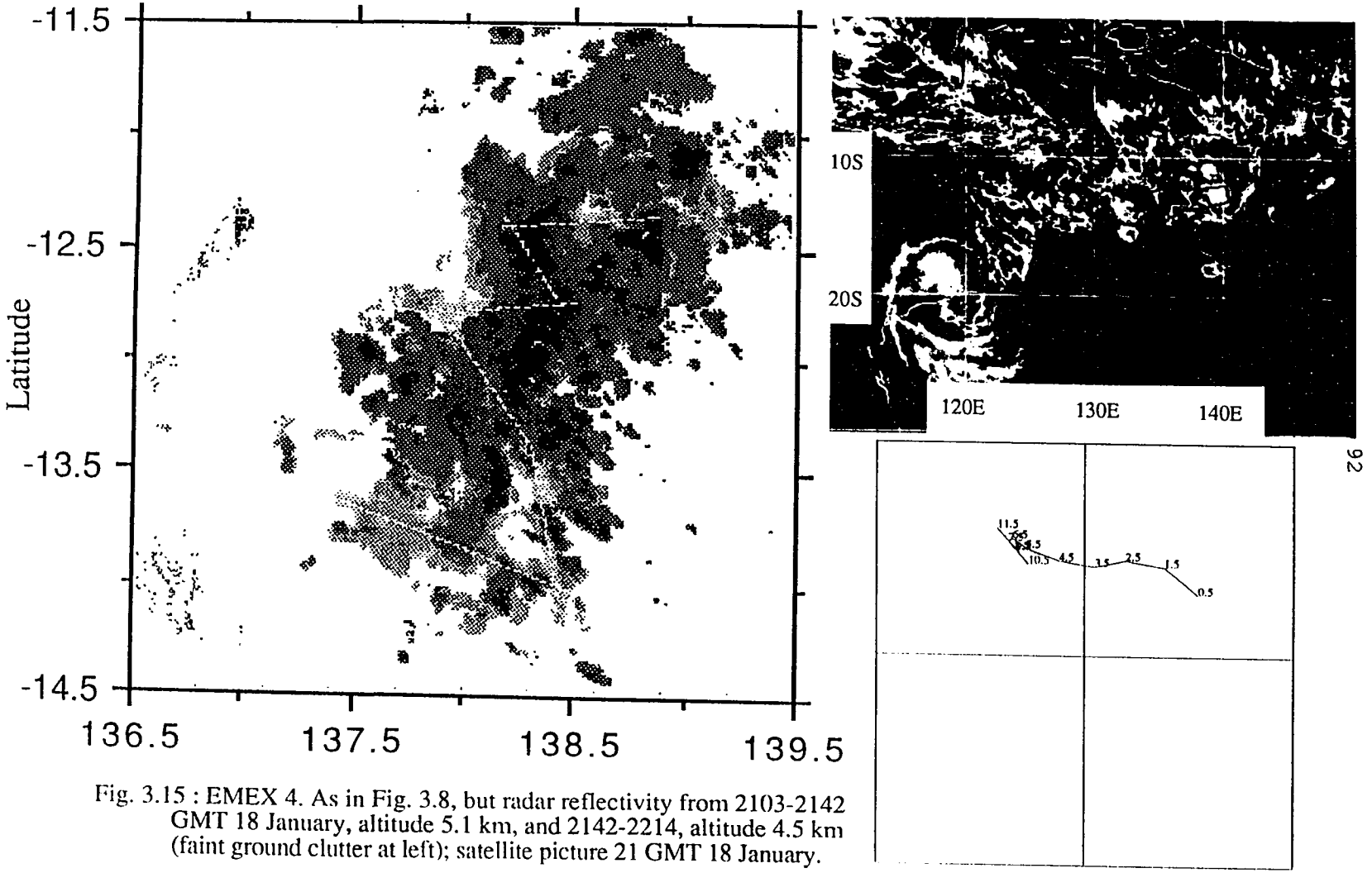


Fig. 3.15 : EMEX 4. As in Fig. 3.8, but radar reflectivity from 2103-2142 GMT 18 January, altitude 5.1 km, and 2142-2214, altitude 4.5 km (faint ground clutter at left); satellite picture 21 GMT 18 January.

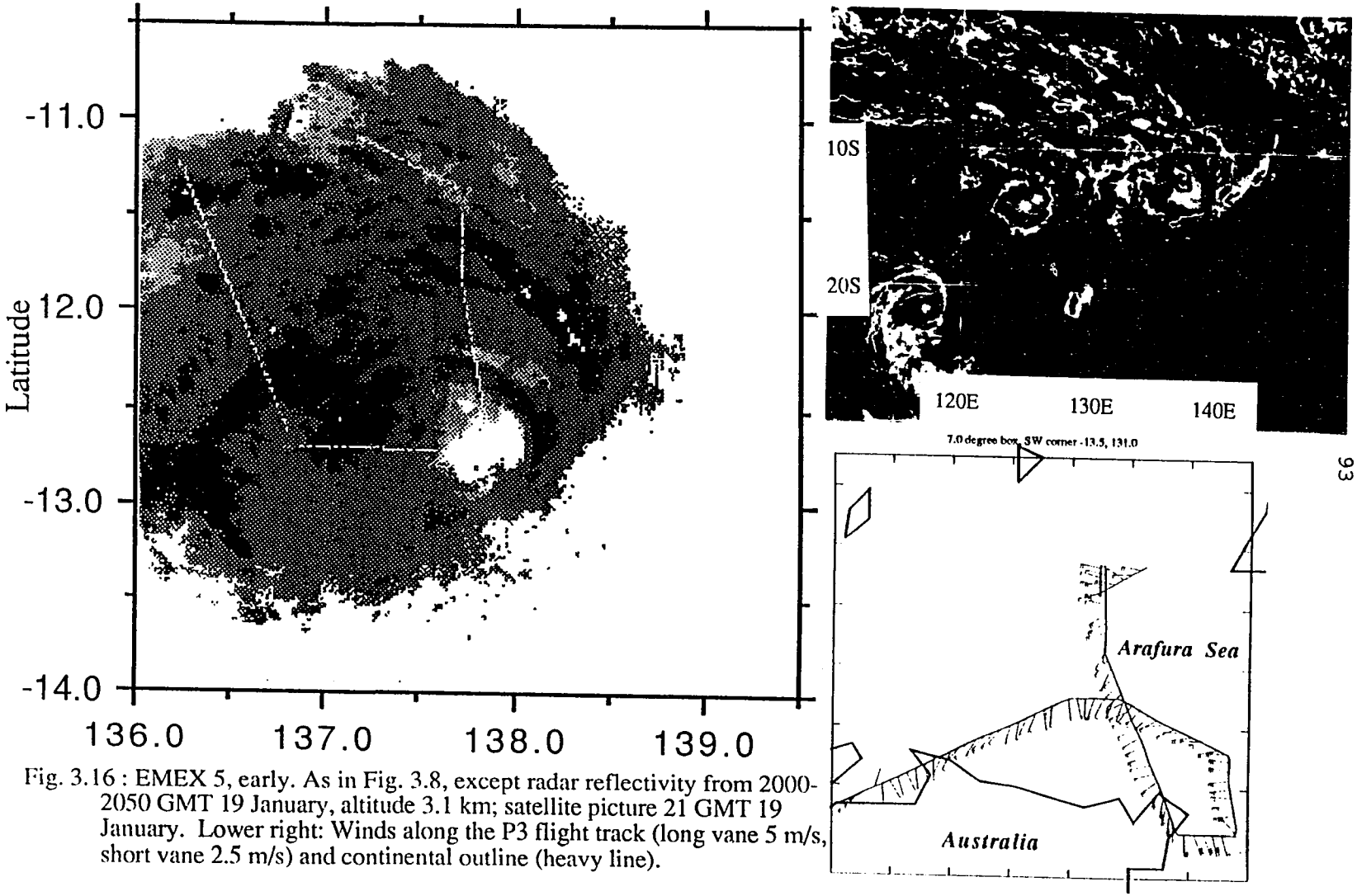


Fig. 3.16 : EMEX 5, early. As in Fig. 3.8, except radar reflectivity from 2000-2050 GMT 19 January, altitude 3.1 km; satellite picture 21 GMT 19 January. Lower right: Winds along the P3 flight track (long vane 5 m/s, short vane 2.5 m/s) and continental outline (heavy line).

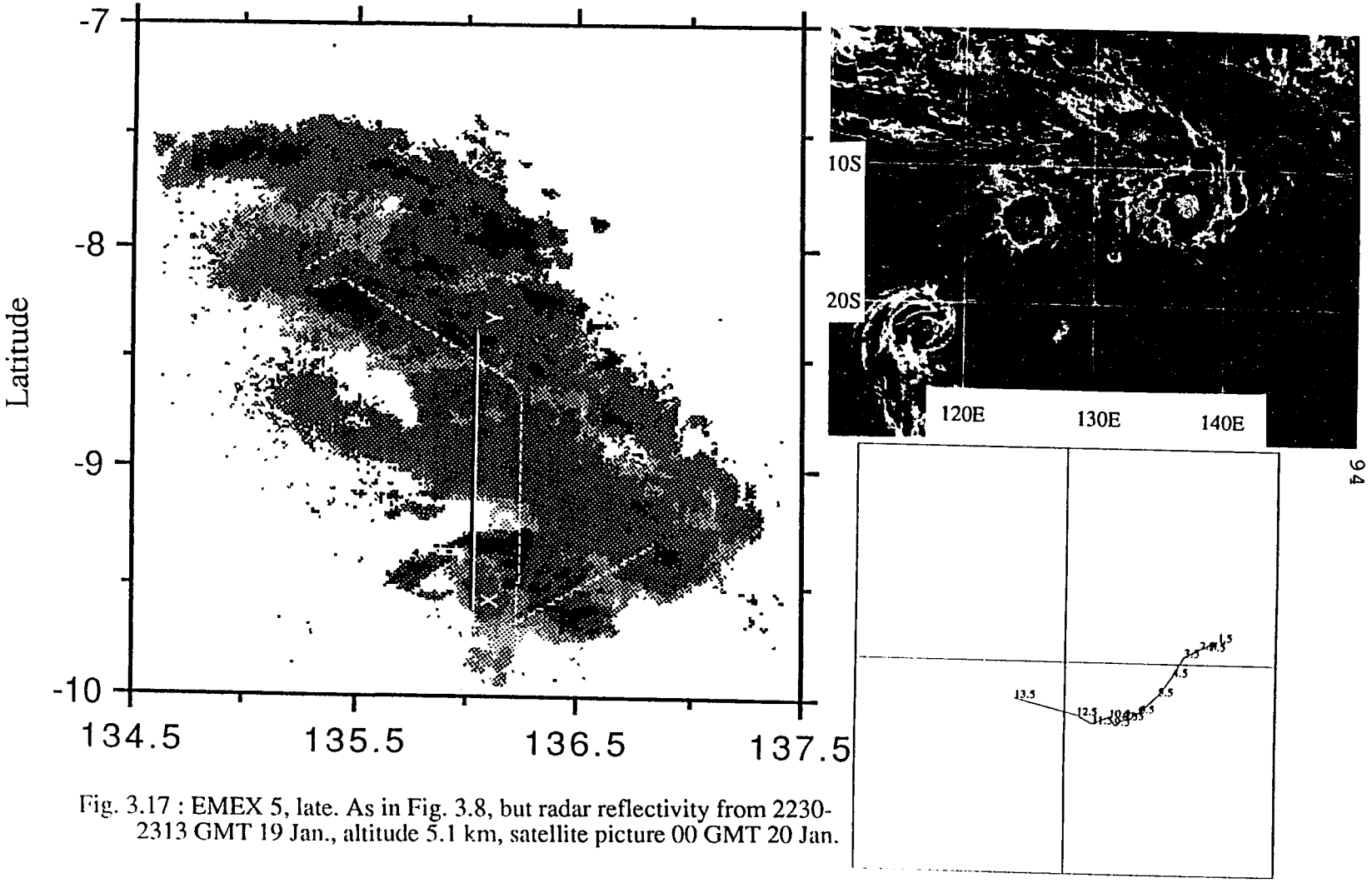


Fig. 3.17 : EMEX 5, late. As in Fig. 3.8, but radar reflectivity from 2230-2313 GMT 19 Jan., altitude 5.1 km, satellite picture 00 GMT 20 Jan.

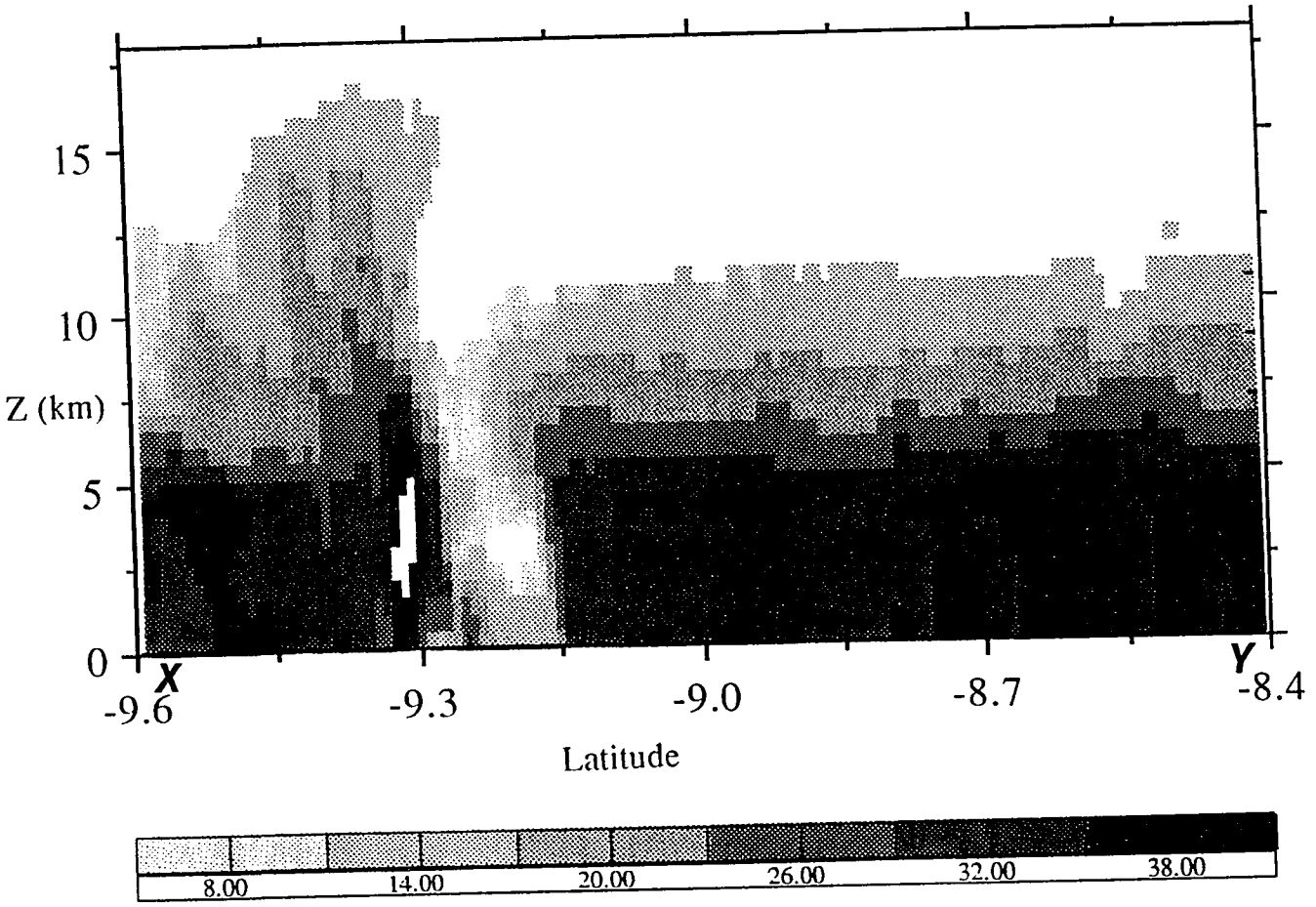


Fig. 3.18 : EMEX 5 squall cross section. Radar reflectivity cross-section along line XY in Fig. 3.17 (but from a later flight track than that indicated on Fig. 3.17).

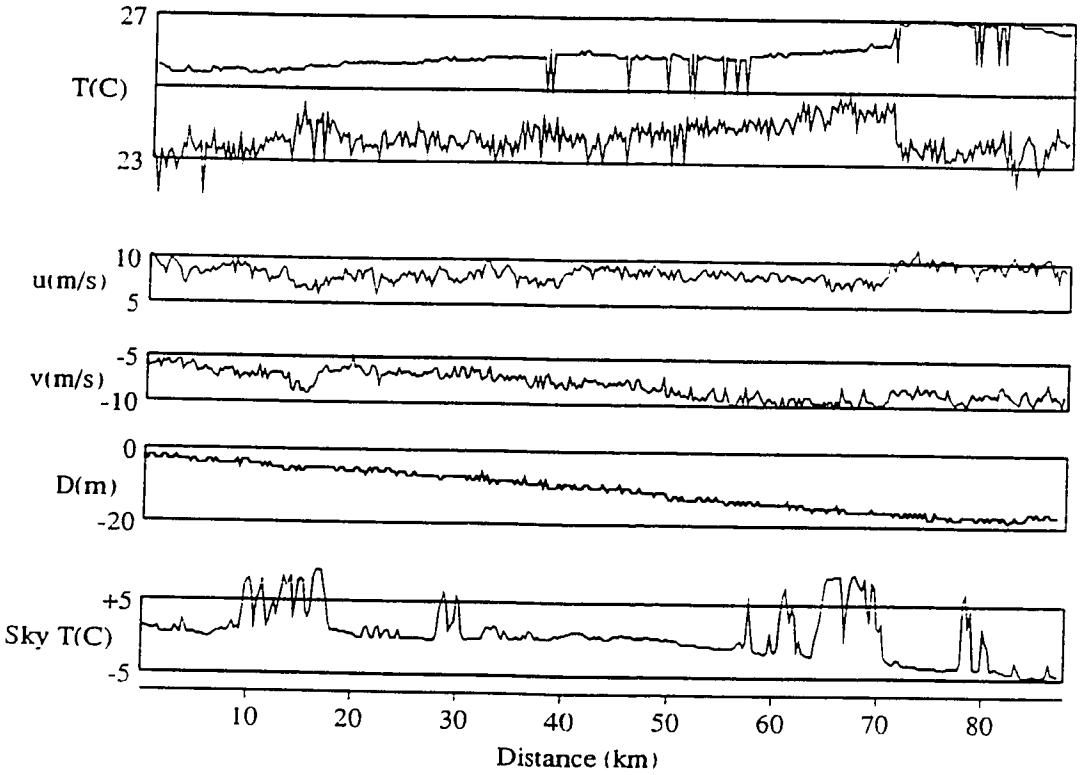


Fig. 3.19 : Back edge of a cold pool. Time series of boundary-layer data from an Electra flight segment at 987 mb (200 m altitude), 0127-0139 GMT 20 January, from 8.6 to 9.4 °S along 135.8 °E. Temperature and dewpoint, zonal wind, meridional wind, D-value (relative), and upward-looking radiometric temperature.

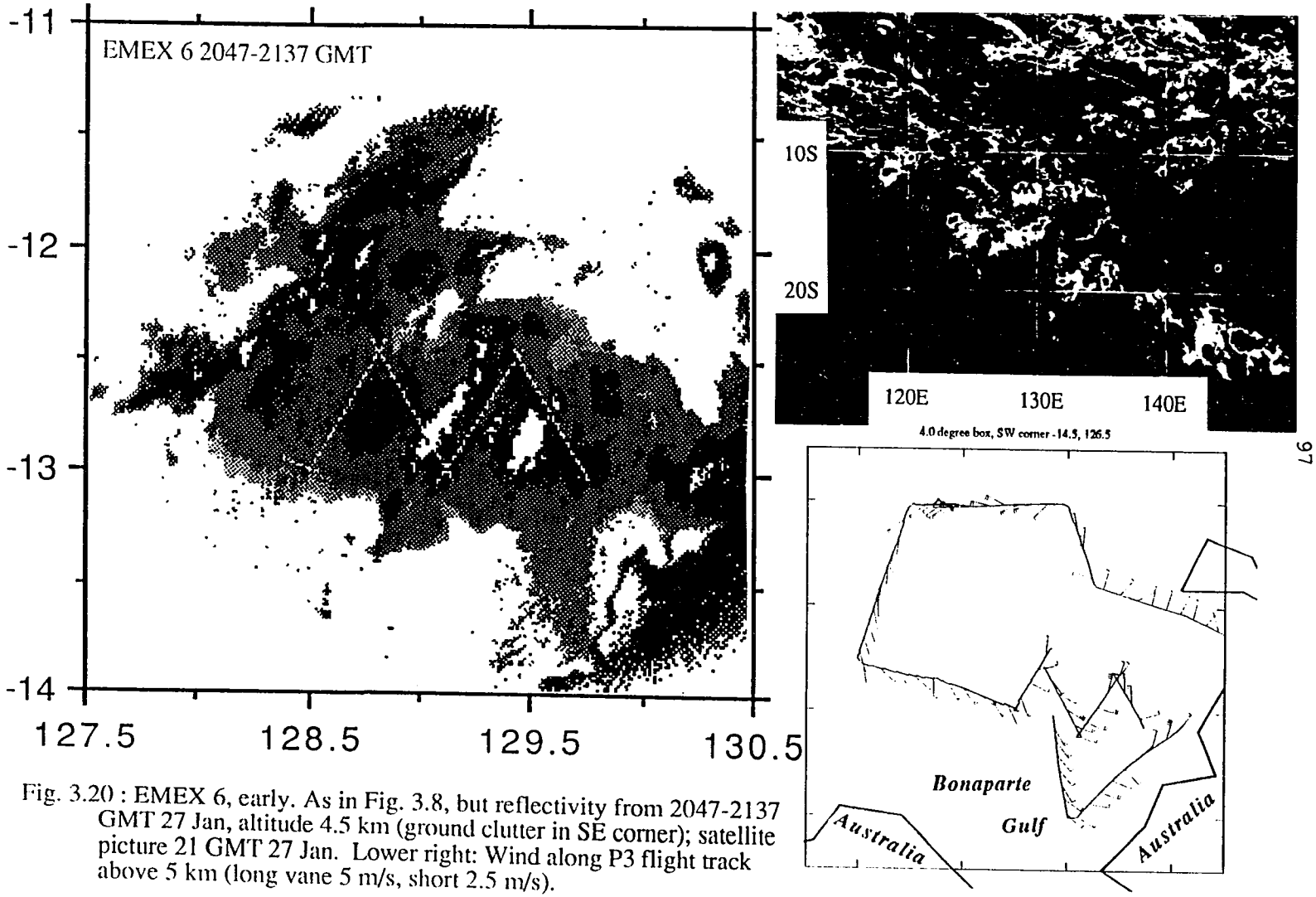


Fig. 3.20 : EMEX 6, early. As in Fig. 3.8, but reflectivity from 2047-2137 GMT 27 Jan, altitude 4.5 km (ground clutter in SE corner); satellite picture 21 GMT 27 Jan. Lower right: Wind along P3 flight track above 5 km (long vane 5 m/s, short 2.5 m/s).

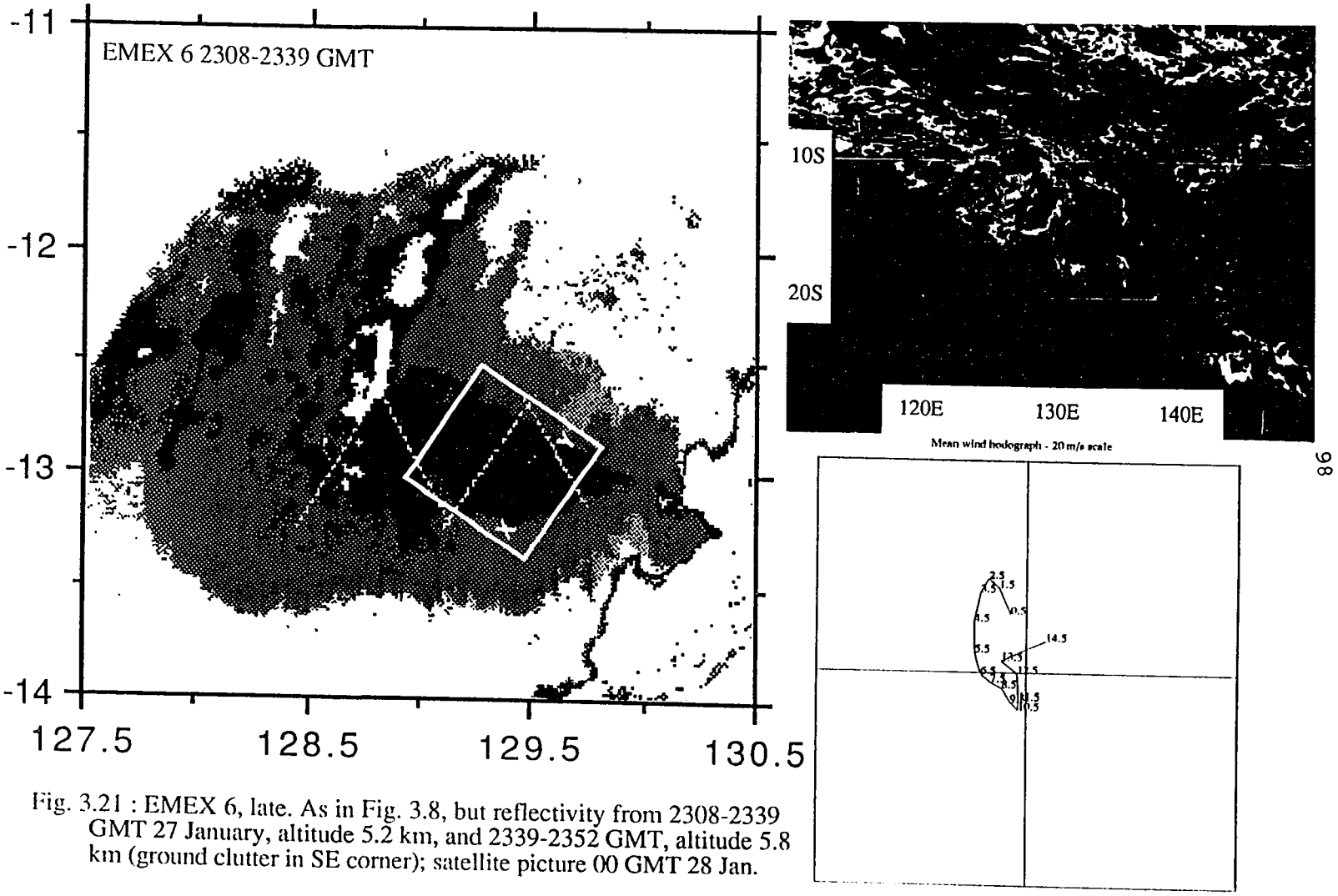


Fig. 3.21 : EMEX 6, late. As in Fig. 3.8, but reflectivity from 2308-2339 GMT 27 January, altitude 5.2 km, and 2339-2352 GMT, altitude 5.8 km (ground clutter in SE corner); satellite picture 00 GMT 28 Jan.

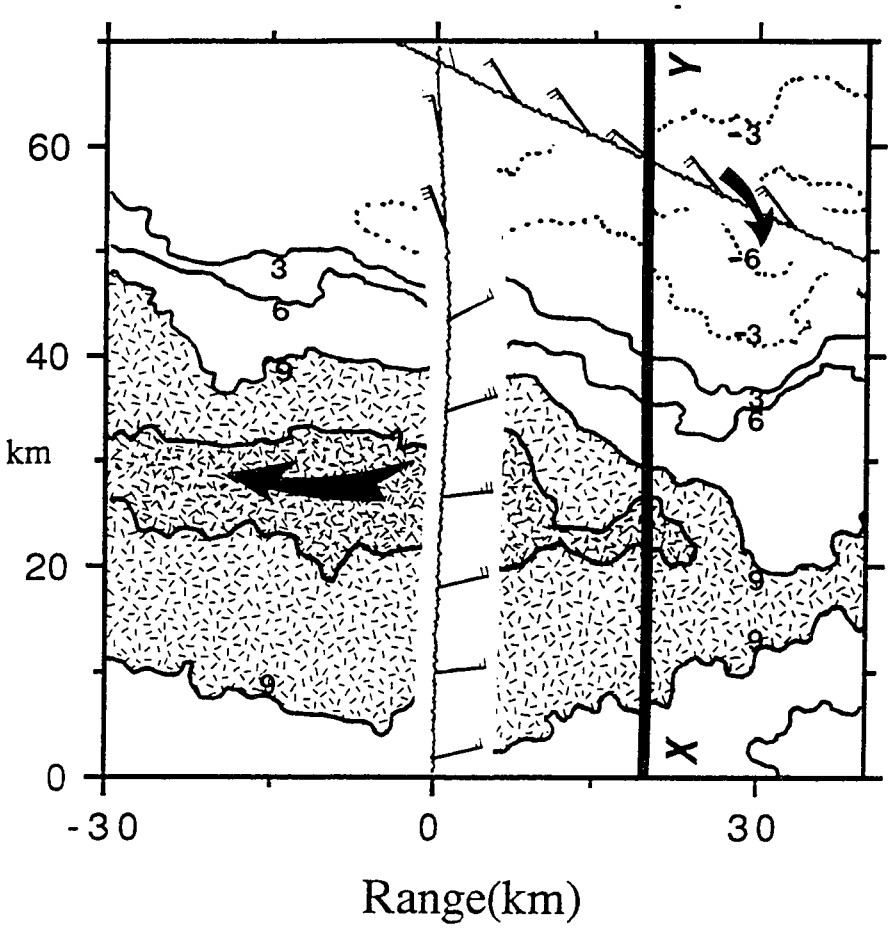


Fig. 3.22 : EMEX 6 midlevel shear. Doppler radar radial velocities (contours 3,6,9,12 m/s; hatching denotes values exceeding 9 m/s) at 5 km (P3 flight level), and P3 wind measurements (long vane 5 m/s, short vane 2.5 m/s), in the box indicated on Fig. 3.21.

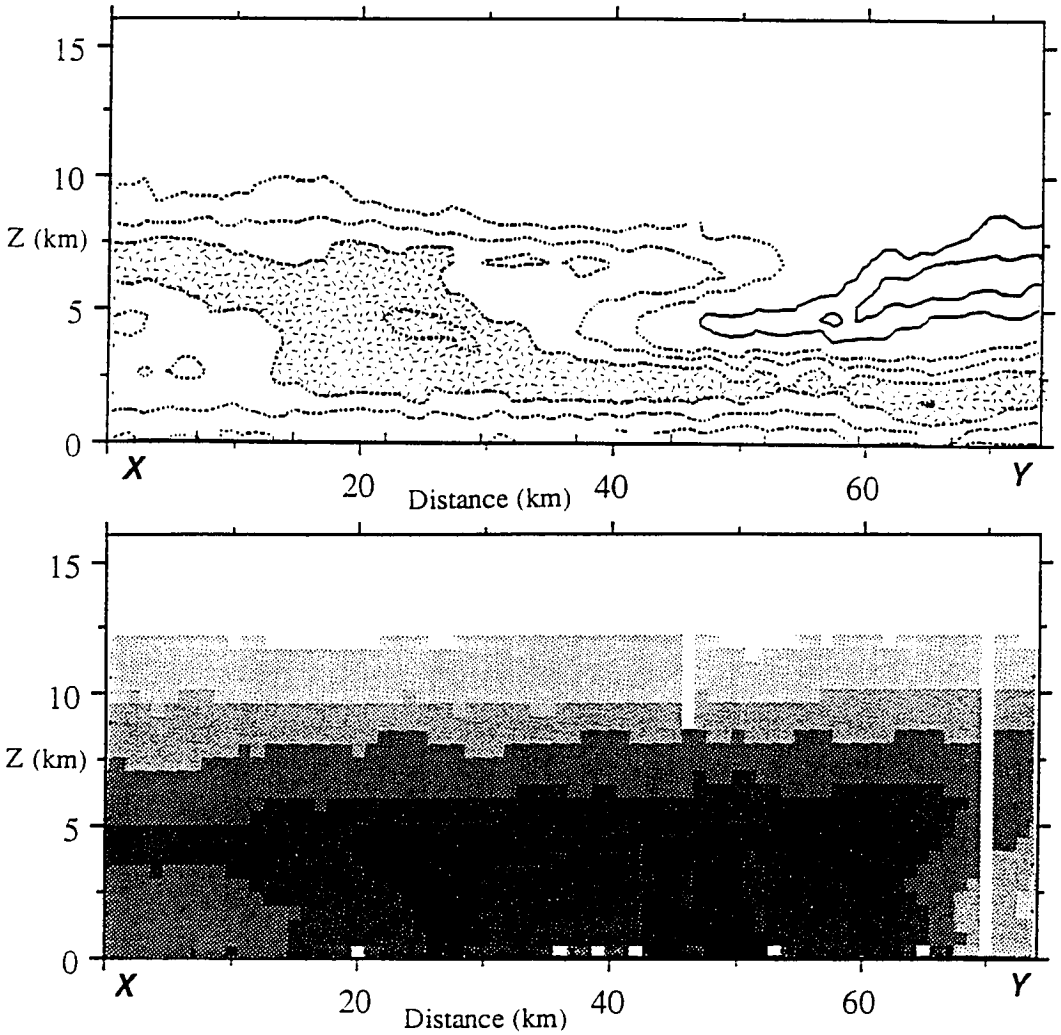


Fig. 3.23 : EMEX 6 midlevel shear cross-section. Cross-section along segment XY in Figs. 3.21 and 3.22, of Doppler radial velocities (contour interval and hatching as in Fig. 3.22) and of radar reflectivity (6 dbZ intervals starting with 8 dbZ)

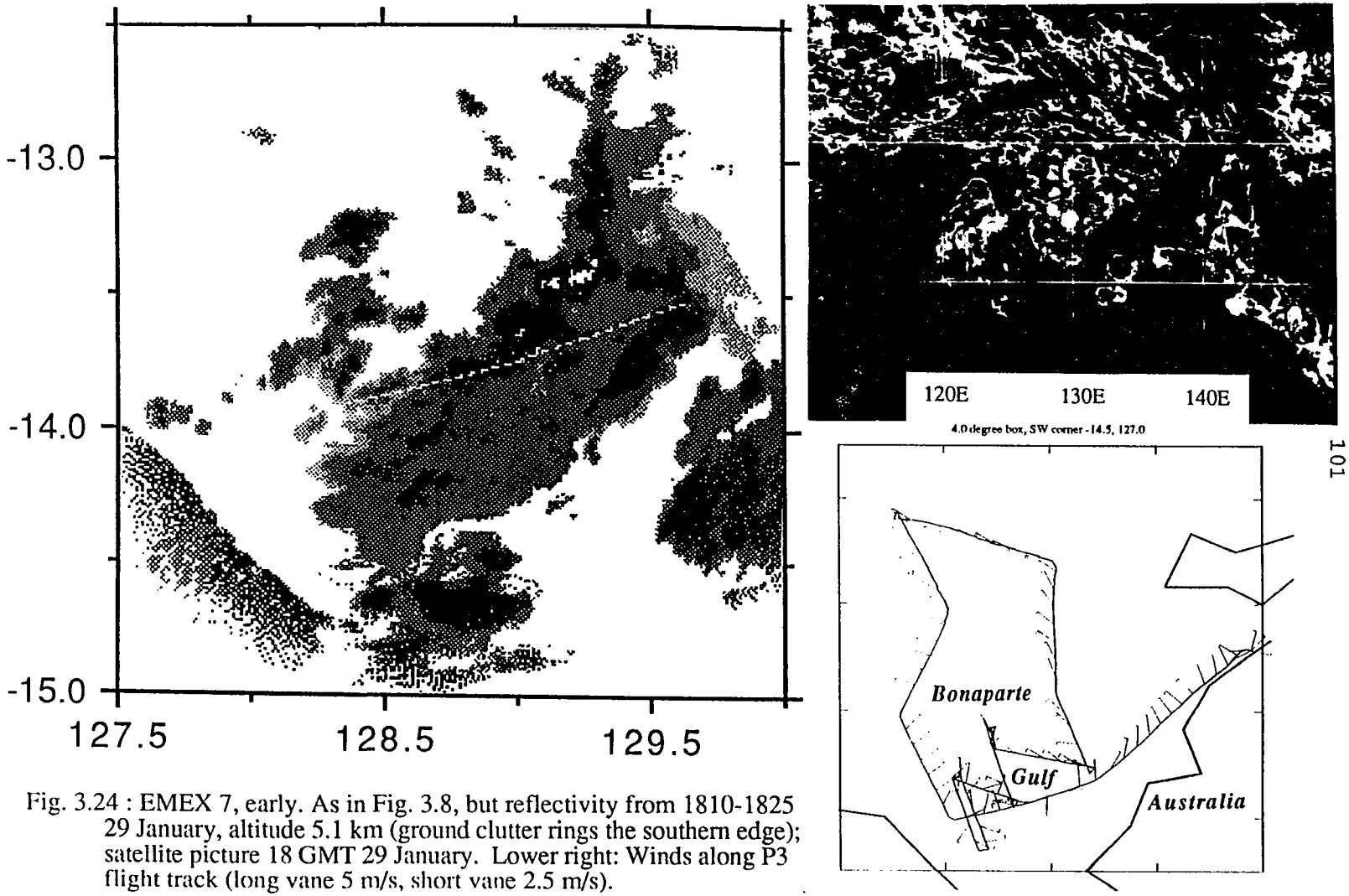


Fig. 3.24 : EMEX 7, early. As in Fig. 3.8, but reflectivity from 1810-1825 29 January, altitude 5.1 km (ground clutter rings the southern edge); satellite picture 18 GMT 29 January. Lower right: Winds along P3 flight track (long vane 5 m/s, short vane 2.5 m/s).

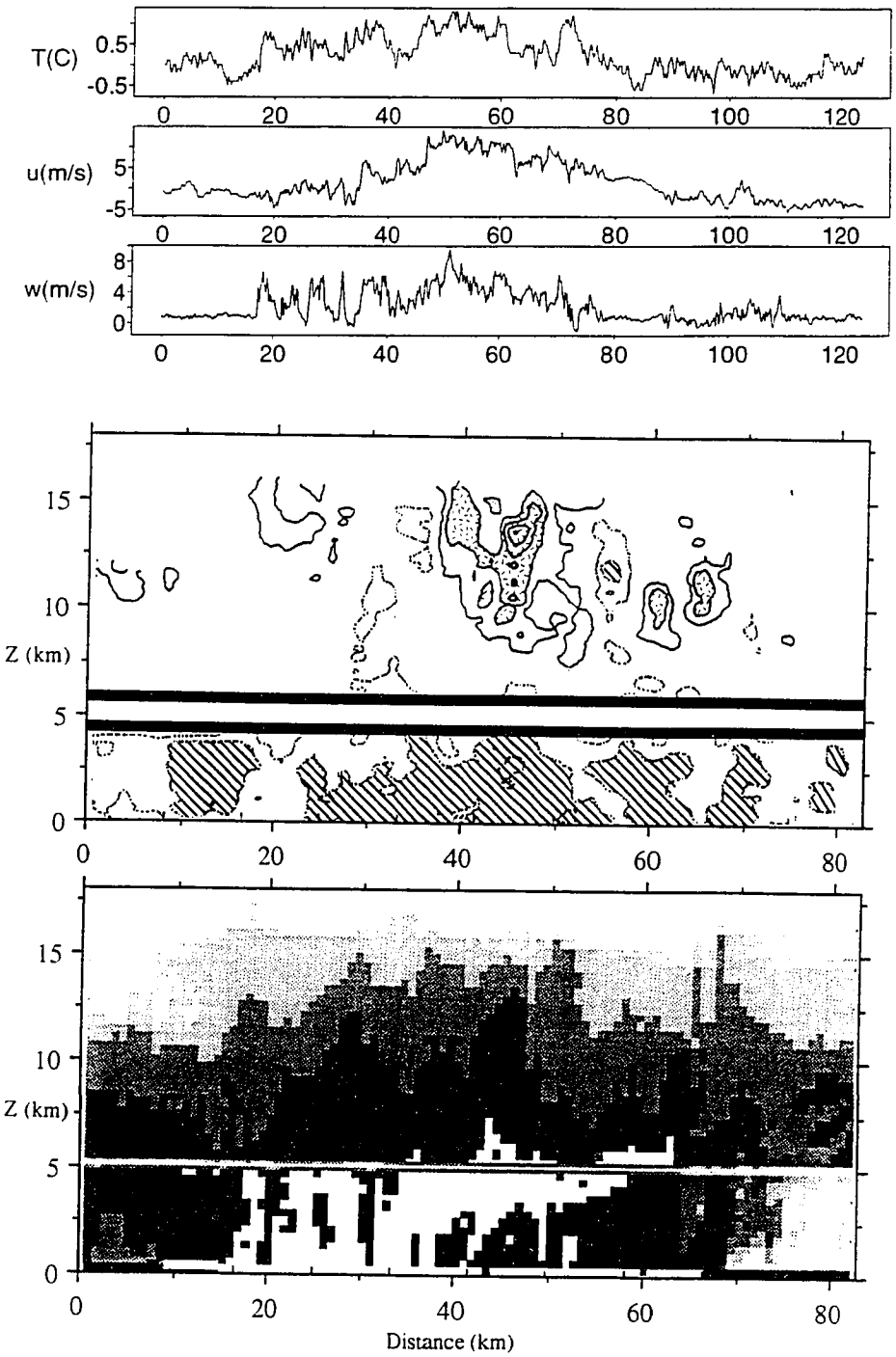


Fig. 3.25 : EMEX 7 giant updraft. Time series data from the P3, along the flight track indicated on Fig. 3.24. Top: radiometric temperature (0.7 °C correction added), zonal wind, and vertical wind. Middle: Time-height section of Doppler velocity at vertical incidence, positive upward: solid contours 3, 6 (stippled), 9... m/s; dashed contours -3, -6 (hatched), -9 m/s. Bottom: Reflectivity in dbZ.

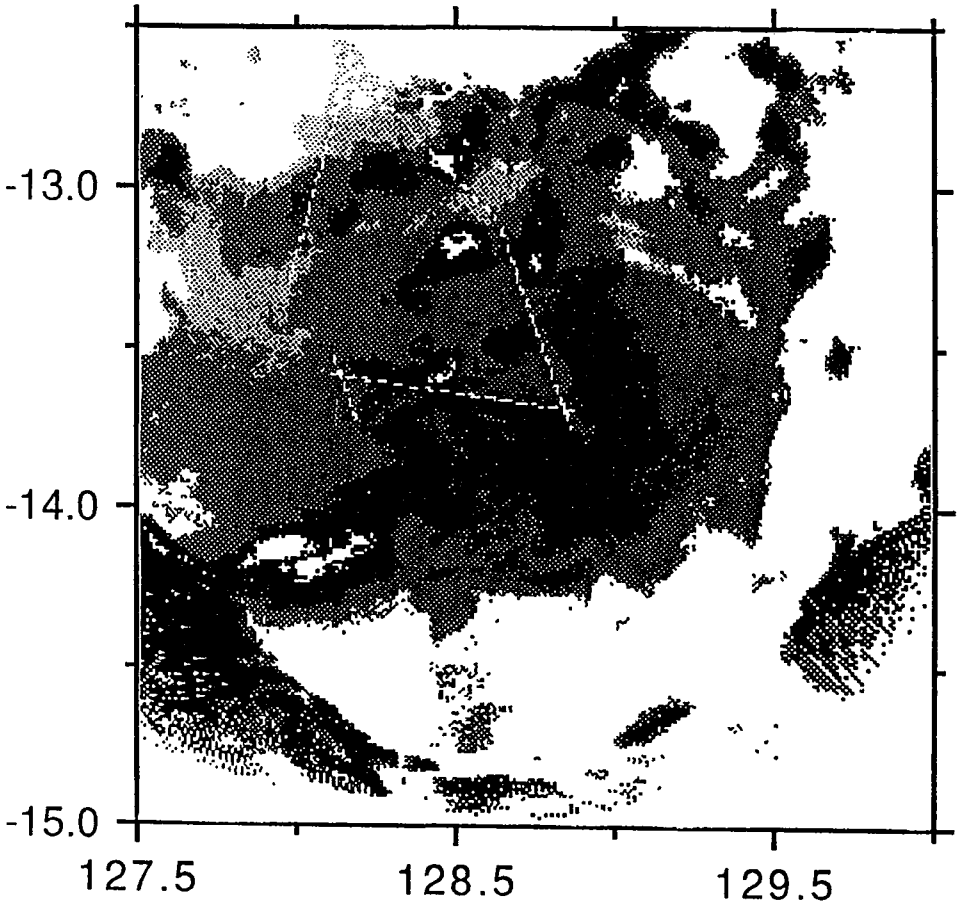


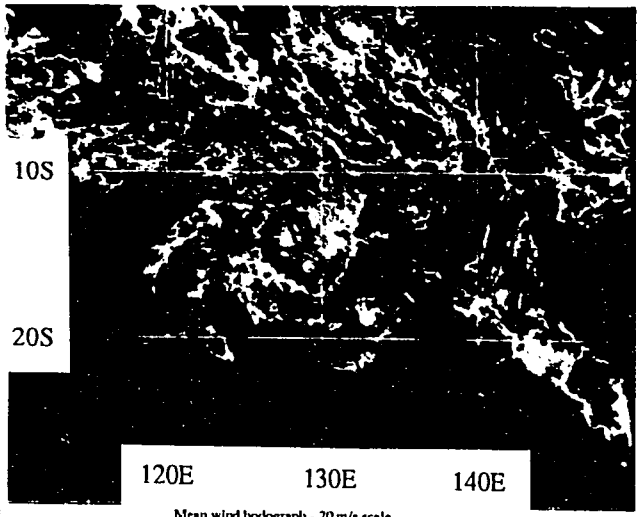


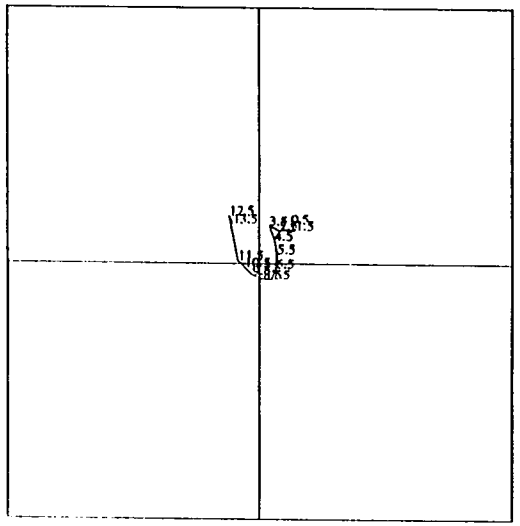


Fig. 3.26 : EMEX 7, middle. As in Fig. 3.8, except radar reflectivity from 2100-2143 GMT 29 January, altitude 5.1 km (ground clutter rings the southern edge); satellite picture 21 GMT 29 January.

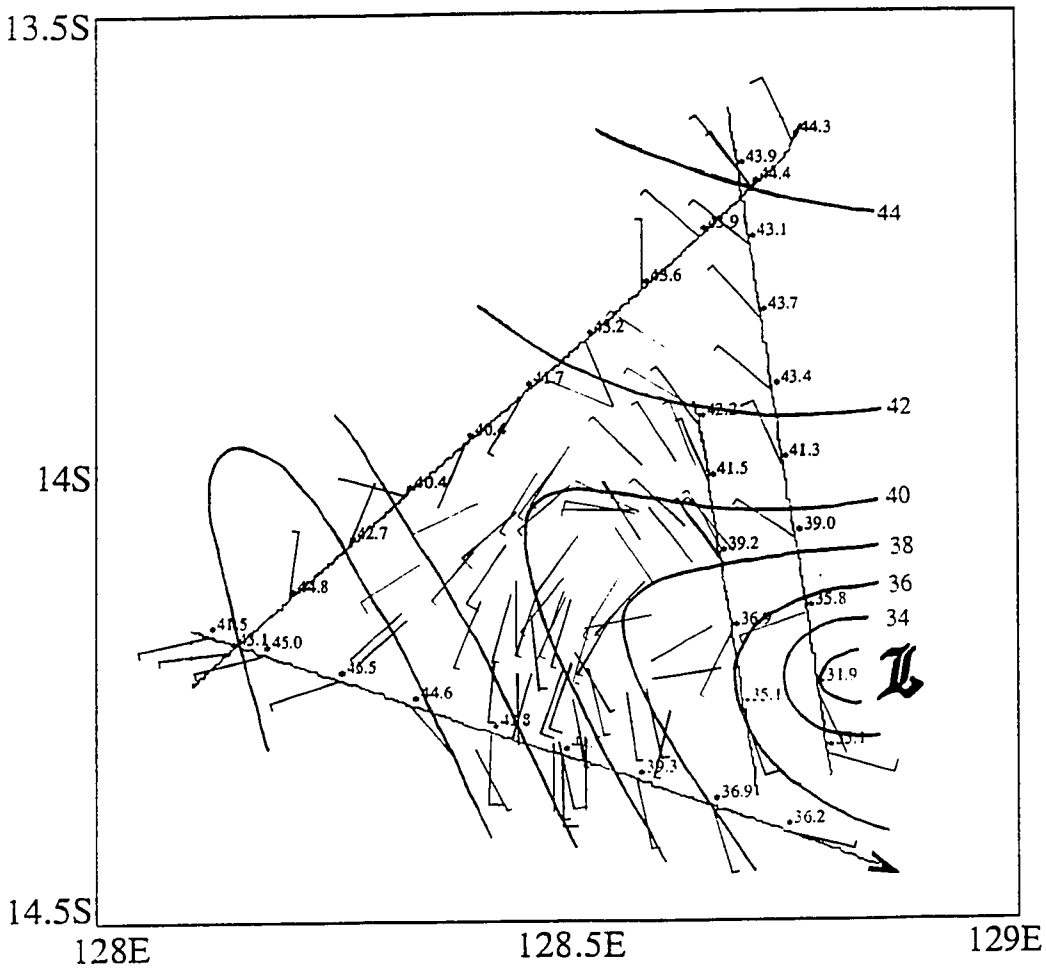


Fig. 3.27 : A midlevel depression. Wind and D-value analysis of midlevel mesolow, from P3 data, 2342 GMT 29 January to 0025 GMT 30 January, flight altitude 6.5 km. Along the solid flight track, 1 min mean winds (heavy barbs) and D-value (plotted along flight track and contoured at 2m intervals, absolute value arbitrary). Also Doppler-derived mean winds (light barbs) in 6-7 km layer, calculated from Doppler measurements obtained during three pairs of adjacent flight legs centered at 2342 GMT, 0004 GMT, and 0014 GMT.

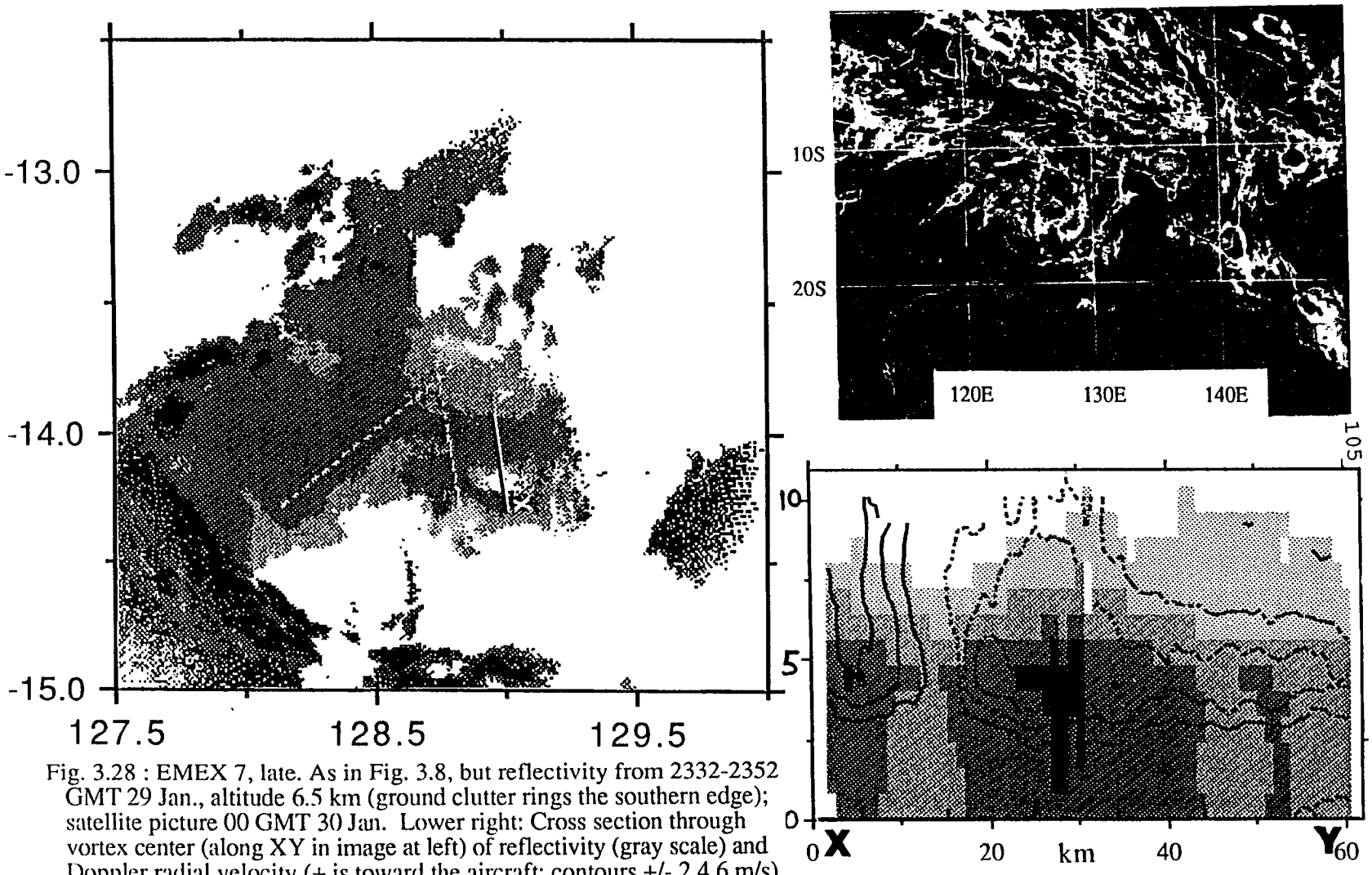


Fig. 3.28 : EMEX 7, late. As in Fig. 3.8, but reflectivity from 2332-2352 GMT 29 Jan., altitude 6.5 km (ground clutter rings the southern edge); satellite picture 00 GMT 30 Jan. Lower right: Cross section through vortex center (along XY in image at left) of reflectivity (gray scale) and Doppler radial velocity (+ is toward the aircraft; contours +/- 2,4,6 m/s).

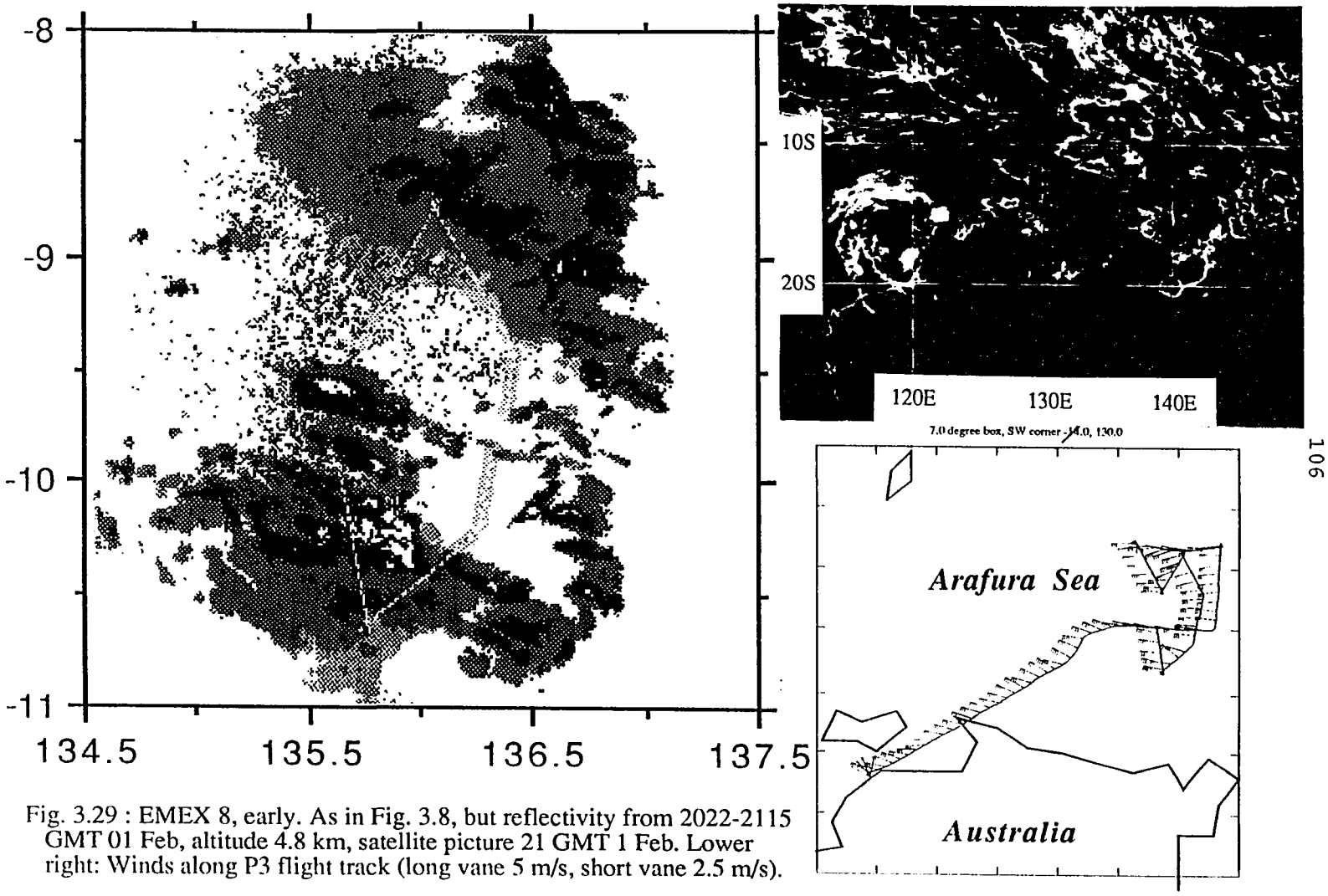


Fig. 3.29 : EMEX 8, early. As in Fig. 3.8, but reflectivity from 2022-2115 GMT 01 Feb, altitude 4.8 km, satellite picture 21 GMT 1 Feb. Lower right: Winds along P3 flight track (long vane 5 m/s, short vane 2.5 m/s).

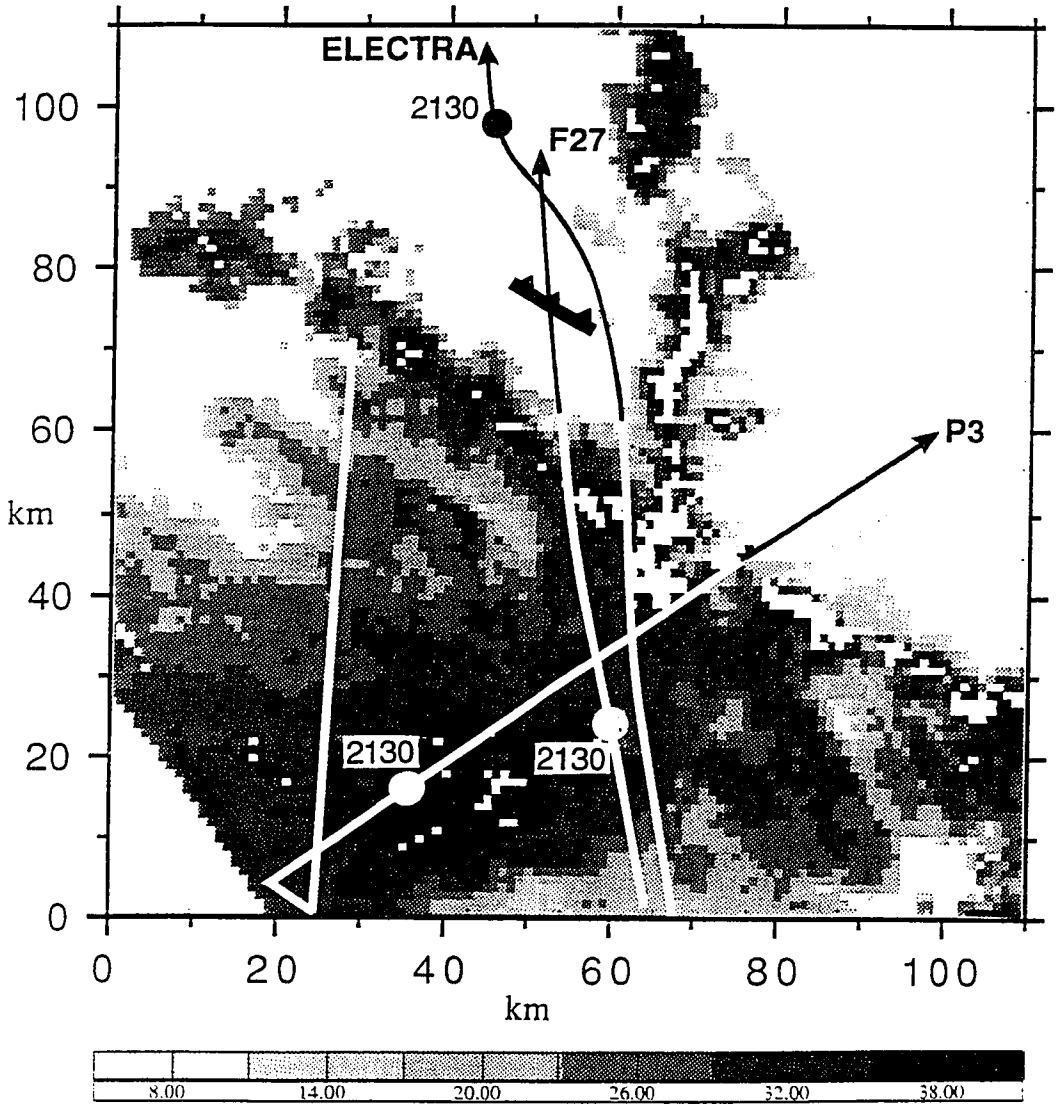


Fig. 3.30 : Intersection of squall arc and along-wind line. Radar reflectivity at 3 km and aircraft tracks near 2130 GMT 1 February, with all data translated to its approximate 2130 GMT position using storm translation vector of 19 m/s from 290°. F27 gust front is indicated with a cold front symbol.

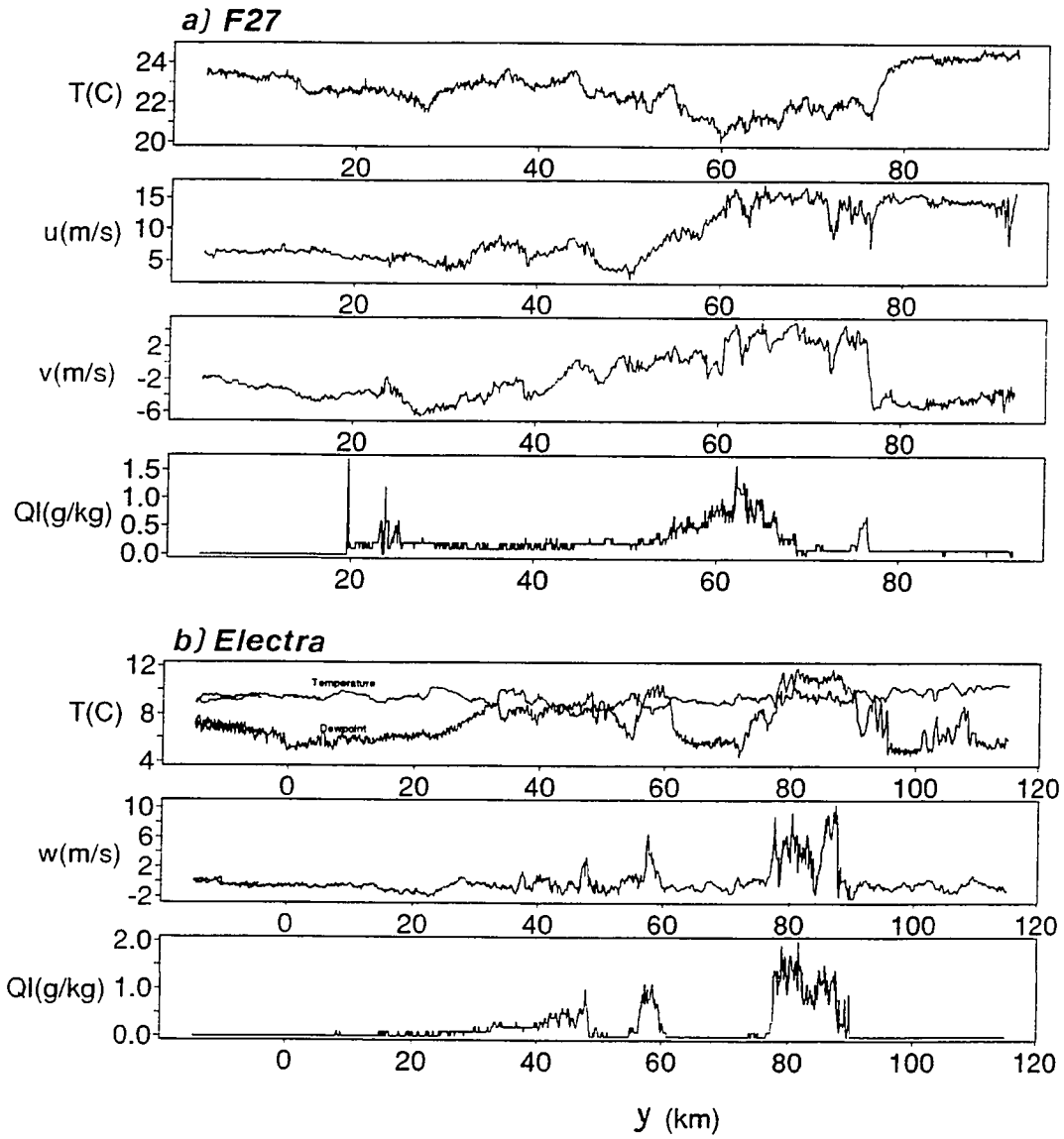


Fig. 3.31 : Transects of a discrete propagation event. Time series of aircraft data from the area depicted in Fig. 3.30 (y axis as in 3.30), illustrating the double convective zone. a) F27 data at 952 mb (500 m): temperature, zonal and meridional winds, and liquid water mixing ratio. b) Electra data at 695 mb: vertical velocity, and FSSP liquid water mixing ratio.

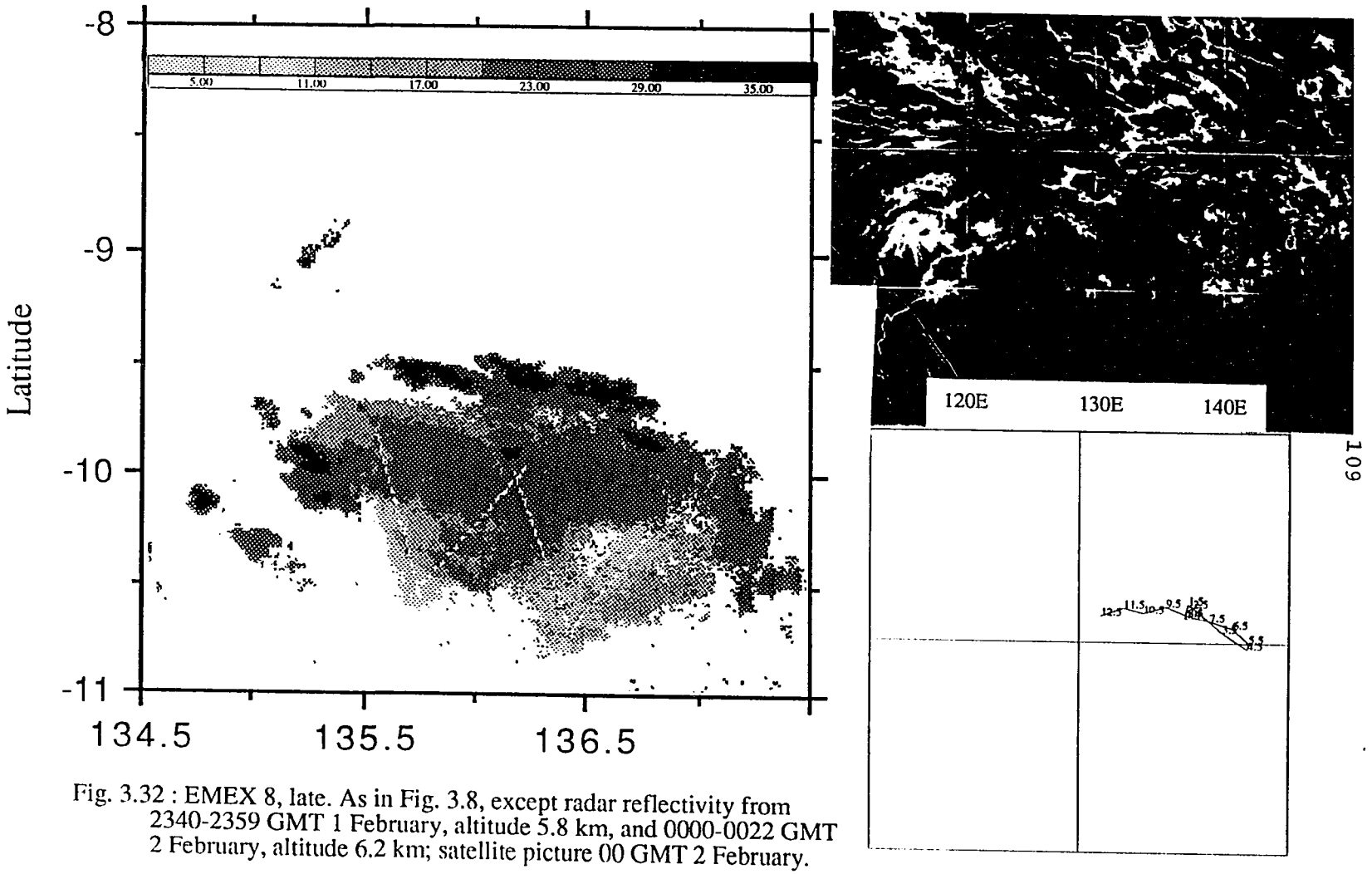


Fig. 3.32 : EMEX 8, late. As in Fig. 3.8, except radar reflectivity from 2340-2359 GMT 1 February, altitude 5.8 km, and 0000-0022 GMT 2 February, altitude 6.2 km; satellite picture 00 GMT 2 February.

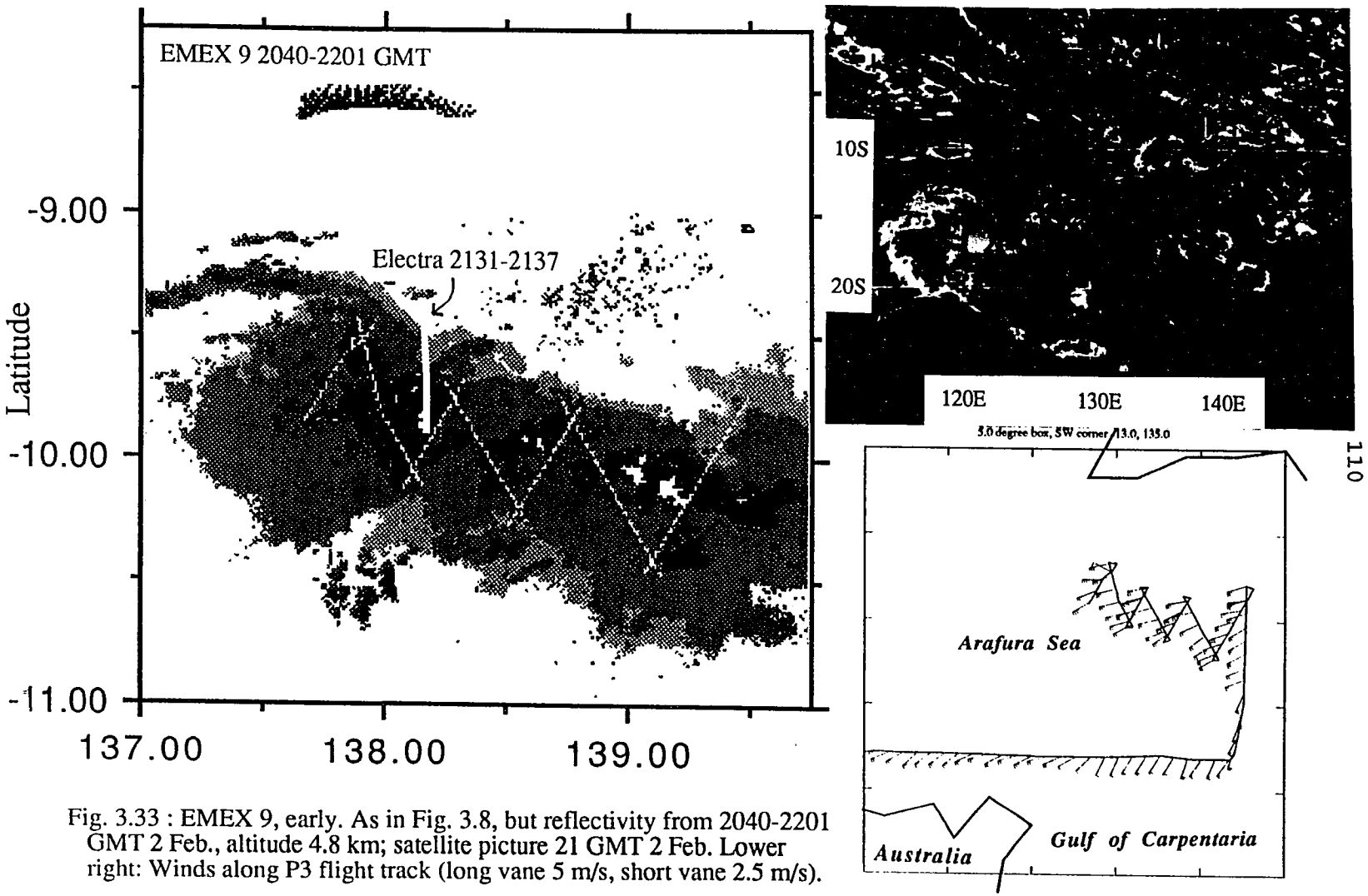


Fig. 3.33 : EMEX 9, early. As in Fig. 3.8, but reflectivity from 2040-2201 GMT 2 Feb., altitude 4.8 km; satellite picture 21 GMT 2 Feb. Lower right: Winds along P3 flight track (long vane 5 m/s, short vane 2.5 m/s).

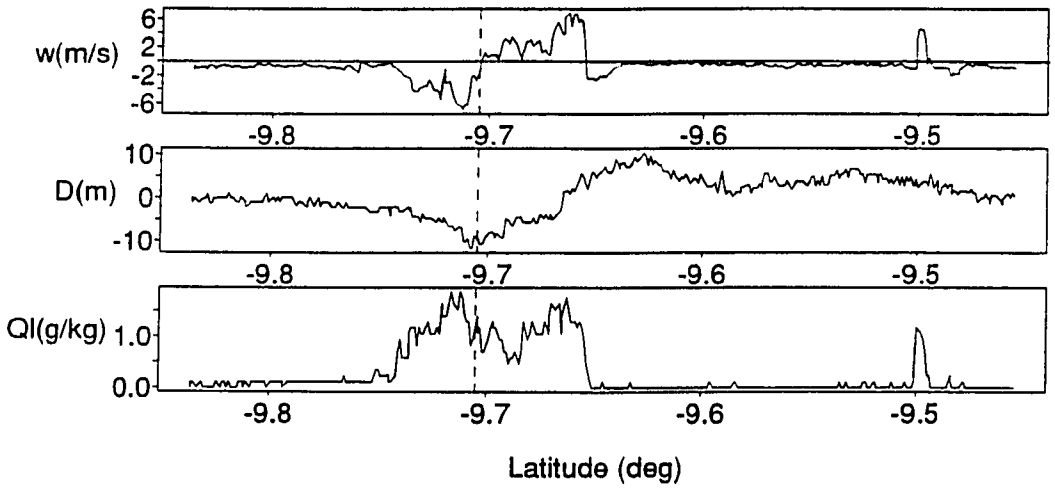


Fig. 3.34 : Nonclassical momentum transport. Electra data, 2131-2137 GMT 2 February, northbound along 138.1 °E at 695 mb: vertical wind, D-value, and liquid water mixing ratio (from FSSP).

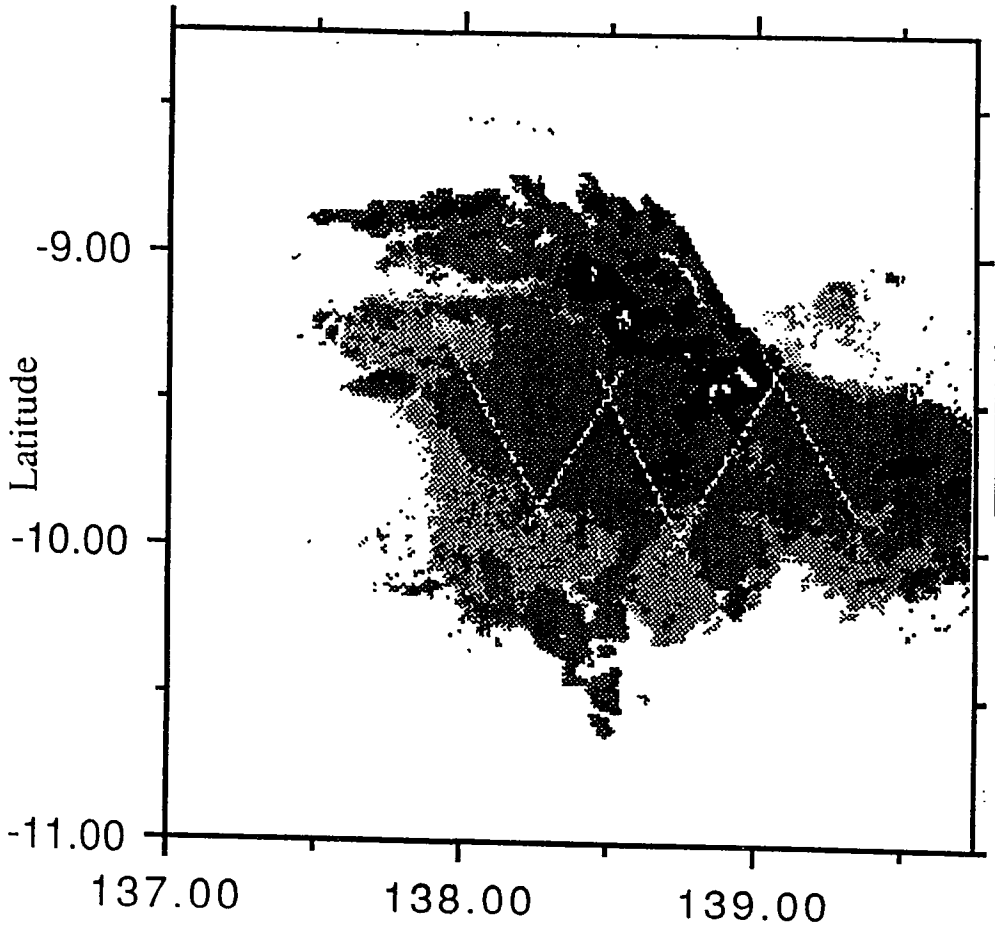


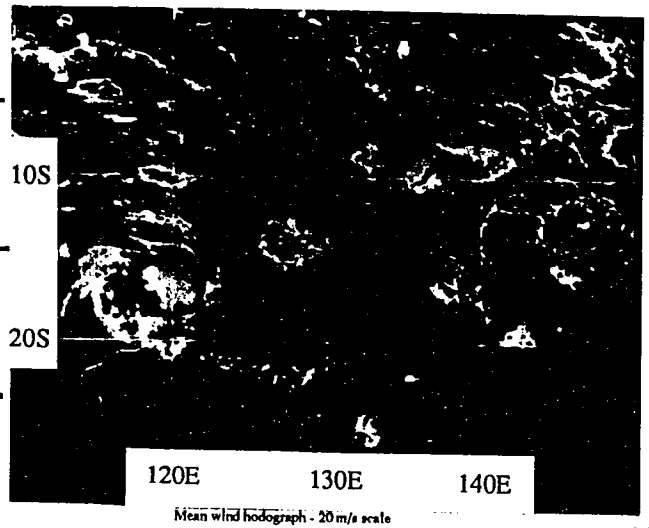


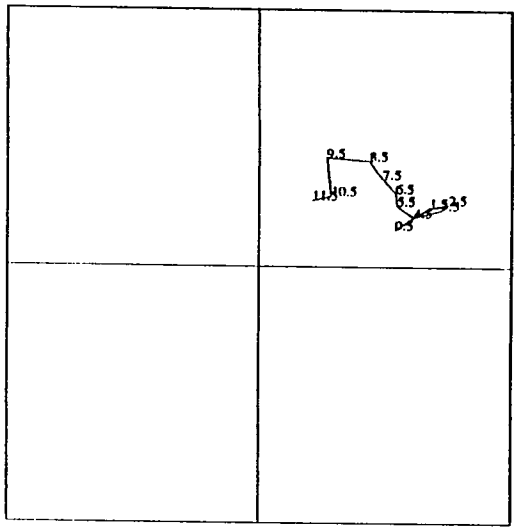


Fig. 3.35 : EMEX 9, late. As in Fig. 3.8, except radar reflectivity from 2253-2305 GMT 2 February, altitude 4.8 km, and 2305-2350 GMT, altitude 5.5 km; satellite picture 00 GMT 3 February.

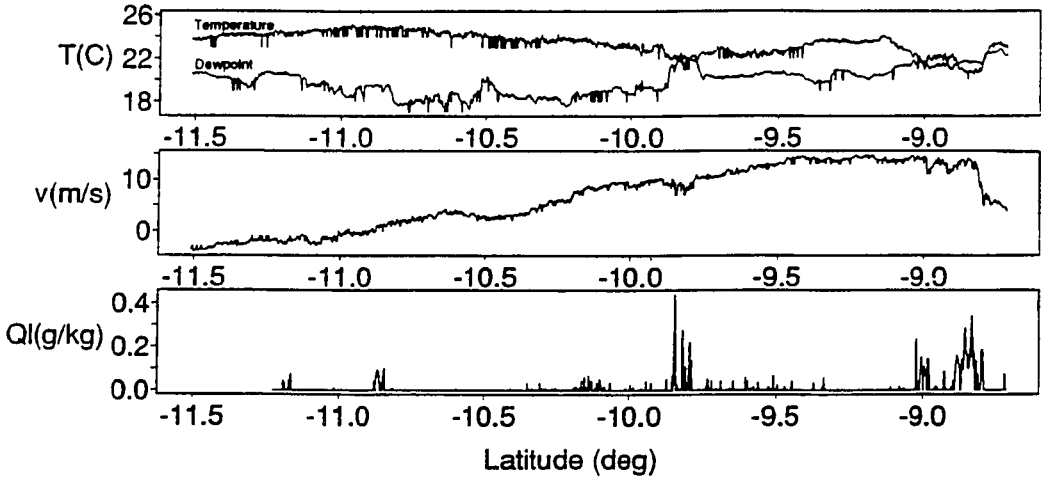


Fig. 3.36 : Broad divergent cold pool. F27 data at 953 mb (500 m), 2200-2255 GMT 2 February, tracking NNE from 11.5 °S, 137.3 °E to 9.9 °S, 138.0 °E, then north along 138 °E. See Fig. 3.35 for mesoscale context.

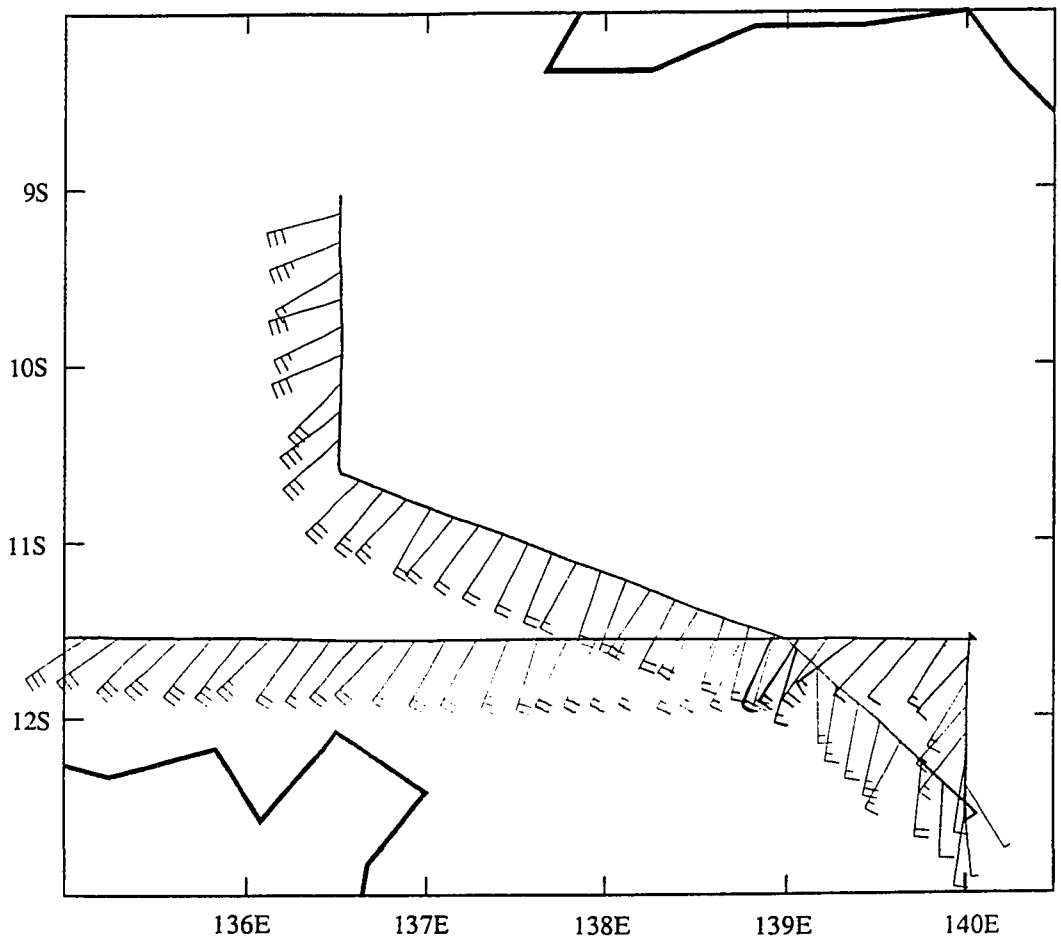


Fig. 3.37 : Midlevel rear inflow to a non-squall line. Winds measured by the P3, 1930-2200 GMT 3 February, with continental outline (heavy line).

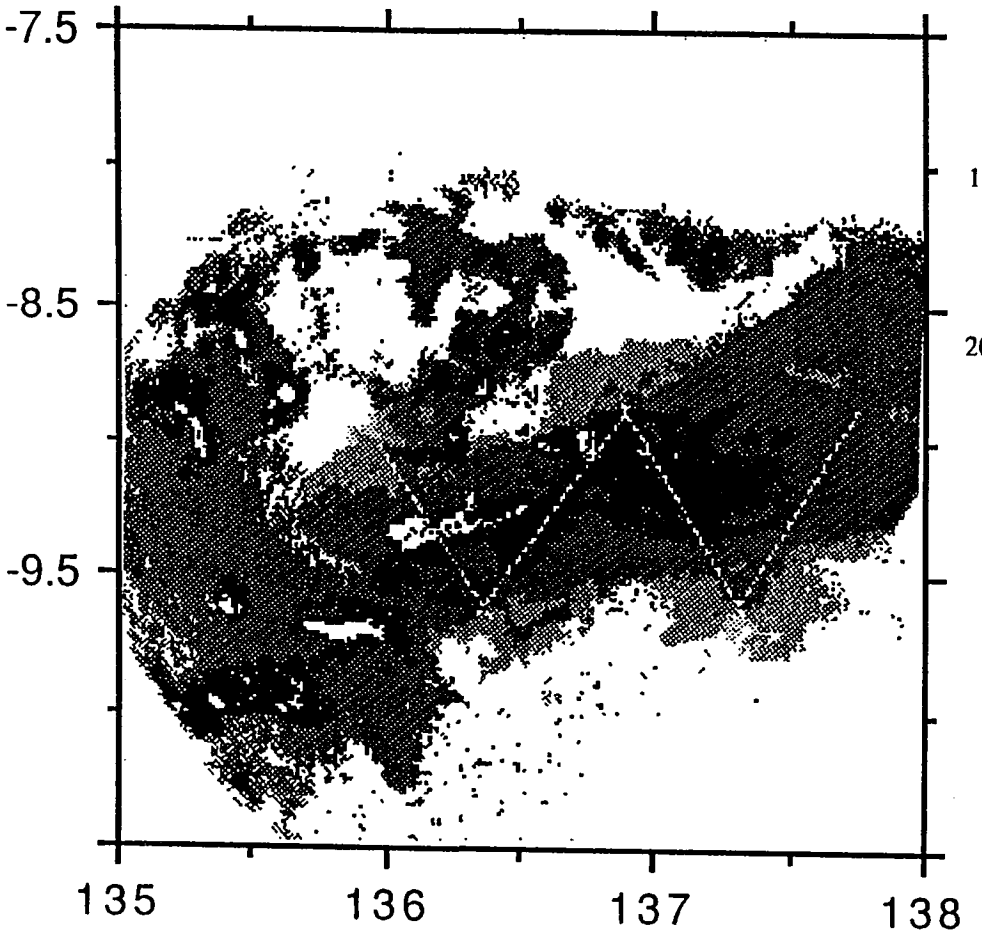


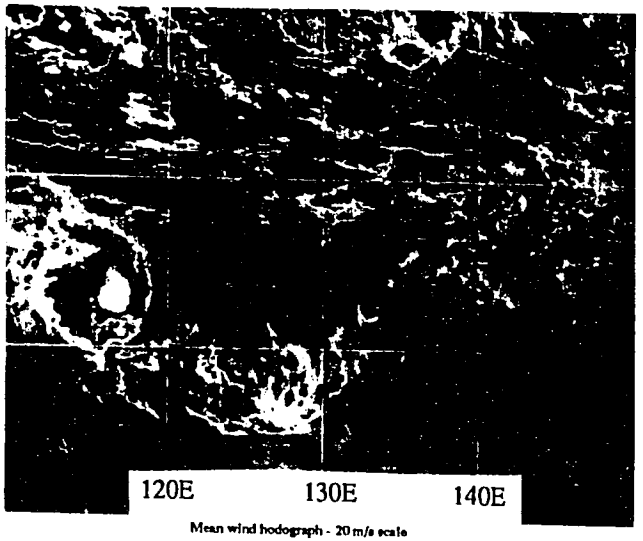


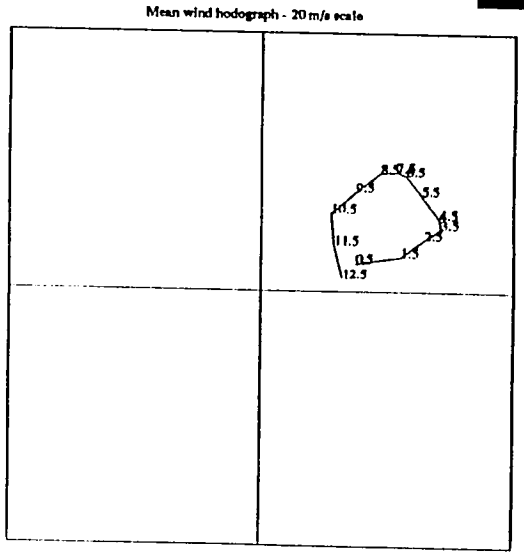


Fig. 3.38 : EMEX 10. As in Fig. 3.8, except radar reflectivity from 2310-2350 GMT 3 February, altitude 4.5 km, and 2350-2359 GMT, altitude 5.8 km; satellite picture 00 GMT 4 February.

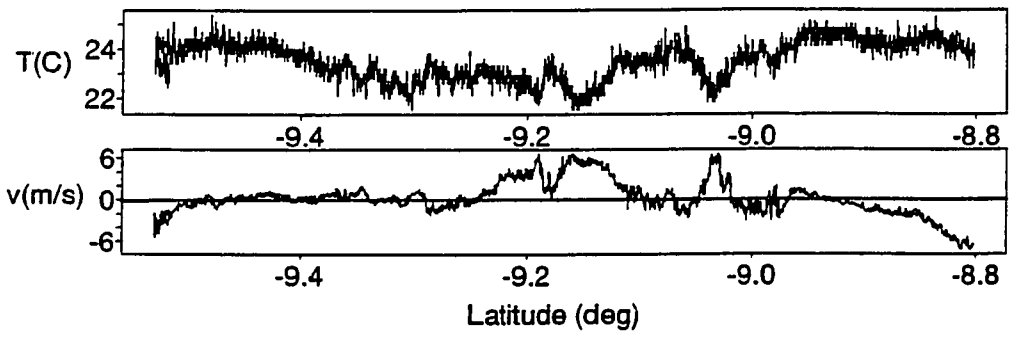


Fig. 3.39 : Apparent conservation of southerly momentum in downdrafts. F27 data at 970 mb (350 m), 2339-2356 GMT 3 February, along 136.5 °E.

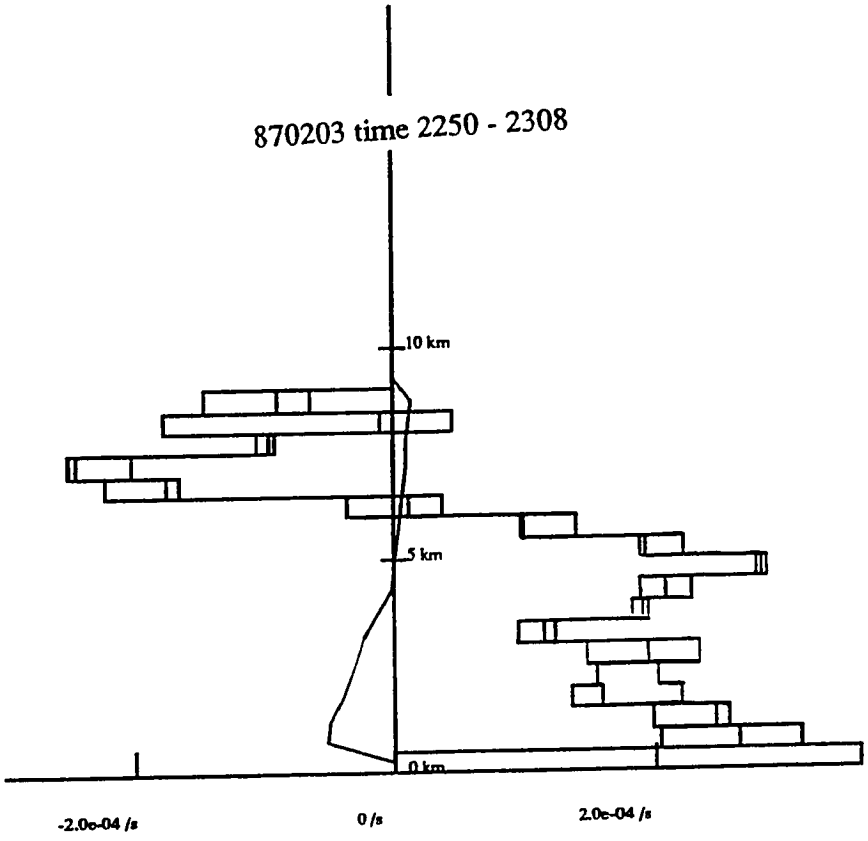


Fig. 3.40 : A buoyancy bore? Doppler radar divergence profile from EMEX 10, 2250-2308 GMT 3 February 1987.

# CHAPTER 4

## ENVIRONMENTAL FACTORS MODULATING MONSOON CONVECTION

Deep convection is small with respect to the synoptic circulations within which it is embedded. It is therefore convenient in studying the so-called "scale interaction problem" to consider separately the effects of the large scale on the small, and vice-versa. This chapter examines mechanisms by which larger-scale processes in the tropical atmosphere modulate convection. It is an axiom of the present work that convection responds only to its local environment, meaning primarily the thermodynamic stratification (including water vapor), but also the wind profile. In other words, the effects of large-scale circulations on convection should, in principle, be apparent in soundings. If large-scale lifting "forces" convection, it must do so by means of initially adiabatic upward *displacements* of the ambient air, which then favor the growth of deep convection.

Energy quantities are used to assess the thermodynamic conditions for convection. Convective available potential energy (CAPE), and an extension called integrated CAPE (ICAPE), are discussed in section 4.1.1. ICAPE is very sensitive to water vapor in the lowest few hundred meters, which varies considerably on small space and time scales, obscuring its large-scale or long-term variations. A composite of the AMEX soundings with respect to satellite-observed cloudiness is used to show the much smaller variation of CAPE and ICAPE associated with the deep monsoon thermal structure. Convective inhibition (CIN), an "activation energy" which must be expended in order to release the much larger CAPE, is examined in section 4.1.2.

Section 4.2 contains a discussion of various feedback processes by which convection affects subsequent convection. With the exception of the low-$\theta_e$ downdraft outflows of MCSs, these feedbacks are positive. To the extent that the lower boundary is able to supply the vapor and heat necessary to restore downdraft air to convective readiness, then, the monsoon can be viewed as a runaway convective system. The result, as seen in satellite data, is "superclustering:" the monsoon convection is so gregarious that its MCSs cannot really be called entirely distinct (as seen earlier, in Figs. 1.5 and 1.6).

Section 4.3 examines how large-scale forcing appears in soundings, in places in which it was known to exist. The passage (advection) of a small upper-tropospheric potential vorticity (PV) cyclone is detailed in section 4.3.1. Its effects (cool lens below, warm lens above) did not reach down low enough to trigger any convection. Low temperatures were also observed beneath a PV cyclone near the 0°C level (section 4.3.2). Such a cooling of the ambient air at low levels could increase the buoyancy of both updrafts and downdrafts, leading to more convection with fewer downdrafts, such that the peak convergence might be near the surface rather than a few km aloft. Elevated cyclonic circulation is in fact observed to precede surface spinup during tropical cyclogenesis (Fig. 5.7).

## *4.1 Energy indices of convective potential*

### *4.1.1 CAPE and ICAPE: typical values and sensitivities*

The AMEX soundings used in this section differed relatively little from one another, as is typical of tropical soundings (Betts 1974, Aspliden 1976, Xu and Emanuel 1989). For this reason, individual soundings are expressed as deviations from a reference sounding (Fig. 4.1), the mean of all AMEX Phase II soundings (4 times daily, 13 January to 14 February) from the EMEX ship *Xiang Yang Hong No. 5* at 11°S, 139°E.

Since tropical deep convection is based in the boundary layer, it is traditional to assess the viability of convection on the basis of the buoyancy of unmixed updraft parcels of boundary-layer air. While downdrafts are an important part of MCSs, the bulk of convective energy comes from buoyant updrafts, the *sine qua non* of deep convection. Real updrafts undergo entrainment, but the arbitrary parameters introduced in attempts to quantify it (see *e.g.* Betts 1974) would add more uncertainty and clutter than insight to this discussion.

A useful energetic measure of the viability of convection is convective available potential energy (CAPE, or "positive area" on a thermodynamic chart), defined as the integral over height of the upward (positive) buoyancy acceleration B felt by a parcel rising pseudoadiabatically from its level of free convection (LFC) to its level of neutral buoyancy (LNB):

$$\text{CAPE} = \int_{\text{LFC}}^{\text{LNB}} B\,dz \qquad (4.1.1)$$

CAPE is a parcel property (units J/kg). The integrand and limits of integration, and therefore CAPE, depend only on the parcel's equivalent potential temperature $\theta_e$ (in graphical terms, the moist adiabat along which it ascends), and on the ambient density profile through which it is assumed to rise.

*4.1.1.1 Boundary-layer $\theta_e$.*

Figure 4.2 shows profiles of buoyancy, relative to the ship-mean reference sounding, for parcels with specified values of $\theta_e$, lifted pseudo-adiabatically (liquid water assumed to fall out instantly as it condenses) and reversibly (all liquid water retained, but with its small heat capacity neglected). Aircraft measurements of liquid water in deep convection indicate that nature is closer to the pseudo-adiabatic idealization than to the reversible. Area under the curves is proportional to CAPE in this figure; for reference, the 350, 355, and 360 °K parcels, rising adiabatically, have CAPE values of 260, 1180, and 2370 J/kg, respectively. Inclusion of the neglected latent heat of freezing would increase these values slightly. By comparison, summertime midwestern U.S. values of CAPE "...can be as large as 4500...but generally range between 1500 and 2500." (Weisman and Klemp 1986). Parcels have positive buoyancy, and therefore upward acceleration, throughout the troposphere. If entrainment and drag forces are weak, the altitude of the maximum convective updraft velocities can be quite high (as in EMEX 7, chapter 3). The area to the right of the 340 °K curve in Fig. 4.2 indicates the energy available to accelerate a saturated downdraft with that value of $\theta_e$.

The dependence of $\theta_e$ on parcel temperature and humidity (at 1000 mb) is shown on Fig. 4.3. Using numbers from that figure, the sensitivity of CAPE to some basic parcel properties can be quantified as follows. Writing the functional dependence of CAPE as CAPE(sounding, parcel $\theta_e$(T, RH, p)), where RH is relative humidity, and evaluating derivatives at a typical Australian monsoon boundary-layer value (T = 28 °C, RH = 75%, p = 1000 mb, with $\theta_e$ = 355 °K), yields:

$$\frac{\partial\,\text{CAPE}}{\partial T} = \frac{\partial\,\text{CAPE}}{\partial \theta_e}\cdot\frac{\partial \theta_e}{\partial T}\Bigg]_{\text{RH, p}} \approx \frac{1100\ \text{J/kg}}{5\ °\text{K}}\cdot\frac{5\ °\text{K}}{1\ °\text{C}} \approx \frac{1000\ \text{J/kg}}{1\ °\text{C}} \qquad (4.1.2a)$$

$$\frac{\partial \text{CAPE}}{\partial \text{RH}} = \frac{\partial \text{CAPE}}{\partial \theta_e} \cdot \frac{\partial \theta_e}{\partial \text{RH}} \Bigg]_{T,p} \approx \frac{1100 \text{ J/kg}}{5 \text{ °K}} \cdot \frac{8 \text{ °K}}{10\%} \approx \frac{1000 \text{ J/kg}}{6\%} \qquad (4.1.2b)$$

$$\frac{\partial \text{CAPE}}{\partial p} = \frac{\partial \text{CAPE}}{\partial \theta_e} \cdot \frac{\partial \theta_e}{\partial p} \Bigg]_{T,RH} \approx \frac{1100 \text{ J/kg}}{5 \text{ °K}} \cdot \frac{5 \text{ °K}}{-31 \text{ mb}} \approx \frac{1000 \text{ J/kg}}{-28 \text{ mb}} \qquad (4.1.2c)$$

The large magnitudes of these sensitivities illustrate the basis for Xu and Emanuel's (1989) exhortation that processes affecting subcloud layer moist entropy (or $\theta_e$) be emphasized when evaluating the energy supply of convectively driven tropical circulations. Note that humidity measurement errors by radiosonde (Elliott and Gaffen 1991), dropsonde (Powell 1990b), and even aircraft are quite substantial in terms of CAPE.

Although (4.1.2) are in terms of *convective* available potential energy, they are valid for any circulation system drawing its energy from saturated ascent. One example is Emanuel's (1986) idealized mature hurricane, in which ascent in the eyewall is slantwise neutral (CAPE is zero), owing to the very warm environment there. In that case, the energy goes directly into the cyclone-scale circulation, rather than into the kinetic energy of convective turbulence.

Maximum values of $\theta_e$ observed in the boundary layers feeding into the EMEX convection, as observed by the F27 and Electra aircraft, were 355 to 360 °K. The maximum aircraft-observed value of $\theta_e$ was 364 °K, measured by the F27 at very low altitude on 23 January, during suppressed conditions (Fig. 4.9). Dropwinsondes routinely reported values over 370 °K, but their moisture sensors are known to overestimate (*e.g.* Powell 1990b). In this limited range between the lowest $\theta_e$ capable of positive buoyancy and the highest observed, the linear approximation CAPE = 260 + 211($\theta_e$-350) is quite adequate. With this formula, profiles of $\theta_e$(p) from soundings through the boundary layer can be converted to profiles of CAPE(p).

Figure 4.4 shows a climatology of boundary-layer $\theta_e$ in the *Xiang Yang Hong No. 5* soundings, with $\theta_e$ converted to CAPE using the linearized formula above. Generally, CAPE decreased monotonically with height, reflecting the fact that the subcloud "mixed layer," while well-mixed in terms of potential density (or virtual potential temperature $\theta_v$), is typically not well-mixed in terms of water vapor and $\theta_e$ (Xu and Emanuel 1989). Mean values (curve m) decreased from ~1000 J/kg at the surface to

near 0 at 900 mb, while the mean of the quartile of the soundings with the highest integrated CAPE (curve h) had CAPE values approximately twice as large at all levels. Cold penetrative downdrafts in convection (curve c), and dry subsidence (curve d), led to reduced values of CAPE.

Consider now an integrated CAPE ("ICAPE"), or, in discrete form, the mass-weighted sum of CAPE for all planetary boundary-layer (PBL) parcels (defined as those parcels with positive CAPE) in a sounding:

$$\text{ICAPE} \equiv \sum_{\text{PBL}} \text{CAPE}\,(p)\,\frac{\delta p}{g} \qquad (4.1.3)$$

The units of ICAPE are $Jm^{-2}$, so ICAPE is a property of an area of the atmosphere rather than of an arbitrarily chosen parcel. Boundary-layer convergence increases ICAPE, as each sub-layer in the sum (4.1.3) gets deeper . Note that vertical resolution better than the "standard levels" of 1000 mb, 950 mb, *etc.*, may be needed to evaluate ICAPE accurately.

Fig. 4.5 shows a time series of CAPE and ICAPE at the ship, along with other weather conditions (surface temperature and dewpoint, surface pressure, satellite-observed high cloud top coverage). The surface pressure trace (dashed, top panel) indicates the two cyclone-affected periods near Julian days 20 and 40. Dewpoints hovered at 24-26°C, while surface temperature showed wider swings, highly anticorrelated to the cloudiness indices (bottom panel). The center panel shows smoothed series of CAPE at 1000 mb (plotted '1'), integrated CAPE up to 950 mb (plotted '5'), and ICAPE (line), while dots show the highly scattered individual ICAPE values. A gross tendency for anticorrelation with PHC may be seen, but the relationship is weak.

The comparable figure for Darwin (Fig. 4.6) has weaker and less systematic features in the pressure trace. Again, dewpoint varied less than temperature, which was highest in the cloudless period near day 23. ICAPE was substantially larger in the mean, and peaks in ICAPE did seem to lead the three major periods of cloudiness centered on days 15, 30, and 40. Rutlege *et al.* (1992) have presented in their Fig. 1 seasonal time series for what amounts to an ICAPE measure for Darwin. It bears no apparent relation to Darwin rainfall, although there is some tendency for an anticorrelation with 850 mb zonal wind (indicator of monsoon "active" and "break" periods).

*4.1.1.2 Deep Tropospheric Sounding Variability.*

A consistent, though small, synoptic modulation of CAPE was associated with changes in the deep tropospheric temperature structure. These changes in the CAPE experienced by parcels *with a given value* of $\theta_e$ can also be represented as areas on a buoyancy-height diagram, with virtual temperature deviations (at constant pressure) expressed as buoyancy, relative to the ship-mean reference sounding.

Figure 4.7 shows composite daily-mean virtual temperature perturbations in six categories, determined according to satellite-observed daily percentage high cloudiness (PHC) in the vicinity of each of the five northernmost coastal sounding sites. Category 6, with PHC exceeding 40%, is composed of soundings near named tropical cyclones, plus some Darwin soundings from the *onset* period (Fig. 1.10), while the soundings of category 1 come largely from the *inactive* period (Fig. 1.12). The peak-to-peak composite upper-tropospheric buoyancy variation was approximately 0.1 m $s^{-2}$, corresponding to a virtual temperature variation of 2-3 °C.

Three major features are apparent in Fig. 4.7: First, the deep upper tropospheric warming from 5-14 km or so makes CAPE, for a given parcel $\theta_e$, *decrease* by 280 J/kg (the area between curves 1 and 6) during convectively active periods. Second, the curves cross at 14 km, indicating cooling aloft during active convective periods. This may reflect a higher mean tropopause, or possibly the mesoscale cold lenses above individual tropical MCSs, as reported by Johnson and Kriete (1982, their Fig. 3a) and analytically reproduced by Nicholls *et al.* (1991, their Fig. 6d). Third, the boundary layer tends to be cooler in the mean during active (cloudy) periods, owing to the large area covered by disturbed (cold) boundary-layer air, typically 30% in GATE for example (Gaynor and Ropelewski 1979). This observation does not necessarily imply that the boundary-layer air *feeding into the deep convection* is cooler during more active periods.

In addition, cooler air does not necessarily have lower $\theta_e$. The disturbed (cold) boundary layer includes ambient subcloud-layer air cooled by the evaporation of light rain (with increased humidity but unchanged $\theta_e$), as well as the low-$\theta_e$ cold air from downdrafts in heavier rain areas (Barnes and Garstang 1982). In fact, the boundary-layer $\theta_e$ profiles of the 6 composite mean soundings are essentially indistinguishable, except for the higher $\theta_e$ during the supressed conditions of category 1. This increased $\theta_e$ and and ICAPE during suppressed conditions apparently arises from an accumulation of

moisture below an inversion and very dry layer aloft. When MCSs do form in such "break monsoon" conditions, they are vigorous and highly electrified storms. One is called the "Arnhem express," a frequently observed squall line which starts in the afternoon over the north-south oriented Arnhem Land escarpment southeast of Darwin, travels rapidly westward with its lights flashing (lighning) and arrives in the Darwin area near or after midnight.

It is possible to compare values of ICAPE with the kinetic energy content of the tropospheric monsoon winds. Profiles of kinetic energy for the six composite categories are shown in Fig. 4.7c. Only the cloudiest category (hurricane-associated) has a kinetic energy "mixing ratio" exceeding 100 J/kg at low levels, while a second peak of kinetic energy near the tropopause (a deep layer in height, but not so deep in the pressure coordinate) can reach 200 J/kg. A typical mass-integrated kinetic energy is thus ~ 75 J/kg x $10^5$ Pa / g = $7.5 \times 10^5$ $Jm^{-2}$, roughly four times the typical ICAPE at Darwin and 7-8 times that at the ship.

### *4.1.2 Convective Inhibition*

In order for deep convection to occur, high-$\theta_e$ parcels must reach their LFC. The negative buoyancy experienced by such a parcel below its LFC may be integrated over height, by analogy to (4.1.1), to yield a measure of the energy needed to trigger convection and thereby liberate the CAPE. This energy is called convective inhibition (CIN):

$$CIN = \int_{Z_o}^{LFC} B\,dz \qquad (4.1.4)$$

CIN is more difficult to quantify than CAPE, because it is not clear what to use for $Z_o$. Ultimately, what is needed is a convection model: what air "parcels" from what levels are involved in the initiation of convection?

Fig. 4.8 shows time series data of CIN from the ship and Darwin soundings, using as an "operational definition" the value of CIN reported by the NCAR sounding analysis package. The program takes as a parcel a mixture of all the air below a user-specified height (500 m), and returns that parcel's CAPE, CIN, and other indices. In order to isolate the effects of the overlying stratification from the wide swings in low-

level $\theta_e$, a standard PBL (from the ship mean sounding, Fig. 4.1) has been inserted in each sounding up to the 500 m level. It should be noted at the outset that the scale for the CIN values is in the tens of J/kg, just a few percent of the CAPE.

The resulting time series fron the ship shows that CIN was very small during active periods, but that it was much larger in magnitude during the suppressed period around days 22-28. Some inhibition was also evident during the slight break in cold cloudiness near day 41. The Darwin CIN also tended to have very small values during the cloudy periods, with some significant exceptions, such as the strong inhibition near day 40. CIN for the actual soundings, including their measured boundary layers, is also shown on Fig. 4.8 (smoothed dashed line). It differs from the solid curve in cases when the Darwin boundary layer differed from the ship mean boundary layer.

Apparently neither of these energetic indices (ICAPE or CIN) is a capable of explaining much of the day-to-day or week-to-week variability in convective cloudiness. The scatter of data points around the smoothed curves makes clear that these indices vary a lot on short time scales and/or small spatial scales. The problem is ultimately one of sampling. Pre-scheduled, 6-hourly sounding releases whose actual time of release is not accurately known simply cannot be taken as indicators of the boundary layer air which formed the observed convection. As a result, any large-scale controls on convection via CAPE or CIN are obscured by large sampling uncertainties. For this reason, they will be discussed in a qualitative way.

### *4.2 Forcing, triggering and feedbacks: controls on the incidence of convection within the monsoon*

Betts (1974) found that the Venezuelan troposphere was slightly cooler during active convective periods, and interpreted the results to mean that convection acted in response to large-scale uplift destabilizing the lapse rate, consistent with the ideas underlying the Arakawa and Schubert (1974) cumulus parameterization scheme. But Fig. 4.7 indicates that more deep convection occurred when the troposphere was warmer, and therefore CAPE (for a given parcel $\theta_e$) was lower. A similar condition characterizes easterly waves over the oceans (Reed and Recker 1971, Thompson et al. 1979). Betts's land-based results remain the anomaly. In general, although the vertical velocity in synoptic-scale areas containing convection has an upward *mean* value through the whole troposphere, there is no evidence that convection is caused by *large-scale* deep upward

motions destabilizing the troposphere. [Note, however, that Cohen and Frank (1989) found, in a 2-D model with parameterized convection, that the domain-mean tropospheric lapse rate was slightly warmer aloft during runs in which they imposed greater large-scale deep lifting.]

Instead, it seems that the dynamical processes which modulate convection are those at low levels, including the *frequency* of small-scale intense lifting events necessary to trigger convection, as well as widespread mean mass convergence. Low-level mean mass convergence favors convection in two ways: it increases the depth of the high-$\theta_e$ layer near the surface, thereby increasing ICAPE, and it causes adiabatic cooling of the ambient air, which lowers the LFC of any and all ascending parcels, thereby decreasing the CIN. Which of these mechanisms is more important over the warm tropical ocean is unknown.

Many of the low-level processes modulating convection act as positive feedbacks (detailed below). In other words, convection is favored by previous convection, as long as the lower boundary conditions remain favorable. The sharpness of monsoon onset, and the substantial interannual variability in its date (Holland 1986) support the notion that the monsoon is an unstable positive-feedback process, waiting for a trigger, once the seasonal conditions are ripe (*e.g.* the warm water is in place). Disturbances which may trigger monsoon onset include the intraseasonal (40-50 day) oscillation (Fig. 4.17; Hendon and Liebmann 1990) and midlatitude disturbances (Fig. 4.11; Keenan and Brody 1988). Active sub-periods within monsoon season also tend to persist once they begin.

The high degree of overlap and interconnectedness of monsoon MCSs can be objectively demonstrated from infrared (IR) satellite data. Consider the following definition of a "cloud cluster," from Williams and Houze (1987). A "cluster element" is a spatially connected area (at 10 km resolution), of at least moderate size (>5000 $km^2$), with blackbody temperature colder than -65 °C (Williams and Houze used -60 °C) in an IR satellite image. A "cloud cluster" is a set of temporally connected cluster elements, where two cluster elements are said to be part of the same cloud cluster if their spatial overlap from one image to the next (3 h intervals) exceeds half the size of either cluster element or 10000 $km^2$. By the above definition, most of the monsoon convection from 14 to 21 January 1987, including both cyclones Connie and Irma, constituted *a single giant cloud cluster* (the plotted "177" on Fig. 1.5) Other Australian monsoon superclusters extended from 31 January to 4 February and from 5 to 9 February (Table 1

of Mapes 1992). Monsoon convection, once triggered, lasted until hurricanes formed and eventually died of the usual causes (landfall or poleward drift).

What are the mechanisms of positive feedback? An obvious one is that convective downdrafts form a surface cold pool, which triggers further convection by lifting adjacent high-$\theta_e$ boundary-layer air. As emphasized by Houze and Betts (1981), this mechanism is so efficient that MCSs, rather than individual cumulonimbus clouds, are the basic unit of tropical precipitation. While the cold air supresses deep convection locally, surfaces fluxes restore the boundary layer to a state of convective readiness in about half a day (Houze 1977, Zipser 1977, Fitzjarrald and Garstang 1981, Nicholls and Johnson 1984, Powell 1990b), so twice-daily overturning could theoretically be sustained even in the absence of horizontal advection, as long as the oceanic heat source lasts. Apparently, triggering frequency increases with amount of convection, and therefore tends to be a positive feedback.

Other feedback mechanims, detailed below, can be divided into two types: *thermodynamic* and *dynamical.*

One *thermodynamic* feedback is the humidification of the deep troposphere by initial convection, which can create more favorable conditions for the growth of later convective cells, as found by Dudhia and Moncrieff (1987) in a modeling study of a GATE MCS. A condition unfavorable for convection in the composite category 1 (suppressed) mean sounding is low humidity aloft. This drying aloft (accompanied by temperature inversions) is illustrated in Fig. 4.9. An upward displacement of ~500 m amplitude would be necessary to increase mid-tropospheric category 1 mean humidity to category 2 values. A forced (adiabatic) displacement of this magnitude would cause an absurd 5 °C temperature decrease. Hence, humidification is probably largely accomplished by horizontal advection and by deep convection.

Another *thermodynamic* feedback is the wind-evaporation feedback, in which enhanced surface moisture fluxes result from the surface winds associated with convectively-driven circulations. Heat flux from the ocean is dominated by latent heat flux, which is primarily sensitive to wind speed (*e.g.* Aspliden 1977). Wind-evaporation feedback is well-known in the case of hurricanes, has been shown to be of some importance to the intraseasonal oscillation (Emanuel 1987, Neelin *et al.* 1987), and may have global significance. For example, in a zonally symmetric model, the same amount

of atmospheric heating causes much greater globally-integrated surface winds if it is a few degrees off the equator than if it is on the equator (Lindzen and Hou 1988).

An additional *thermodynamic* feedback important in hurricanes is the pressure-evaporation feedback, whereby surface fluxes are enhanced owing to the pressure drop experienced by boundary-layer air as they spiraling into the central low (Emanuel 1986). *Convective* available potential energy (CAPE), however, tends to be lower in environments with lower surface pressure. For example, the 140 J/kg CAPE increase (at constant T and RH) indicated by Eq. (4.1.2c), for the 4 mb surface pressure difference between PHC composite categories 1 and 6 (see Fig. 5.5), is just half the 280 J/kg CAPE decrease associated with the hypsometrically related upper-tropospheric warming (the area between curves 1 and 6 in Fig. 4.7a). At the extreme extent of this pressure feedback, the sloping ascent of very high-$\theta_e$ air in hurricane eyewalls may be nearly convectively neutral (CAPE = 0), as in Emanuel's (1986) theory, with the available potential energy (APE) from the saturated ascent of high-$\theta_e$ boundary-layer air going directly into the cyclone-scale circulation, rather than into convective-scale turbulence. As a result, hurricanes can persist even in environments with no ambient CAPE (Emanuel 1986). In that limit, the saturated ascent is not really convection at all, but rather is just the vertical branch of the secondary circulation of the hurricane.

Hurricane secondary circulation is a well-known example of a *dynamical* positive feedback. Any surface pressure minimum is necessarily surrounded by a divergent pressure gradient, which causes convergence of the frictional cross-isobaric component of flow in the boundary layer. This convergence leads to convection, which further strengthens the cyclone and its surface pressure field, and so on. This positive-feedback mechanism was denoted CISK (Conditional Instability of the Second Kind) by Charney and Eliassen (1964).

An inviscid, nonrotating version of CISK also exists for heating with a profile shaped like that observed in Australian monsoon MCSs (Mapes 1992). This fact may seem surprising, as convection has often been assumed to supress additional convection in its vicinity by means of its "compensating subsidence" field. But the environmental state induced by MCS heating in fact consists, at low levels, of a large remote area in which "overcompensating subsidence" has depressed material surfaces, and a smaller region near the heat source in which inviscid ascent has lifted material surfaces above their undisturbed levels (Fig. 4.10). Convection is therefore favored in the region near

previous convection, so this mechanism constitutes another *dynamical* feedback, denoted "inviscid CISK" by Mapes (1992).

Observations suggest that all of these positive feedbacks — increased cold pool frequency, tropospheric moistening, wind-enhanced evaporation, pressure-enhanced evaporation in the cyclone cores, and dynamical CISK — are active in the Australian monsoon. An implication of this is that even bulk measures of the monsoon, like seasonal precipitation amount, may depend, as monsoon onset timing certainly does, on hard-to-predict triggering disturbances.

## *4.3 Observations of larger-scale forcings in the monsoon region*

The discussion of large-scale forcings and feedbacks above was completely unconstrained by observations, because as seen in section 4.1, evidence of large-scale forcing in the soundings is obscured by other sources of variation. In this section a slightly different tack is taken: known, well-observed large-scale forcings are examined. Section 4.3.1 examines two midlatitude upper-tropospheric troughs which intruded into tropical northern Australia. One of them coincided (coincidentally?) with monsoon onset, while the other, a cutoff low, drifted lazily through the sounding array during the *inactive* period and did not set off any convection. The thermal structure of this latter cutoff low illustrates the thermal structure of PV anomalies generally, and leads into section 4.3.2, on the possible effects of midlevel PV cyclones. The eastward-moving intraseasonal oscillation, of which the Australian monsoon was a part, is examined briefly in section 4.3.3.

### *4.3.1 Upper-tropospheric troughs in tropical north Australia*

Upper-tropospheric westerlies accompanying the monsoon onset (14-16 January) are evident in the zonal wind time-height section Fig. 1.9. The ECMWF-analyzed 200 mb synoptic charts for this period are shown in Fig. 4.11. On 14 January, a trough along 130 °E divided the north Australian anticyclone, which was more typically centered over the Australian continent (Fig. 1.8). The following day, this trough had apparently pushed the anticyclone center north over the sea, bringing the westerly winds seen at the northern Australian coastal stations in Fig. 1.9. By this time, extensive deep convection was underway along the coast, and especially in the Bonaparte Gulf (Fig. 1.10b).

It is difficult to quantify the impact of this upper-tropospheric trough on the monsoon onset process. But 200 mb westerlies at Darwin were not observed at any other time in the AMEX sounding data set. Keenan and Brody (1988) found a similar association between midlatitude troughs and monsoon onset. It is not difficult to imagine that quasi-geostrophic lifting could set off a day or two of deep convection, enough to initiate the cycle of monsoon feedbacks.

An interesting counterpoint to the "onset trough" just described is an upper-tropospheric cutoff low which drifted through the Gulf of Carpentaria during the *inactive* period. This little upper cyclone is readily apparent in both wind fields and temperature soundings, but appears in satellite imagery only as a delicate curved cirrus streak; it did not trigger any deep convection. Wind charts at 300 mb (Fig. 4.12) show the history of this feature, as a stretched trough on 21 January, and a cutoff low by 22 January, drifting across north Australia on 23-24 January. Soundings from Thursday Island (station indicated on Fig. 4.12) indicate the consistent wind and thermal structure of this isolated potential vorticity (PV) anomaly (Fig. 4.13). The meridional wind component at 200 mb switched from +20 to -20 m/s between 23 and 24 January. A cold lens below the wind anomaly, and warm lens above, were hypsometrically related to low geopotential heights at the level of maximum cyclonic circulation.

"PV thinking" (*e.g.* Hoskins *et al.* 1985) provides a way of understanding the vertical motions which such a feature would induce in its environment via quasi-balanced dynamics. The PV is concentrated at the level of the circulation anomaly and stratification anomaly, near 200 mb. The cold air at, say, 400 mb is simply the dynamical response of the column to the presence of the overlying PV anomaly. As 200 mb flow advects the (conserved) PV, columns of air over which it drifts adjust, via adiabatic vertical motions, to create the hypsometrically required cold lens at 300-400 mb. This case makes it clear that adiabatic ascent and cooling at those levels does not set off deep convection.

The "Rossby depth" through which a PV anomaly affects its underlying column is related to the horizontal scale L of the PV anomaly by H~fL/N [see (33) of Hoskins *et al.* 1985]. This relation is simply a rearrangement of the relationship of Rossby deformation radius to the depth of a heat source, as discussed in Chapter 2. For PV vortices at large Rossby number (fL small), this Rossby depth H is small, such that small isolated PV anomalies do not affect their underlying and overlying columns very much (Raymond 1992). Hence the shallow depth affected by this little cutoff low, and its

consequent inability to set off any PBL-based deep convection, were consequences of its small *horizontal* scale and the low latitude at which it was observed.

### *4.3.2 A cold lens at 600 mb: snow melting or a midlevel cyclone?*

Temperature perturbations were commonly observed at low levels. As shown in Fig. 4.7b, there was a substantially larger temperature variation below the melting level than above it. This fact suggests a mesoscale, microphysical source for this temperature variation. Such local features obscure what evidence there may be for cold lenses underlying midlevel cyclonic PV anomalies. But it is worth examining some data, even if the results are ambiguous. Daily-mean soundings at Gove for the four days Jan 31 to Feb 4 are shown in Fig. 4.14, expressed as deviations from the ship mean reference sounding (Fig. 4.1). The layer from 700 to 500 mb was anomalously cool. All of the dropsondes from EMEX flights 9 and 10, conducted in the same vicinity during this period, show a similar pronounced cooling below ~5 km. Many of the dropsondes did not record the low-level warming also seen in Fig. 4.14, especially at the hot land stations.

The mean of the 16 Gove soundings (Fig. 4.15) makes clear that the low-level warm layer was also unsaturated. At first glance this cold-above-warm structure appears to be the familiar mesoscale downdraft observation of cool temperatures near the melting level, overlying the warm dry "onion shaped" sounding at low levels (Zipser 1977). Persistent convection, including plenty of stratiform precipitation, was occurring in the vicinity of Gove during this *long zonal fetch* period (Fig. 1.14). But the strength and persistence of the midlevel cool layer is uncanny, in light of the rest of the AMEX/EMEX sounding and dropwinsonde data set. There is some evidence that balanced rotational dynamics were at work. And of course there is *a priori* reason to expect cyclonic circulations to spin up in the convergent flow just above the strong cooling at the melting level (see *e.g.* the mesoscale vortex in Fig. 3.27-3.28).

Fig. 4.16 shows ECMWF analyses of the 700-500 mb thickness field and the wind difference ($U_{500}$-$U_{700}$) vectors for 31 January to 4 February 1987. The cool layer seen in Fig. 4.14 is apparent as a thickness minimum in the Gulf of Carpentaria in the 31 Jan and the 1 and 2 Feb frames, associated with a barely discernable cyclonic pattern of wind difference vectors, in qualitative accord with thermal wind balance considerations. Vorticity profiles calculated from the Gulf of Carpentaria rawinsonde array indicate a

pronounced cyclonic circulation with its peak at 4-6 km altitude on 31 Jan and 1 Feb, though not later.

On 3 and 4 Feb, a persistent cold lens strikingly similar to that in Fig. 4.14 was simultaneously observed at the dry inland stations of Burketown, Tennant Creek, and Mt. Isa (Fig. 4.14bcd), at which no convection was occurring. These stationss are indicated on Fig. 4.16e as heavy dots, and the low thickness anomaly in that panel is clearly associated with a poorly resolved cyclonic thermal wind feature. Obviously, this is at the resolution limits of these data. But it is worth making the point that an elevated cyclonic circulation tends to induce a cool lens of air below it, and that such a dynamically induced low-level cooling of a degree or two could be significant to the development of deep convection. Perhaps such a rotational balance mechanism underlies the observations that tropical cyclogenesis is preceded by elevated cyclonic circulation (Fig. 5.7).

### *4.3.3 The intraseasonal oscillation*

It is difficult to deny the the existence of a very large scale eastward-propagating intraseasonal variation (ISV), as shown in Fig. 4.17, a time-longitude plot of GMS-observed CE's (connected areas with infrared temperature < 208K). Numerous other 1986-7 time-longitude plots, of every conceivable variable, have been presented in Hendon *et al.* (1989). The mechanism of this intraseasonal wave is thought to be a CISK-like interaction between convection and Kelvin waves of at least two different vertical wavelengths (Chang and Lim 1988). Note, however, that the *inactive* period in the Australian monsoon appears as a real break in the ISV: no other convection stepped in to fill the gap when the monsoon cyclones died at landfall and left suppressed (no convection) conditions for several days.

The relatively loose structure of the ISV means that ISV modulation of monsoon onset (Hendon and Liebmann 1990) is not inconsistent with the idea that exceptionally strong midlatitude troughs also modulate monsoon onset (Keenan and Brody 1988). Once the right seasonal (SST) and intraseasonal conditions are right, it still takes a more intense and localized midlatitude trough to administer the *coup de grace* and actually set off the monsoon. Unfortunately, the AMEX soundings are not adequate to evaluate the thermodynamic differences between the enhanced and suppressed parts of the ISV. This

difference is a question ripe for the answering with a longer time series of decent tropical soundings.

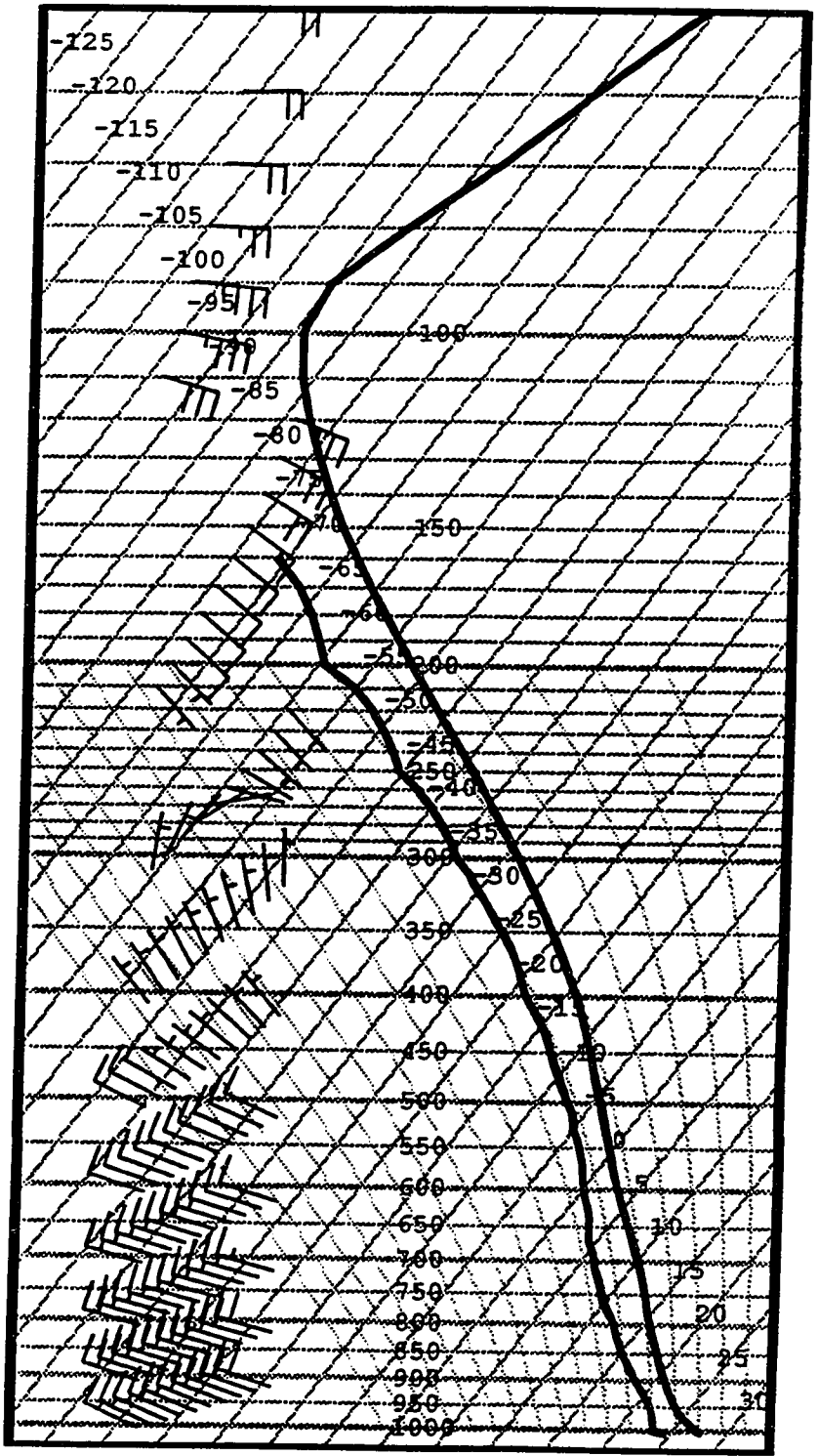


Fig. 4.1 : Ship mean sounding. Mean of all AMEX Phase II (4 per day, 13 January - 15 February 1987) soundings from the Xiang Yang Hong No. 5 at 11 °S, 139.5 °E. Skew-T, log-p format.

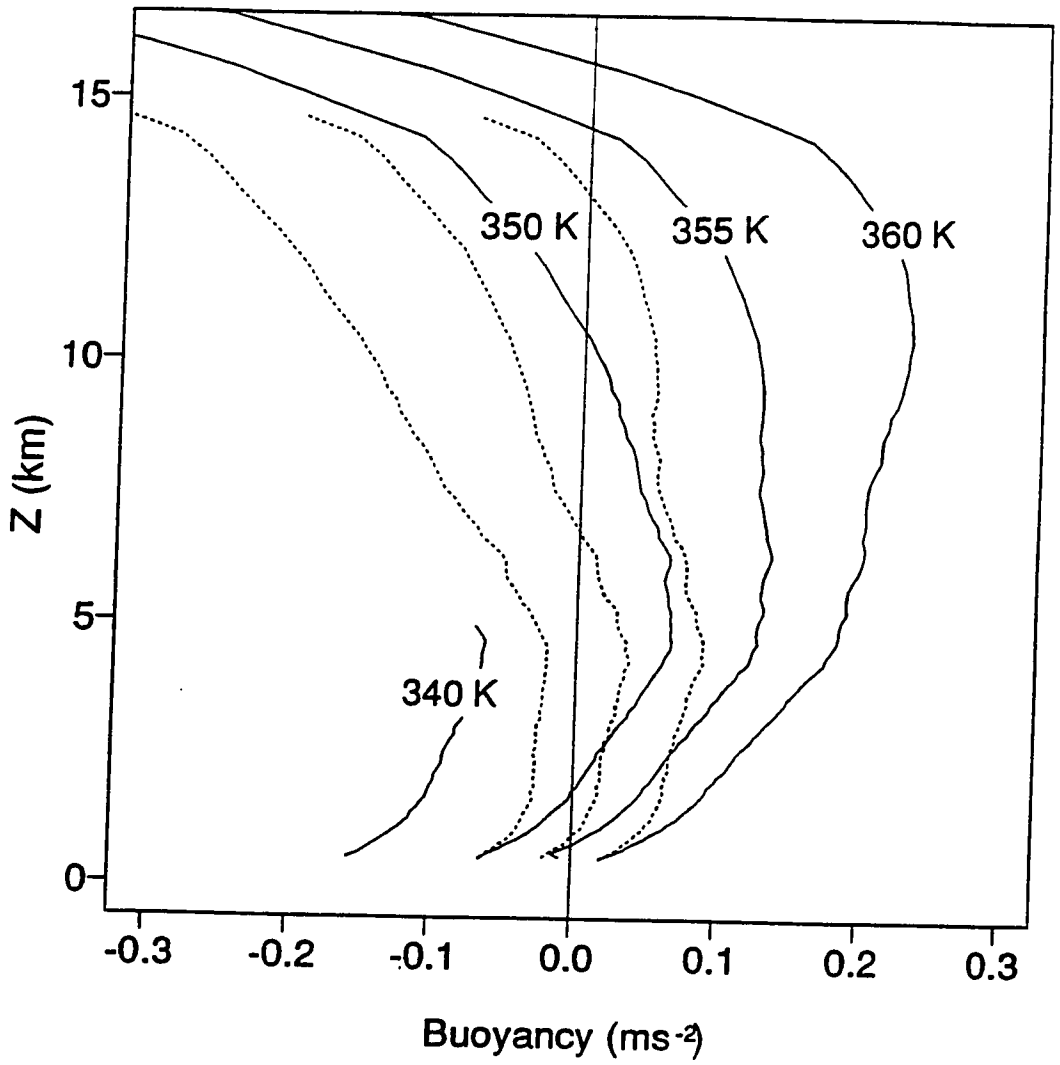


Fig. 4.2 : Buoyancy vs. height for saturated parcels with the indicated values of $\theta_e$, relative to the ship mean sounding (Fig. 4.1). Solid lines: pseudo-adiabatic ascent, dashed lines: reversible ascent. CAPE is the area under the curves.

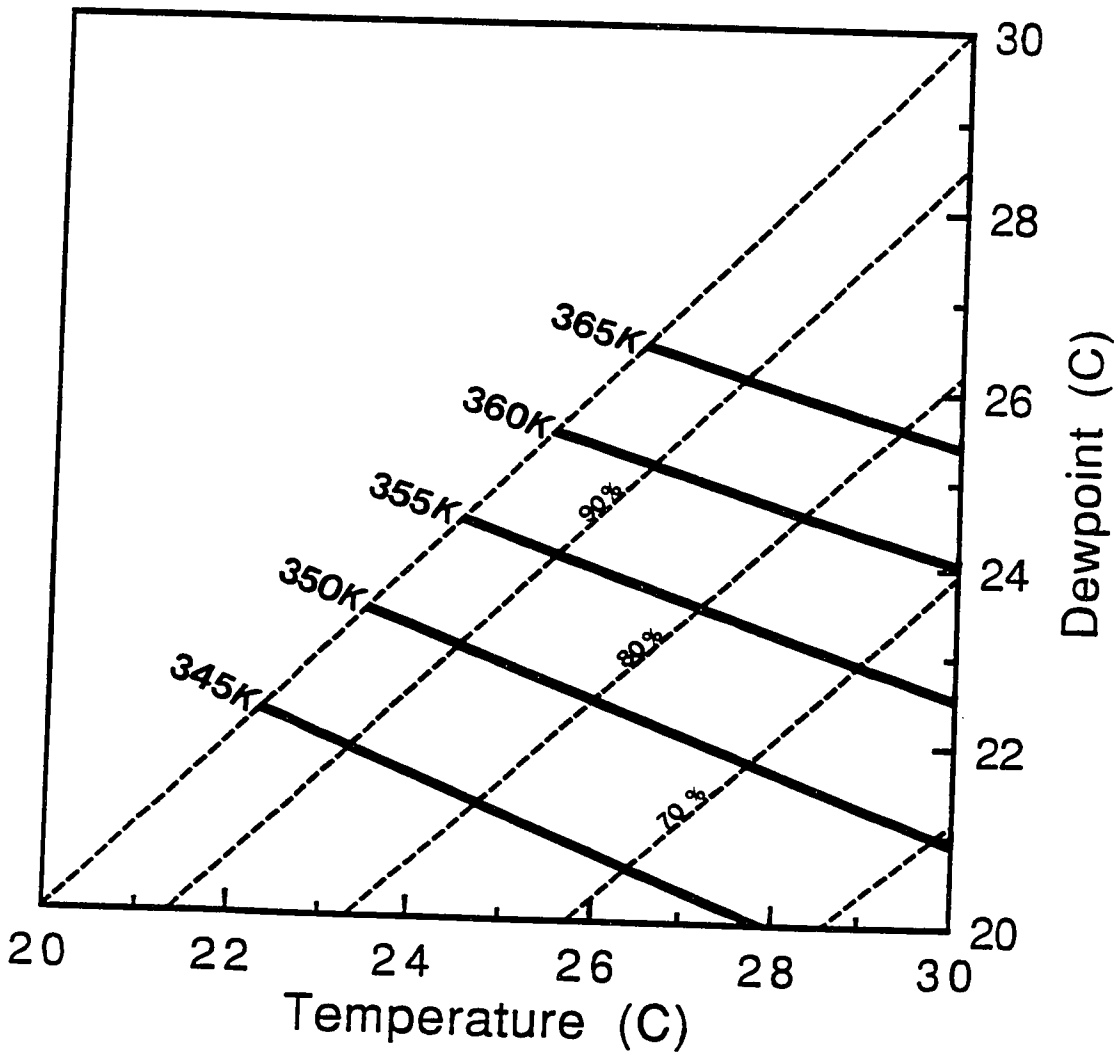


Fig. 4.3 : Equivalent potential temperature $\theta_e$ (solid) and relative humidity (dashed) as a function of temperature and dewpoint at 1000 mb.

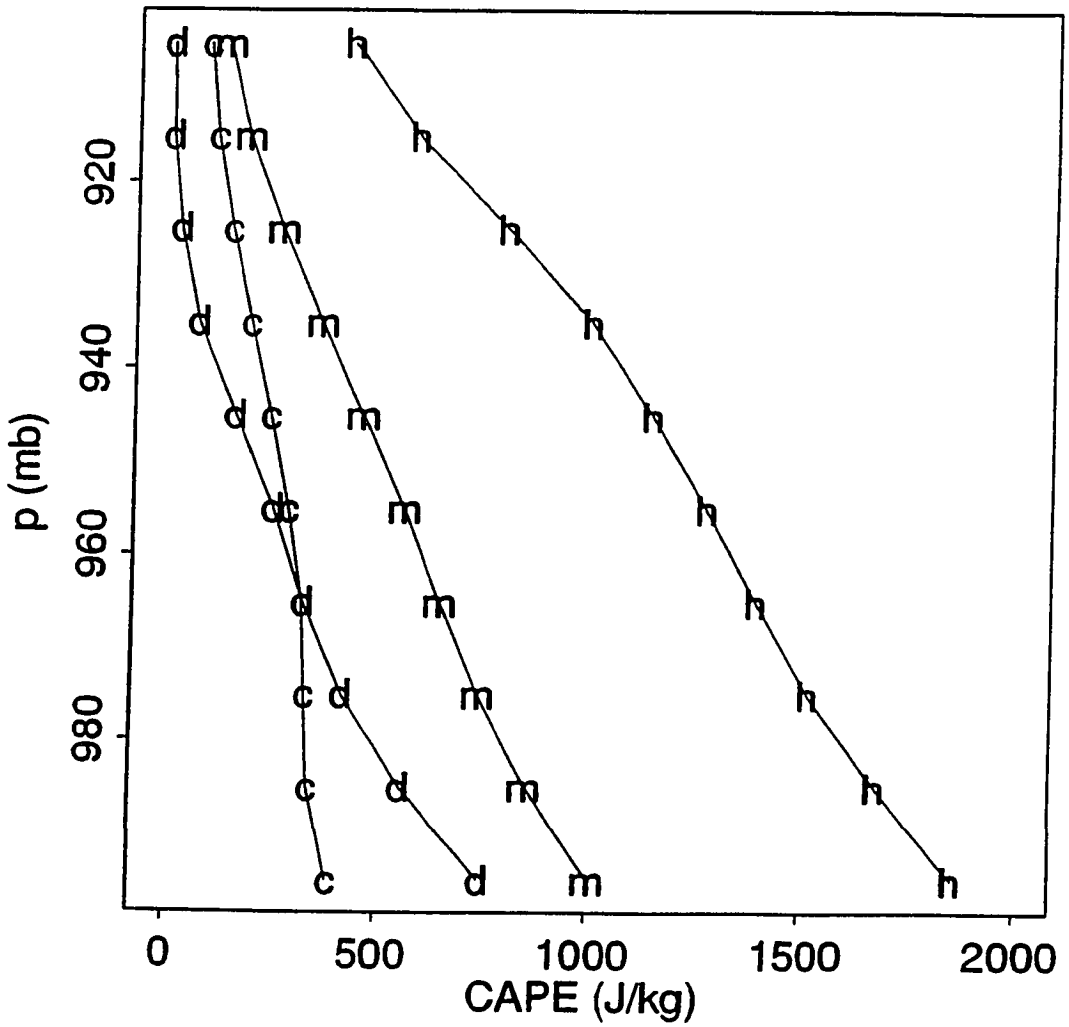


Fig. 4.4 : CAPE as a function of pressure in the boundary layer, from soundings at the ship (11°S, 139°E). The curves represent mean soundings: m, the mean of all 130 soundings; h, the mean of the quartile of the soundings with the greatest integrated CAPE; d, the mean of the quartile with the greatest dewpoint depression at 920 mb; c, the mean of the quartile with the lowest surface air temperature (Ts<26.8 °C).

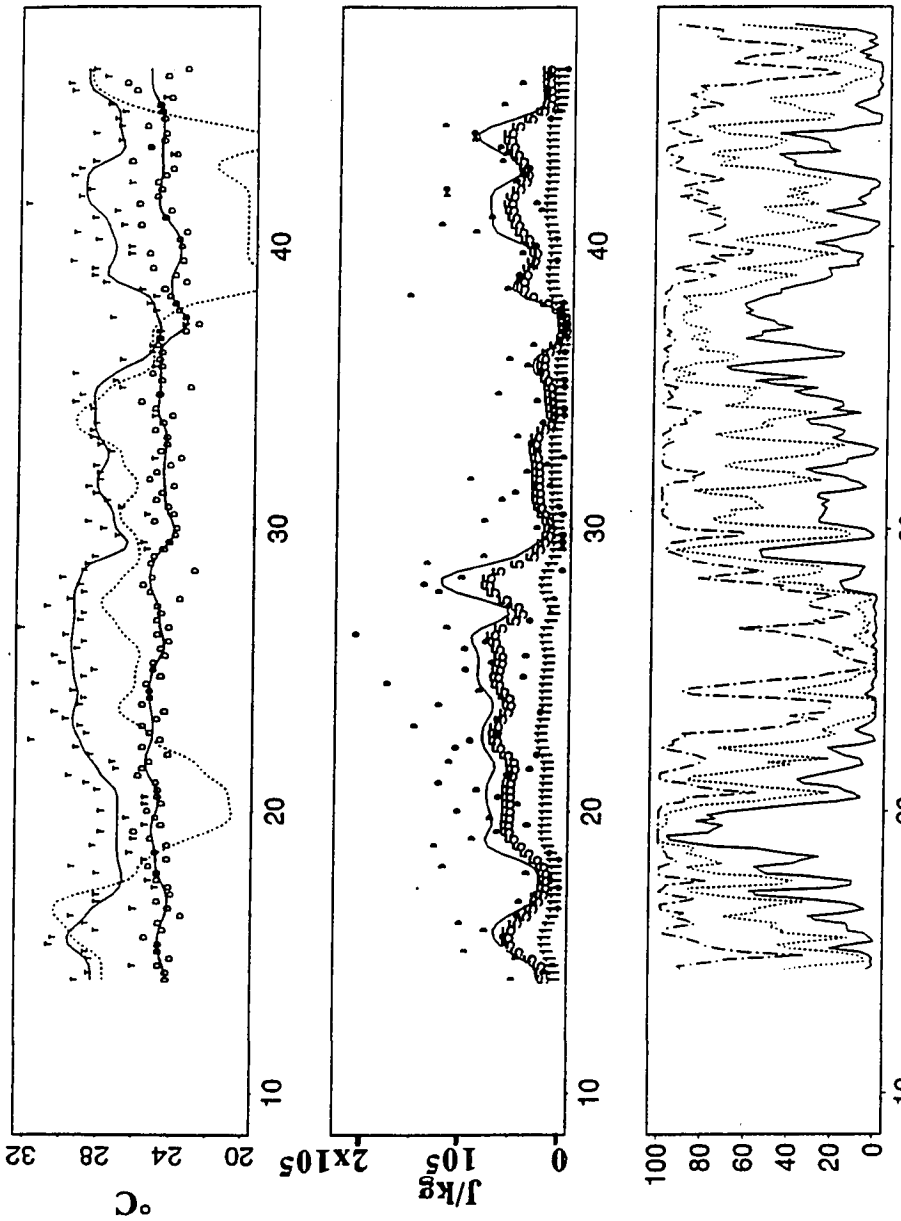


Fig. 4.5 : Ship CAPE and cloudiness time series (vs. Julian day). Upper panel: Temperature and dewpoint ("T," "D" and smoothed solid lines, scale at left), and surface pressure (dotted, scale 1003-1010 mb). Middle panel: Smoothed CAPE at 1000 mb ("1"), CAPE integrated from 1000-950 mb ("5"), and ICAPE (solid line), and instantaneous ICAPE (dots). Lower panel: Percent High Cloudiness (PHC) in a 400x400 km box centered on the station, with IR temperature thresholds 218 (solid), 243 (dotted), 273 (dashed).

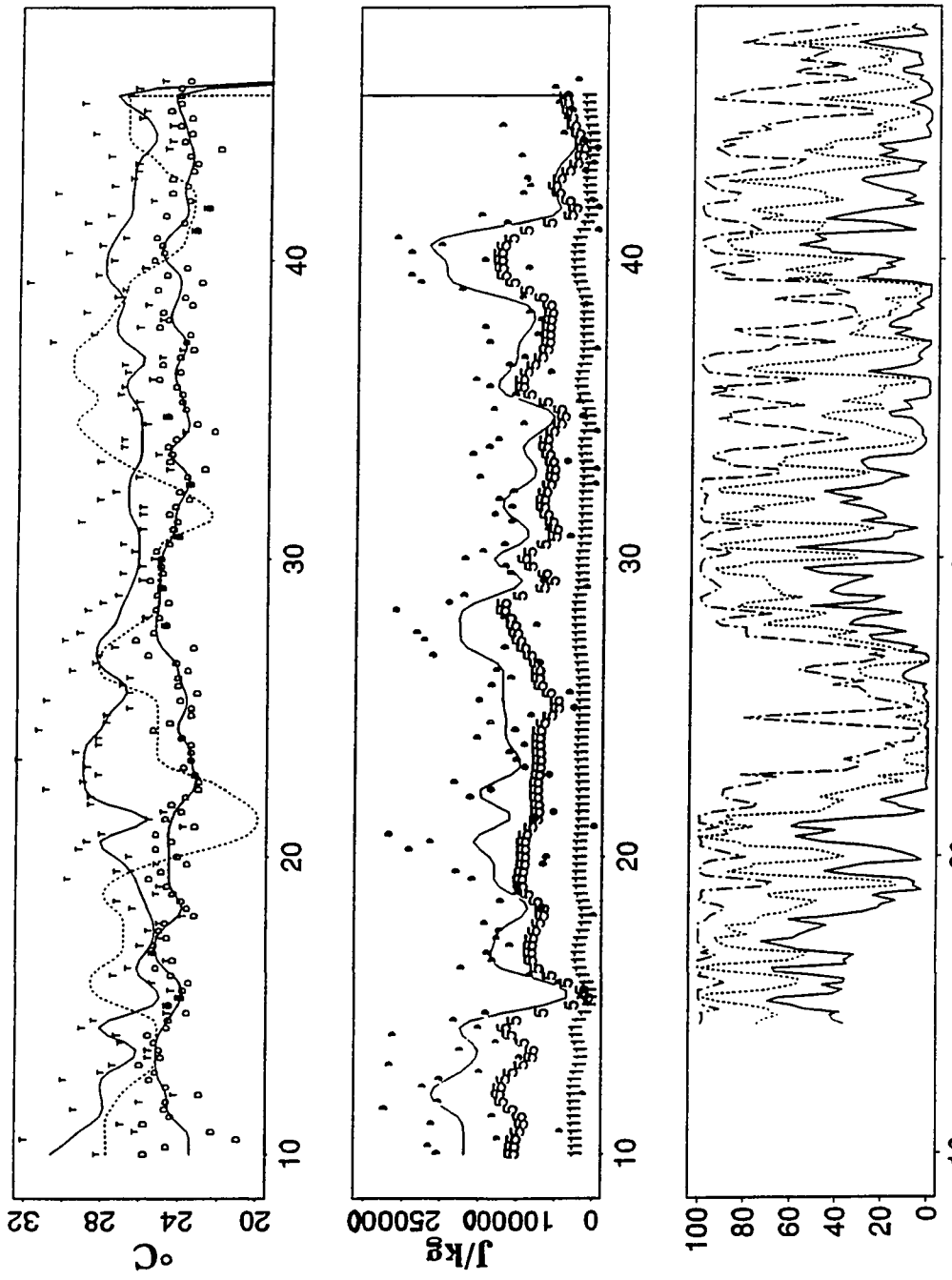


Fig. 4.6 : Darwin CAPE and cloudiness. As in Fig. 4.5, except pressure scale is 1000-1007 mb.

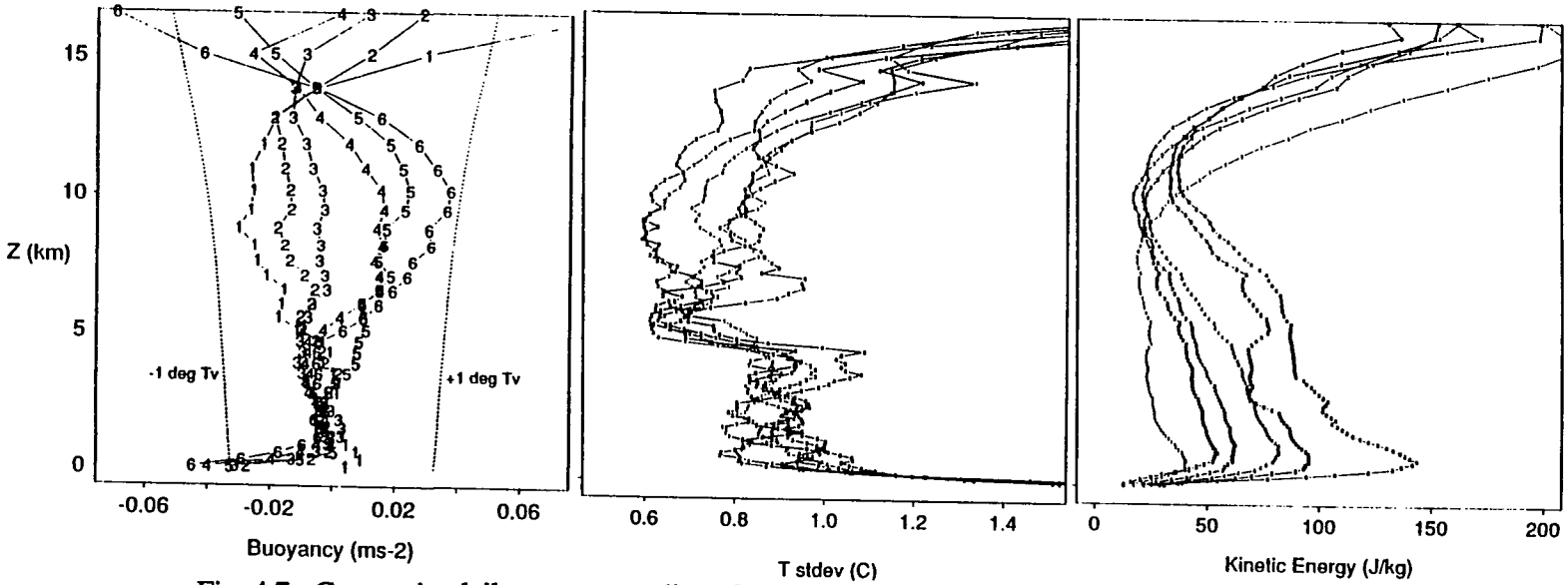


Fig. 4.7 : Composite daily-mean soundings from the 5 AMEX sites north of 15 °S. The categories, defined by daily PHC ($T_{IR}$ < -55 °C) in square areas 400x400 km centered on the sounding sites (number of daily-mean soundings in parentheses), are: category 1: 0-5% (29); 2: 5-10% (29); 3: 10-20% (38); 4: 20-30% (29); 5: 30-40% (11); 6: >40% (18). a) Buoyancy, relative to the ship mean sounding. b) Standard deviation of temperature at each level. c) Wind kinetic energy (from individual, not daily-mean, soundings).

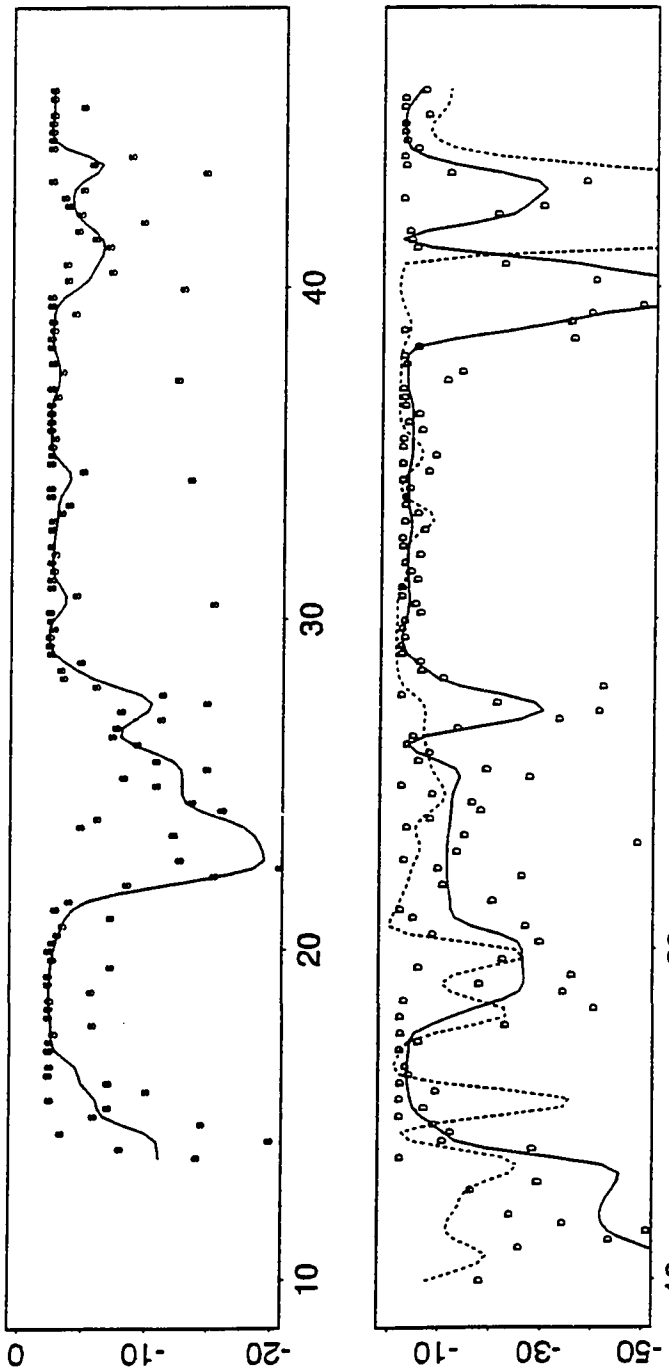


Fig. 4.8 : Convective inhibition (J/kg) in ship and Darwin soundings, with the ship mean boundary layer inserted into the lowest 500 m of each sounding. Dashed line is smoothed CIN for the actual soundings, including boundary layer, at Darwin.

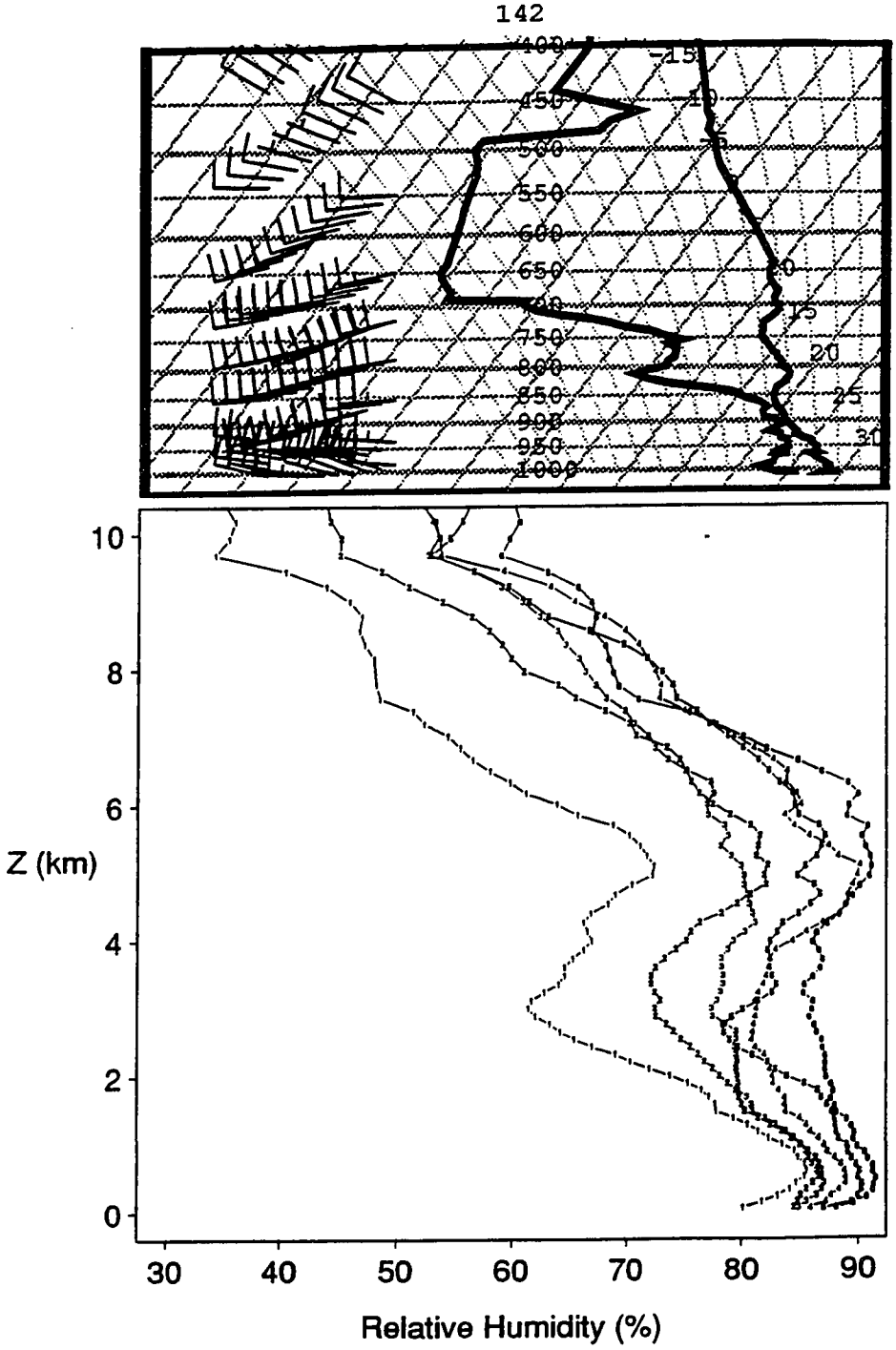


Fig. 4.9 : Humidity variations and temperature inversions. Upper: a skew-T sounding during suppressed conditions, constructed from F27 aircraft data (1000 to 690 mb) and the Darwin sounding at 23 GMT 22 January (690 to 400 mb). Lower: composite profiles of relative humidity for the 6 composite categories in Fig. 4.7.

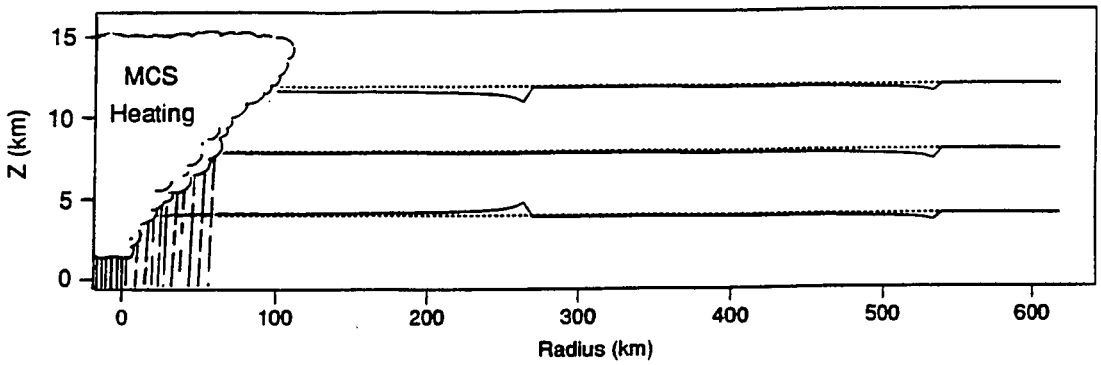


Fig. 4.10 : Linear response of a stratified fluid to a point heat source, consisting of two vertical modes, scaled such that the divergent wind $U_{max}$ = 5 m/s at a radius of 100 km. Discontinuities result from the artifice of all the heating at a point. The positions of three material surfaces (solid), initially horizontal (dashed), a time $\tau$ = 3h after commencement of heating. From Fig. 4 of Mapes (1992).

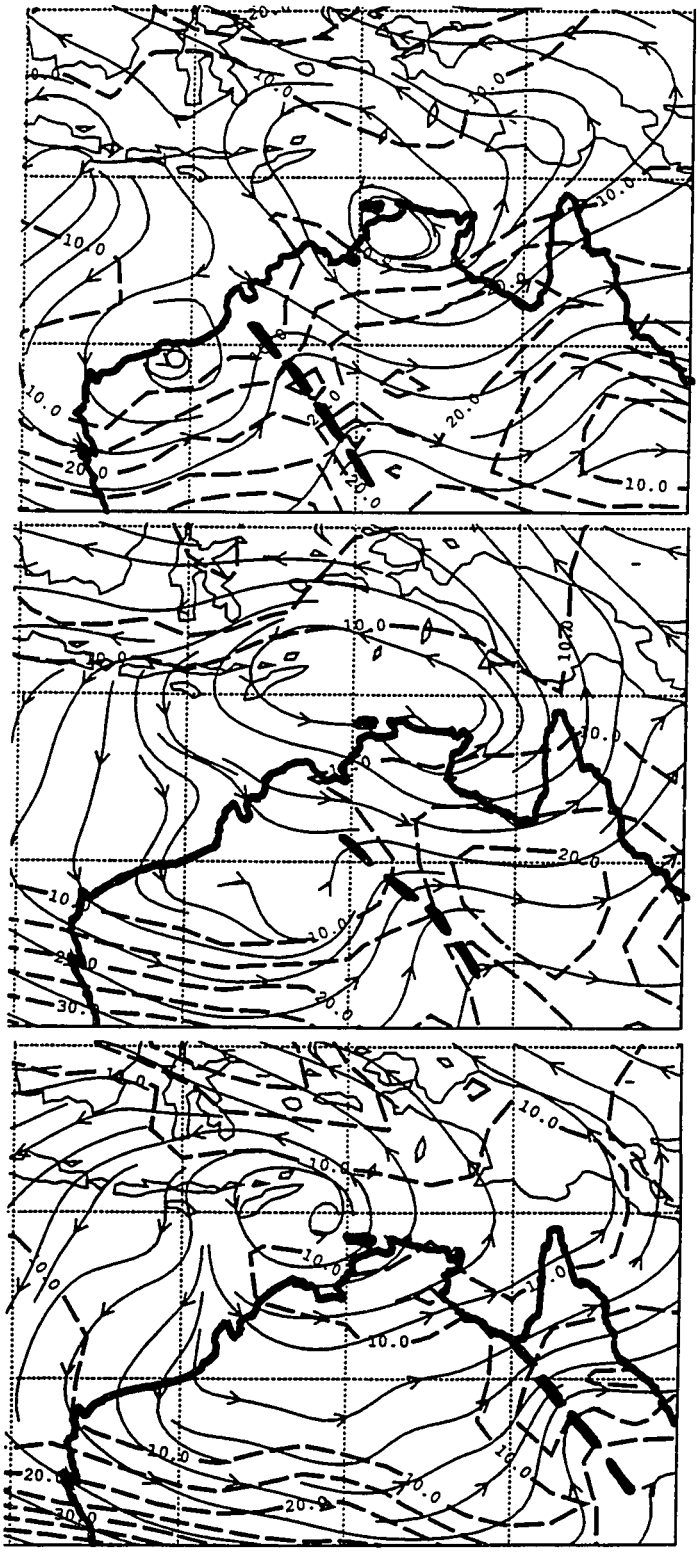

Fig. 4.11 : Streamlines and isotachs at 200 mb 14-16 January 1987, ECMWF analyses.

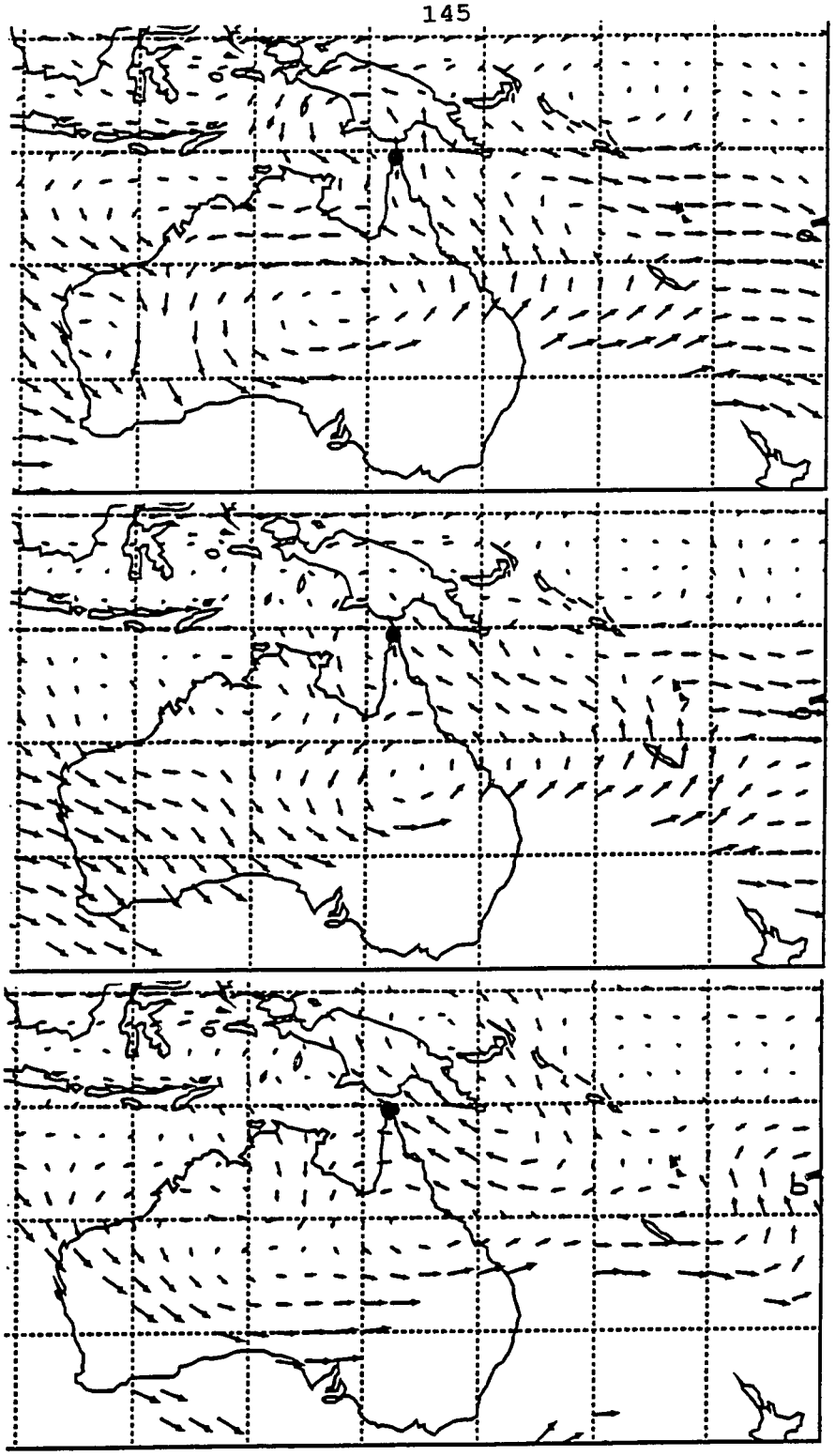

Fig. 4.12 : Wind vectors at 300 mb 20-24 January 1987, from ECMWF analyses. Maximum vector length 25 m/s.

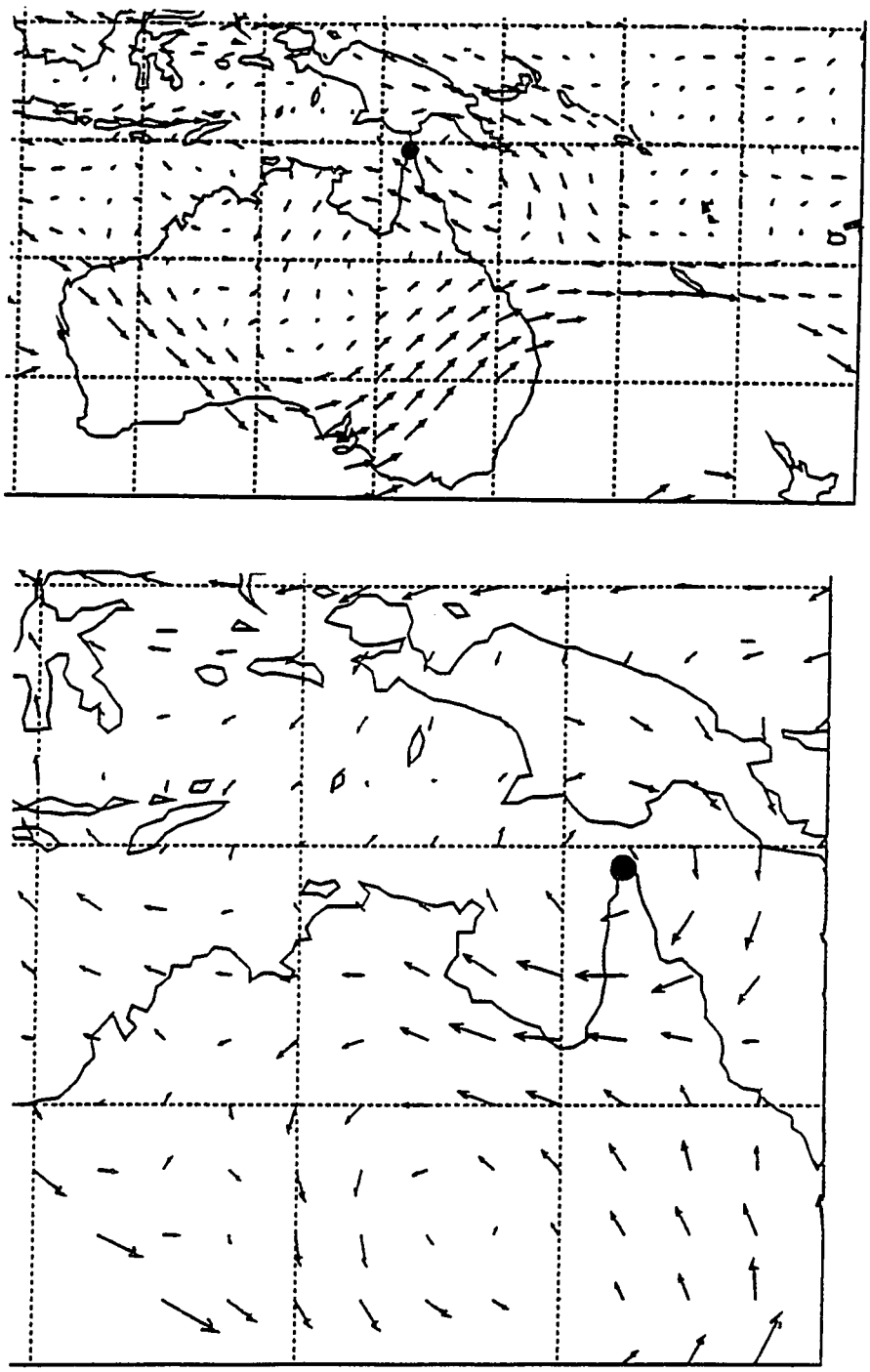

Fig. 4.12 (continued)

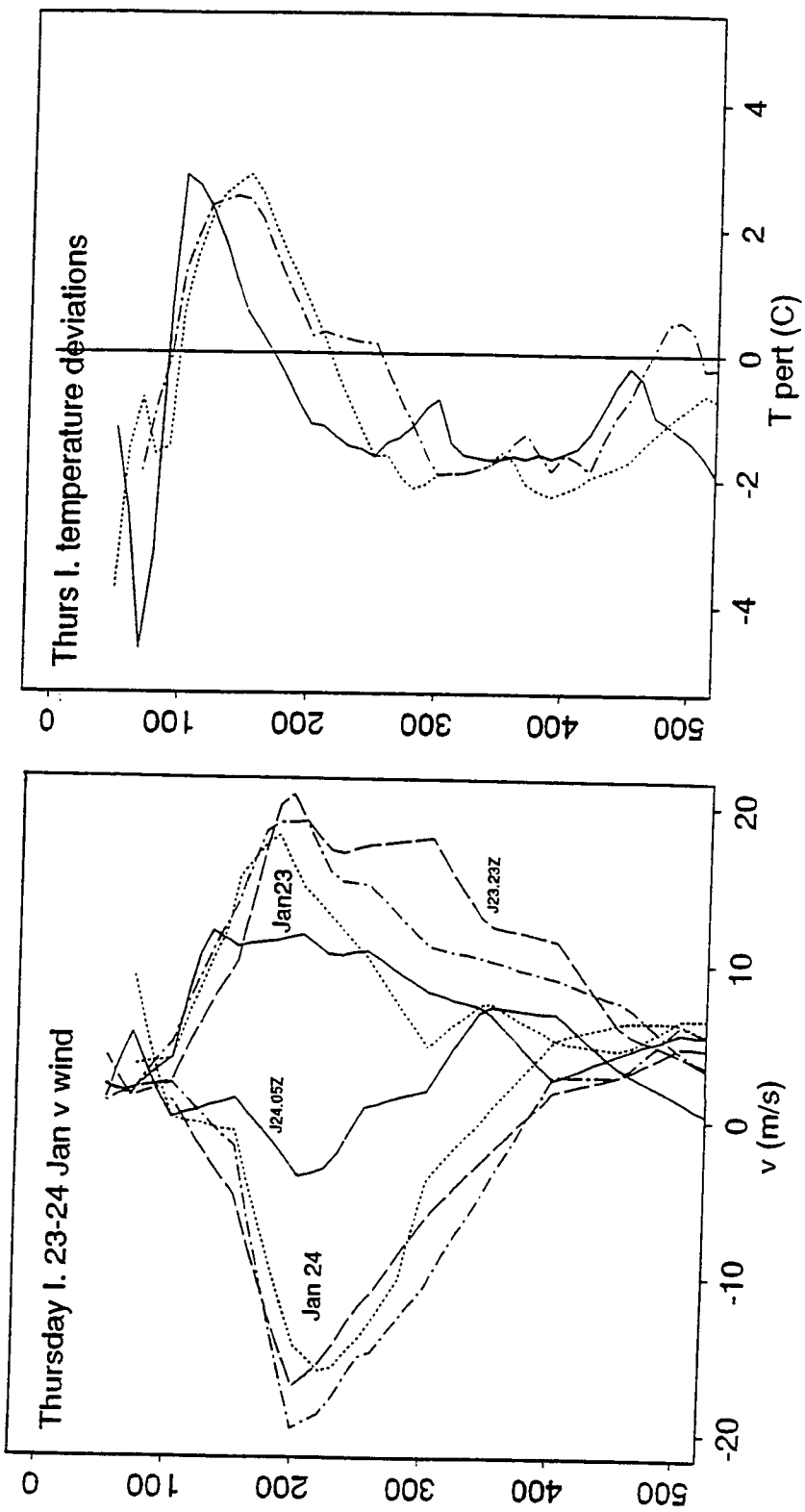


Fig. 4.13 : Thursday Island soundings 23-24 January. Upper: meridional wind component. Lower: temperature deviation from the ship mean, 23 GMT 23 January (solid), and 05 GMT (dotted) and 11 GMT (dashed) 24 January.

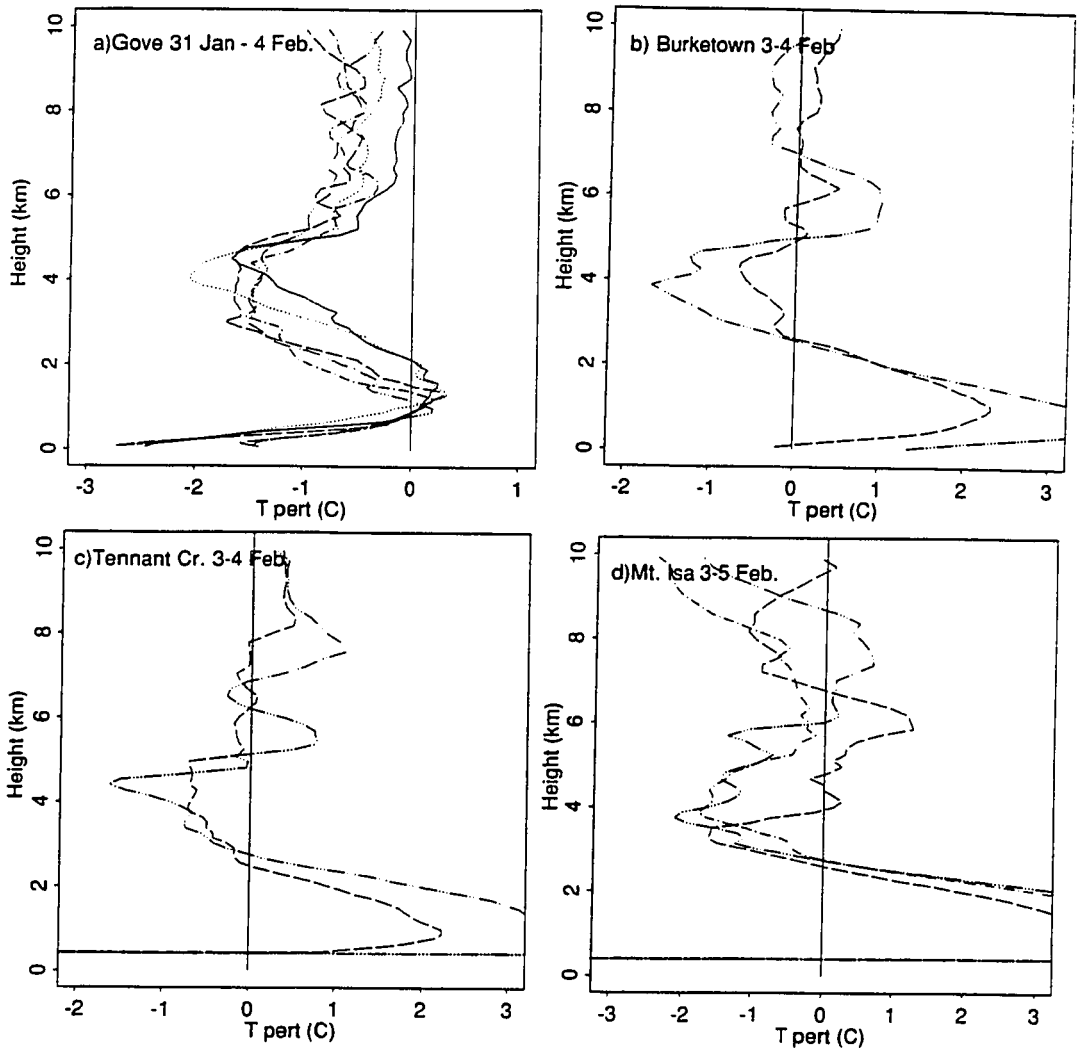


Fig. 4.14 : Temperature deviations from ship mean. Upper left: Gove, daily means 31 Jan to 4 Feb 1987. Upper right: Burketown 3-4 Feb. Lower left: Tennant Creek 3-4 Feb. Lower right: Mt. Isa 3-5 Feb.

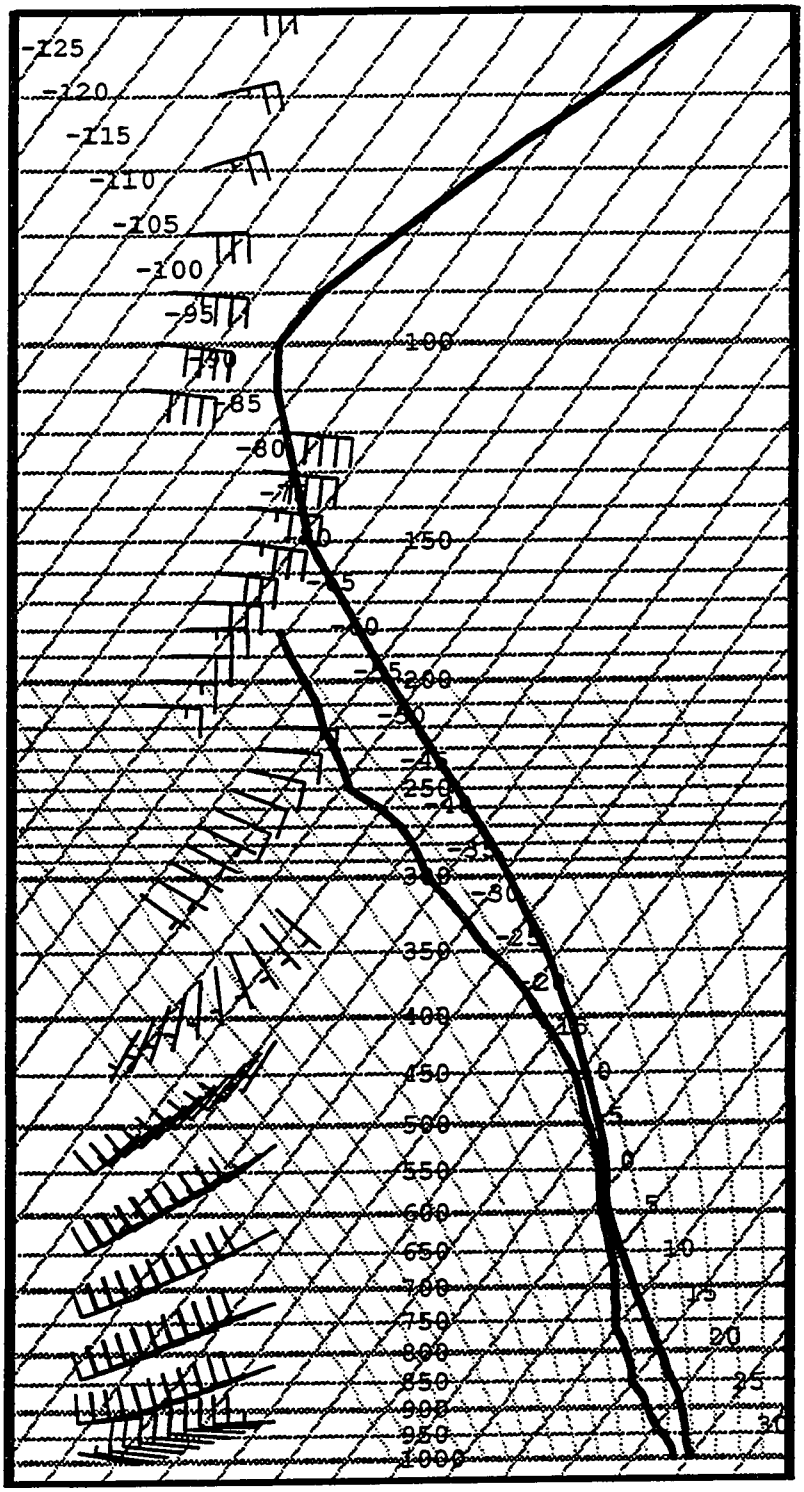


Fig. 4.15 : Gove mean sounding 31 Jan to 4 Feb.

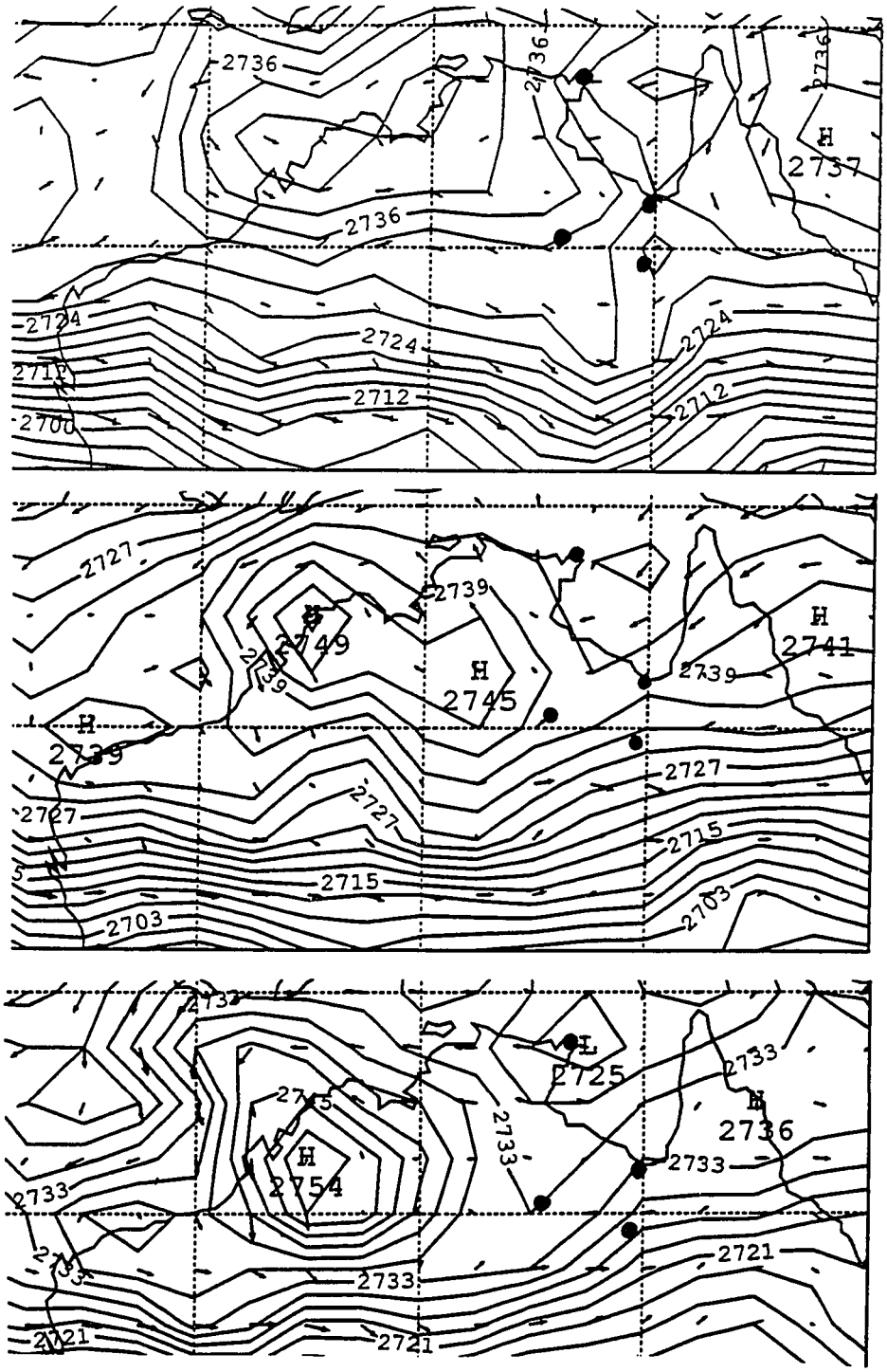


Fig. 4.16 : Thickness and wind difference, 500 mb - 700 mb, 31 January to 4 February. Heavy dots are, from north to south: Gove, Burketown, Tennant Creek, Mt. Isa.

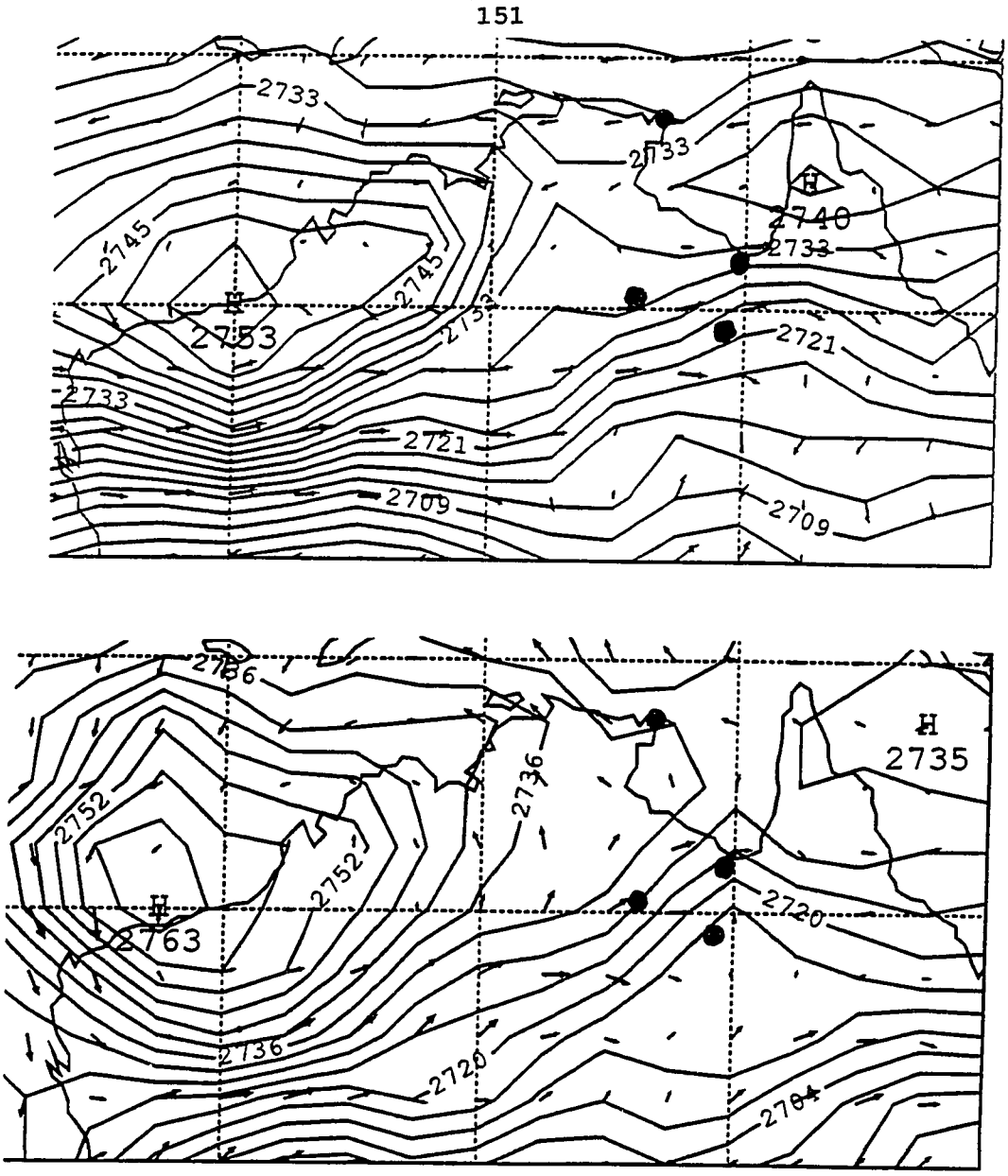


Fig. 4.16 (continued)

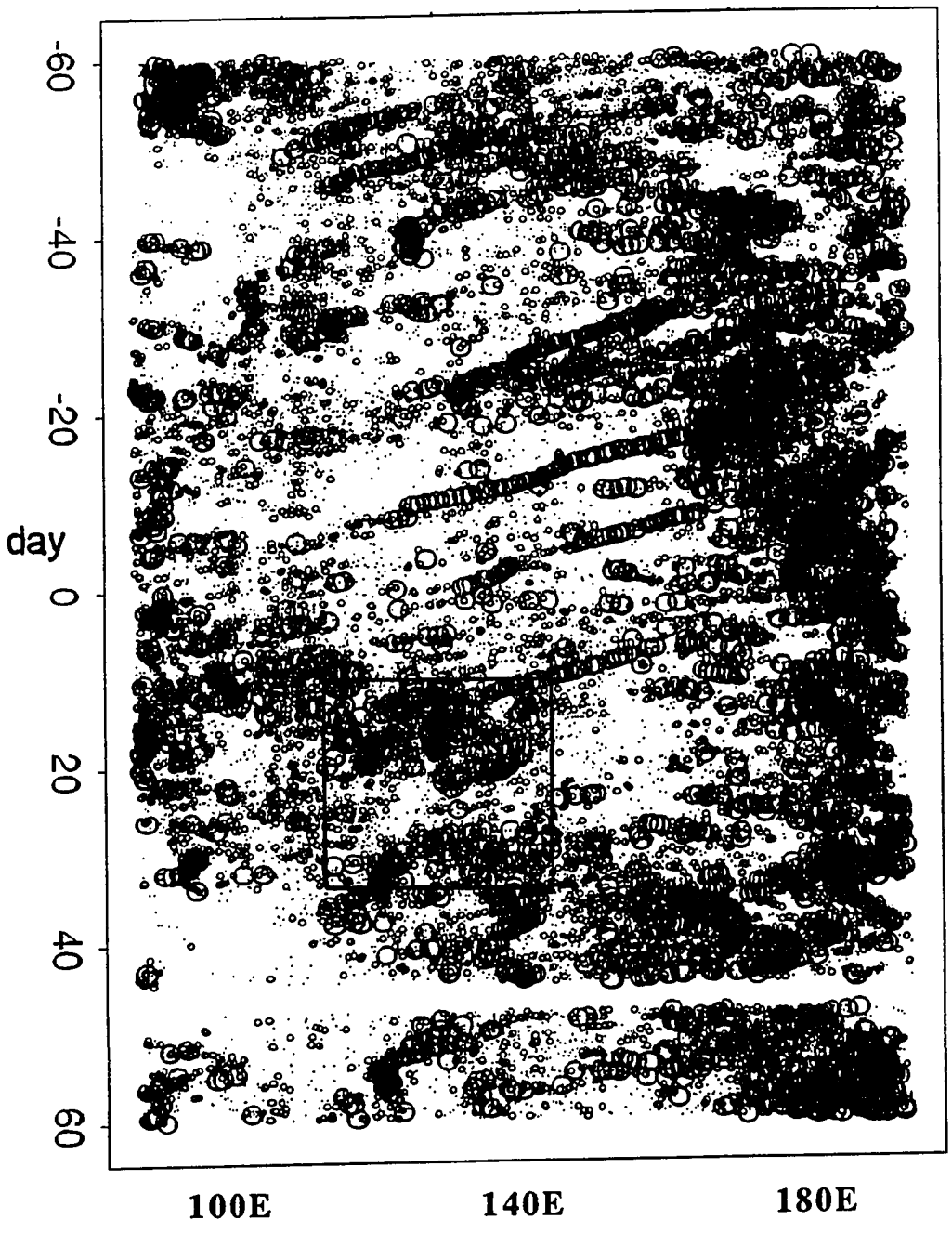


Fig. 4.17 : Time-longitude plot of CE's 2,000-4,000 km2 (dots), 10,000 to 40,000 km2 (small circles), and >40,000 km2 (large circles). The EMEX domain is boxed. Day measured from 1 January 1987.

# CHAPTER 5

## COLLECTIVE (UPSCALE) EFFECTS OF CONVECTION

Convection, while small in inherent scale, is widespread in the tropics, at least over the areas with favorable lower boundary conditions (warm ocean or moist land). It is therefore a process of large-scale importance. Indeed, the motivation for EMEX was to better quantify the large-scale heating which results from numerous mesoscale convective systems. But convection has other effects on its environment. Most notably, it transports momentum in the vertical. This transport is not simply analogous to a passive tracer ["momentum shoveled like coal" in E. Zipsers characterization of Schneider and Lindzen's (1976) parameterization]. Pressure gradients across updrafts and downdrafts in organized convection may alter the momentum of the ascending and descending air (Fig. 3.34; LeMone 1983, LeMone *et al.* 1984). From a climatic (radiative) point of view, the convective detrainment of moisture, both vapor and cloud particles, may be more important than either of these dynamic effects (Betts 1990 and reply by Lindzen; Emanuel 1991). EMEX has little to offer on that question.

An early heat budget calculation illustrating the effects of convection was presented by Riehl and Malkus (1958). They emphasized that the ascending branch of the Hadley cell flows through a midtropospheric minimum in the conserved variable moist static energy. Hence a substantial penetrative (non-downgradient) vertical eddy heat flux is needed to balance the budget of moist static energy. This led to their "hot tower" conceptual model of convection (Chapter 1). More local heat budgets have been computed by Reed and Recker (1971), Yanai *et al.* (1973) (hereafter YEC) and numerous successive authors (reviewed in Yanai and Johnson 1992). The imbalance in the moist static energy budget appears in YEC's terminology as a mismatch between the "apparent heat source" $Q_1$ and "apparent moisture sink" $Q_2$. YEC and subsequent papers use this observed imbalance to fit the parameters of models of cloud ensembles, which parameterize the necessary upward eddy heat fluxes. Formalisms lifted directly from these heat budgets have also been extended to vorticity, momentum and divergence budgets (*e.g.* Stevens 1979).

YEC and subsequent literature contain, in additional to their correct and interesting daignostic results, the fallacious statement that adiabatic subsidence "between

the clouds" compensates the upward mass flux in convection. In section 5.1, a rearranged form of YEC's "compensating subsidence" equation is used to clarify its meaning and relationship to the actual process of compensating subsidence (as discussed in chapter 2).

The *net* dynamical effects of convection on the large-scale (balanced) flow may be diagnosed in terms of potential vorticity (PV). A PV framework, while nontrivial to actually implement in models, is a formally complete description of all balanced flows. In a balanced flow, the wind and mass fields may be diagnostically obtained from the PV field. The only prognostic equation is that for PV, and it includes frictional and diabatic effects (which, above the boundary layer, are largely confined to regions undergoing deep convection). Hence, if one can determine the effects of convection on PV, then the upscale half of the dynamical scale interaction between convection and balanced large-scale flows may in principle be considered solved. Much literature on this topic has appeared in recent years (Hoskins *et al.* 1985; Haynes and MacIntyre 1987, 1989; Schubert *et al.* 1991; Raymond and Jiang 1990, Raymond 1991). Section 5.2 presents a view of the monsoon trough, in a composite sense, in terms of PV. As we shall see, at low latitudes PV perturbations appear almost entirely as vorticity perturbations, since the isentropes are nearly flat and level. Hence the effects of convection on PV are essentially the effects of convection on vorticity.

In section 5.3, the vorticity equation is presented in a useful form, with two terms on the RHS which correspond to the two effects of convection: net heating (represented by mean divergence), and vertical momentum transport ("cumulus friction"). The divergent circulation associated with convective heating spans many decades of horizontal scale, and hence spins up the large-scale monsoon as well as its embedded depressions and vortices. By contrast, cumulus friction creates small-scale vortex pairs, with no net circulation around them.

### *5.1 "Compensating subsidence" in rawinsonde budget studies*

Rawinsonde budgets remain the best available evidence for the effects for the bulk effects of deep convection on larger-scale flows. The purpose of this section is to offer a critique of a particular method of interpreting such budgets, in terms of ensembles of cumulus clouds. It is no mystery by now that convection includes downdrafts and mesoscale diabatic circulations, and therefore it is not difficult to criticize simple cumulus

ensemble models. Actually, from a practical point of view, even unrealistic cumulus ensembles with enough internal free parameters are capable of adequately representing the condensation heating and mean vertical eddy fluxes which constitute the bulk effects of convection. The Arakawa-Schubert scheme (1974) does not fail to give adequate results in GCMs. But in the course of these cumulus ensemble studies, fallacious or at least misleading *physical statements* have been promulgated concerning the subsidence which compensates the net upward mass flux in deep convection. The present section is my critique of this view of compensating subsidence.

The strategy in YEC was to decompose the diagnostic equations for dry static energy (s) and water vapor (q) into mean and "eddy" components. In their calculations, the area enclosed within the Marshall Islands rawinsonde array constituted the large-scale area A over which the mean was taken. All the mean flow terms in the equations were lumped together and denoted $Q_1$ and $Q_2$, the "apparent heat source" and "apparent moisture sink," written as:

$$Q_1 \equiv \frac{\partial \bar{s}}{\partial t} + \nabla \cdot \bar{s}\bar{\mathbf{V}} + \frac{\partial \bar{s}\bar{\omega}}{\partial p} = Q_R + L(c-e) - \frac{\partial}{\partial p}\overline{s'\omega'} \qquad (5.1.1)$$

$$Q_2 \equiv -L\left(\frac{\partial \bar{q}}{\partial t} + \nabla \cdot \bar{q}\bar{\mathbf{V}} + \frac{\partial \bar{q}\bar{\omega}}{\partial p}\right) = L(c-e) + L\frac{\partial}{\partial p}\overline{q'\omega'} \qquad (5.1.2)$$

where horizontal eddy fluxes have been neglected. YEC modelled the terms on the right with an ensemble of entraining plume cumulus clouds of different heights (resulting from different entrainment rates). Rawinsonde estimates of the terms on the left hand side were then used to calculate values for the parameters of the cumulus ensemble. The idea of representing convection as such an ensemble can be traced back to Ooyama (1971). This same idea underlies the influential Arakawa and Schubert (1974) cumulus parameterization scheme.

The next step in YEC was to introduce the new variable $\overline{M} \equiv -\overline{\omega}$, so that the in-cloud portion $M_c = -\sigma\omega_c$ (where $\sigma$ is the cloud area fraction) could be verbalized as "cumulus mass flux," positive upward. The authors then introduced the assumption that the clouds cover a small fraction of the large-scale area. This permitted a simplification of the eddy flux terms in (5.1) and (5.2). In addition, the small area assumption was used to justify their (19):

$$\overline{s} \cong s_e \text{ and } \overline{q} \cong q_e \tag{5.1.3}$$

where the subscript e denotes the "environmental" (intercloud) value. After thirty more equations introducing the cumulus ensemble, they combined four of their resulting cloud ensemble equations to arrive at the result [their (49)]:

$$Q_1 - Q_R = -M_c \frac{\partial s_e}{\partial p} - Le \tag{5.1.4}$$

In Yanai and Johnson (1992), $\overline{s}$ rather than $s_e$ appears in the analogous equation, but in light of (5.1.3), the difference is small.

Comparing (5.1.1) with (5.1.4), it is clear that the result of the small-area assumption and the introduction of the cumulus ensemble model has been that Lc plus the vertical eddy heat flux divergence have been combined into the first term on the right. As shown by Houze (1982), the eddy flux term tends to be the smaller contributor. YEC's interpretation of (5.4) was that it:

> "shows that the *apparent heat source,* in addition to $Q_R$, consists of *an adiabatic warming due to a component of downward motion which compensates* $M_c$, and a *cooling due to the re-evaporation of cloud drops.*" (italics theirs)

That is indeed what the equation appears to say: minus-cloud-mass-flux-times-environmental-stratification. However, the italicized verbal statement above is a mistranslation of the mathematical statement (5.1.4), disguised by the suggestive symbology of (5.1.4).

To make its true interpretation apparent, I would rewrite (5.1.4) as follows:

$$\overline{\omega} \frac{\partial \overline{s}}{\partial p} = \sigma\omega_c \frac{\partial \overline{s}}{\partial p} - Le + Q_R + SH \tag{5.1.5}$$

where SH represents the (small) storage and horizontal advection parts of $Q_1$, $\sigma\omega_c$ has been retained in favor of $-M_c$, and the assumption (5.1.3) has been used (to undo its previous use). The meaning can be clarified even further by dividing out the mean stratification:

$$\omega_e \approx (1-\sigma)\omega_e = \overline{\omega} - \sigma\omega_c = \frac{Q_R - Le + SH}{\partial \overline{s}/\partial p} \qquad (5.1.6)$$

It is now apparent that this equation for environmental vertical motion does not say that it compensates the upward mass flux in convection. In fact, quite to the contrary, (5.1.6) shows that *the environmental downward motion is simply that which balances radiative cooling and the evaporation of cloud water, to the extent that heat storage within A and horizontal advection are small.* Since $Q_R$ and Le are both treated crudely in YEC, the authors were not really in a position to be making strong statements about intercloud downward motion.

In fact, the adiabatic subsidence compensating heated convective updrafts occurs in buoyancy bores, which propagate rapidly away from the convection when it starts (chapter 2). In the idealization of a steady heat source, no subsidence occurs in the vicinity of the heating. To the extent that the buoyancy bores associated with recently-initiated heating are still within YEC's rawinsonde array at a given moment, some adiabatic subsidence is occurring within the array, causing $\partial \overline{s}/\partial t > 0$ in the SH term in (5.1.6). But that internal warming is not measured by the rawinsondes, which lie along the perimeter of the Marshall Islands array used in YEC. In other words, that tiny part of the adiabatic subsidence which does occur within the array is specifically *not* included in the budget estimates of "apparent heat source!"

The results of YEC's (entirely valid) computations (their Fig. 13) show that there is indeed a small downward motion between the clouds. Examination of their figures makes clear that it corresponds almost precisely to their assumed radiative cooling profile plus their computed profile of detrained liquid water (which was unrealistic, in light of the existence of downdrafts). And yet, YEC's conclusions reiterate that "the most important conclusion in the study is that *the cloud mass fluxes exceed the mean vertical mass flux required by the large-scale convergence, thus causing a compensating sinking motion between active clouds. The large-scale heating of the environmental air is primarily due to its adiabatic compression in the compensating downward motion.*" Neither of these sentences, when read very literally, is completely incorrect (although "causing" is a loaded term). But the juxtaposition misleadingly suggests that the *radiative and evaporative* subsidence between the updrafts, mentioned in the first sentence, has something to do with the *adiabatic* subsidence mentioned in the second, which occurs far far away, where the s profile may differ appreciably from $\overline{s}$ or $s_e$ in the Marshall Islands.

YEC spawned, in addition to the literature of convective heat budgets, a generation of copycat budget formulations for other quantities, most notably the scalar vertical component of vorticity (Reed and Johnson 1974, Shapiro 1978, Stevens 1979, Cho *et al.* 1979, Cho and Cheng 1980, Chu *et al.* 1981, Esbensen *et al.* 1982, Yanai *et al.* 1982, Tollerud and Esbensen 1983, Pearce and Omotosho 1986, Sui and Yanai 1986, Sui *et al.* 1989) but also vector momentum (Cho 1985). The subsidence misconception from YEC has been carried over into vorticity budgets. For example, Sui and Yanai (1986) conclude, based largely on the above preconception, that "the vertical advection of the large-scale vorticity due to cumulus-induced subsidence in the environment is the dominant mechanism for generating Z (vorticity budget residuals) in the middle troposphere." The YEC prime-and-bar process, applied to the vorticity equation, results in a horrific proliferation of terms, particularly if the equation was written in a noncompact form at the outset. As a result, the YEC-inspired vorticity budget literature has unfortunately perpetuatued the impression that vorticity budgets are terribly complicated, and that clouds have a lot of "effects" on the large-scale vorticity.

### *5.2 A potential vorticity view of the Australian monsoon*

Potential vorticity, first considered by Ertel in 1942, is defined as:

$$PV = \rho^{-1} \zeta_a . \nabla \theta \qquad (5.2.1)$$

where $\rho$ is density, $\zeta_a$ is vector absolute vorticity, and $\theta$ is potential temperature. P is conserved, following the motion of the fluid, for adiabatic, frictionless flow. Under the hydrostatic assumption, the density factor may be absorbed to give the isentropic coordinate version of (5.1):

$$PV = -g \zeta_\theta \partial\theta/\partial p \qquad (5.2.2)$$

where $\zeta_\theta$ is the vorticity on an isentropic surface. This equation follows directly from (14) of Hoskins *et al.* (1985), noting that $(\partial p/\partial\theta)^{-1} = \partial\theta/\partial p$, since both partial derivatives are taken with x and y held constant.

As discussed by Keyser and Rotunno (1990), it is impossible to evaluate unambiguously (5.2.2), the mathematical product of differential quantities, from real data. A vertical resolution scale is implicit in the finite-difference measurement of static stability, and a horizontal resolution scale is implicit in the measurement of vorticity as

circulation. It is useful to let the choice of those scales be dictated by the natural scales of the phenomenon being described, rather than by, say, data resolution limits.

The idea behing PV, in integral form, is that between any two material surfaces (isentropes, for adiabatic flow) the mass ($\Delta p/g$, hydrostatically) is changed only by mass convergence / divergence in the layer, which also increases / decreases the (layer-averaged) vorticity proportionately. Isentropic vorticity is, in the absence of friction, changed *only* by divergence, because entropy (or $\theta$) is a function solely of density and pressure, so that there is no solenoidal term in the isentropic vorticity equation. [This is not true, for example, of vorticity on a $\theta_e$ surface.] In a balanced flow, the PV is expressed partly as vorticity and partly as thermal perturbations, which are necessary to make the (hydrostatic) pressure gradient force balance the other terms in the horizontal momentum equation (Coriolis and advection, in the case of gradient wind balance). In the tropics, the Coriolis force is weak, so outside of the highly curved flow near hurricane cores, PV anomalies are expressed almost purely as vorticity.

The composite thermal structure of the monsoon trough may be estimated from Fig. 5.1, a pressure-coordinate potential temperature version of Fig. 4.7a. The most cloudy category 6 environments constitute the center or core of the trough, and the clear category 1 environments constitute the out-of-trough environment. It is useful to transcribe these measurements onto a two dimensional idealized cross-section of isentropes depicted in a pressure-coordinate diagram (Fig. 5.2). The pressure coordinate was selected in order to make area on the diagram proportional to mass. Smaller-scale perturbations of the isentropes associated with hurricanes and convective cells have also been represented on Fig. 5.2. The aircraft measurements from which the hurricane isentrope disturbance was derived are shown in Fig. 5.3.

The point of Fig. 5.2 is that the mass ($\Delta p$) within a column of, for example, the isentropic layer from 305-335 °K, varies by only a few percent across the composite monsoon trough. One rather literal way of interpreting potential vorticity is the vorticity which would result if the isentropes were flattened by adiabatic motions. In the present case, that would require a horizontal area-contraction of a few percent within the central disturbed part of the layer to stretch the 335 °K isentrope back to flat, and this area-contraction would increase vorticity by a few percent. In other words, for the deep layer considered here, which is the natural depth of the balanced monsoon wind system, *potential vorticity is simply proportional to vorticity, within a few percent.* This

conclusion follows from the deep vertical structure, and does not depend on the horizontal scale in Fig. 5.2.

Variations of monsoon vorticity, on a horizontal scale small enough to capture synoptic details, yet large enough not to be dominated by unbalanced noisy winds, can be examined using data from the AMEX radwinsonde array around the Gulf of Carpentaria. The daily percent high cloudiness index of convective activity, for a 600 km square area centered on the Gulf, was used to divide days into categories, similar to the categories used in the composite of the monsoon thermal structure. For each category, the composite Gulf-mean absolute vorticity, calculated as a line integral, is shown in Fig. 5.4. Note that the absolute vorticity varies over a range of ~100 percent, much larger than the range of variation of isentrope spacing.

The circulation in Fig. 5.4 was evaluated on isobaric surfaces, rather than isentropic surfaces. To see that the difference is small, consider a simplified one-component equation for shear vorticity:

$$\zeta_\theta \equiv \left.\frac{\partial v}{\partial x}\right)_\theta = \zeta_p + \frac{\partial v}{\partial p} \cdot \left(\frac{dp}{dx}\right)_\theta \qquad (5.2.3)$$

The difference between the two vorticities is that a small component of the *vertical* shear in pressure coordinates appears as *horizontal* shear vorticity in isentropic coordinates. This small component is proportional to the slope of an isentropic surface. If a 2 °C $\theta$ gradient at 300 mb prevails across the 600-km Gulf of Carpentaria (a generous estimate), then the slope of an isentrope is approximately 1 mb /22 km, and a healthy vertical shear of 10 m $s^{-1}$ / 200 mb corresponds to only $10^{-5}$ $s^{-1}$ in vorticity difference. For layer-averaged vorticity, the difference is much smaller: mass-weighted averages of isobaric and isentropic vorticity, between any two flat isentropes in Fig. 5.2 (say, 305 and 375 °K), are equal. Hence, errors incurred by using $\zeta_p$ instead of $\zeta_\theta$ tend to cancel in the vertical. A similar scaling argument for geometric coordinates leads to the conclusion that

$$\zeta_\theta \cong \zeta_p \cong \zeta_z. \qquad (5.2.4)$$

The arguments above suggest that convective heating affects the monsoon primarily through vorticity generation, not by creating temperature perturbations. This idea is supported by Fig. 5.5, which shows that the upper-tropospheric temperature

variation, shown in Fig. 5.1 to be positively correlated with PHC, and therefore with latent heating rate, is hydrostatically related almost entirely to *low-level* geopotential height variations. If the observed increase in temperature with PHC were due to a local buildup of the heat from the increased instantaneous latent heating rate, one might expect it to be associated also with an increase in upper-tropospheric geopotential height.

It appears that the observed temperature increase aloft is hypsometrically related to low surface pressure accompanying the low-level cyclonic circulation, which happens to be associated with increased PHC (for reasons explored in chapter 4). In other words, the monsoon thermal structure is dynamically related to the rotational wind fields in the thermal wind sense, similar to the thermal structure of easterly waves (Cho and Jenkins 1987). Temperature rises aloft are only indirectly related to heating, in that the low-level monsoon cyclonic vorticity is due mainly to a history of persistent low-level convergence into areas of MCS heating. A similar warm core and low pressure structure would presumably accompany a (very hypothetical) synoptic-scale cyclone, with vorticity structure like that in Fig. 5.4, but created through the action of the force-curl term in Eq. (5.3.2), with no local heating involved at all.

This implies that the impact of MCSs heating on the larger-scale flow can be profitably viewed as divergence rather than as heating *per se*; i.e. as a small-scale "mass source," a function of height or $\theta$, with a nearly zero mass-weighted vertical integral (some water mass falls out as precipitation). Since the temperature varies little, vertical motion compenstates the diabatic heating (Charney 1963), so by mass continuity, divergence is related to the vertical gradient of heating in pressure coordinates [$DIV = -\partial\omega/\partial p \sim -\partial/\partial p(Q/\sigma)$, where $\sigma$ is the static stability parameter $T/\theta\ \partial\theta/\partial p$]. The utility of focusing on divergence, a measurable quantity, as opposed to heating, is a major theme of this research.

### *5.3 A vorticity view of the monsoon*

In this section vorticity observations are presented and interpreted. First the vorticity equation is presented in forms useful for the interpretation of observations. For analyzed fields on a grid, a "filtered" equation for the vorticity field at the resolution of the analyses is the appropriate tool. For raw rawinsonde observations, a flux form, integrated over the area enclosed by the rawinsonde network is more useful. Both are presented in section 5.3.1. Observations of the horizontal distribution of monsoon

vorticity are presented in section 5.3.2. Instantaneous values are not well measured, so only time-mean observations are presented. In section 5.3.3, the vertical structure of monsoon divergence and vorticity illustrates the fact that as one goes to larger *horizontal* scales of distance from the small-scale forcing by convection, larger and simpler *vertical* structure predominates.

### *5.3.1 Vorticity equations*

In this section we consider two forms of the vorticity equation in pressure coordinates. The first is in field form, and describes the processes affecting the vorticity field in gridded analyses at a given resolution. The second is a flux form, which can be integrated over area to give a circulation equation relevant to the circulation observed by rawinsondes around the perimeter of an area.

#### *5.3.1.1 "Filtered" form of the p-coordinate vorticity equation*

In understanding the effects of convection on the synoptic-scale flow, it is useful to refer to the equation governing the vertical component of vorticity calculated from synoptic-scale wind fields (*viz.*, the ECMWF analyzed winds). The use of gridded analyses in vorticity budgets is temptingly (and dnagerously) simple. For example, it is easy to evaluate derivatives of derivatives ($\nabla\zeta$) at every gridpoint. However, as shown by Lewis and Reed (1984), different analysis techniques can lead to substantially different patterns of divergence (one velocity derivative) and the resulting vertical velocity. Surely the sensitivity of $\nabla\zeta$ to the analysis scheme is even greater.

Vorticity budget equations for regions containing convection have been presented by other authors (*e.g.* Sui and Yanai 1986), and elaborate mathematical theories have been suggested to parameterize cloud effects on large-scale vorticity (*e.g.* Cho *et al.* 1979). But as pointed out by Esbensen *et al.* (1987) and by Haynes and McIntyre (1987, 1990), vorticity has important conservation properties which can be obscured by the expansion of cloud effects into multiple terms, and can be lost entirely in schemes that evaluate or parameterize those terms independently.

In the spirit of the latter authors, a simple yet complete vorticity equation can be derived from the momentum equation governing a hydrostatic, pressure-coordinate synoptic-scale representation ($\mathbf{U},\omega$) of an actual flow field, $\mathbf{U}$ being the horizontal wind vector (u,v,0) and $\omega$ the rate of change of pressure following a parcel of air. The

ECMWF analyses, on a 2.5° grid, would constitute such a representation, if they were perfect. The horizontal momentum equation is:

$$\frac{\partial \mathbf{U}}{\partial t} + \mathbf{U}\cdot\nabla\mathbf{U} + \omega\frac{\partial \mathbf{U}}{\partial p} = -f\hat{\mathbf{k}}\times\mathbf{U} - \nabla\Phi + \mathbf{F} \qquad (5.3.1)$$

where f is the Coriolis parameter, $\Phi$ is geopotential, and **F** is the residual or apparent acceleration on the resolved scale resulting from all sub-resolvable sources of momentum, including horizontal and vertical eddy transports and non-hydrostatic pressure-gradient forces. In the case of tropical synoptic-scale momentum studies, **F** is typically assumed to be dominated by the vertical transport of momentum in convection.

Now after taking the vertical component of the pressure-coordinate curl of (1), an equation for the vorticity of the resolved flow is obtained:

$$\begin{aligned}\frac{D\zeta_a}{Dt} &\equiv \left(\frac{\partial}{\partial t} + \mathbf{U}\cdot\nabla_p\right)\zeta_a \\ &= \frac{D\zeta}{Dt} + \beta v \\ &= -\zeta_a(\nabla_p\cdot\mathbf{U}) - \hat{\mathbf{k}}\cdot\nabla_p\times\left[\omega\frac{\partial \mathbf{U}}{\partial p} - \mathbf{F}\right]\end{aligned} \qquad (5.3.2)$$

where $\nabla_p \equiv \left\{\frac{\partial}{\partial x}, \frac{\partial}{\partial y}, \frac{\partial}{\partial p}\right\}$, $\zeta = \hat{\mathbf{k}}\cdot\nabla_p\times\mathbf{U}$ is the vertical component of relative vorticity, $\zeta_a$ is the absolute vorticity $f+\zeta$, $\beta$ is $\partial f/\partial y$, and v is the meridional component of **U**.

The first term on the right, often called "vortex stretching," acts to increase the magnitude of absolute vorticity of either sign in the presence of convergence and to decrease it in the presence of divergence. The *net* mass sink at low levels and mass source at upper levels associated with the net heating in precipitation systems will be reflected in the divergence of the resolved-scale winds, even if the flow on the scale of the precipitation systems is not resolved *per se*. This is not to say that the ECMWF analyzed fields contain the correct divergent winds; they do not. However, the actual divergence patterns, which can be qualitatively inferred from the satellite-observed population of cloud systems, do help explain the evolution of the vorticity, and thus of

the rotational winds, which, being of much larger magnitude, are probably more accurately represented in the ECMWF analyses. This interplay of the rotational and divergent winds has been exploited, for example, by Sardeshmukh and Hoskins (1987) in their "$\chi$-problem" calculation of accurate global 200 mb divergent wind fields from the evolution of the ECMWF-analyzed rotational winds.

The second term on the RHS of (2) is the curl of the apparent acceleration resulting from the total vertical advection of momentum, "mean" plus "eddy" (plus all other neglected accelerations). The eddy and mean separation is arbitrary and resolution-dependent, so any further expansion of the force-curl term would be purely a mathematical exercise, which might obscure the conservation properties inherent in the curl form.

Since vertical velocity, and therefore divergence, are small in the tropics in the absence of diabatic heating (*e.g.* Charney 1963), the first term on the RHS of (2) will be concentrated in areas of precipitation, where in general net low-level convergence and upper-level divergence prevail (the detailed vertical structure of this divergence will be the subject of Part II). If, in addition, the subgridscale momentum source **F** is dominated by vertical transports within MCSs, the acceleration vector (in brackets) in the second term on the RHS of (2) is, like divergence and $\omega\partial U/\partial p$, localized in areas of MCS activity. Hence, the curl of this patchy vector field should be manifest in the appearance of vorticity couplets flanking cloudy areas, positive to the left and negative to the right of **F**. Such vorticity couplets flanking MCSs have been reported in the eastern Atlantic (Tollerud and Esbensen 1983, Sui and Yanai 1986).

*5.3.1.2 Flux form of the p-coordinate vorticity equation*

If the filtered wind $(U,\omega)$ in (5.3.1) is replaced with the actual wind $(V,\omega)$, the **F** term can be dropped [neglecting molecular viscosity, electrical forces, and some non-hydrostatic pressure effects]. Then the curl operation gives:

$$\frac{\partial \zeta}{\partial t} = -\nabla\cdot\left[(\zeta+f)\mathbf{V}\right] - \hat{\mathbf{k}}\cdot\nabla\times\left[\omega\frac{\partial \mathbf{V}}{\partial p}\right] \qquad (5.3.3)$$

With integration over a fixed area A, *e.g.* an area with rawinsondes launched around its perimeter, the terms on the right are converted to boundary integrals:

$$\frac{\partial C}{\partial t} = A\frac{\partial \bar{\zeta}}{\partial t} = -\oint f U_n \cdot d\ell - \oint \zeta U_n \cdot d\ell - \oint \left[ \omega \frac{\partial U_t}{\partial p} \right] \cdot d\ell \qquad (5.3.4)$$

(i) (ii) (iii)

where C is the circulation and $U_n$ and $U_t$ are the wind components normal and tangential to the boundary. Equation (7) states that the processes which change the mean vorticity in an area are horizontal fluxes of planetary and relative vorticity through the boundary of the area, and vertical advection of tangential momentum along the boundary. Observed vorticity profiles should reflect the time-mean vertical structure of the source terms on the right.

The first term (i) can be evaluated directly from rawinsonde array data. Its vertical structure is essentially identical to rawinsonde divergence profiles, since f is of a single sign all across northern Australia. Term (ii) is quite difficult to measure accurately, as discussed above in the advection form. At a minimum, it takes three wind measurements to obtain the crudest estimate of relative vorticity flux $\zeta U$, and at least three measurements of $\zeta U$ to obtain the crudest estimate of its divergence.

Term (ii) is very important in ridding the lower troposphere over northern Australia of the vorticity accumulated by the first term during active monsoon rain periods. I refer of course to tropical cyclones which cross the array boundary (*e.g.* Figs. 1.10-1.14). Obviously this vorticity flux is not well resolved by rawinsondes hundreds of km apart. Nonlinear advection in (ii) is also very important in the upper-troposphere, as found by Sardeshmukh and Held (1984) and Sardeshmukh and Hoskins (1985). Without it, a very strong artificial damping — which has on occasion been erroneously interpreted as "cumulus friction" — is needed to balance time-mean vorticity budgets (*e.g.* Holton and Colton 1972). The action of term (ii) is also evident on occasion as an increase followed by decrease of cyclonic vorticity, when upper-tropospheric troughs from midlatitudes advect through the rawinsonde array.

Term (iii) is also difficult to measure, but may be estimated in a scaling sense. Where the boundary of the array runs through clear air, $\omega$ may be approximately as "radiative subsidence," the vertical motion necessary for adiabatic warming to balance the radiative cooling of clear air. Since clear-air cooling is typically ~1 °C per day (Cox and Griffith 1979), dividing by a 6 °K/km lapse rate implies a vertical velocity of ~150 m/day.

In a week, then, features in the vertical wind profile, and therefore the profile of vorticity, would descend 1 km. This is a small effect, compared to horizonmtal fluxes which spin up the monsoon and its cyclones from a state of rest on the same 1 week time scale.

The contribution to term (iii) by vertical momentum transports in deep moist convection along the boundary is more difficult to estimate. In essence, term (iii) reflects the process of vorticity couplet production in the upper troposphere by convective momentum transports (as discussed in section 5.3.1.1), where one half of the couplet lies within the array and one half lies outside. One such vorticity couplet, produced by well-sampled convection transporting low-level westerly momentum upward, is presented below (see also Tollerud and Esbensen 1983, Sui and Yanai 1986).

In the case of the north Australian rawinsonde array, upper-tropospheric winds were usually directed outward all along its northern perimeter where convection was happening. Hence any mesoscale vorticity couplets produced near or straddling the array boundary were quickly advected out of the array (for example, the vorticity couplet in Fig. 5.6c is streaked out to the northwest, downwind along the 200 mb flow). In essence, vorticity produced near but inside the boundary by term (iii) was quickly fluxed out of the array by action of term (ii).

In the case of the small Gulf of Carpentaria array, during periods when it was within a tropical cyclone, term (iii) was probably not neglegible. With widespread deep convection happening in a strong anticyclone of vertical wind shear, upward momentum fluxes probably contributed strongly to the maintenance of cyclonic absolute vorticity at upper levels in the cyclones (Fig. 5.7b).

### *5.3.2 Observed vorticity structure*

Fields of mean absolute vorticity (from ECMWF analyses), corresponding to Figs. 1.7a and 1.8a, are shown in Fig. 5.6. In these plots, the units of absolute vorticity are degrees latitude, corresponding to the "rest latitude" at which the planetary vorticity is equal to a given value of absolute vorticity. This convention makes explicit the idea that absolute vorticity can be used as a tracer of meridional displacements, with the proviso that the terms on the RHS of (5.3.2) will modify it, mostly in convectively active areas and in the frictional boundary layer. In this context it is useful to note that divergence can never change the *sign* of absolute vorticity, only its magnitude. Friction, if it is assumed

to oppose the wind, will tend to bring the relative vorticity to zero, such that the absolute vorticity contours relax back toward their rest latitudes.

It is instructive to examine the time-mean vorticity fields of Fig. 5.6 for evidence of (i) the mean 850 mb mass sink / 200 mb mass source associated with the convection; (ii) the mean meridional flows in Figs. 3a and 4a; and (iii) momentum fluxes by convection. In addition, transient eddy fluxes of vorticity must also be considered.

The mean vorticity pattern at 850 mb, corresponding to the winds in Fig. 1.7a, is shown in Fig 5.6a. The contour of zero absolute vorticity lies roughly 5° south of the equator, because the relative vorticity north of there was positive. This positive vorticity was evidently advected in from the northern hemisphere by the persistent mean northerly winds across the equator. To the south of the zonal jet at 10 °S, contours tended to lie equatorward of their rest latitudes, indicating cyclonic relative vorticity. Cyclonic (negative) vorticity in these areas was locally increased by the low-level convergence associated with the convective systems along the Australian coast, as well as advected from the south by the mean southerlies in western Australia and the eastern Indian Ocean (not as persistent as the cross-equatorial northerlies). Transient eddy fluxes of vorticity removed cyclonic vorticity from the time-mean trough, as hurricanes formed in the trough and then moved out during the averaging period.

The 200 mb pattern of mean absolute vorticity, corresponding to the winds in Fig. 1.8a, is shown in Fig. 5.6b. At this level, divergence from the convective systems near the Australian coast acted to lessen any vorticity of either sign, and this outflow air with near-zero vorticity flowed northwestward across the equator at all longitudes, and southward over western Australia. Hence, the vorticity field in Fig. 5.6b shows very small absolute vorticity near and north of the equator and in western Australia. In the southern hemisphere, almost all the contours lie poleward of their rest latitudes, indicating anticyclonic relative vorticity.

One particularly notable feature is the area of positive absolute vorticity south of the equator (0-8°S), north of the PHC maximum, from 130-140°E. Since divergence can never change the sign of absolute vorticity, and the mean meridional wind in this area was southerly, reference to (2) suggests that this feature must reflect a subgridscale source of momentum, presumably a vertical transfer by convective systems. In fact, this feature was very pronounced from 1-3 February (Fig. 5.6c), when persistent, well-

sampled (EMEX flights 8, 9, 10, chapter 3) MCSs in the Arafura sea (10 °S, 135 °E on Fig. 1.14b) were observed to be transporting westerly momentum upward.

### *5.3.3 Vertical structure and its upscale simplification*

In this section I briefly consider the vertical structure of circulation, as measured by rawinsondes around the perimeter of the Gulf of Carpentaria and much larger North Australian rawinsonde arrays. This circulation should reflect the terms in Eq. (5.3.4). Consider first the circulation around the Gulf of Carpentaria during pre-cyclone and cyclone periods (Fig. 5.7). Low-level cyclonic circulation in the pre-cyclone periods (Fig. 5.7a) had its maximum at ~3 km altitude, consistent with the Doppler radar and rawinsonde measurements (Figs. 3.3-3.6) of similarly elevated convergence in MCSs. Davidson *et al.* (1990) also found that elevated cyclonic vorticity maxima preceeded the formation of cyclones Irma and Jason. As the cyclones intensified, the level of maximum circulation descended to near the surface (Fig. 5.7b). Presumably this surface spinup process reflects the transition from vortex stretching by the elevated convergence typical of MCS's, to vortex stretching by the strong surface inflow associated with the secondary circulation of the intensifying cyclones themselves.

Vorticity and divergence profiles on a larger scale have been calculated from the whole north Australian sounding array (heavy dots on Fig. 1.1), which surrounded the mean monsoon trough (Fig. 1.7). The time-mean profiles from all of AMEX Phase II are shown in Fig. 5.8, and compared to the mean Gulf of Carpentaria profiles. Over the Gulf, the convergent and cyclonic lower layer of the monsoon extended to ~11 km height. On the larger scale of all North Australia, however, the vertical structure of both divergence and vorticity was more nearly symmetric through the troposphere, more nearly approximating the "gravest vertical mode" of the troposphere. The geostrophic deformation radius (e-folding distance for the absorption of buoyancy rolls, as described in chapter 2) for a 30 km wavelength at 15° latitude is ~1200 km, so vertical structure of this depth should be well-observed by the large array. However, for a wavelength half as large, the deformation radius is ~600 km, comparable to the scale of the array, indicating that this shallower vertical structure information would be mostly ($e^{-1}$) trapped within the array. The observations are in qualitative agreement with those predictions.

This trapping of shallow vertical structures at small horizontal scales underlies the success of simple reduced gravity shallow water models in simulating large-scale wind

fields forced by specified tropical heat sources (*e.g.*, Gill 1980, Silva Dias *et al.* 1983). All heating profiles positive through the troposphere project strongly onto the gravest baroclinic mode (see Fig. 6 of Salby and Garcia 1987). However, the superposition of vertical structures of different scales is extremely important for predicting low-level convergence (Mapes 1992, Chang and Lim 1988), which is necessary in models in which convective heating is predicted rather than specified. Tropical cyclogenesis is also apparently a problem which involves complex vertical structure at low levels (Fig. 5.7). Reliable, direct measurements of the mean divergence profiles of MCSs in their entirety are needed to address these important questions.

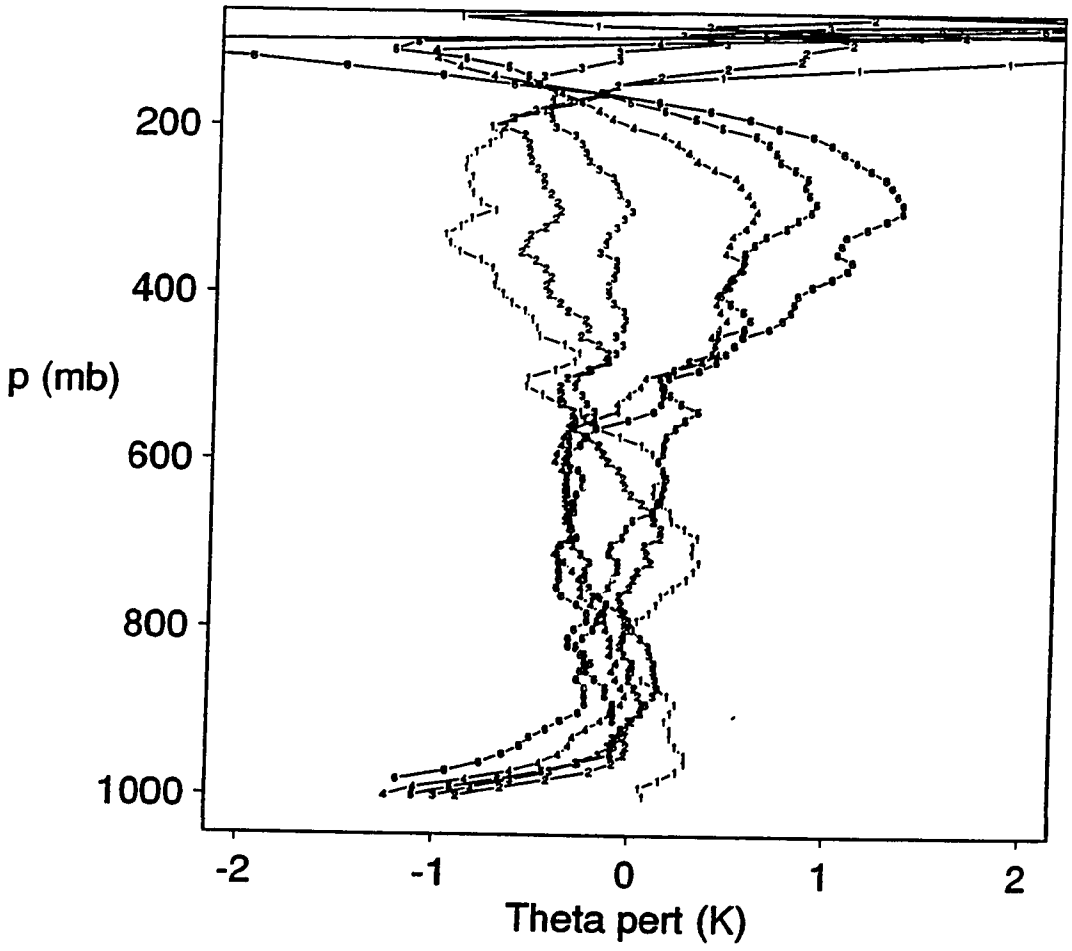


Fig. 5.1 : Potential temperature deviations of daily-mean soundings, relative to the ship-mean sounding, for the six composite categories described in Fig. 4.7.

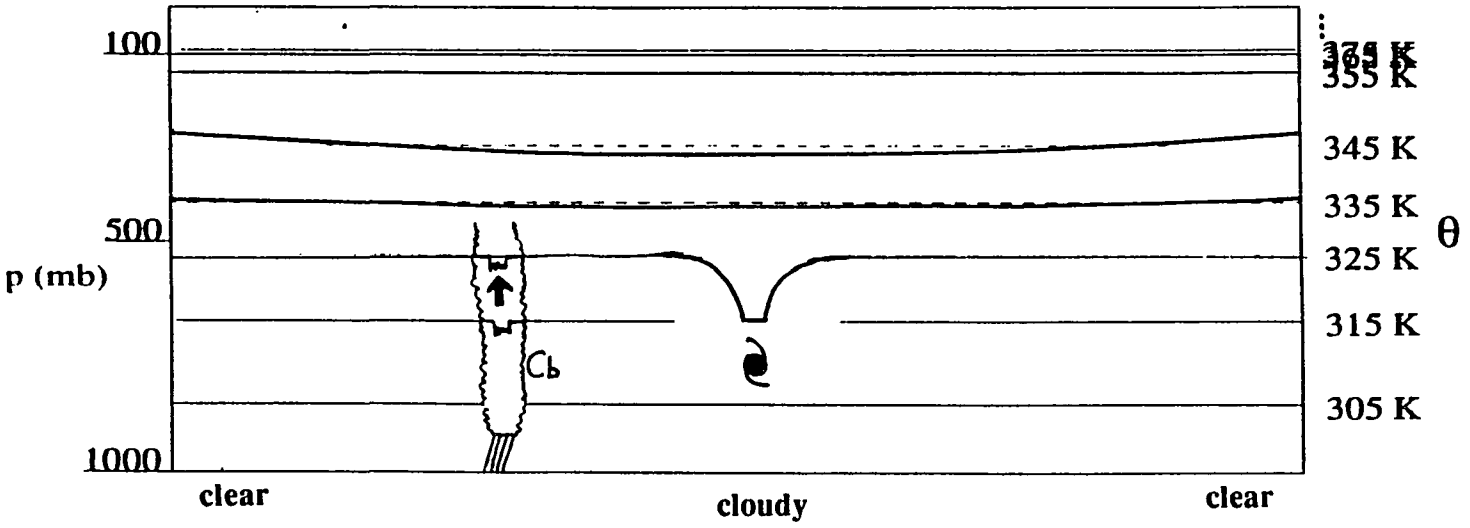


Fig. 5.2 : Isentropic disturbance, in a pressure-coordinate diagram, corresponding to the potential temperature variation in Fig. 5.1. The thin and dashed horizontal lines are mean isentrope positions, while the heavier lines at 335 and 345 °K indicate the bending of those isentropes across a schematic monsoon depression. Hurricane and convective cell disturbances of the isentropes, inferred from aircraft measurements, are also indicated.

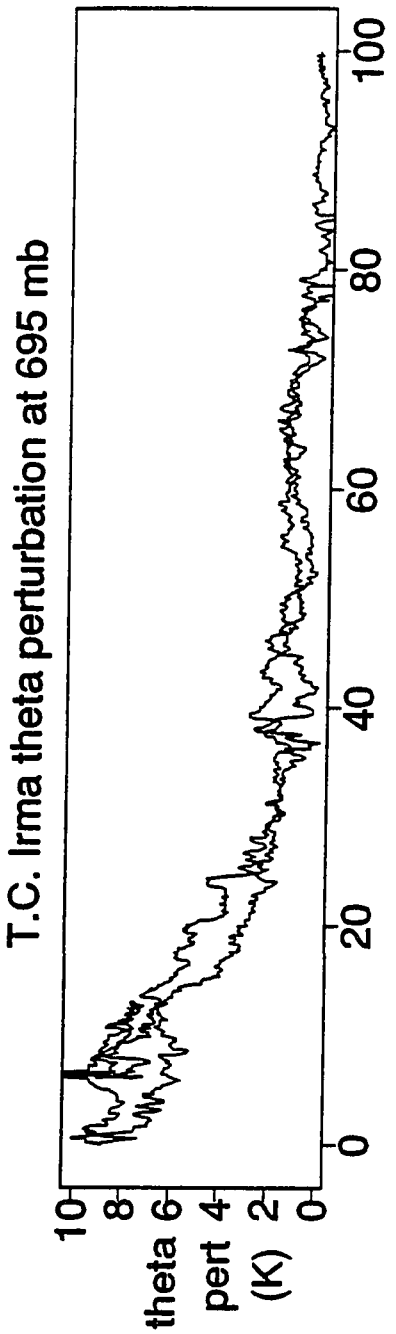


Fig. 5.3 : Cyclone Irma's potential temperature deviations from the ship mean sounding, from P3 data on EMEX flight 5.

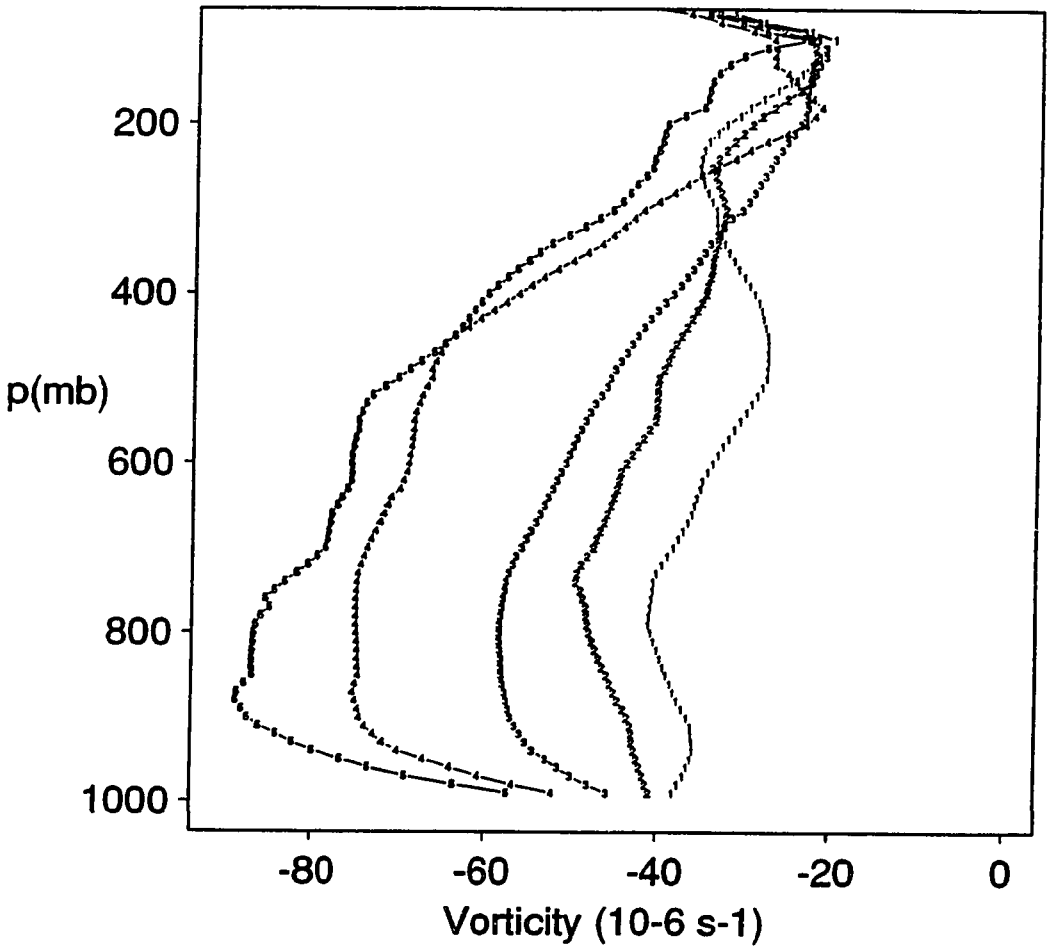


Fig. 5.4 : Mean absolute vorticity profiles (f + circulation around the Gulf of Carpentaria sounding array), for 5 composite categories based on PHC in a 600 km square area centered in the Gulf. Category 1: 0-5%; 2: 5-10%; 3: 10-20%; 4: 20-30%; 5: >30%.

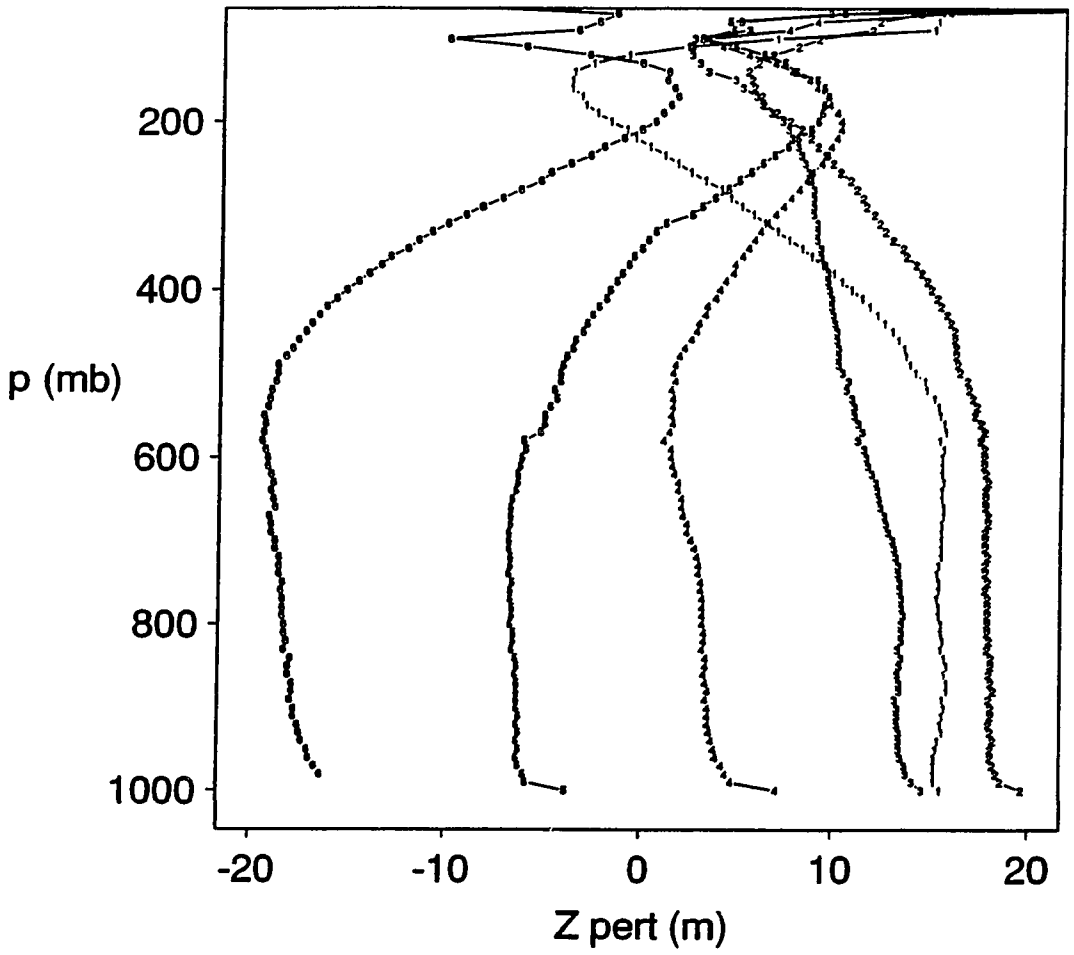


Fig. 5.5 : Geopotential height deviations, relative to the ship-mean sounding, for the composite soundings of Fig. 5.1.

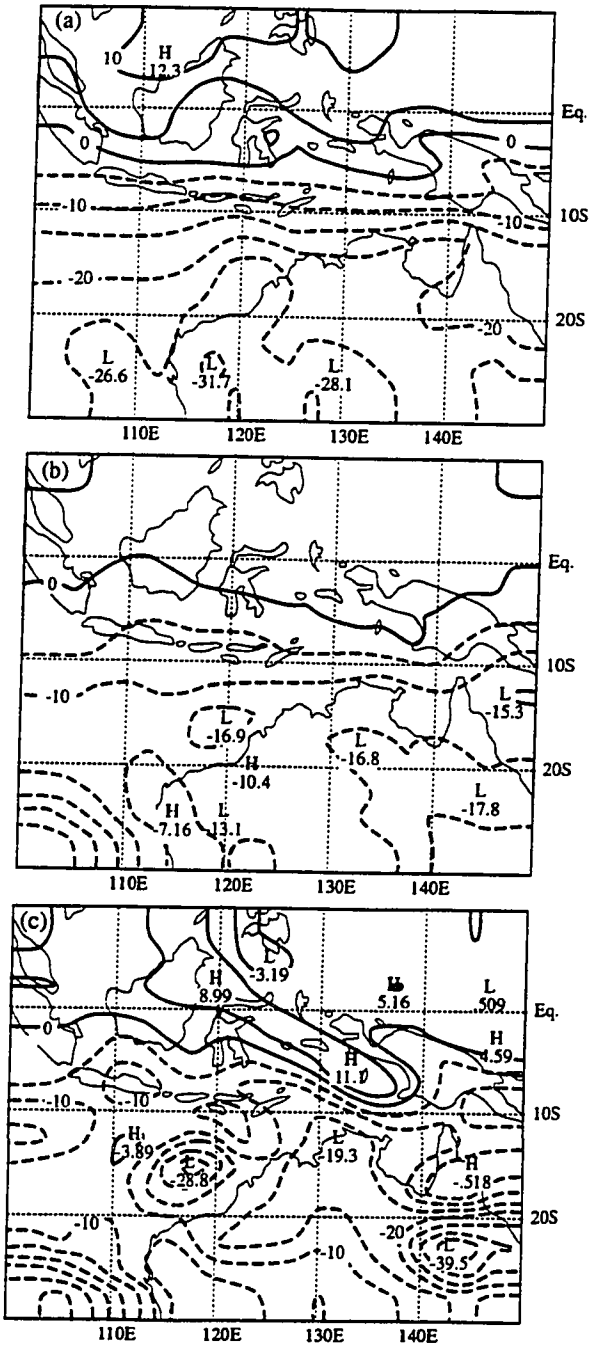


Fig. 5.6 : Absolute vorticity, from ECMWF analyses, in "rest latitude" units (the latitude in degrees at which the planetary vorticity has the given value). a) mean for the period 14 January - 3 February at 850 mb. b) mean for the period 14 January - 3 February at 200 mb. c) mean for the period 1-3 February 1987 at 200 mb.

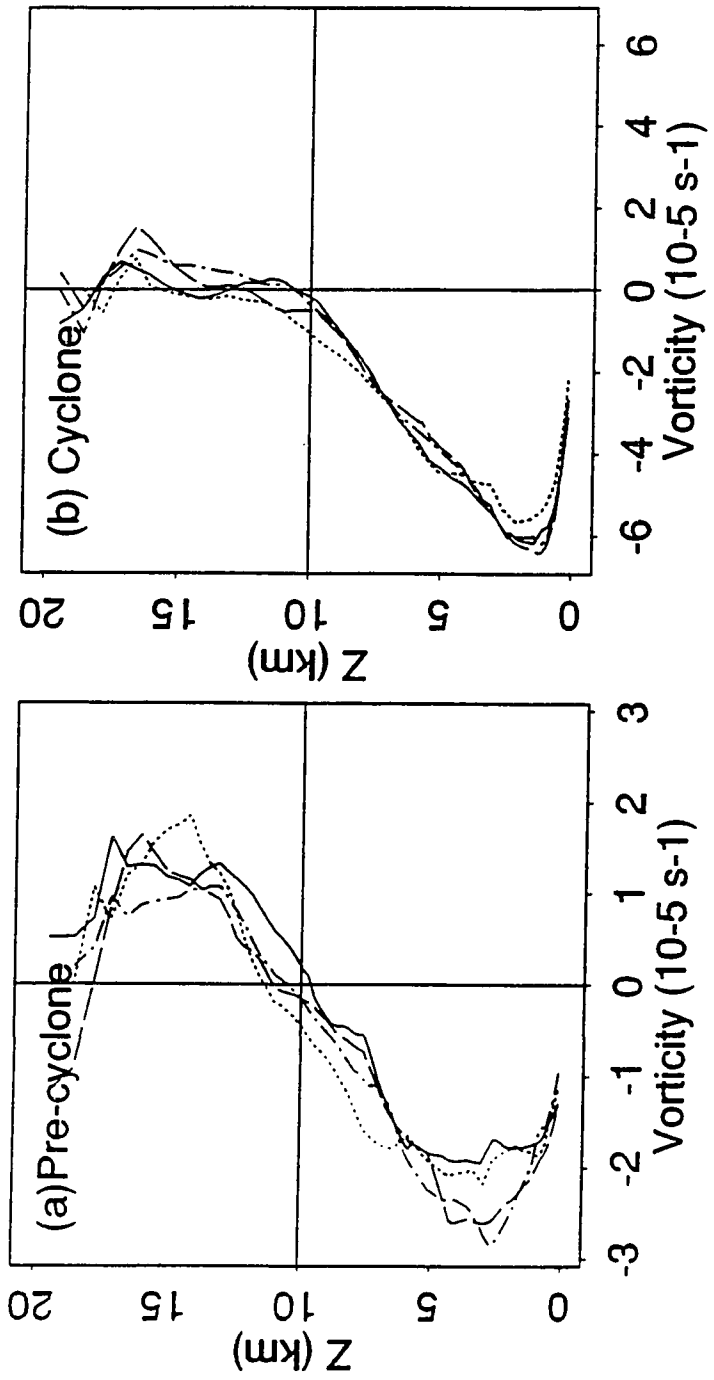


Fig. 5.7 : Vorticity profiles for the Gulf of Carpentaria. The four curves are for the four times of day [5 GMT (afternoon) solid, 11 GMT (nightfall) dotted, 17 GMT (after midnight) dashed, 23 GMT (morning) dash-dotted]. a) Pre-cyclone active periods 15-17 Jan. and 30 Jan. to 4 Feb. 1987. b) Cyclone periods 18-20 Jan. and 7-13 Feb. 1987.

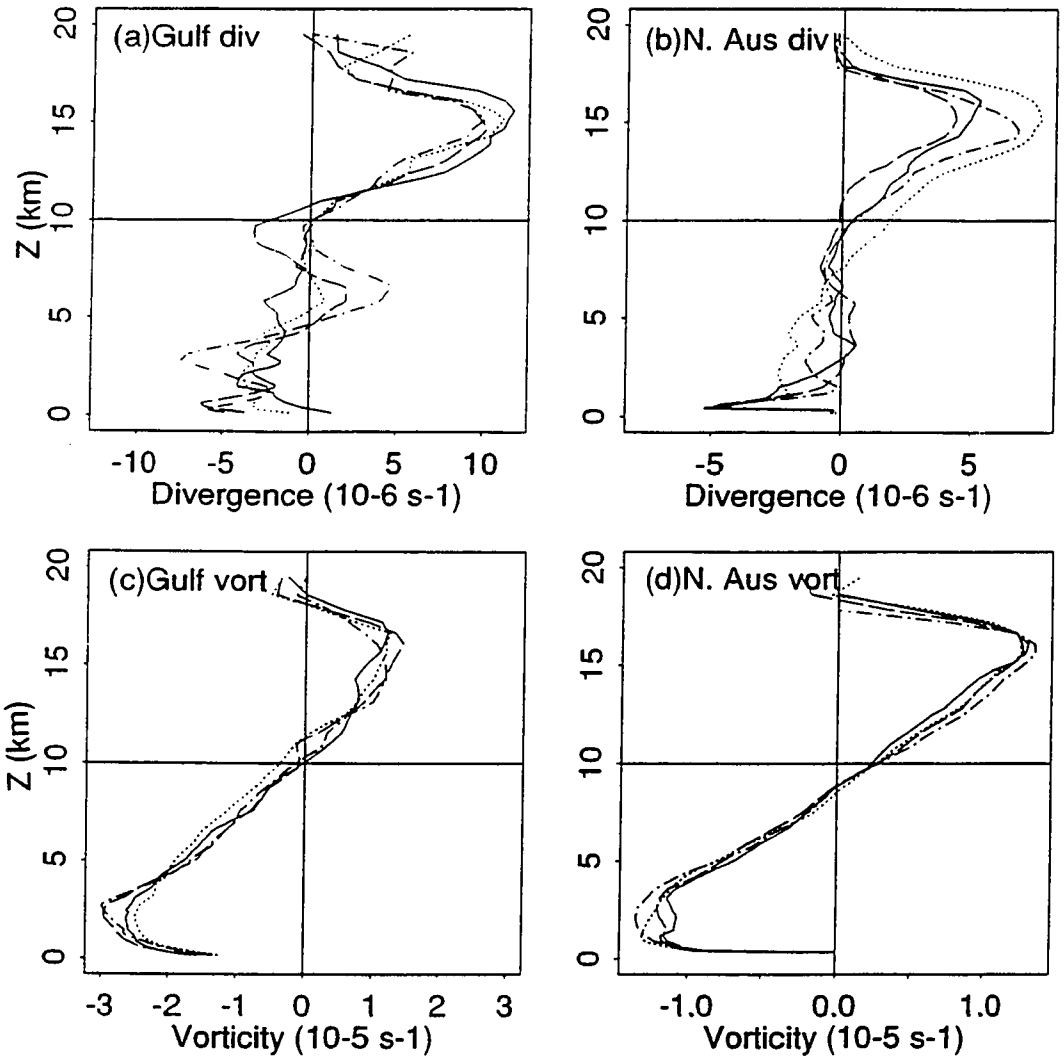


Fig. 5.8 : Mean divergence (top) and vorticity (bottom) profiles, during all of AMEX (14 Jan. - 15 Feb. 1987) for the Gulf of Carpentaria (left) and larger North Australia (right) rawinsonde arrays. The four curves are the four times of day, as in Fig. 5.7.

## AFTERWORD

In this dissertation I have attempted to portray the monsoon as a circulation arising from thermal forcing by embedded MCSs (as expressed in horizontal wind divergence). The mechanism of response of a stratified fluid to thermal forcing with complex vertical structure was laid out in chapter 2. In chapter 3, divergence profiles in the convective, intermediary, and stratiform sub-parts of MCSs were shown to be surprisingly similar in all nine observed MCSs, in all synoptic environments within the monsoon. Mesoscale analyses of the MCSs showed how the stratiform precipitation areas evolved from earlier deep convective cells, which in turn tended to occur in lines along the boundaries of convective downdraft outflow air at the surface. This quasi-universal temporal sequence of events was shown to give rise to a diverse menagerie of MCS spatial structures, depending on environmental wind conditions. Chapter 4 examined the difficult and still unsolved question of why the monsoon convection occurs when and where it does. Positive feedbacks abound, suggesting that once the monsoon gets triggered, it "runs away." Chapter 5 outlined the mechanisms by which the collective effects of MCSs led to the observed vorticity (or PV) structure of the monsoon.

Outstanding questions which remain include: Exactly how much "intermediary" and "stratiform" precipitation (with their characteristic divergence profiles) does a unit of "convective" activity (as measured by, say, mass flux) give rise to? Does it vary with mesoscale organization? Why does convection occur when and where it does? Is the monsoon (amount of rain, kinetic energy, *etc.*) chaotic and sensitive to small features of the initial conditions (within climatic constraints), or is it controlled by hard to observe but inescapable large-scale processes? In other words, is it predictable?

Some of these questions can be addressed in the upcoming TOGA-COARE field program. A well-planned airborne Doppler radar program could easily measure mean divergence profiles on the scale of whole MCS's. A high-quality sounding data set, with high resolution at low levels and detailed notes about the mesoscale environments into which each sonde is launched, could at last answer the age-old question of whether large-scale upward displacements precede or "force" tropical convection.

I hope that this work has increased human comprehension of that tiny part of the tropical troposphere's mystery which lies within the realm of the measurable.

## BIBLIOGRAPHY


Arakawa, A., and W.H. Schubert, 1974: Interaction of a cumulus cloud ensemble with the large-scale environment, Part I. *J. Atm. Sci.*, **31**, 674-701.

Aspliden, C.I., 1976: A classification of the structure of the tropical atmosphere and related energy fluxes. *J. Appl. Met.*, **15**, 692-697.

Balsley, B.B., Ecklund, W.L., Carter, D.A., Riddle, A.C., and K.S. Gage, 1988: Average vertical motions in the tropical atmosphere observed by a radar wind profiler on Pohnpei (7°N latitude, 157 °E longitude). *J. Atm. Sci.*, **45**, 396-405.

Barnes, G.M., and M. Garstang, 1982: Subcloud layer energetics of precipitating convection. *Mon. Wea. Rev.*, **110**, 102-117.

Barnes, G.M., E.J. Zipser, D. Jorgensen, and F. Marks, Jr., 1983: Mesoscale and convective structure of a hurricane rainband, *J. Atmos. Sci.*, **40**, 2125-2137.

Betts, A.K., 1974: Thermodynamic classification of tropical convective soundings. *Mon. Wea. Rev.*, **102**, 760-764.

Betts, A.K., 1990: Greenhouse warming and the tropical water budget. *Bull. Amer. Meteor. Soc.*, **71**, 1464-1465.

Bograd, S.J., 1989: *The mesoscale structure of precipitation in EMEX cloud clusters.* M.S. thesis, University of Washington.

Bretherton, C.S., 1987: A mathematical model of nonprecipitating convection between two parallel plates. *J. Atm. Sci.*, **44**, 1809-1827.

Bretherton, C.S., and P.K. Smolarkiewicz, 1989: Gravity waves, compensating subsidence, and detrainment and detrainment around cumulus clouds. *J. Atm. Sci.*, **46**, 740-759.

Chang, C.-P., 1970: Westward propagating cloud patterns in the tropical Pacific as seen fron time composite satellite photographs. *J. Atm. Sci.*, **27**, 133-138.

Chang, C.-P., and H. Lim, 1988: Kelvin wave-CISK: a possible mechanism for the 30-50 day oscillations. *J. Atm. Sci.*, **45**, 1709-1720.

Charney, J.G., 1963: A note on large-scale motions in the tropics. *J. Atm. Sci.*, **30**, 1100-1111.

Charney, J.G., and A. Eliassen, 1964: On the growth of the hurricane depression. *J. Atm. Sci.*, **21**, 68-75.

Cho, H.-R., L. Cheng, and R.M. Bloxam, 1979: The representation of cumulus cloud effects in the large-scale vorticity equation. *J. Atm. Sci.*, **36**, 127-139.

Cho, H.-R., and L. Cheng, 1980: Parameterization of horizontal transport of vorticity by cumulus convection. *J. Atm. Sci.*, **37**, 812-826.

Cho, H.-R., and M.A. Jenkins, 1987: The thermal structure of tropical easterly waves. *J. Atm. Sci.*, **44**, 2531-2539.

Cho, H.-R., 1985: Rates of entrainment and detrainment of of momentum of cumulus clouds. *Mon. Wea. Rev.*, **113**, 1920-1932.

Chu, J.-H., M. Yanai, and C.-H. Sui, 1981: Effects of cumulus convection on the vorticity field in the tropics. Part I: the large-scale budget. *J. Met. Soc. Japan*, **59**, 535-546.

Cohen, C., and W.M. Frank, 1989: A nemerical study of lapse-rate adjustments in the tropical atmosphere. *Mon. Wea. Rev.*, **117**, 1891-1905.

Cox, S.K., and K.T. Griffith, 1979: Estimates of radiative divergence during phase III of the GARP Atlantic Tropical Experiment. Part II. Analysis of the phase III results. *J. Atm. Sci.*, **36**, 586-601.

Davidson, N.E., and G.J. Holland, 1987: A diagnostic analysis of two intense monsoon depressions over Australia. *Mon. Wea. Rev.*, **115**, 380-392.

Davidson, N.E., G.J. Holland, J.L. McBride and T.D. Keenan, 1990: On the formation of AMEX cyclones Irma and Jason. *Mon. Wea. Rev.*, **118**, 1981-2000.

Dudhia, J., and M.W. Moncrieff 1987: A numerical simulation of quasi-stationary tropical convective bands. *Quart. J. Roy. Meteor. Soc.*, **113**, 929-967.

Durran, D.R., and R.L. Grossman, 1984: Interaction of low-level flow with the Western Ghat mountains and offshore convection in the summer monsoon. *Mon. Wea. Rev.*, **112**, 652-672.

Elliott, W.P., and D.J. Gaffen, 1991: On the utility of radiosonde humidity archives for climate studies. *Bull. Amer. Met. Soc.*, **72**, 1507-1520.

Emanuel, K.A., 1986: An air-sea interaction theory for tropical cyclones. Part I: Steady state maintenance. *J. Atmos. Sci.*, **44**, 585-604.

Emanuel, K.A., 1987: An air-sea interaction model of intraseasonal oscillation in the tropics. *J. Atmos. Sci.*, **44**, 2324-2340.

Emanuel, K.A., 1988: A scheme for representing cumulus convection in large-scale models. *J. Atmos. Sci.*, **48**, 2313-2335.

Esbensen, S.K., L.J. Shapiro, and E.I. Tollerud, 1987: The consistent parameterization of the effects of cumulus clouds on the large-scale momentum and vorticity fields. *Mon. Wea. Rev.*, **115**, 664-669.

Fitzjarrald, D.R., and M. Garstang, 1981a: Vertical structure of the tropical boundary layer. *Mon. Wea. Rev.*, **109**, 1512-1526.

Fitzjarrald, D.R., and M. Garstang, 1981b: Boundary layer growth over the tropical ocean. *Mon. Wea. Rev.*, **109**, 1762-1772.

Frank, W.M., 1978: The life cycles of GATE convective systems. *J. Atm. Sci.*, **35**, 1256-1264.

Frank, W.M., 1980: Modulation of the net tropospheric temperature during GATE. *J. Atm. Sci.*, **37**, 1056-1064.

Frank, W.M., and J.L. McBride, 1989: The vertical distribution of heating in AMEX and GATE cloud clusters. *J. Atm. Sci.*, **46**, 3464-3478.

Gaynor, J.E., and C.F. Ropelewski, 1979: Analysis of the convectively modified GATE boundary layer using *in situ* and acoustic sounder data. *Mon. Wea. Rev.*, **107**, 985-993.

Gamache, J.F., F.D. Marks, Jr., and R.W. Burpee, 1987: EMEX data report: The Equatorial Mesoscale Experiment. AOML/HRD Report, National Oceanic and Atmospheric Administration, Atlantic Oceanographic and Meteorological Laboratory, Hurricane Research Division,4301 Rickenbacker Causeway,Miami, FL 33149, USA.

Geisler, J.E., and D.E. Stevens, 1982: On the vertical structure of damped steady circulation in the tropics. *Q. J. Roy. Meteor. Soc.*, **108**, 87-93.

Gill, A.E., 1982: *Atmosphere-Ocean Dynamics*. Academic Press, San Diego. 662pp.

Gill, A.E., 1980: Some simple solutions for heat-induced tropical circulation. *Quart. J. Roy. Meteor. Soc.*, **106**, 447-462.

Gordon, N.D., 1981: Comments on: A three-dimensional model of an isolated thunderstorm. *J. Atm. Sci.*, **38**, 1798.

Gunn, B.W., J.L. McBride, G.J. Holland, T.D. Keenan, and N.E. Davidson, 1989: The Australian summer monsoon circulation during AMEX Phase II. *Mon. Wea. Rev.*, **117**, 2554-2574.

Haynes, P.H., and M.E. McIntyre, 1987: On the evolution of vorticity and potential vorticity in the presence of diabatic heating and frictional or other forces. *J. Atm. Sci.*, **44**, 828-841.

Haynes, P.H., and M.E. McIntyre, 1990: On the conservation and impermeability theorems for potential vorticity. *J. Atm. Sci.*, **47**, 2021-2033.

Hendon, H.H., N.E. Davidson, and B.W. Gunn, 1989: Australian summer monsoon onset during AMEX 1987. *Mon. Wea. Rev.*, **117**, 370-390.

Hendon, H.H., and B. Liebmann, 1990: A composite study of the onset of the Australian summer monsoon. *J. Atm. Sci.*, **47**, 2227-2240.

Holland, G.J., 1986: Interannual variability of the Australian summer monsoon at Darwin: 1952-82. *Mon. Wea. Rev.*, **114**, 594-604.

Holton, J.R., 1972: A one-dimensional cumulus model with anelastic pressure forces. *Dynamics of the tropical atmosphere*, NCAR summer colloquium notes.

Holton, J.R., and D.E. Colton, 1972: A diagnostic study of the vorticity balance at 200 mb in thhe tropics during northern summer. *J. Atmos. Sci.*, **29**, 1124-1128.

Hoskins, B.J., M.E. McIntyre, and A.W. Robertson, 1985: On the use and significance of isentropic potential vorticity maps. *Quart. J. Roy. Meteor. Soc.*, **111**, 877-946.

Houze, R.A., Jr., 1977: Structure and dynamics of a tropical squall-line system. *Mon. Wea. Rev.*, **105**, 1540-1567.

Houze, R.A. Jr., and A.K. Betts, 1981a: Convection in GATE. *Rev. Geoph. Space Phys.*, **19**, 541-576.

Houze, R.A., Jr., S.G. Geotis, F.D. Marks, Jr., and A.K. West, 1981b: Winter monsoon convection in the vicinity of north Borneo, Part I: Structure and time variation of the clouds and precipitation. *Mon. Wea. Rev.*, **109**, 1595-1614.

Houze, R.A., Jr., 1982: Cloud clusters and large-scale vertical motions in the tropics. *J. Meteor. Soc. Jap.*, **60**, 396-410.

Houze, R.A., Jr., and E.N. Rappaport, 1984: Air motions and precipitation structure of an early summer squall line over the eastern tropical Atlantic. *J. Atmos. Sci.*, **41**, 553-574.

Houze, R.A., Jr., 1989: Observed structure of mesoscale convective systems and implications for large-scale heating. *Q. J. Roy. Meteor. Soc.*, **115**, 425-461.

Janowiak, J.E., and P.A. Arkin, 1991: Rainfall variations in the tropics during 1986-1989, as estimated from observations of cloud-top tempearture. *J. Geophys. Res*, **96** (supplenment), 3359-3374.

Johnson, R.H., and D.C. Kriete, 1982: Thermodynamic and circulation characteristics of winter monsoon tropical mesoscale convection. *Mon. Wea. Rev.*, **110**, 1898-1911.

Johnson, R.H., and M.E. Nicholls, 1983: A composite analysis of the boundary layer accompanying a tropical squall line. *Mon. Wea. Rev.*, **111**, 308-319.

Johnson, R., and R.A. Houze, Jr., 1987: Precipitating cloud systems of the Asian monsoon. *Monsoon Meteorology*, C. P. Chang and T. N. Krishnamurti, Eds., Oxford University Press, pp. 298-353.

Johnson, R.H., W.A. Gallus, Jr., and M.D. Vescio, 1991: Near-tropopause vertical motion in the trailing stratiform region of a midlatitude squall line. *J. Atmos. Sci.*, **47**, 2200-2210.

Jorgenson, D.P., and M.A. LeMone, 1989: Vertical velocity characteristict of oceanic convection. *J. Atmos. Sci.*, **46**, 621-640.

Keenan, T. D., and L.R. Brody, 1988: Synoptic-scale modulation of convection during the Australian summer monsoon. *Mon. Wea. Rev.*, **116**, 71-85.

Keenan, T.D., J. McBride, G. Holland, N. Davidson, and B. Gunn, 1989: Diurnal variations during the Australian Monsoon Experiment (AMEX) Phase II. *Mon. Wea. Rev.*, **117**, 2535-2552.

Keyser, D., and R. Rotunno, 1990: On the formation of potential vorticity anomalies in upper-level jet front systems. *Mon. Wea. Rev.*, **118**, 1914-1921.

Leary, C.A., and R.A. Houze, Jr., 1979: The structure and evolution of convection in a tropical cloud cluster. *J. Atmos. Sci.*, **36**, 437-457.

LeMone, M.A., 1983: Momentum transport by a line of cumulonimbus. *J. Atmos. Sci.*, **40**, 1815-1834.

LeMone, M.A., G.M. Barnes and E.J. Zipser, 1984: Momentum flux by lines of cumulonimbus over the tropical oceans. *J. Atmos. Sci.*, **41**, 1914-1932.

Lewis, R.M., and R.J. Reed, 1984: Comments on "Modulation of convective activity by large-scale flow patterns observed in GATE." *J. Atmos. Sci.*, **41**, 305-307.

Lilly, D.K., 1988: Cirrus outflow dynamics. *J. Atm. Sci.*, **45**, 1594-1605.

Lindzen, R.S., and A.Y. Hou, 1988: Hadley circulations for zonally averaged heating centered off the equator. *J. Atmos. Sci.*, **45**, 2416-2427.

Lipps, F.B., 1990: On the anelastic approximation for deep convection. *J. Atmos. Sci.*, **47**, 1794-1798.

Mapes, B., and R.A. Houze, Jr., 1992a: An integrated view of the 1987 Australian monsoon and its mesoscale convective systems. Part I: Horizontal structure. *Q. J. Roy. Meteor. Soc.*, in press.

Mapes, B., and R.A. Houze, Jr., 1992b: An integrated view of the 1987 Australian monsoon and its mesoscale convective systems. Part II: Vertical structure. *Q. J. Roy. Meteor. Soc.*, submitted.

Mapes, B., and R.A. Houze, Jr., 1992c: Cloud clusters and superclusters over the oceanic warm pool. In preparation.

Mapes, B.E., 1992: Inviscid CISK and the superclustering of tropical convection. *J. Atm. Sci.*, submitted.

Marks, F.D., and R.A. Houze, Jr., 1987: Inner core structure of hurricane Alicia from airborne Doppler radar observations. *J. Atm. Sci.*, **44**, 1296-1317.

McBride, J. L., 1987: The Australian Monsoon. *Monsoon Meteorology*, C. P. Chang and T. N. Krishnamurti, Eds., Oxford University Press, pp. 203-230.

Nakazawa, T., 1988: Tropical super clusters within intraseasonal variations over the western Pacific. *J. Met. Soc. Japan*, **66**, 823-839.

Neelin, J.D., I.M. Held, and K.H. Cook, 1987: Evaporation-wind feedback and low-frequency variability in the tropical atmosphere. *J. Atmos. Sci.*, **44**, 2341-2348.

Nicholls, M.E., and R.H. Johnson, 1984: A model of a tropical squall line boundary layer wake. *J. Atm. Sci.*, **41**, 2774-2792.

Nicholls, M.E., R.A. Pielke, and W.R. Cotton, 1991: Thermally forced gravity waves in an atmosphere at rest. *J. Atm. Sci.*, **48**, 1869-1884.

Ogura, Y., and M. Yoshizaki, 1988: Numerical study of orographic-convective precipitation over the eastern Arabian sea and the Ghat mountains during the summer monsoon. *J. Atmos. Sci.*, **45**, 2097-2122.

Ooyama, K., 1971: A theory on parameterization of cumulus convection. *J. Met. Soc. Japan*, **49**, 744-756.

Ooyama, K.V., 1987: Scale-controlled objective analysis. *Mon. Wea. Rev.*, **115**, 2479-2506.

Pearce, R.P., and J.B. Omotosho, 1986: An analysis of convective systems on a 100 km scale during GATE. *Mon. Wea. Rev.*, **114**, 1425-1444.

Powell, M.D., 1990a: Boundary layer structure and dynamics in outer hurricane rainbands. Part I: Mesoscale rainfall and kinematic structure. *Mon. Wea. Rev.*, **118**, 891-917.

Powell, M.D., 1990b: Boundary layer structure and dynamics in outer hurricane rainbands. Part II: Downdraft modification and mixed layer recovery. *Mon. Wea. Rev.*, **118**, 918-938.

Ramage, C.S., 1971: *Monsoon Meteorology*. Academic Press, New York, 271 pp.

Raymond, D.J., 1983: Wave-CISK in mass flux form. *J. Atm. Sci.*, **40**, 2561-2572.

Raymond, D.J., and H. Jiang 1990: A theory for long-lived mesoscale convective systems. *J. Atm. Sci.*, **47**, 3068-3077.

Raymond, D.J., 1992: Nonlinear balance and potential vorticity thinking at large Rossby number. *QJRMS*, submitted.

Reed, R.J., and E.E. Recker, 1971: Structure and propagation of synoptic-scale wave disturbances in the equatorial western Pacific. *J. Atm. Sci.*, **28**, 1117-1133.

Reed, R.J., and R.H. Johnson, 1974: The vorticity budget of synoptic-scale wave disturbances in the tropical western Pacific. *J. Atm. Sci.*, **31**, 1784-1790.

Riehl, H., and J.S. Malkus, 1958: On the heat balance in the equatorial trough zone. *Geophysica*, **6**, 503-538.

Rutlege, S.A., E.R. Williams, and T.D. Keenan, 1992: The Down Under Doppler and Electricity Experiment (DUNDEE): Overview and preliminary results. *Bull. Amer. Meteor. Soc.*, in press.

Ryan, B.F., G.M. Barnes, and E.J. Zipser, 1992: A wide rainband in a developing tropical cyclone. *Mon. Wea. Rev.*, in press.

Salby, M.L., and R.R. Garcia, 1987: Transient response to localized episodic heating in the tropics. Part I: Excitation and short-time near-field behavior. *J. Atm. Sci.*, **44**, 458-498.

Sardeshmukh, P.D., and I.M. Held, 1984: The vorticity balance in the tropical upper troposphere of a general circulation model. *J. Atm. Sci.*, **41**, 768-777.

Sardeshmukh, P.D., and B.J. Hoskins, 1985: Vorticity balances in the tropics during the 1982-83 El Nino-Southern Oscillation event. *Q.J. Roy. Meteor. Soc.*, **111**, 261-278.

Sardeshmukh, P.D., and B.J. Hoskins, 1987: On the derivation of the divergent flow from the rotational flow: the $\chi$ problem. *Quart. J. Roy. Meteor. Soc.*, **113**, 339-360.

Sardeshmukh, P.D., and B.J. Hoskins, 1988: The generation of global rotational flow by steady idealized tropical divergence. *J. Atm. Sci.*, **45**, 1228-1251.

Silva Dias, P.L., W.H. Schubert, and M. DeMaria, 1983: Large-scale response of the tropical atmosphere to transient convection. *J. Atm. Sci.*, **40**, 2689-2707.

Schubert, W.H., P.E. Ciesielski, D.E. Stevens, and H. Kuo, 1991: Potential vorticity modeling of the ITCZ and the Hadley circulation. *J. Atm. Sci.*, **48**, 1493-1509.

Schlesinger, R.E., 1980: A three-dimensional model of an isolated thunderstorm. Part II: Dynamics of updraft splitting and mesovortex evolution *J. Atm. Sci.*, **37**, 395-420.

Schneider, E.K., and R.S. Lindzen, 1976: A discussion of the parameterization of momentum exchange by cumulus convection. *J. Geophys. Res.*, **81**, 3158-3160.

Shapiro, L.J., 1978: The vorticity budget of a composite Afriacl easterly wave disturbance. *Mon. Wea. Rev.*, **106**, 806-817.

Smull, B.F., and R.A. Houze, Jr., 1987: Rear inflow in squall lines with trailing stratiform precipitation. *Mon. Wea. Rev.*, **115**, 2128-2148.

Srivastava, R.C., T.J Matejka, and T.J. Lorello, 1985: Doppler radar study of the trailing anvil region associated with a squall line. *J. Atm. Sci.*, **43**, 356-377.

Stevens, D.E., 1979: Vorticity, momentum, and divergence budgets of synoptic-scale wave disturbances in the tropical eastern Atlantic. *Mon. Wea. Rev.*, **107**, 535-550.

Sui, C.-H., and M. Yanai, 1986: Cumulus ensemble effects on the large-scale vorticity and momentum fields of GATE. Part I: Observational evidence. *J. Atm. Sci.*, **41**, 1618-1642.

Sui, C.-H., M.-D. Cheng, X. Wu, and M. Yanai, 1989: Cumulus ensemble effects on the large-scale vorticity and momentum fields of GATE. Part I: Parameterization. *J. Atm. Sci.*, **46**, 1609-1629.

Thompson, R.M., Jr., S.W. Payne, E.E. Recker, and R.J. Reed, 1979: Structure and properties of synoptic-scale wave disturbances in the intertropical convergence zone of the eastern Atlantic. *J. Atmos. Sci.*, **36**, 53-72.

Tollerud, E.I., and S.K. Esbensen, 1983: An observational study of the upper-tropospheric vorticity fields in GATE cloud clusters. *Mon. Wea. Rev.*, **111**, 2161-2175.

Webster, P.J., 1987: The Elementary Monsoon. *Monsoons*, J. S. Fein and P. L. Stephens, Eds., Wiley Interscience, pp. 3-32.

Webster, P.J., and R.A. Houze, Jr., 1991: The Equatorial Mesoscale Experiment (EMEX): An overview. *Bull. Amer. Meteor. Soc.*, **72**, 1481-1505.

Webster, P.J., and G.L. Stephens, 1980: Tropical upper-tropospheric extended clouds: Inferences from Winter Monex. *J. Atm. Sci.*, **37**, 1521-1541.

Weisman, M.L., and J.B. Klemp, 1986: Characteristics of isolated convective storms. *Mesoscale Meteorology and Forecasting*. AMS, Boston.

Williams, M., and R.A. Houze, Jr., 1987: Satellite-observed characteristics of winter monsoon cloud clusters. *Mon. Wea. Rev.*, **115**, 505-519.

Xu, K.-M, and K.A. Emanuel, 1989: Is the tropical atmosphere conditionally unstable? *Mon. Wea. Rev.*, **117**, 1471-1479.

Yanai, M., S. Esbensen, and J.-H. Chu, 1973: Determination of bulk properties of tropical cloud clusters from large-scale heat and moisture budgets. *J. Atm. Sci.*, **30**, 611-627.

Yanai, M., C.-H. Sui, and J.-H. Chu, 1982: Effects of cumulus convection on the vorticity field in the tropics. Part II: interpretation. *J. Met. Soc. Japan*, **60**, 411-424.

Yanai, M., and R.H. Johnson, 1992: Impacts of cumulus convection on thermodynamic fields. *Cumulus Parameterization*, AMS monograph (in production).

Young, J.A., 1972: A simple model relating anelastic pressure and buoyancy. *Dynamics of the tropical atmosphere*, NCAR summer colloquium notes.

Zipser, E.J., 1969: The role of unsaturated convective downdrafts in the structure and rapid deacy of an equatorial disturbance. *J. Appl. Meteor.*, **8**, 799-814.

Zipser, E.J., 1977: Mesoscale and convective-scale downdrafts as distinct components of squall-line circulation. *Mon. Wea. Rev.*, **105**, 1568-1589.

Zipser, E.J., and C. Gautier, 1978: Mesoscale events within a GATE tropical depression. *Mon. Wea. Rev.*, **106**, 789-805.

## VITA

Brian Mapes was born February 2, 1964 in Pueblo, Colorado. He graduated from Boulder High School, Boulder, Colorado, and completed a BS degree in Chemistry at the Califronia Institute of Technology in 1985. He spent one semester at the University of Colorado, then entered the University of Washington in Autumn 1986.